DOCTOR OF PHILOSOPHY

Advanced multiphase flow monitoring through electromagnetic measurements

Arellano, Yessica

Award date:
2020

Awarding institution:
Coventry University

Advanced multiphase flow monitoring through electromagnetic measurements

By

Yessica Alexandra Arellano Prieto

PhD

February 2020

Advanced multiphase flow monitoring through electromagnetic measurements

By

Yessica Alexandra Arellano Prieto

February 2020

Coventry University

A thesis submitted in partial fulfilment of the University's requirements for the Degree of Doctor of Philosophy

Certificate of Ethical Approval

Applicant:

Yessica Arellano-Prieto

Project Title:

Advanced multiphase flow monitoring through electromagnetic measurements

This is to certify that the above named applicant has completed the Coventry University Ethical Approval process and their project has been confirmed and approved as Medium Risk

Date of approval:

02 October 2019

Project Reference Number:

P94861

Content removed on data protection grounds.

Abstract

Electrical tomography relies on a new generation of non-intrusive soft-field imaging modality which is used for imaging internal material distribution. The main purpose of this research is to investigate the feasibility of using electrical tomography for multiphase flow measurement within the petroleum industry. Accurate in-line multiphase flow measurement is of paramount relevance for the industry to face the current global oil market challenges due to its potential to decrease operational and development costs.

The use of tomography techniques for multiphase flow measurement in the petroleum industry, which has not been fully explored in the literature, provides opportunities to extract key information that can assist with the fundamental understanding of multiphase flows that are found at various stages between the well and the service station pump. Tomography based measurements can be used to improve, develop, or validate empirical flow transport equations as well as to enhance measurement accuracy.

This work is focused on the design and application of an electromagnetic induction meter and an electrical capacitance tomography system for the investigation of co-current hydrocarbon flow in horizontal pipelines. It has been conjectured that magnetic induction tomography may eventually be an attractive and low-cost alternative to multiphase flow imaging. The work addresses the challenges of multiphase flow measurement and gives an insight into the use of tomography technologies for flow regimes identification, *in situ* phase fractions, and flow velocity information. This is achieved by numerical modelling and experimental work.

The developed electromagnetic induction-based meter consists of a novel hardware design and data analysis approach which allows the simultaneous extraction of information of conductive and non-conductive fluid species whose electrical properties correspond directly to real field industrial applications.

In this work, interface profiles are extracted from tomography measurements which allows instantaneous flow pattern identification. Analysis of the experimental data reveals a recently studied intermittent flow regime structure, whose interactions between the fluids are detailed. The distribution of the phases was found to depend on the inlet conditions and the ratio of inertial to gravity forces given by the Froude number. This characterisation of the flow structures has a significant effect on the flow transitions with potential extended.

Results of this work broaden the operational limits of both electrical capacitance tomography (ECT) and electromagnetic induction tomography (MIT) by enlarging their operational envelopes. It is concluded that provided the noise in the data acquisition system remains within a certain level, single-

pair electrical capacitance measurements can be used for non-intrusive measurement of flow with high water contents within a conduit. Furthermore, MIT has the potential to differentiate between non-conductive species for bulk conductivities below 0.6 Sm^{-1}. However, imaging small permittivity changes in a conductive medium is unfeasible, as the changes in conductivity dominate the induced signal. This problem may be overcome by using a multimodal approach combining ECT and MIT for low and high-water contents, respectively.

To my loved family, the Arellano Prieto, the extended Prietos, and the Cabas

Acknowledgement

This acknowledgement is my way to thank the people, who in their own way, held my hand through this journey. Because a PhD is not a journey one can complete on one's own. This is my letter of appreciation to all of you.

First and foremost, my roots, my pillars, my family. You shaped me to believe in dreams and hard work. Mami, Papi, Ale, a lifetime will not be enough to pay back all the support and unconditional love.

My supervisor, Dr Andy Hunt, for the confidence placed in me. For giving me the opportunity to cross metaphorical and literal frontiers. Your expertise, brightness, and hands-on approach significantly shaped my vision and development as a researcher. Without your human quality, your mentorship, and your enthusiasm for science, this path would not have been as exciting or enriching, professionally nor personally.

Also inspiring has been the collaboration with Dr Lu Ma. A bright and respected young scientist in the tomography community. Lu, I feel this PhD would not have been possible without the strategic vision, attention to detail and emphasis on quality that you attach to your work. I have been inspired for the future by your work ethics and dedication to science.

Dr Olivier Haas, to you I'm indebted for sharing your knowledge and for always making time for me. I value your thorough, challenging, out-of-the-box and constructive feedback in all the different stages of my research. It was an absolute pleasure to be supervised by you. I also acknowledge the support of Dr Hafiz Ahmed, who kindly stepped-in to supervise the final stages of my research.

Many thanks to Coventry University for funding this research and to the Doctoral College, for enthusiastically providing me with the necessary tools to carry it out. My gratitude with the family of the Fluids and Complex Systems Research Centre, staff and PhD students. Your support and camaraderie were key in making the work environment one where it provoked to do science. I am particularly thankful to Mr Ian for sharing the lab, his knowledge and tools with me, with Dr Phil for the inspiration and for taking the time to proofread my manuscripts and this thesis, and with Dr Lorna for brilliantly managing us all.

I also thank iPhase for their support in granting me access to their facilities, software, and equipment, which were key for Chapters III, VI and VII. I will always value the opportunity given to me to collaborate with such talented professionals. Many thanks to Atout ltd for providing the equipment for tests in Chapter VI, as well as to Richard Hunt and Lawrence Tom for their collaboration to complete the referred tests. I also owe many thanks, to the University of Bergen for granting the use of the gamma-ray tomography system and laboratory facilities. I would particularly like to acknowledge Stipendiat Stian Stavland and Dr Rashid Ahmed with whom I had many in-depth discussions about various research problems and collaboration ideas, and for making the tests in Chapter VI possible.

Many thanks to NEL management for funding the tests in Chapter VIII, and the NEL team and Dr Hunt for undertaking the practical work. I acknowledge the support of the team from the MultiFlowMetII project, NORCE, and Roxar for supporting the acquisition of the data presented in Chapter VI and to Stein-Arild Tjugum particularly for sharing his insight to the MFM market. I also thank the DTA Energy alliance for broadening my network and providing a vibrant space for high-level research discussion.

Last but not least, my most sincere gratitude to all my friends for walking with me. Knowing you, your cultures, your families, and your hearts was by far the highlight of the ride.

Table of contents

List of Figures

List of Tables

Nomenclature

Symbols:

$\vec{A}$	Magnetic vector potential
$\overrightarrow{A_r}$	Reduced magnetic vector potential
$\overrightarrow{A_s}$	Magnetic vector potential due to the current source
A_{dB}	Absorption loss
$\vec{B}$	Magnetic Flux
c	speed of light
C	Capacitance
$\vec{D}$	Electric displacement or electric flux density
D	Diameter
D_c	Coil outer dimension
d_w	Wire diameter
$\vec{E}$	Electric Field
F_r	Froude Number
F_{rf}	Relative performance parameter
g	Gravitational constant
G	Coil shape index
$\vec{H}$	Magnetic Field
H_i	Incident magnetic Field
H_L	Liquid holdup
H_t	Transmitted magnetic Field
I	Electrical current
$\mathbf{I}$	Identity Matrix
$\mathbf{J}$	Jacobi Matrix
$\vec{J}$	Current density
J_i	Induced current density performance factor
M_{dB}	Multiple reflection loss
$\vec{M}$	Magnetisation vector
$\hat{n}$	Normal vector
n_c	Number of sensors
N	Number of turns
N_{Re}	Reynolds Number
N_{We}	Weber Number
Q	Flowrate
R	Spatial Resolution
R_{dB}	Reflection loss
R_x	Receiving coil
s	Covariance
S_i	Sensitivity performance factor
T_x	Transmitting coil
U_m	Mixture velocity
U_{gs}	Gas superficial velocity
U_{os}	Oil superficial velocity
U_{Ls}	Liquid superficial velocity
V	Voltage
V_i	Voltage performance factor
W_t	Total mass ratio
α	Regularisation parameter

α	Volumetric fraction
δ	Skin depth
ε	Permittivity
γ	Interfacial tension
ϕ	Scalar potential
Γ	Boundary
μ	Fluid Viscosity / Magnetic Permeability
ν	Reluctivity
ν	Velocity
ρ	Density
ρ	Spearman correlation coefficient
σ	Electrical conductivity
φ	Pipe inclination
ω	Angular frequency
Ω	Imaging region

Abbreviations and terms:

AC	Alternating Current
CEM	Computational Electromagnetics
CI	Confidence Interval
CMU	Capacitance Measurement Unit
ECT	Electrical Capacitance Tomography
e.m.f.	Electromotive force
EMT	Electromagnetic Tomography
EMIT	Electromagnetic Inductance Tomography
FE	Finite Element
FEM	Finite Element Method
FS	Full slug
GCS	Gas-core slug
IBC	Impedance Boundary Condition
ID	Inner diameter
IPT	Industrial Process Tomography
LBP	Linear Back Projection
MFM	Multiphase Flow Measurement
MIT	Magnetic Induction Tomography
OD	Outer diameter
PML	Perfectly Matched Layers
PVC	Poly Vinyl Polymer
SE	Shielding Effectiveness
sf	Stand-off distance
TBC	Transition Boundary Condition
VIA	Vertical Interconnected Access
WMS	Wire Mesh Sensor
WTI	West Texas Intermediate is a grade of crude oil used as a benchmark in oil pricing

Glossary terms:

ANOVA. Statistical technique that indicates whether two variables (one independent and one dependent) are related based on whether the means of the dependent variable are different in the categories or groups of the independent variable.

Capacitance. Property of bodies to maintain an electric charge. The capacitance is a measure of the amount of electrical energy stored for a given electrical potential difference.

Coil. Electromagnetic structures constructed form successive turns of wire in the form of a spiral or helix.

Confidence Interval. Measure of the degree of uncertainty in a sampling method by referring to the probability that a population parameter will fall between two set values.

Descriptive statistics. Statistic methods that describe the data.

Electric conductivity. Represents the ability of a material to conduct electric current.

Froude number. Ratio of inertial forces to gravity forces -strongly relevant for wave structures.

Holdup. The volume locally occupied by the liquid component of a multiphase flow, relative to the total volume at a given position.

Inferential statistics. Use data to draw inferences (i.e., derive conclusions) or to make predictions.

Permittivity. A measure of the electric polarizability of a dielectric material. A material with high permittivity polarizes more in response to an applied electric field than a material with low permittivity, thereby storing more energy in the electric field.

Plug flow. Type of flow pattern of intermittent sequence of liquid slugs followed by short gas bubbles flowing at the top of the pipe

Q-factor. Quality factor of an inductor, defined as the ratio of reactance of the coil to its resistance at a given operating frequency

Reynolds number. Ratio of dynamic forces to viscous forces and -relevant to turbulence onset and structure.

Skin effect. Tendency of an alternating electric current to become distributed within a conductive medium such that the current density is largest near the surface of the material, and decreases with greater depths in the medium.

Slip velocity. Velocity difference between the different phase components of a multiphase flow.

Slug flow. Type of flow pattern of intermittent sequence of liquid slugs followed by longer gas bubbles flowing through a pipe.

Standard Deviation. A statistical measure of the spread of a set of samples.

Superficial velocity. Velocity that one phase of a multiphase flow would have if it travelled alone and completely filled the pipe.

Volumetric flowrate. The volume of fluid flowing through a cross-section of a pipe per unit Time.

Volume fraction. Is the volume flowrate of one of the phases of a multiphase flow, relative to the total multiphase volume flowrate.

Chapter I Introduction

During the past decades, industrial systems have been subjected to automation, on what has been called the Second Industrial Revolution, Industry 4.0 [1]. The Oil and Gas Industry is not alien to this worldwide common interest for process optimisation via system automation. Automation technology creates opportunities to increase accuracy, reduce cost, increase uptime and improve safety across the full oil and gas lifecycle [2]. This includes the upstream and midstream sectors encompassing production and transport processes, which are dominated by the presence of multiphase mixtures. Fluids flowing from an oil reservoir to the surface, in the upstream production sector, undergo accentuated drops in pressure and temperature. These changes lead to variations in the flow regime, ranging from a single-phase liquid, for near the wellbore production pipes in unsaturated reservoirs, to several types of multiphase configurations in the upstream facilities of the production sector, with mixtures of gas, liquids and solids. Furthermore, the concentration of the phases in the multiphase mixture varies throughout the reservoir life. Increasing gas and water fractions is inherent in mature fields, as is the need for enhanced oil recovery. These conditions give rise to varying flow patterns and unstable flow conditions [3].

The transport of hydrocarbons is an essential activity in the production sector of the petroleum industry, with the costs of new pipelines accounting for up to 60% of a project development costs [4]. Understanding multiphase flow behaviour is, therefore, of paramount importance for cost savings, systems optimisation, increased operational integrity, and reduced energy and environmental impact. The complex phenomena of multiphase flow transport have yielded numerous challenges to the industry. Limitations arise when the production characteristics, for which the pipeline and process facilities were designed, change. These changes can develop from long-term reservoir production or instantaneous volumetric increments due to, for example, intermittent flow. In addressing this, the development of Multiphase Flow Measurement (MFM) technologies have been a major focus within the industry, growing exponentially since the mid-’90s. There is a general recognition of the benefits that flow meters provide to the petroleum industry in terms of cost reduction, process simplification and optimisation opportunities [3]. This embracement of MFM applications is closely related to the need for accurate and fast flow measurement. It is precisely in this necessity that tomography measurement technologies find their niche of application. Accurate flow measurement allows to reduce measurement uncertainty associated with improper placement of monitoring device; environmental effects on measurement instruments, such as pressure considerations or flow pattern dependency; drift of an instrument between successive calibrations; electrical interference with electronic components; and/or variation between the calibration and usage conditions. The present research proposes alternative technologies that could complement traditional flow meters. It can reduce the measurement uncertainty related to the intrinsic processes conditions while leveraging on available high temporal resolutions able to capture relevant multiphase flow phenomena.

The present chapter serves as an introduction to the research subject. The background of the research, presented in Section 1.1, aims to address the relevance of the research topic within the discipline of multiphase flow measurement. Section 1.2 provides the research motivation and discusses the gap that the research intends to address. Subsequently, the main aim of the thesis is discussed in Section 1.3, along with the research objectives. The questions that the present work tries to answer are then outlined. The novelty and deliverables of the present work are discussed in Section 1.4, followed by the thesis organisation in Section 1.5.

1.1 Background

MFM technologies have the capability of measuring the flow rates of each individual phase in a multiphase flow. Traditionally, processing of the multiphase mixture produced from wells takes place in centralised facilities where the heavier stream is separated, settled and collected from the bottom section of separator vessels [5][6]. The use of flow meters reduces the hardware requirements by replacing test separators and avoiding dedicated test lines. MFM also provides continuous well monitoring, which gives access to real-time data in contrast to the cumulative volumes at discrete times. This enables improved decision-making processes and production optimisation.

A global solution for multiphase flow meters does not exist, yet various metering developments address specific industrial applications. The intrinsic characteristics of the petroleum industry demand that measuring devices meet high standards in terms of robustness, accuracy, and processing speed. This provides opportunities on the prospective use of tomography technologies.

Imaging or tomography techniques have witnessed significant advancement and applications from the first quarter of the XXth century when they were employed for earth exploration until their recent use in bioscience and medicine. Traditionally, tomographic technology has had a significant presence in the medical industry [7], but an increasing interest has been witnessed during the past decade targeting industrial applications. Industrial Process Tomography (IPT) comprises a series of technologies whose operating principle is based on the use of remote sensors to acquire data, which in most cases is inaccessible, from the cross-section of a vessel or pipe to obtain quantitative measurements of the properties of the materials. Even though the concept of tomography in process engineering is far from new, recent developments in digital electronics and computational capacities have positively impacted their application reach.

IPT provides a broad range of opportunities for process control by encompassing multiphase flow metering and process monitoring. The selection of particular tomography techniques is limited by the properties of the materials to be analysed, the dynamics of the process, the process environment and the length scale of the phenomena to be monitored [7].

Previous investigations on tomography techniques for multiphase fluid assessment have identified specific application niches for various IPT technologies for industrial application related to MFM [8]–[10]. However, there is little evidence of previous use of electromagnetic-based tomography systems to monitor dynamic multiphase flow processes. Furthermore, the novelty of IPT techniques and the limited available literature, provide room for further evaluation on the capabilities of electric tomography techniques, e.g. Magnetic Induction Tomography (MIT) and Electrical Capacitance Tomography (ECT).

This research aims to develop a tomography-based system to monitor multiphase flow transport through pipelines. In doing so, the work addresses the capabilities of the instruments to measure and characterise multiphase flow mixtures. A better understanding of the multiphase flow phenomena leverages the optimisation of the highly interconnected complex transport systems and hence of the production process, which have an immediate impact on the production value chain.

1.2 Project motivation

Accurate prediction of flow patterns, pressure drop, and liquid holdup is of paramount importance in multiphase flow transport. In the Oil and Gas industry, most of the flow transport systems have been either designed or operated using empirical flow correlations. However, empirical correlations are limited to process conditions similar to those at which they were derived. In recent years mechanistic models, based on mathematical description of the physical phenomena, have gained ground on the estimation of pressure drops and the prediction of flow regimes. This practice, however, is only valid when there are no perturbations that alter the flow, and therefore the steady-state equations and the simplifying assumptions can provide a fairly good approximation. This gap between the theoretical approach and the real behaviour of hydrocarbon flow transport creates room for a better understanding of the multiphase phenomena, which is intended to be addressed as part of this project by means of a novel approach for the characterisation of hydrocarbon mixtures using tomography-based MFM.

The selection of the measurement principle exploited in present work responds to the necessity to address some of the industry challenges. In the market, there are various commercial MFM metering solutions. Many of them combine capacitance, microwaves, ultrasound, and nuclear sources to measure multiphase flow. However, their limited operational envelope due to multiple operational factors, including inner scale build-up and limited range and gas content [11], enable the application of other measuring techniques, like IPT. Previous studies on IPT have proven the feasibility of the use of tomography for phase recognition and flow measurement [8] [11] [12] [13]. Regarding the former, in controlled laboratory conditions, complex flow regimes have proven to be difficult to detect and classify even with the aid of high-speed cameras. The use of IPT can be of great value in assessing multiphase flow mixtures, as they provide high temporal resolution and allow non-intrusive visualisation of the multiphase flow phenomena with an adequate spatial resolution. IPT has the potential to provide the means to identify flow patterns that other measurement methods cannot infer. The knowledge derived from flow pattern identification could potentially decrease the uncertainty of the measurement from traditional multiphase flow meters. Considering this, the present work proposes the use of tomography measurements to identify flow patterns based on the contrasts of the properties of the fluids.

This work is the first attempt to use electrical properties from low contrast mixtures to extract detailed simultaneous information in multiphase flows. For this, a MIT for measurement of low conductivity contrast mixtures was designed and manufactured. The research aims to redefine the operational envelope and application of electric tomography by encompassing flow pattern recognition algorithms and high-speed measurements.

The proposed research on the combined use of MIT and ECT for enhanced oil-water and oil-gas mixtures is not only feasible given the existing knowledge, but it will also contribute to a better understanding of the transport process of hydrocarbon mixtures at field conditions.

1.3 Aims and objectives

Electromagnetic induction systems are sensitive to the electrical conductivity of fluids, a measurement that, although feasible, has challenged the scientific community. The most advanced tomography techniques either fail to accurately detect conductivity or rely on nuclear sources. Electromagnetic induction-based technologies, such as MIT, have previously been used for phase recognition under static and semi-static conditions. However, MIT technology is still novel, and so, further research must be conducted to enable MIT meters to meet the industry requirements regarding real-time data acquisition and sensitivity.

This reality prompts the present research, which aims to develop a tomography-based measurement system to monitor multiphase flow transport processes. To achieve this, six objectives have been drawn as follows:

- Investigate different geometries of coil arrays and electromagnetic shield for the intended application.
- Evaluate the effect that the design of the various hardware components has on the performance of electromagnetically induced signals.
- Study the capabilities of electromagnetic measurements for conductive and non-conductive fluids.
- Develop an electromagnetic induction-based metering system for multiphase flow monitoring.
- Conduct experimental trials in flow rigs to establish the operability envelope and capability of the metering systems.
- Characterise multiphase flow dynamics based on tomography imaging measurements.

The present work addresses the fundamental questions below.

- What is the potential for tomography systems to address the challenges faced by the industry for multiphase flow measurements in terms of environmental impact, deployment, and costs?
- What are the design parameters of the sensors and electromagnetic shields that enable MIT systems to detect, recognise and identify key features of multiphase flow?

- What are the practical limitations that the intrinsic measurement principles, and hence operational envelop, of MIT and ECT pose for the use for multiphase processes?

- How do MIT and ECT conductivity and phase fraction measurement compare to reference process monitoring techniques?

- What is the future direction of IPT for MFM?

1.4 Novelty and deliverables

The research conducted is based on original prototype design and encompasses empirical work that has not been undertaken before and original interpretation of results that provides novel knowledge on intermittent flow patterns and electric-based multiphase flow measurements, as in Chapter VIII and Chapter VII, respectively.

The design of the hardware prototype encompasses a series of design premise, manufacturing techniques, and materials that allows, for the first time, the implementation of the MIT technology in an industrial environment. In this regard, the hardware design has been patented under the applications GB1810735.9 [14], where the PhD candidate is a co-inventor. The MIT sensor design has also been submitted for IP protection under the application number GB1810733.4 [15]. The main contribution from the present research to the patent documents above is based on the numerical model used for the sensor selection following the work presented in Chapter III, Chapter IV and Chapter V. Details of the contributions are found in Appendix A and Appendix B.

The present work studies an alternative data acquisition method using secluded capacitance measurement sensors, which led to enhanced operational envelops of present ECT technology, as demonstrated in Chapter VI.

A novel approach for flow pattern characterisation combining tomography measurements and an automatic flow pattern recognition algorithm is used here for the first time. This resulted in a thorough characterisation of a recently identified flow pattern with relevant implications in flow regime prediction and measurement accuracy as detailed in Chapter VIII.

An original interpretation of shielding materials for low radio frequencies is presented here alongside novel statistical-based models for sensor design. This work has the potential to be used for MIT prototype design without the need to solve the full electromagnetic Forwards Problem or to conduct extensive empirical analyses.

As a result of the work above, the research has been published in five peer-reviewed journals and presented in three international conferences (refer to Appendix A). In this sense, the sensor design in Chapter IV is published in Journal Measurement Science and Technology [16] and the study on attenuation materials for the shield design in Chapter V is disclosed in a manuscript published in the IEEE sensor journal [17]. The multimodal Gamma-ray and Electric Capacitance approach detailed in Chapter VI is published in the proceedings for the 2020 IEEE International Instrumentation & Measurement Technology Conference [18]. The proof of concept derived from the results in Chapter VII are publicly available in IEEE Access [19] and the intermittent flow characterisation from Chapter VIII are published in the Journal of Natural Gas Science and Engineering [20].

1.5 Thesis organisation

It is intended in the following chapters to conduct an investigation that achieves the proposed objectives. After an introductory Chapter I, which addressed the motivation and intention of the present research, Chapter II gives an overview of the application niche where this research sits and reviews the principles of operation of tomography meters, focusing on the governing physics of electromagnetic induction, treated in Chapter III by solving the Forward Problem through Finite Element Method (FEM). These chapters are intended as an introduction to the hardware design, operability and implementation addressed in the remaining chapters.

Electromagnetic measurement is highly sensitive to external interference and capacitive coupling, which can cause large measurements errors. Consequently, a comprehensive hardware design is provided in Chapter IV and Chapter V. Chapter IV focuses on the sensor design and characterises its performance capabilities based on various sensor geometries. This section intends to provide the reader with tools to design MIT sensors without the need to solve the full electromagnetic Forward Problem. Chapter V addresses electromagnetic shielding and provides an overview of the shielding mechanisms of interest for the intended application.

At this stage, we have an electromagnetic instrument, whose measurements are chain-traced to reference measurements and legacy meters in Chapter VI. In Chapter VI dielectric and conductivity measurements are contrasted, and the operational boundaries for MIT and ECT are challenged. The emphasis in the chapter, as elsewhere, is on measurement accuracy and traceability, which underlie the flow measurement and characterisation presented in the final chapters.

Chapter VII expands the applicability of electromagnetic measurements beyond conductivity contrast measurements. In this section, a comprehensive evaluation of the measured signals proves the feasibility of the use of MIT for three-phase flow characterisation.

Chapter VIII is devoted to flow pattern identification. The point is to show the potentiality of tomography systems for flow regime characterisation, to ultimately result in enhanced measurement accuracy. As part of this section, an intermittent flow pattern is characterised, including the transition boundaries based on empirical work and mechanistic criteria.

The conclusions and recommendations are addressed in the final Chapter IX. To avoid repetition and allow easy location of relevant literature, the reference list has been placed at the end of the document, followed by the Appendixes. Appendix A provides a summary of the publications derived from this work, Appendix B details the filed patent documents, and Appendix C summarises the numerical models used throughout this thesis.

Chapter II Literature Review

2.1 Introduction

This chapter presents an overview of the challenges that the petroleum industry faces and portrays the niche application through which multiphase flow measurement has aided the industry to decrease production and development costs. The relevance of flow pattern characterisation for accurate multiphase flow measurement is addressed here. A review of relevant literature on multiphase flow measurement within the oil and gas industry is provided, with a focus on a new generation of non-intrusive meters based on electrical tomography.

The present chapter describes how the output from tomography systems can be exploited for oil and gas process monitoring based on either tomographic reconstructed images or through raw electrical measurements. The principle of operation of electromagnetic induction systems, hardware setups, and data processing through the resolution of electromagnetic governing equations are addressed following.

The chapter is organised as follows. Section 2.2 provides an overview of the petroleum industry that serves to identify the challenges of the industry and contextualise the role of MFM within it, as discussed in Section 2.3. The opportunities for Process tomography for MFM are addressed in Section 2.4. Section 2.5 describes Electrical Tomography together with technologies of interest based on electromagnetic induction and electrical capacitance metering. The governing principles of electromagnetic induction measurement are detailed in Section 2.5, together with concepts of Forward and Inverse Problems. Finally, Section 2.6 summarises the topics discussed in this chapter and provides the justification of the methods and design premises undertaken in the remainder of the thesis.

The present chapter is partly published in the proceedings of the ICESF-19 [21].

2.2 Petroleum industry: an overview

The oil industry faces significant challenges imposed by the global market and the finiteness of the resources. From Figure II-1, it is evident that the rate of discoveries of reservoirs and the world oil consumption show opposite trends. This reality yields the consensus within the energy community that, at the present rate, oil production will reach a historic maximum before 2050 [22]. After a global production peak, the world oil offer would unavoidably decline, leading to an increase in prices of fossil fuels and adding to the already volatile oil price market.

Since the early seventies, the oil price has largely fluctuated, with a historic record variation registered during the year 2008 (see Figure II-1). In July of 2008, the oil price peaked at nearly USD135/bbl, the highest ever registered, before dropping by 69% by the end of the same year, following turmoil in the Middle East. Similarly, a 20% drop over a month is currently unfolding within the petroleum market, triggered by the coronavirus Covid-19 epidemic of January 2020. This shows that the volatility of the oil prices is caused not only by the market forces of supply and demand, but also by other aspects like economic and political stability, climate station changes, and geopolitical strategies, which are key in the establishment of the oil price [23] [24].

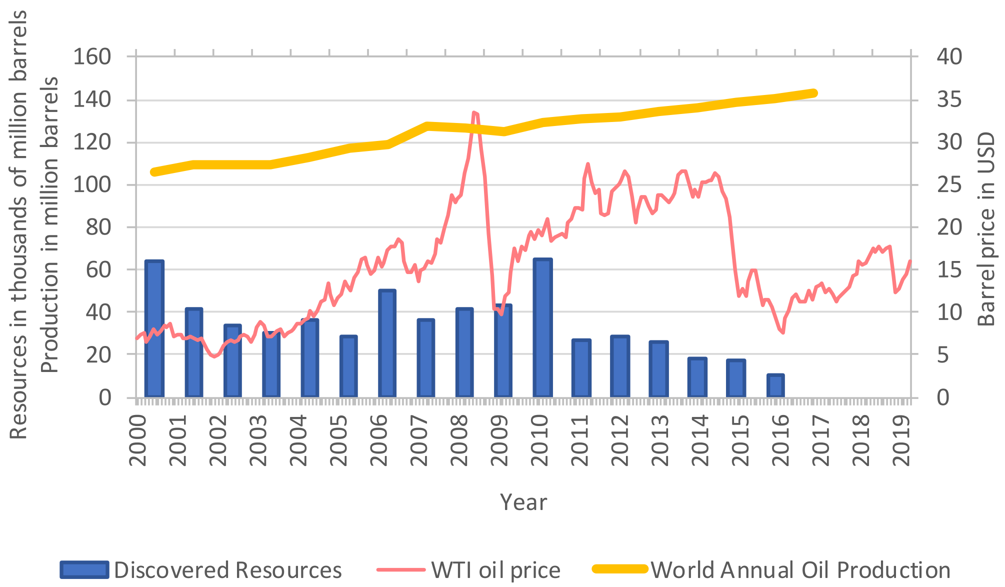

Figure II-1. Historical figures of world annual oil production, rate of discovery of resources and oil prices
Source: EIA (2019, p.1), IEA (2017, p.1), Rodrigue, J. (2016, p. 1.), & BP (2018, p.14.)

Production depletion rates from marginal fields and geopolitics are difficult to predict, yet technology development can play a mitigating role in the challenges that the petroleum industry faces. Technology developments in the petroleum industry are fuelled by the need to make marginal fields more cost-effective, to exploit reservoirs in difficult physical environments, e.g. in deep-water offshore fields, to reduce development costs, and to improve the energy efficiency and sustainability of fields [29]. Of particular interest are the challenges associated with production from mature fields, where increasing gas and water fractions create complex flow phenomena and unstable flow conditions which require flexible multiphase solutions.

2.3 Multiphase flow

Fluid flow transport from oil reservoirs to surface facilities comprises the simultaneous movement of varying fluids types and phases through pipelines. Typically, a combination of oil, gas and water flows are present throughout the petroleum industry value chain. Other phases, like organic and inorganic particles, are also common. Examples of multiphase flows are gas-liquid flows, liquid-solid flows, immiscible liquid-liquid flows, and gas-liquid-liquid flows, which can be co-current or counter-current at any given point of the process. Unlike single-phase flows, which represent the simplest configuration and can be described by the Navier-Stokes equations, the analysis of multiphase of flow is more complex. Multiphase flow entails interaction between the different phases, which yield momentum and mass transfer, dynamic phase distributions, and varying interfacial forces. The measurement and analysis of multiphase flow are particularly complex due to the different spatial distribution of the phases that can arise in the piping system. These configurations, known as flow regimes, represent the particular distribution of the phases as they flow together in the pipe and can significantly vary depending on the process conditions and the characteristics of the multiphase flow system.

The classification of multiphase flow in pipelines has undergone significant research resulting in numerous flow pattern maps as described in detail in Chapter VIII. Commonly, flow classification depends on two main conditions, namely, the fluid species and the flow direction. The identification of dynamic flow regimes is an arbitrary process traditionally done via visual observation of the flow spatial arrangements. The flow regimes are characterised based on intermittency, scale, and structure. This process is time-consuming, and observations are limited to what can be seen through a transparent pipe wall. The drawback of optical techniques is that complex or detailed flow configurations that are not visible using the human eye or machine vision could lead to misinterpretation. Examples of flow structures whose externally visible assembly may not be entirely representative of the overall flow configuration include fluids with significant bubble structures or opaque fluids, and in particular oilfield multi-phase flows [30].

Most flow pattern maps found in the literature are based on empirical work where flow regime zones are assembled based on superficial velocities or average velocities. These types of maps are restricted to the conditions and fluid properties for which the map was developed. A more generic approach, with potential broader applicability, is that of flow pattern maps based on dimensionless numbers, i.e. velocity ratios, fluid correction factors, or dimensionless numbers. Of these, the use of dimensionless numbers, that correlate the forces governing the systems, has been found to have enhanced applicability over a wider range of operational conditions [31]. Dimensionless numbers like Reynolds, Weber, Froude, or Eotvös have been successfully used to characterise both gas-liquid flow dispersions patterns [32][33] and liquid-liquid flow in horizontal pipes [31].

Prediction of flow patterns is key in the design and operation of surface facilities, e.g. separation capacities, equipment sizing, pipeline cleaning frequency, etc. Furthermore, the accuracy of existing MFM technologies are susceptible to the spatial distribution of the phases within the pipe. Hence, accurate flow patterns identification is of major relevance in MFM with extended impact over forecast of oil and gas production throughout the reservoir life [34].

The development of new technologies has aided petroleum companies to shift their traditional production schemes and face the challenges described above and in Section 2.2. Significant savings in exploration and production activities have been reported due to the use of innovative technologies [35], MFM being one of them.

Having said that, the complexity and dynamicity of the multiphase flow structures impact on the accuracy of available flow measurement technologies [36], leading to measurement uncertainties ranging from ±5% to ±20% or more on each of the flowing phases. These uncertainty values exceed the level of accuracy that is, in general, agreed for production allocation (±95%±98%) [3]. There is, however, not a firm threshold of what constitutes an ‘acceptable level of uncertainty’ as to date no international regulation for MFM accuracy is available. Yet, to the author’s knowledge, the flow measurement community has been working on an international standard for MFM, an initiative led by TUV-NEL, that should be made available in the near future.

2.3.1 Multiphase flow measurement

MFM is key in providing solutions to the oil and gas industry by enabling alternative production scheme strategies. These new schemes result in an increasing number of developments of subsea resources and co-mingled production which means that there is no longer the possibility to separate oil, gas, and water before metering for production allocation or fiscal purposes. In this regard, MFM enables fast production allocation yielding an increasing number of company alliances to share production and transport facilities in order to continue producing from depleting marginal fields or to exploit in increasingly deeper waters economically. MFM allows continuous well monitoring which provides higher resolution of the information compared with random well testing with a test separator. Furthermore, MFM allows production allocation, which provides a survey of the reservoir life [35], optimises the overall cost-revenue of oil production, replaces bulky well-test separators, and reduces the development footprint, of great significance in offshore facilities [36] [37].

MFM comprises a large number of measurement principles. Multiphase flow meters, that rely on phase separation prior to flow measurement, generally use a single-phase flowmeter, like vortex or Coriolis flowmeters, to measure the gas phase, and phase fraction measurement via impedance or microwave, for example, to determine the spatial distribution of the liquid stream. These techniques are usually combined with a velocity measurement for flowrate computation, typically via a Venturi tube [36]. By separating the phases, the complexity and challenges imposed by the dynamicity of the flow in the temporal and spatial domain are decreased if not eliminated. Ultimately, separation of the phases yields high accuracy measurements (typically ±0.25% rate for oil and ±1% rate for gas) and is feasible by using readily available single-phase technologies. In this sense, the accuracy of Venturi tubes ranges around ±1.0 to ±2.0, whereas Coriolis meters provide accuracies as high as ±0.05% [38].

Multiphase flow meters that do not account for upstream phase separation use techniques such as IPT for phase fraction measurement combined with velocity measurements, e.g. cross-correlation, for flowrates determination. The benefits of in-line non-intrusive multiphase flow measurements come at the cost, of reduced accuracy when contrasted to single-phase measurement. In this regard, independent tests of multiphase flow meters performance reported in the literature state uncertainties in the measurement of volumetric gas flowrate and volumetric liquid flowrate under controlled conditions of ±8.78% to ±10% and ±3.5% to ±5%, respectively [36].

Section 2.3.1.1 discusses some of the most commonly MFM technologies available in the market. It is noteworthy that every commercial solution responds to a unique design, with significant differences in the way the raw measurements are combined and the intrinsic premise for flowrate determination.

2.3.1.1 MFM market

Ever since the implementation of early generations of MFM in oil fields, the use of flowmeters has exponentially increased, as seen in Figure II-2. Furthermore, the size of the global market for MFM reached $7,500 Million in 2018 and is expected to grow at a 5.9% compound annual growth rate in the following five years [39]. This is partly due to MFM being essential within the petroleum industry for many field developments to measure production in real-time and continuously monitor well performance.

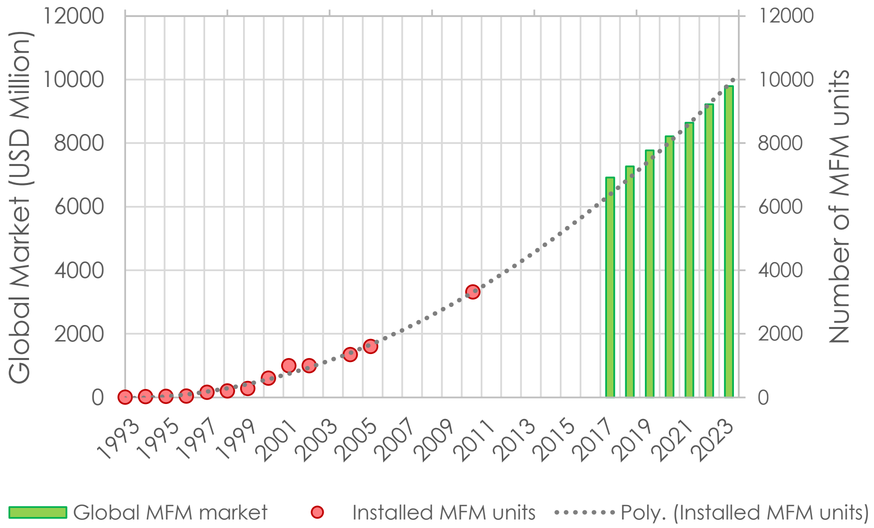

Figure II-2. Worldwide multiphase flow measurement trends showing installed units and the size of the market Adapted from Falcone, G and Harrison, B 2011:4 and kbv research [online: https://www.kbvresearch.com/flow-meters-market]

The complexity of the multiphase phenomena within the oil production system precludes the development of a generic MFM solution enveloping all possible conditions. However, different MFM solutions have found various application niches and the variety of technologies in the market demonstrates this. A thorough review of the MFM solutions proved challenging due to in-house developments and the limited commercial information available. However, as the result of retrieving available data online and interviews with manufacturers, Table II-1 summarises the meters currently available on the market to the best of the author's knowledge. Meters under development are not included, such as those from iPhase Ltd [40] and LeEngSTAR Technology [41].

Table II-1 classifies commercial MFM systems according to a) the type of flow conditioning; b) the use of gamma sources and; c) intrusiveness as proposed in [36] [42]. It can be seen that a majority of the available technologies are either intrusive or use some radiation source, which limits their extended applicability.

Table II-1. Multiphase flow measurement solutions available in the market

MFM solution	Manufacturer	Measurment principle	Flow conditioning	Gamma source	Intrusive
Flowatch3I	Pietro Fiorentini	- Venturi -Impedance -Velocity (via sensor cross-correlation)	No	No	No*
Flow-itometer	ITS	-Electric Resistance tomography -Electric Capacitance Tomography	No	No	No
APL-C-900	ATOUT	Electric Capacitance Tomography	No	No	No
ADMAG series	Yokogawa	Dual frequency capacitance meter	No	No	No
Flowatch HS	Pietro Fiorentini	- Venturi -Impedance -Velocity (via sensor cross-correlation) - Gamma densitometer	No	Yes	No*
Roxar 2600 MFM	Roxar-Emerson	- Venturi - Electrical impedance -Gamma densitometer (alternative non-gamma solution available)	No	Yes	No*
Vx Spectra	Schlumberger	-Gamma spectroscopy -Venturi	No	Yes	No*
MPM	FMC technologies	-Multimodal tomography (gamma detector & radiofrequency dielectric measurment)	No	Yes	No*
C6+ CR6+	ESMER	-Cone meter -Impedance measurment -Infrared transmitter	No	No	Yes (cone)
iVIM	TEA Sistemi	-Orifice meter -Water cut sampling	No	No	Yes (Orifice)
VEGA	TEA Sistemi	Isokinetic sampling (flow mixed and sampled)	Isokinetic sampling	No	Yes
MPFM50	AGAR Corportaion	-Coriolis mass measurement -Venturi -AGAR water cut measurement	In-line separation	No	Yes
Full range MPFM	Haimo	-Venturi -Gamma ray phase fractions measurment -Inline sampling -Multivariable transmitter	In-line separation	Yes	Yes
DG6+	ESMER	-Gamma ray densitomer -Cone meter -Impedance measurment -Infrared transmitter	No	Yes	Yes (cone)
Accuflow	Accuflow	The phases are separated. The single phases are measured through conventional meters, i.e. coriolis or turbine for liquid and vortex, turbine or ultrasonic for gas. Water cut measured through density difference or microwaves.	In-line separation	No	Yes
CCM	Phase Dynamics	The phases are separated. The single phases are measured through Coriolis meters.	In-line separation	No	Yes

*Technology containing a Venturi is not considered intrusive

2.4 MFM through tomography methods

IPT, first introduced in the late 1980s, covers a set of the most novel MFM techniques. Tomography technology is based on the acquisition of signals from an array of sensors located on the perimeter of an imaging region, e.g. a pipeline, and the abstraction of information to build an image from the cross-section [43]. The output from tomography systems can be either in the form of reconstructed images, i.e. tomograms, or in process parameters related to the fluids distribution within the imaging region, e.g., voltage measurements, phase angles, induced currents, etc [44] [45]. These features make them highly attractive for flow pattern reference and validation, particularly since most of the existing multiphase flow meters are flow regime dependent [36].

There are three main principles of operation of IPT systems (see Table II-2). The operation of acoustic based tomography differs significantly from the tomography technologies used in this thesis [7] and is outside the scope of the present study. For tomography systems based on electromagnetic radiation, otherwise known as hard tomography, the only factor that can affect the strength of the transmitting signal along a straight path is the material along the imaging path, regardless of its position [46]. Hard tomography based on radiation attenuation methods are well studied for the determination of the gas fraction distribution in two-phase gas-liquid flows, and are known to give reliable measurements [47]. Comparisons with soft tomography technology (ECT) shows excellent agreement [47][48], and will be used further in this thesis for instrument calibration.

The measurement principle of soft tomography methods relies on the measurement of electrical properties of the material in the imaging region. Conversely to hard tomography, the transmitting signal in soft tomography is significantly affected by the position of the sensors and the distribution of electrical parameters in the surrounding area.

Soft tomography systems, which do not rely on nuclear sources, offer the opportunity of similar metering accuracy as existing systems but with substantially less environmental impact and greater ease of deployment and maintenance, which results in lower costs. Furthermore, given the intrinsic operation principle of tomography techniques, the technology offers significant advantages for MFM. The measurement outputs, i.e. tomograms, are reconstructed images of the distribution of the phases within the pipe derived from the real-time measurement of the sensor array. Tomograms have the potential to be used for reference and validation of existing multiphase flowmeters, most of which are flow regime dependent. In this sense, flow pattern recognition from tomography measurements could increase the accuracy of the flow measurement by determining the relationship between the volumetric distribution of each phase for every time frame and the outputs from the independent flow meters. As stand-alone flow meters, tomography technologies leverage on the complex spatial distribution of the phases in the pipe to measure the flow velocity. This is done by using parallel measurement planes and cross correlating the transit time of the dynamic structures between the twin measurement planes.

Table II-2. Principles of operation for process tomography

Principle	Practical realisation	Comments
Electromagnetic radiation	Optical	Temporal resolution ~ 10 ps [49] Optical access required
	X-ray and γ-ray	Temporal resolution ~ 20 ms [50] Radiation confinement
	Positron emission	Labelled particle Not on-line
	Magnetic resonance	Temporal resolution ~ 35-200 ms [51] [43] Expensive for large vessels
Measurement of electrical properties	Capacitive Conductivity Inductive Impedance	Temporal resolution ~ 3 ms [51] Suitable for small or large vessels Non-invasive
Acoustic	Ultrasonic	Sonic speed limitation Complex to use

Adapted from Beck & Williams (1996: 218)

The interest of the research community in this type of technology is illustrated in Figure II-3, which shows the rate of studies published by the International Society of Industrial Process Tomography (ISIPT) using soft tomography systems applied to MFM to the total number of research in other fields accounting for 924 publications over the period 2003-20018. The analysis of the research outputs over the past two decades provides evidence of an increasing amount of research in soft tomography metering systems targeting oil and gas flow applications.

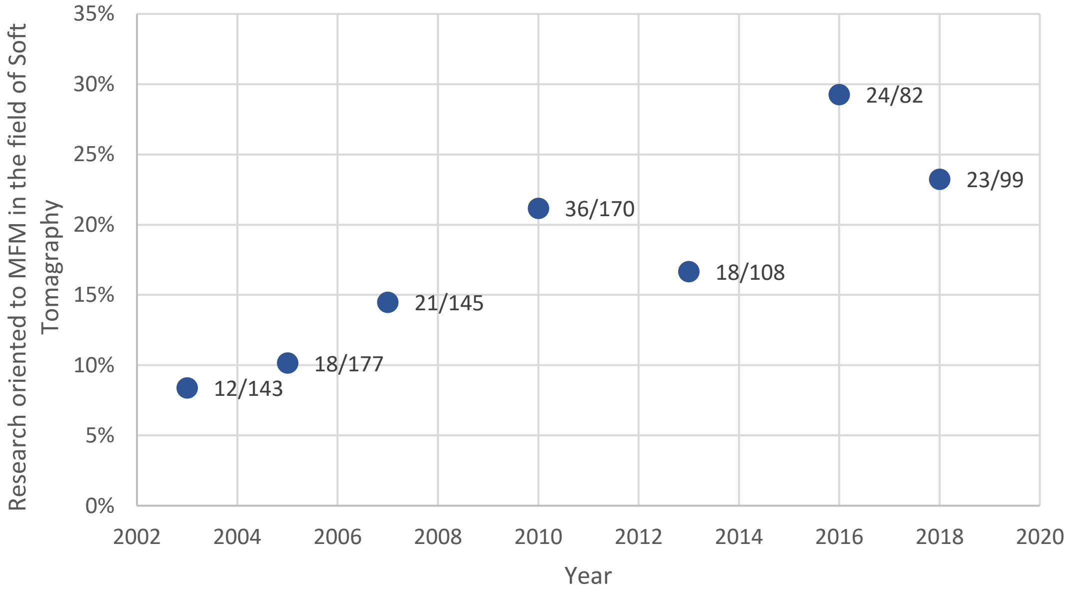

Figure II-3. Research trend showing the ratio of publications on soft-field-based meters to overall tomography studies based on the repository of the International Society for Industrial Process Tomography. The figures next to the markers are the number of publications in MFM vs the yearly total publication

Current research trends also show a significant number of studies accounting for multi-modal and multi-spectral imaging methods that address various process monitoring. Amongst the most novel techniques are the combination of dual-modality tomography to reconstruct the geometric configuration of the inclusions inside the observation domain and to improve the typically low spatial resolution [52] [53] [54] [55]. This approach can be potentially useful for measurement traceability and validation, as explored in Chapter VI.

2.5 Electrical Tomography

Soft tomography comprises a series of non-intrusive techniques that rely on the sensitivity of the sensors to changes in the electric properties of the fluids contained within the imaging region. Electrical tomography comprises several non-invasive techniques that can, either separately or combined, address some of the shortcomings of other MFM technologies, e.g. invasiveness, use of nuclear sources or low temporal resolution.

Many of the electrical capacitance techniques have been available for years for monitoring phase distributions. However, there is room to increase their application reach by combining them with other MFM technologies. The exploitation of the electrical tomography could aid improvement of flow measurement accuracy by incorporation of their capabilities to accurately map the distribution of the phases across the pipe cross-section based on intrinsic electrical properties of the fluids. Electrical tomography leverages on high temporal resolutions and advancements in digital electronics and computational capacities. These features offer opportunities that allow the implementation of the multimodal measurements, which could lead to real-time measurement corrections based on reconstructed phase distributions, as investigated in Chapter VI and Chapter VIII.

In electrical tomography the measurements reflect the distribution of electrical parameters withing the pipe in relation the by the position of the sensors. The difference between the electrical properties of the fluids gives rise to variations in the inter-sensor measurement. Measuring the temporal evolution of the phase fractions of multiphase flows can be achieved via different techniques, which rely on capacitive, conductive, impedance, or induction measurements [56]. Capacitive tomography or ECT, is a non-invasive method for determination of the dielectric permittivity distribution based on measurement of the capacitances between unique combinations of sensing electrodes placed around the perimeter of the pipe. Similarly, combined conductivity and permittivity distribution can theoretically be measured through MIT by measuring the changes in the phase and amplitude of an alternating electromagnetic field caused by eddy currents induced in the conductive species. Electrical impedance tomography (EIT) and Electrical Resistance Tomography (ERT) infer the electrical properties of the medium from measurements of inter-electrode potentials from electrodes placed in contact with the fluids. The key difference between EIT and ERT is that the former combines resistance and reactance measurements. Generally, each soft tomography technology provides essential information of the electrical properties of the flowing streams, however, there are some systems where some particular properties carry useful information hence benefiting the utilisation of a given technology over another or the combinations of two or more of them. The choice of the sensing system largely depends on the nature of the multiphase mixture, the operation conditions, the maintenance requirements, and the safety regulations framework.

Therefore, each tomography technique for multiphase fluid assessment has a specific application niche. ECT is, for instance, the best-developed flow metering technology based on electrical measurements. The inter-electrode capacitance measurements of the ECT are sensitive to the distribution of the dielectric properties of the fluids. ECT has been largely used for imaging and velocity measurement of non-conducting two-phase flows [57] [58]. Among the most relevant applications concerning the Oil and Gas Industry, we find flow pattern identification and volumetric rates [59], hydrocarbon phase separation [60] [61], tanker loading [62], and the collapse of oil foams [63]. Given the technology readiness level and its high accuracy for measurement of flows of contrasting permittivity, as reported for oil-gas mixtures [64] [45], ECT is to be used in this thesis to advance research on oil-gas pattern identification techniques (see Chapter VIII).

On the opposite side of the spectrum, MIT is the most novel and least developed soft-field technology to date. Its development is still mostly confined to the academic research field, and it is within the aim of the study to characterise the features that would enable the use of the technology in industrial environments and to provide a prototype sensor head for industrial use (see Chapter IV and Chapter V).

One of the shortcoming of the ECT is that its use for conductive phases has been restricted to mixtures with low water cuts [59], a feature that is further challenged in this study by contrasting its measurements with an MIT system. The measurement principle of MIT, based on the measurement of the eddy-currents induced in the conductive phase, is discussed in detail in Section 2.5.1.2.

2.5.1 Magnetic Induction Tomography

Nowadays, Magnetic Induction Tomography is the most widely accepted name for the tomographic technology that measures changes in an induced electromagnetic field. However, it can be frequently referred to in the literature as Electromagnetic Tomography (EMT), Electromagnetic Inductance Tomography (EMIT) or eddy current tomography, the latter in explicit reference to the technology operating principle.

The first published studies date from the early nineties. Initial work on MIT with implications for industrial applications were based on metallic imaging [65]. For example, in [7] and in [66] MIT was used to distinguish metallic from ferromagnetic objects, in [67] and [68] molten metal flow monitoring was performed through MIT measurements, and in [69] the authors detected the position and assessed the integrity of steel reinforcing bars embedded in concrete through MIT reconstructed images.

These previous studies, although relevant to the development of MIT systems, have had a less significant impact on the use of the technology for multiphase flow measurement, given the low conductivity of production fluids compared to that of metallic elements. Therefore, developments in the medical field are the ones that are more closely related to the present case study due to the similarities in the conductivity of produced water to that of human tissues [70].

A significant paper in this field was a feasibility study for the use of MIT for biomedical tissues [71] in which the authors were able to differentiate fat from fat-free tissue with a simple MIT system consisting of two coils at a frequency of 2 MHz. This research was the first publication suggesting the use of MIT for biomedical purposes and stimulated significant interest in the scientific community, although later studies questioned their results. Given the large-signal measurements reported in [71], Griffiths implied in [72] that there might have been significant capacitive coupling promoting the equipment behaving like an ECT rather than an MIT. A similar two-coil system was developed in [73], in which the experimental results of the variation of the sensed magnetic field in relation to the conductivity of the medium were in agreement with the analytical prediction based on electromagnetic theory.

The first studies to suggest potential capabilities of MIT for imaging water and oil within pipelines and vessels are those conducted by Albrechtsen et al. [12] and Peyton et al. [66]. The response of a single channel MIT system to three idealised static flow patterns (annular flow, bubble flow, and stratified flow) was evaluated in [12]. Based on the system response and an observed correlation between the positions of the coil and the fluids interphase. These first preliminary results addressing the possibility of MIT capabilities for phase detection were encouraging and led to a new line of research on the subject that had been closely related to biomedical research.

In 2005 a study based on Finite Element Method simulations resulted in parallel excitation generating an even and parallel magnetic field within the pipeline interior [74]. This excitation mechanism has been adopted by the vast majority of the recently developed MIT systems.

The first full MIT prototype to image sample conductivities under 10 Sm^{-1} was designed in [11]. The system allowed an accurate reconstruction of images for different fractions of the saline solution simulating stratified flow of an oil-gas-seawater mixture in a pipeline. Later studies identified smaller conductivities below 1.5 Sm^{-1} [8][75]. In [8], the authors conducted a series of tests on various samples of conductivities ranging from 1.5 Sm^{-1} to 5.94 Sm^{-1} with total imaging area cross-sectional area ratios of 2.28%, 8.69%, and 14.57%. The 16 coil MIT system employed successfully reconstructed conductivity contrasts as low as 0.06 Sm^{-1} for inclusions occupying 8.69% of the imaging area.

There is a vast number of MFM technologies that rely on secondary measurements for mass flow rate determination [36]. Tomography technology is not foreign to this concept [64] [72] [76] [77] [78] [79] [80]. Accordingly, the use of MIT as a complementary technique given its ability to recognise conductive fluids has also been addressed in the literature [10] [36] [81].

Even though there is an increasing number of studies for MIT use in flow imaging, the technology is still regarded as academic [82]. There is no publicly available evidence of significant industrial collaboration to date [78], although, to the knowledge of the author, at least two manufacturers are working on incorporating MIT into MFM technologies, i.e. iPhase Ltd. and LeEngSTAR Technology [83].

In the latest workshop on IPT for Process Control, diverse industry sectors and members of academe appointed to mixing, sampling and flow monitoring as the areas of major industrial interest within the Oil &Gas and mining sector [84], all of which represent a potential field of application for MIT technology.

2.5.1.1 Fundamental Principles

MIT is a tomography technology based on electromagnetic field induction. The principle of operation is via the energisation of a sensor array with a time-harmonic current that generates a magnetic field. This generated alternating magnetic field induces a voltage in the receiving coils, following Faraday's Law [85]. The induced signal received by the sensing coil is directly proportional to the strength of the primary magnetic field. If an electrically conductive object is placed within the induced field, eddy currents are induced in the object, disturbing the initial field distribution and producing a secondary magnetic field [86]. The resultant changes are measured on the periphery of the space by an array of detection coils [87].

Consequently, the signal detected by the sensing coils in an MIT system is a combination of two signals. The signal from the primary field (B), and that of the induced eddy currents, also known as the secondary signal (ΔB). The secondary signal is produced by the conduction and displacements currents induced in the object. The MIT signal phasor representation is illustrated in Figure II-4.

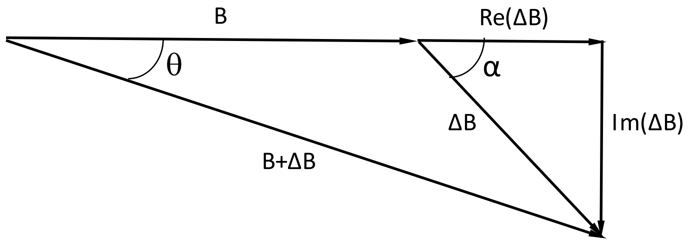

Figure II-4. MIT Signal phasor representation
Modified from Griffiths 2001 p.1127 [86]

The displacement current, an apparent current produced by a time-varying electric field, creates a real in-phase component which is proportional to the square of the operating frequency and the permittivity, but it is independent of the conductivity [11]. Conduction currents give rise to an imaginary part that lags 90° behind the primary signal and is proportional to the conductivity of the object and the operational frequency [86], as expressed in Equation (1). It can be seen that the permittivity (ε) is obtained from the real part component, whereas the conductivity signal is related to the imaginary element [72].

$$\frac{\Delta B}{B} \propto \omega(\omega\varepsilon_0\varepsilon_r - j\sigma) \tag{1}$$

where B is the primary field, ΔB is the secondary field, ω is the angular frequency of the excitation signal, ε_r is the relative permittivity of the medium, ε_0 is the absolute dielectric permittivity of vacuum (8.854×10^{-12} F.m^{-1}), σ is the object electrical conductivity, and $j = \sqrt{-1}$.

In an electrically conductive medium the alternating current is distributed through the outer-most part of the surface. At a depth δ, known as skin depth, the current density drops to $1/e$ of the near-surface value. In cases where the skin depth of the electromagnetic field in the material is larger than the dimensions of the object, the magnitude of the secondary signal (ΔB), is much smaller than that of the primary field (B) [73]. The secondary signal has been proven to be dominated by the object conductivity [7], i.e. $\alpha \approx 90°$. The ratio of induced potential difference to primary voltage can be regarded as a phase measurement by Equation (2) [88]

$$\theta = \tan^{-1}\left(\frac{\Delta V}{V}\right) \approx \left|\frac{\Delta V}{V}\right| = Q\omega\mu_0[\omega\varepsilon_0(\varepsilon_r - 1) - j\sigma] + R(\mu_r - 1) \tag{2}$$

where Q and R are geometrical constants, V is the excitation voltage, ΔV is the difference in voltage induced by the secondary field ΔB, and μ_r is the relative magnetic permittivity given by the ratio of the absolute permeability of the medium (μ) to permeability of free-space ($\mu_0 = 4\pi \times 10^{-7}$ H/m). $\Delta V \ll V$, in the same way, $\Delta B \ll B$. A non-unity relative permeability gives rise to a non-frequency dependent real component. However, the absolute magnetic permeability of water and hydrocarbons is very small, i.e. $\sim 1 \times 10^{-6}$ H/m, and of the same order of magnitude as is that of μ_0 yielding relative permeabilities close to unity; hence the second term on the right-hand side of (2) is often neglected. This is referred to as the eddy-current approximation. However, theoretically, the real and imaginary parts of the phase measurement can be used for imaging permittivity and conductivity distributions within the imaging region, respectively, as addressed in Chapter VII.

The distribution of the magnetic field, represented by the set Maxwell's Equations, is discussed in Section 2.5.1.3. This set of equations describe the distortion of the primary field due to the excitation frequency, electrical conductivity, magnetic permeability, size, shape, and position of the conductive object relative to that of the surrounding coils. Maxwell's equations are based on an uniform distribution of the object conductivity σ and permeability μ and assume the relative permittivity to be constant while neglecting free charges [7]. Electromagnetic metering is only feasible for wavelengths several orders of magnitude larger than the dimensions of the object space (see Equation (3)).

$$\omega \ll \frac{2\pi c}{l} \tag{3}$$

where c is the speed of light and l is the maximum width of the imaging area.

The detection of induced eddy currents is closely related to the operating frequency and the depth of penetration of the magnetic field into the conductive object, i.e., skin depth (δ). The skin depth at the operational frequency, from (4), must be comparable to the sensor dimensions for the secondary field to be detected [7].

$$\delta = \sqrt{\frac{2}{\omega\mu\sigma}} \tag{4}$$

Note that objects with low conductivities would require high excitation frequencies (in the low megahertz range) to give considerably small skin depth.

It has been demonstrated that there is a substantial increase in signal amplitude when imaging water samples (0.011 Sm^{-1}) as the excitation frequency is increased beyond 1 MHz [12]. Hence, to ensure a detectable signal at the receiving end for measurement of low conductivity contrasts, such as in multiphase flow, higher excitation frequencies than for other industrial applications are used [72].

Even though a high-frequency operation is desirable because the signal level from the object increases with increasing induced frequency, the induced frequency must be kept below that of the resonance level of the coils to decrease the effect of capacitive coupling [89]. Capacitive coupling at high operating frequencies arises when the excitation coil not only induces a magnetic field but also radiates an electric field that is capacitively detected by the sensors. Various unwanted coupling mechanisms can originate in MIT systems, i.e. direct capacitive coupling, capacitive excitation-detection, capacitive excitation-inductive detection, and inductive excitation-capacitive detection. The latter, even though smaller than the former, may become significant when the object is close to the coils [90]. Capacitive coupling can be attenuated by electrostatic screening and grounding [66] [72] [75] [88] [90] [91] [92] [93] [94] [95] as detailed in Chapter V.

2.5.1.2 MIT System Configuration

The main elements of a typical MIT system are illustrated in Figure II-5. The system consists of three subsystems, namely the hardware array, the interface electronics, and the processing computer [92]. The hardware array is composed of the transmitting and receiving sensors, the sensor-pipe fastening system and the electromagnetic shield.

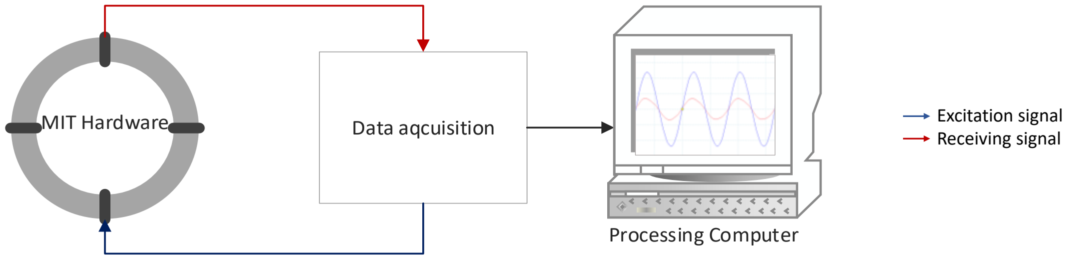

Figure II-5. Block Diagram configuration of an MIT system
(Adapted from Williams & Beck 1995:88)

The following steps constitute the general procedure for tomography imaging, excluding hardware preparation.

i. Define the experimental setup including hardware configuration, operating frequency, and input signal.
ii. Develop a numerical model that represents the physical problem to solve.
iii. Solve the electromagnetic Forward Problem which relates the measurements in the imaging area to the electrical properties of the medium (see Section 2.5.1.2. A).
iv. Analyse the sensitivity of the signals from the receiving sensors to the measured values and distribution of electrical properties and build a sensitivity map.
v. Measure the amplitude and phase of the voltage induced in the receiving sensors.
vi. Apply an inverse algorithm to compute the conductivity distribution from the measured signals and build a reconstructed image, i.e. tomogram.

The Inverse Problem and image reconstruction above are usually post-processing stages performed offline in the processing computer. Details of the electronic components and circuitry are outside the scope of this study. However, detailed background on MIT electronic developments is presented in Section B below.

A. MIT Hardware configuration

Given the dependence of the MIT signal on the physical configuration of the conductive object to achieve good image quality, the system must be designed to account for a number of field measurements and of spatially distinct field strength profiles, namely, projections [92]. For process applications, it is recommended to use an arrange of coils, which enhances the spatial resolution by covering a larger perimeter and providing a greater number of independent measurements [66]. Early

MIT developments incorporated dual coil arrays [12] [71] [89]. However, enhanced measurement accuracy has been accomplished by surrounding the imaging area with an array of coils. The MIT system from The University of Aveiro was the first prototype to consider a multipole arrangement to scan low conductive materials [66]. In parallel, the University of Manchester developed a multipole MIT system with a parallel excitation field that accounted for simultaneous coil excitation allowing high spatial independence and measurement with high central detectability [65] [93]. Most recent MIT system developments are equally based on arrays of coils surrounding the perimeter of the imaging area in various configurations, i.e. angular interleaved excitation-receiving coils [93] [96], parallel large excitation coils [92], planar rectangular coils [92] [93] [97], concentric pairs of coils [66] [88] [92] [94], circular array of exchangeable coils [11] [81] [95], Archimedean-shaped coil [98] or parallel arrays of excitation and receiving coils [99], see Figure II-6. The arrays of coils are designed aiming for a configuration that provides enhanced accuracy.

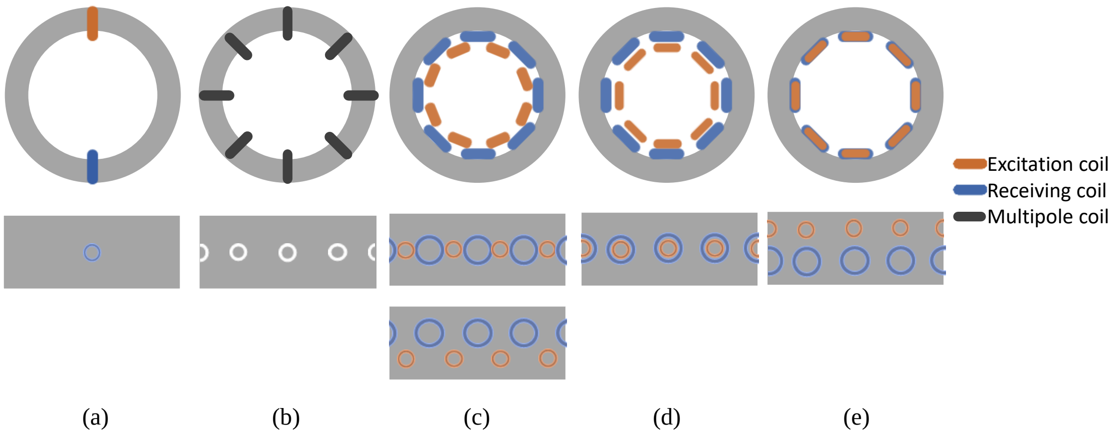

Figure II-6. Coil configurations of (a) a dual coil array, (b) multipole coils. (c) angular interleaved coils (bottom – crosswise circular exchangeable array), (d) concentric arrangement, and (e) circular exchangeable array

The sensitivity of the electromagnetic measurements is affected by the various hardware characteristics. Considering a solenoidal array of air-core coils, the optimal number of turns in the coils is closely related to the inductance and the input impedance. It can be found that at high frequencies, the parasitic capacitance resonates with the inductance, altering the ideal behaviour of the coil [11] [13] [95]. The selection of circular helix coils for MIT is not well developed in the literature. Few studies addressing the enhanced designs of excitation coils are available. The features addressed are changes in coil radius, length, architectural construction [98] and assembly [88] [95]. An improvement in the system's sensitivity was reported when the radius of the solenoid increases, while in contrast, the sensitivity declines with increasing solenoid length [98].

Furthermore, the performance of MIT devices is closely related to the insulation of the system from the interference of external electromagnetic fields and the presence of capacitance coupling. Wei and

Wilkinson [95] reported difficulties during their experimental tests due to capacitive coupling and the noise induced by the associated instrumentation, which was not properly screened, thus affecting the system readings.

Successful elimination of capacitive coupling due to electric field attraction for low conductive environments has been achieved by installing external electromagnetic shielding [88]. There are two main types of externals shields: magnetic confinement shields and electromagnetic screens. A magnetic confinement shield is built from a material with high permeability that yields a low reluctance path for the flux, avoiding interaction with the exterior [72]. This type of confinement doubles the measurement sensitivity to objects inside the imaging area [100]. Electromagnetic screens are built from highly conductive materials and, provided the thickness is greater than the skin depth, total insulation from the exterior can be achieved. Additionally, electromagnetic shielding reduces the capacitive coupling between the coils [72]. Adversely, electromagnetic shields reduce the imaging sensitivity of the cross-section in proportion to the proximity of the screen to the coils [94].

In addition to electromagnetic shielding, coil screening has also been used in MIT systems to insulate the coils from electric fields and avoid capacitive coupling. The individual coil screening technique most recently used, due to its effectiveness and ease of assembly [95], consists on winding coaxial cable or PVC-insulated wire as shielded turned coils [11] [73] [75]. Other authors have proposed screening the coils by enclosing them in a metal cylinder with radial, and longitudinal incises, simulating a comb configuration, which avoids the formation of eddy currents within the shield [72] [90]. Alternative coil shielding considers building a Faraday cage for the coils with conductive materials, i.e. foil envelope [90], Cho-Foil, or Chomerics [88].

B. Electronics

The primary functions of MIT electronics are induction and control of the sinusoidal alternating current, conditioning the MIT signal from detection coils, and real-time data acquisition. Basic inductance principles dictate that to avoid affectation of the MIT signal, and hence the system sensitivity, high impedances of the circuitry connected to the sensor array must be ensured. Additionally, preventing resonance lies in minimizing parasitic interconnections from cable capacitances in high-frequency operating systems [7]. Furthermore, conditioning electronics generally include programmable gain amplifiers, to account for large signal variations between coils depending on their relative position around the imaging area; and demodulation devices that extract the amplitude from the input signal blacking out the reference signal.

Since its early development, MIT technology has undergone significant research to optimise the systems' performance. Wei [101], listed at least fifteen major research groups that had developed MIT systems for low conductivity measurements worldwide. There is not a universal consensus on the optimum MIT design approach, however, and like any other MFM technology, MIT systems must comply with the specific application requirement of the process to be monitored. In the particular case study addressed in this thesis, MIT instrumentation should be able to detect, recognise and identify secondary signals expected to be around 1% of the primary ones [86]. Special consideration must be taken regarding ambient experimental conditions, such as temperature since MIT systems operating at high frequencies experience performance degradation due to temperature fluctuations [95] [102]. Hence, the selection of the amplifiers and of the phase-detection instruments responds to the particular requirements of the process where MIT is to be used.

In previous work, various electronics optimisation approaches have been evaluated. MIT systems developed by Manchester University, Lancaster University and the University of Bath, use I/Q demodulation for signal digitalisation [90] [95]. The use of Signal Demodulation for phase measurement by direct digitalisation in substitution of centralised signal processing was proposed in [103]. This approach, while achieving lower noise levels than the previous architectures, suffered from significant drift fluctuations. Similarly, a later study proved that I/Q demodulation algorithms for phase measurement offer better stability than the FFT tone measurement technique [75]. A novel approach involves the use of reference sensors, i.e. gradiometers, to improve long term measurement stability [104]. The majority of MIT systems with multiple sensors in the literature use multiplexers to switch between the operation of the excitation and receiving coils. However, this approach introduces complex signal processing, given the system's non-linear behaviour due to the spatial distribution of sensors around the imaging area.

2.5.1.3 Data Processing

In general, data processing of signals from tomography systems comprise two main stages: solution of the Forward Problem and solution of the Inverse Problem. For MIT, the Forward Problem addresses the nonlinear relationship between the conductivity distribution and the measurement readings caused by the soft field effect that characterises the eddy current phenomenon [105]. For ECT, the Forward Problem comprises the combined effect of the permittivity values inside the imaging region have on the inter-electrode capacitances measured between the electrode-pairs. The Inverse Problem, on the other hand, is non-linear and ill-posed, since even large changes in the properties of an object have been proven to create arbitrarily small variations in the measured readings [106].

Tomography measuring techniques rely on the construction of sensitivity maps from the resolution of the Forward and Inverse Problems. The sensitivity matrices consist of identifying the affectation on the readings of each sensor by the location of a sample of known characteristics along each pixel in the imaging area. Accordingly, each combination of sensors will have an associated sensitivity matrix of 'p' pixel elements that indicate whether a change in conductivity or permittivity in a pixel affects the induced voltage in MIT or the capacitance measured by ECT between a particular sensor pair [107].

Calibrated sensitivity matrices lead to two further computation requirements to be solved via the Forward and the Inverse Problems, namely: quantification of measured changes given an unknown electric property distribution within the imaging area, and calculation of normalised property for every pixel element given a set of sensor-pair measurements.

A. The electromagnetic Forward Problem

The Forward Problem addresses the estimation of measured signals from the sensors. Solving the electromagnetic Forward Problem entitles the knowledge of the interaction between the electric and magnetic fields at every pixel element, given by Equation (5) [108]

$$F = \int_V f(\vec{E}\,\vec{H})dV \tag{5}$$

where the electric and magnetic fields, $\vec{E}$ and $\vec{H}$ respectively, are implicit functions (f) of the system parameters: conductivity, permeability, and permittivity, which in general vary along the imaging area.

Solving the Forward Problem requires the development of a mathematical model that relates the measurements in the imaging area to the electrical properties of the medium. Numerical models based on the approximate solution of Maxwell's equations, considering quasi-static electromagnetic field conditions are usually employed [105] [109]. Quasi-static electromagnetic conditions are valid for wavelengths of the electromagnetic field much larger than the maximum dimension of the system, such as in the case of interest of the present work (see discussion in Section 2.5.1.1).

Assuming a two-phase medium, one of which is conductive (see Figure II-7). Maxwell's Equations derive from the general equations in Table II-3 to both phases and the interface as follows.

Table II-3. Maxwell's Equations in matter

	Integral Equation	Differential Equations	Harmonic Time Case
Gauss' Law	$\oint \vec{D}\, d\vec{s} = \int_V \rho\, dV$	$\vec{\nabla} \cdot \vec{D} = \rho$	$\vec{\nabla} \cdot \vec{D} = \rho$
Gauss' Law for Magnetism	$\int \vec{B}\, d\vec{s} = 0$	$\vec{\nabla} \cdot \vec{B} = 0$	$\vec{\nabla} \cdot \vec{B} = 0$
Faraday's Law of Induction	$\oint \vec{E}\, d\vec{l} = -\frac{d}{dt}\int_s \vec{B}\, d\vec{s}$	$\vec{\nabla} \times \vec{E} = -\frac{\partial \vec{B}}{\partial t}$	$\vec{\nabla} \times \vec{E} = -j\omega\vec{B}$
Ampere – Maxwell's Law	$\oint \vec{H}\, d\vec{l} = \int_s \vec{J}\, ds + \varepsilon \frac{d}{dt}\int_s \vec{E}\, d\vec{s}$	$\vec{\nabla} \times \vec{H} = \vec{J} + \varepsilon \frac{\partial \vec{E}}{\partial t}$	$\vec{\nabla} \times \vec{H} = \vec{J} + \varepsilon j\omega\vec{E}$

where $\vec{B}$ is the magnetic flux, $\vec{J}$ is the current density, $\vec{D}$ is the displacement field, ε is the relative permittivity, ρ is the total electric charge density, and ω is the angular frequency.

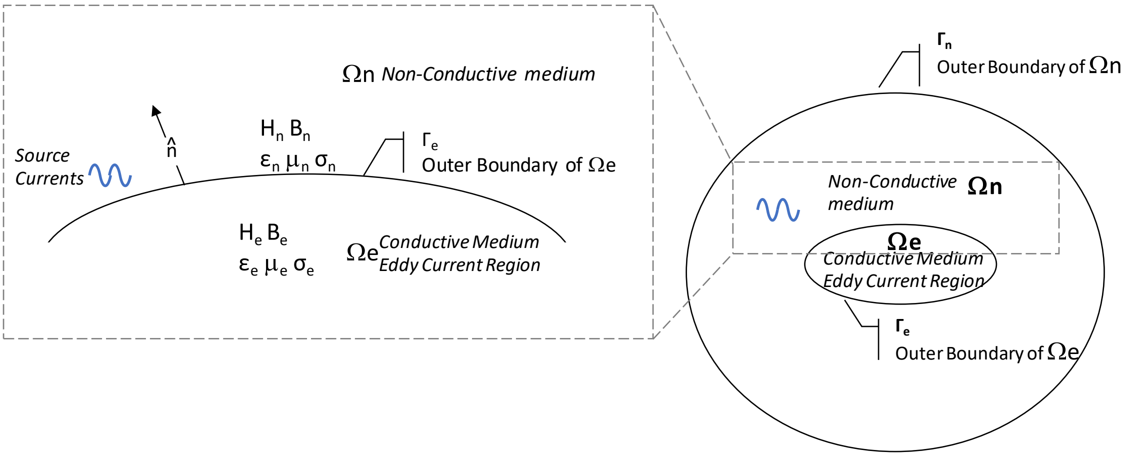

Figure II-7. Variable of the Forward Problem for the Conductive region (Ω_e), the Non-Conductive Regions (Ω_n) and the Interface (Γ_e)

The constitutive relationships that define the correlation between the material properties: conductivity (σ), permeability (μ), reluctivity (ν) and the fields are given by Equations (6) and (7)

$$\vec{B} = \mu\vec{H}\ , \quad \vec{H} = \nu\vec{B}, \quad \vec{D} = \varepsilon\vec{E} \quad \text{in} \quad \Omega_e \text{ and } \Omega_n \tag{6}$$

$$\vec{J} = \sigma\vec{E} \qquad \text{in} \qquad \Omega_e \tag{7}$$

Neglecting the effect of changing electric field in the system, and that of the eddy current in the current source and assuming that the matter behaves isotropically, the electromagnetic Forward Problem can be represented by the following set of equations. Note that the Gauss law equation is not required to solve the electromagnetic induction Forward Problem in MIT, as purely inductive coupling is assumed. However, it is relevant for capacitive measurements systems (ECT).

Non-Conductive Medium	*Conductive Medium*
$\vec{\nabla} \cdot \overrightarrow{B_n} = 0$ (8)	$\vec{\nabla} \cdot \overrightarrow{B_e} = 0$ (9)
$\vec{\nabla} \times \overrightarrow{H_n} = \overrightarrow{J_s}$ (10)	$\vec{\nabla} \times \overrightarrow{E_e} = -\dfrac{\partial \overrightarrow{B_e}}{\partial t}$ (11)
	$\vec{\nabla} \times \overrightarrow{H_e} = \vec{J_e}$ (12)

where, $\overrightarrow{J_s}$ refers to the current density due to primary field excitation, and $\vec{J_e}$ is the eddy current density.

The boundary conditions provide the coupling between the formulations in the non-conductive and conductive regions and ensure uniqueness of $\vec{B}$ and $\vec{E}$. Assuming homogeneity of the outer boundary of the eddy current region (Γ_e) and the non-conducting region (Γ_n) are represented by Equations (13) and (14) [110].

$$\vec{H} \times \hat{n} \ = \ 0 \quad \text{or} \quad \vec{B} \cdot \hat{n} \ = \ 0 \quad \text{on} \quad \Gamma_n \tag{13}$$

$$\vec{H} \times \hat{n} \ = \ 0 \quad \text{or} \quad \vec{E} \times \hat{n} \ = \ 0 \quad \text{on} \quad \Gamma_e \tag{14}$$

where $\hat{n}$ is the outer normal unit vector. The boundary condition in Equation (14), ensures that the tangential components of the electric field $\vec{E}$ and of the magnetic field $\vec{H}$ are continuous across the boundary between the two physical media. Equation (13) implies a zero normal component of the magnetic flux density, i.e. the magnetic field is purely tangential, and no flux leaves the non-conducting region (Γ_n).

i. Formulation of the Eddy Current Problem

Formulation of the Eddy Current problem can be divided into three main stages, namely: (a) formulation of the magnetic field distribution; (b) computation of the electromotive force (e.m.f.) induced in the receiving coil due to the eddy current distribution in the conductive medium; and (c) development of the Jacobi matrix.

(a) Magnetic field Distribution

Three methods are available in the literature for the solution of the Forward Problem, i.e. direct analysis, direct measurement, and finite element electromagnetic simulation. Direct measurement methods evaluate the response of the system to excitation experimentally by positioning a probe of known electrical properties into every pixel of the object space [66]. Direct analysis is detailed below, whereas finite element electromagnetic simulation, adopted in this work, is addressed in Chapter III.

Direct analysis of magnetic fields uses magnetic potential quantities, i.e. magnetic vector potential or magnetic scalar potential. The introduction of potentials answers to a convenient way to write the laws of classical electromagnetism, i.e. Maxwell's equations and the Lorentz force. These expressions prove that the laws of classical electromagnetism take the same form in any inertial coordinate system, and also provide a way to translate the fields and forces from one frame to another. The most straightforward formulation for eddy current problems with multiple conductors is the magnetic vector potential supplemented by an electric scalar potential in the conductor [111]. The modified approach, named reduced magnetic vector potential (A_r, ϕ), has been proposed for solving the eddy current problem [102]. It avoids modelling the structure of the sensor by interpreting the magnetic flux density as the sum of the impressed Biot-Savart field in free space ($\mu_0\vec{H}$) and the curl of a reduced vector potential ($\vec{\nabla} \times \overrightarrow{A_r}$) [110] . The introduction of the electric scalar potential ϕ takes into account the skin effect problem with voltage excitation.

<u>A_r, ϕ - Formulation in the Non-Conductive Region (Ω_n)</u>

The Magnetic Flux ($\vec{B}$) everywhere within the imaging area (Ω_e and Ω_n) is given by Equation (15)

$$\vec{B} = \vec{\nabla} \times \overrightarrow{A_s} + \vec{\nabla} \times \overrightarrow{A_r} \tag{15}$$

where $\overrightarrow{A_s}$ is the vector potential due to the current sources, and $\overrightarrow{A_r}$ is the reduced magnetic vector potential from all other contributions, in the eddy region.

Assuming the weakly coupled approximation, where the primary field does not change with the induction eddy currents in the conductive region [105], from Equations (6) and (15), we have that the Magnetic Flux due to the source current in the non-conductive region (permittivity equal to μ_0) is:

$$\overrightarrow{B_n} = \vec{\nabla} \times \overrightarrow{A_s} = \mu_0 \vec{H}_n \tag{16}$$

Hence,

$$\vec{B} \;=\; \mu_0 \vec{H}_n \;+\; \vec{\nabla} \times \overrightarrow{A_r} \qquad \text{in} \;\; \Omega_e \text{ and } \Omega_n \tag{17}$$

From Equation (6), (16) and (17), we have

$$\vec{\nabla} \times \overrightarrow{H} \;=\; \vec{\nabla} \times \nu\mu_0 \vec{H}_n \;+\; \vec{\nabla} \times (\nu \vec{\nabla} \times \overrightarrow{A_r})$$

$$\vec{\nabla} \times \overrightarrow{H} \;=\; \vec{\nabla} \times \nu(\vec{\nabla} \times \overrightarrow{A_s}) \;+\; \vec{\nabla} \times (\nu \vec{\nabla} \times \overrightarrow{A_r}) \;\; \text{in} \;\; \Omega_e \text{ and } \Omega_n \tag{18}$$

Combining Equations (10) and (16) yields

$$\overrightarrow{J_s} = \vec{\nabla} \times \left(\frac{1}{\mu_0} \vec{\nabla} \times \overrightarrow{A_s} \right) \tag{19}$$

<u>A_r, ϕ - Formulation in the Eddy Current Region (Ω_e)</u>

As previously stated the Magnetic Flux ($\vec{B}$) in Ω_e is given by Equation (17)

$$\vec{B} \;=\; \mu_0 \vec{H}_n \;+\; \vec{\nabla} \times \overrightarrow{A_r}$$

According to Faraday's Law of induction, the induced electric field can be written, using a magnetic vector potential ($\vec{A}$) and a scalar potential (ϕ) as:

$$\vec{\nabla} \times \overrightarrow{E} \;=\; -j\omega \vec{\nabla} \times (\vec{A} + \vec{\nabla}\phi) \tag{20}$$

Recalling from Equation (15) that the magnetic potential is the sum of the two parts, i.e. $\vec{A} = \overrightarrow{A_s} + \overrightarrow{A_r}$, the Electric Field $\vec{E}$ in the conductive region (Ω_e) is computed from Equation (21)

$$\vec{E} = -j\omega\overrightarrow{A_s} - j\omega\overrightarrow{A_r} - j\omega\vec{\nabla}\phi \tag{21}$$

The eddy current density is derived from Equations (7) and (21) as

$$\overrightarrow{J_e} = \sigma(-j\omega\overrightarrow{A_s} - j\omega\overrightarrow{A_r} - j\omega\vec{\nabla}\phi) \tag{22}$$

Taking the derivation of the field quantities in both the conducting and in the non-conducting regions above and noting Equations (10) and (12), the magnetic field at any point in the imaging area (Ω_n + Ω_e) is obtained from Equation (23)

$$\vec{\nabla} \times \vec{H} = \overrightarrow{J_s} + \overrightarrow{J_e} \tag{23}$$

The result of substituting Equations (18), (19) and (22) in Equation (23) is

$$\vec{\nabla} \times \nu\left(\vec{\nabla} \times \overrightarrow{A_s} + \vec{\nabla} \times \overrightarrow{A_r}\right) = \vec{\nabla} \times \left(\frac{1}{\mu_0}\vec{\nabla} \times \overrightarrow{A_s}\right) + \sigma\left(-j\omega\overrightarrow{A_s} - j\omega\overrightarrow{A_r} - j\omega\vec{\nabla}\phi\right) \tag{24}$$

$$\vec{\nabla} \times \nu\left(\vec{\nabla} \times \overrightarrow{A_r}\right) + \sigma j\omega\overrightarrow{A_r} + \sigma j\omega\vec{\nabla}\phi = \vec{\nabla} \times \left(\frac{1}{\mu_0}\vec{\nabla} \times \overrightarrow{A_s}\right) - \sigma j\omega\overrightarrow{A_s} - \vec{\nabla} \times \nu\left(\vec{\nabla} \times \overrightarrow{A_s}\right) \tag{25}$$

The conservation of the current density, called the continuity equation, which is implicit to Maxwell's equations, considers that the divergence of Equation (12) resulting in Equation (26) (considering that the divergence of a curls of a vector is zero)

$$\vec{\nabla} \cdot \vec{J} = 0 \tag{26}$$

From Equations (22) and (26), the impressed magnetic vector potential as a result of the current source can be expressed as [110]:

$$-\vec{\nabla} \cdot (\sigma j\omega\overrightarrow{A_r} + \sigma j\omega\vec{\nabla}\phi) = \vec{\nabla} \cdot j\sigma\omega\overrightarrow{A_s} \quad \text{in } \Omega_e \tag{27}$$

Given a spatial field distribution, the determination of the potential that satisfies Poisson's generalization of Laplace's equation, can be undertaken through the superposition integral; provided that the potential meets the interphase boundary conditions [112]. The superposition integral for the vector potential $\overrightarrow{A_s}$ can be obtained from the current density $\overrightarrow{J_s}$ in any point P in free space following Equation (28), according to the Biot-Savart Law.

$$\overrightarrow{A_s}(P) = \frac{\mu_0}{4\pi}\int_{\Omega_n} \frac{\overrightarrow{J_s}\,(Q)}{r_{QP}}\; d\Omega_Q \tag{28}$$

where r_{QP} is the vector pointing from a given source point, designated Q, to the field point, designated P.

A widely used technique for solving eddy current problems, outlined by the set of equations derived above, is the use of edge FEM, which is more accurate than the conventional nodal FEM approaches [112]. Biro [110] approximates the reduced vector potentials, by edge basis functions, N_i ($i = 1,2,\dots,n_e$) in a domain of n_e edges, to:

$$A_r \approx A_r^{(n)} = \sum_{k=1}^{n_e} a_k N_k \tag{29}$$

where a_k are the line integrals of A_r along the edges.

Similarly to the non-conductive region, the electric scalar potential can be solved by nodal basis functions as follows

$$\phi \approx \phi^{(n)} = \sum_{k=1}^{n_n} \phi_k N_k \tag{30}$$

where n_n is the number of nodes, and ϕ_k are equivalent to the values of $\phi^{(n)}$ at the kth node.

Substituting the reduced vector potential from Equation (29) and the scalar potential from Equation (30) and using the edge basis functions N_i as weighting factors in Equations (25) and (27), the following Galerkin equations yields

$$\begin{aligned}\int_{\Omega_e} \vec{\nabla} \times N_i \cdot \left(\nu \vec{\nabla} \times \overrightarrow{A_r^{(n)}}\right) d\Omega + \int_{\Omega_e} j\sigma\omega N_i \cdot \overrightarrow{A_r^{(n)}}\, d\Omega + \int_{\Omega_e} \sigma j\omega N_i \cdot \vec{\nabla}\, \phi^{(n)}\, d\Omega,\\ = \int_{\Omega_c} \vec{\nabla} \times N_i \cdot \frac{1}{\mu_0}\left(\vec{\nabla} \times \overrightarrow{A_s}\right) d\Omega - \int_{\Omega_c} j\sigma\omega N_i \cdot \overrightarrow{A_s}\, d\Omega\\ - \int_{\Omega_c} \vec{\nabla} \times N_i \cdot \nu\left(\vec{\nabla} \times \overrightarrow{A_s}\right) d\Omega,\end{aligned} \tag{31}$$

$$i = 1,2,\dots,n_e$$

where Ω_c is the coil region.

$$\int_{\Omega_e} j\sigma\omega\vec{\nabla}N_i \cdot \overrightarrow{A_r^{(n)}}\, d\Omega + \int_{\Omega_e} \sigma j\omega\vec{\nabla}N_i \cdot \vec{\nabla}\phi^{(n)} d\Omega = -\int_{\Omega_e} j\sigma\omega\vec{\nabla}N_i \cdot \overrightarrow{A_s}\, d\Omega,$$

$$i = 1,2, \dots, n_e \tag{32}$$

The only remaining unknown variables are the reduced vector potential $A_r^{(n)}$and the scalar potential $\phi^{(n)}$. Equations (31) and (32) can be solved by using FEM via iterative resolution or implementing direct method for simultaneous resolution of the algebraic equations in the domain. Iterative methods such as BiConjugate Gradients Stabilised Method (BICGSTAB) and the Incomplete Cholesky—Conjugate Gradient (ICCG) have been used in the literature for solving edge-based finite-element equations derived from electromagnetic formulations [106] [110] to obtain Equation (33)

$$SA_r = b \tag{33}$$

where S is the system Matrix, and b is the right-hand side current density or residual term.

By applying FEM, the second order partial differential equations can be computed by a combination of system of linear equations. Considering Equations (31), (32), and (33) assuming constant permeability, the finite element discretisation of the quasi-static electromagnetic fields are governed by (34) [109] [113]

$$\begin{bmatrix} \vec{\nabla} \times \left(\nu \vec{\nabla} \times () \right) + j\sigma\omega() & \sigma j\omega\vec{\nabla} \cdot () \\ \sigma j\omega\vec{\nabla} \cdot () & \sigma j\omega\vec{\nabla} \cdot () \end{bmatrix} \begin{bmatrix} A_r \\ \phi \end{bmatrix} = \begin{bmatrix} -j\sigma\omega\overrightarrow{A_s} \\ -j\sigma\omega\nabla \cdot \overrightarrow{A_s} \end{bmatrix} \tag{34}$$

Note that the linear system in (34) is indeed an approximation of (31) and (32) for a given subdomain [114]. Finite-element discretisation is discussed in Chapter III.

(b) Computation of the induced e.m.f.

The induced voltage in the sensors can be computed from Equation (35) [106]

$$V_{xy} = -j\omega \int_{\Omega c} \vec{A} \cdot \overrightarrow{J_0}\, d\Omega \tag{35}$$

where $\vec{A} = \vec{A}_s + \vec{A}_r$ and $\overrightarrow{J_0}$ is the virtual unit current density through the coil.

(c) Sensitivity Matrix

The Sensitivity Matrix, or Jacobian, correlates the distribution of the electrical properties within the medium to the measured signals. That is, it relates the internal conductivity perturbations to changes in the induced voltage. The sensitivity matrix is a square matrix composed of the first-order partial derivatives of a function [115]. The sensitivity Matrix of an MIT system is represented as follows:

$$\mathbf{J} = \begin{bmatrix} \frac{\partial V_{11}}{\partial \sigma_1} & \frac{\partial V_{12}}{\partial \sigma_2} & \cdots & \frac{\partial V_{1y}}{\partial \sigma_P} \\ \frac{\partial V_{21}}{\partial \sigma_1} & \frac{\partial V_{22}}{\partial \sigma_2} & \cdots & \frac{\partial V_{2y}}{\partial \sigma_P} \\ \vdots & \vdots & \ddots & \vdots \\ \frac{\partial V_{x1}}{\partial \sigma_1} & \frac{\partial V_{x2}}{\partial \sigma_2} & \cdots & \frac{\partial V_{xy}}{\partial \sigma_P} \end{bmatrix} \tag{36}$$

where $\mathbf{J}$ is the Jacobian or Sensitivity Matrix, V_{xy} is the measured voltage between the sensors x and y, and σ_P is the conductivity of the pixel P.

In accordance with [109], the components of the Sensibility Matrix are calculated from Equation (37)

$$\frac{\partial V_{xy}}{\partial \sigma_P} = -\frac{\omega^2}{I_0} \int_{\Omega_P} \overrightarrow{A_x} \cdot \overrightarrow{A_y} \, d\Omega \tag{37}$$

where Ω_P is the volume of the pixel P, A_x and A_y are solutions of the Forward Problem when the excitation coil x is excited by I_0 and when the receiving coil y is excited with a unit current.

Computation of the sensitivity distribution matrix corresponds to the solution of the Forward Problem. Methods for achieving this are discussed in the following section.

ii. Solution of the Forward Problem

Analytical solutions for the Forward Problem outlined by Equation (37) entail significant simplifications of the material properties and geometries [73] [116]. Alternatively, through numerical modelling, Maxwell's equations can be solved with high accuracy, even for anisotropic materials and complex geometries, provided the forward value problem is well defined. These numerical solutions are based on the discretisation of the problem and resolution of the electromagnetic governing equations within the subdomains. The mathematical and engineering literature provides extensive coverage on the use of finite elements in electromagnetics. Details of the electromagnetic model are provided in Chapter III. Discussion of the application of the finite element method to electromagnetic problems, however, is outside the scope of this thesis, yet relevant information can be found in [117] and references therein.

B. The Inverse Problem

After the determination of the sensitivity map, through the Forward Problem, it is possible to compute the induced voltage for a given conductivity distribution between the sensors. The Inverse Problem addresses the following issue: given a set of measurements, calculate the values of conductivity of each pixel within the imaging area that correlates to the sensor's measurements. The purpose of this section is to explain the general framework of the electromagnetic inverse problem, and to review the image reconstruction algorithm used in the remainder of this work.

The MIT Inverse Problem is intrinsically related to the Forward Model and is defined by Equation (38)

$$\mathbf{J}P = M \tag{38}$$

where $\mathbf{J}$ is the sensitivity map computed from the Forward Model, M is a column vector containing the measurements from the sensors, and P is a column vector representing the number of pixels.

Typically, the number of measurements is far less than the number of pixels ($M \ll P$); consequently, the sensitivity map is non-reversible, and the solution P is a discontinuous function of the measured data. The Inverse Problem unavoidably involves inverting the sensitivity matrix, hence resulting in unreliable results [102]. Alternatively, the implementation of indirect methods that use penalty functions and relaxation terms can mitigate this problem [118]. The problem is then to find the optimal regularization parameters, which vary strongly from one flow regime to another [119]. Flow pattern characterisation requires times-difference imaging to calculate the change in electrical properties between two states, separated in time.

The MIT inverse problem is severely ill-posed. This implies that even small perturbations in the measurements, can cause large changes in the solution. Hence, for any given measurement precision, there may be arbitrarily large changes in the obtained electrical properties, since the induced voltage is a measured quantity which is subject to observational errors. However, the ill-posedness of the problem does not mean that a meaningful approximate solution cannot be computed. Rather, it implies that the standard methods in numerical linear algebra cannot be used in a straightforward manner to compute a solution. Therefore, solving the inverse problem requires special treatment. In practice, the formulation of the inverse problem is complicated by well-posedness issues and the numerical solution often requires complex and CPU-expensive algorithms. The optimisation of inverse problems is outside the scope of this work, but dedicated research on the topic is readily available in the literature.

(a) Linear Back Projection (LBP)

One of the most widely used algorithms for image reconstruction, i.e. inverse problem solution, is the Linear Back Projection (LBP) method. The LBP method is based on back-projecting the profiles of an object onto the image plane and superimposing them form an approximation of the original object [120]. LBP treats each pair of sensors independently and considers which pixels inside the imaging area contribute to the variations in the measured signal when the conductivity of the pixel departs from the calibrated values [107]. This method assumes that all pixels contribute equally to the mutual inductance effects, resulting in poor quality images.

The LBP reconstruction method is based on Equation (39)

$$P = \mathbf{J}^T M \tag{39}$$

where $\mathbf{J}^T$ is the normalised transposed sensitivity map.

A variation to LBP is the Weighted Linear Back Projection, which has been proven to be applicable for MIT in low contrast conditions [121]. The technique is expressed by Equation (40)

$$\sigma(x, y) = C \sum_{T} W(x, y, T) \Delta_T^S (s \mid_{x_{xyT}^2(l) + y_{xyT}^2(l) = r^2, l > 0}) \tag{40}$$

where $\sigma(x, y)$ is the reconstructed conductivity at the coordinates (x, y), T is the number of the inductor coil, r is the radius of the imaging area, $x_{xyT}(l)$ and $y_{xyT}(l)$ are the parametric equations of the unperturbed magnetic lines passing through the coordinates (x, y), l is the distance from the point (x, y) measured along the unperturbed line, C is a calibration factor, Δ_T^S is the profile of the measured phase shift filtered by the Ramachandran-Lakshminarayanan and s is the distance along the boundary from the excitation source to the point of intersection with the field line passing through the point being reconstructed.

The LBP algorithm effectively acts as a spatial filter, hence, images produced by this method are approximate solutions. The method spreads the true image over the entire cross-section and can consequently produce blurred images. Moreover, because the image is spread out over the sensor area, the magnitude of the pixels will be less than the true values. This effect imposes challenges in the identification of dispersed flow regimes. Issues particularly associated with flow regime identification include the effective 'smearing' of small structures like bubbles across larger areas of the flow, the difficulty of imaging thin films near the wall and resolving their exact thickness (both parameters very important for fluid mechanics modelling). Tackling these issues may be done in pragmatic ways via thresholding [55] to reduce the effect of smearing, and bubble mapping [122] but these methods to some extent involve fore-knowledge of flow conditions. The implications of the different techniques have not been completely explored in the literature and are beyond the scope of this work.

However, in LBP the sum of all of the image pixels will approximate to the true value, and it is possible to improve the reconstructed images using simple iterative techniques. The method for doing so described in [123] is an ATOUT Ltd proprietary algorithm, which was used in this work to improve the image quality of challenging flow geometries.

The next chapter is dedicated to the solution of the electromagnetic Forward Problem. A thorough design of the MIT sensors accounting for sensor sensitivity is provided in Chapter IV.

2.6 Discussion and Conclusions

An overview of the oil and gas industry and the multiphase flow measurement market was presented in the present chapter. The continuous increase in the use of fossil fuels in hand with the decreasing rate of discoveries has encouraged the industry to venture into deep waters in the search for new field developments and join efforts to continue producing from mature fields at profitable rates. The challenges that the petroleum industry faces involve making marginal fields more cost-effective, developing production facilities for hostile physical environments, and improving energy efficiency. In this context, multiphase flow measurement (MFM) has had an increasing presence in the oil fields to optimise decision-making processes aiming to reduce production and development costs.

It was seen that current MFM systems are mostly based on intrusive pressure drop techniques associated with nucleonic density measurements. The commercial solutions available in the market fail to address all the industry requirements in terms of non-intrusiveness, accuracy, costs, and environmental impact. In this sense, electrical tomography systems, which are based on soft-field tomography measurements, were discussed to be non-invasive and low-cost, and enable data acquisition of the volumetric fractions of multiphase flow in pipes. The intrinsic features of the ECT and MIT, such as direct measurement of the electrical properties of the flow phases without previous separation and the fact that they do not rely on nuclear sources were seen to be attractive to the researchers aiming to provide metering solutions to the Oil industry.

It was discussed that achieving a high spatial resolution from soft tomography systems, like ECT and MIT, entitles, high quality of reconstructed images, high sensitivity of the sensor and accurate solution of the forward problem, which must be representative of the physical phenomena. The sensitivity of the sensor to small changes in the electric properties inside the pipe varies with the radial position of the perturbation and is also a function of the size of the perturbation and the magnitude of its property change. Typically, circular sensor arrays have maximum sensitivity near the sensor wall and minimum sensitivity at the centre of the sensor. Furthermore, the flow material properties along the length of the sensor are axially averaged for every time frame. The axial and radial resolutions limit the measurement accuracy of soft tomography techniques for dispersed flow regimes, which in most cases has transients that cannot be traced.

ECT and MIT are exploited in the remainder of the thesis, building upon the existing body knowledge reviewed in the literature survey above. The hardware for a MIT meter is to be designed based in the premise described in this chapter. In this sense, the MIT sensor head will comprise a circular array of exchangeable air-core coils of the same geometry surrounding the perimeter of the pipe. This assembly has been proven in the literature to provide enhanced measurement accuracy and yield linear behaviour. The size and number of sensors will be determined considering the theoretical spatial resolution and the skin effect in low conductive fluids.

The MIT prototype will account for electromagnetic shielding. Selection of the shield material, size and thickness must account for the elimination of the capacitive coupling between the coils while avoiding the reduction of the system sensitivity. Similarly, the sensors of ECT system used in the remainder of the thesis, are fully guarded, ensuring that the axial sensitivity of the measurement electrodes is well-constrained to the length of the electrodes.

The relationship between the conductivity distribution and the measurements require resolution of the Forward Problem. This is to be undertaken through numerical simulation, which avoids the simplifications of the analytical approach and provides high accuracy. All the MIT experiments conducted in the following chapters follow the general procedure detailed in Section 2.5.1.2.

Chapter III Numerical modelling

3.1 Introduction

The electromagnetic Forward Problem predicts the received signals for a given electrical distribution within the imaging region. The solution of Maxwell's equations, which govern the electromagnetic phenomena, can be approached from two angles: analytical and numerical methods. Analytical solutions of the MIT problem, although theoretically exact, are often of limited validity, due to the inherent simplifications needed to reach a solution, e.g. simple boundary conditions and isotropic materials. Numerical methods solve Maxwell's equations by partitioning the space into subdomains, through an approximate formulation of the problem. This approach provides little physical constraint and a large application range.

The purpose of this chapter is to detail the modelling approach undertaken in this thesis. In this sense, the present study intends to support the simulation models that are exploited in Chapter IV for sensor characterisation, in Chapter V for hardware design, in Chapter VI for measurement reference, and in Chapter VII for the redefinition of the operation envelope of the technology.

Several numerical approaches and computational programmes were used throughout this thesis. In this chapter, details of the computational electromagnetic method used to solve the MIT Forward Problem are provided. The chapter starts with an explanation of the basic principles of Finite Element (FE) and its implementation for MIT simulation in Section 3.2 and Section 3.3. The solution of the Forward Problem using two commercial software is discussed in Section 3.4, with the workflow adopted for simulation provided in Section 3.5. In Section 3.6, the performance of the numerical models is assessed through a series of benchmark tests designed to validate the problem boundary conditions and its well-posedness. Finally, Section 3.7 presents a discussion of the results and provides an overall conclusion.

3.2 Boundary value problem

The boundary value problem comprises the characterisation of the region over which the governing equations are to be solved and the boundary conditions to be applied. To solve Maxwell's equations, derived in Chapter II, the first-order differential equations encompassing two field quantities need to be converted into second-order differential equations with only one field quantity. This is achieved through the implementation of magnetic vector potentials or scalar electric potentials [124]. The defining equation for magnetic vector potential ($\vec{A}$) is derived from the magnetic Gauss' law and the electric potential (ϕ) results from Faraday's law. Their implementation yields the following formulation:

$$\vec{B} = \nabla \times \vec{A} \tag{41}$$

$$\vec{E} = -j\omega\vec{A} - \nabla\phi \tag{42}$$

The simulation models developed consider the effect of displacements currents, neglecting the eddy current approximation. Using the definition of potentials and the constitutive relations $\vec{B} = \mu(\vec{H} + \vec{M})$ and $\vec{D} = \varepsilon\vec{E}$**,** the Maxwell-Ampere's law, including displacement currents, can be expressed as

$$\nabla \times \vec{H} = \vec{J} + \frac{\partial\vec{D}}{\partial t} = \sigma(\vec{E} + \vec{\mathrm{v}} \times \vec{B}) + \vec{J_e} + \frac{\partial\vec{D}}{\partial t} \tag{43}$$

where $\vec{M}$ is the magnetisation vector that describes how the material is magnetised when subjected to a magnetic field $\vec{H}$ and $\vec{\mathrm{v}}$ is the velocity of the conductor.

Considering time-harmonic fields and the field definitions in (41) and (42) yields

$$\nabla \times ({\mu_0}^{-1}\nabla \times \vec{A} - \vec{M}) + \sigma(j\omega\vec{A} + \nabla\phi) + j\omega\varepsilon_0(j\omega\vec{A} + \nabla\phi) - \sigma\vec{\mathrm{v}} \times (\nabla \times \vec{A}) = \vec{J_e} \tag{44}$$

The relevance of including the displacements currents in the problem formulation is demonstrated in Chapter VII.

To obtain unique solutions, constraints are needed via a selection of gauge transformations. Gauge selection possibilities generally comprise the Coulomb gauge, $\nabla \cdot \vec{A} = 0$, or the temporal gauge, $\phi = 0$ [110]. The dynamic formulations in the frequency-domain-study types use a temporal gauge, hence only the magnetic vector potential is considered. This formulation, known as the A-formulation, derives in the Ampere's law rewritten as

$$\nabla \times \left(\mu_0{}^{-1}\nabla \times \vec{A} - \vec{M}\right) + \vec{A}(j\sigma\omega - j\omega^2\varepsilon_0) - \sigma\vec{v} \times \left(\nabla \times \vec{A}\right) = \vec{J_e} \tag{45}$$

By solving the general equation of the Forward Problem, given a set of boundary conditions, the A-field can be estimated anywhere in the domain. Hence, the e.m.f. induced in the receiving sensor is computed from (46) [106]:

$$V = -j\omega \oint_{coil} (\vec{A} \cdot \vec{J_o})\, dl \tag{46}$$

where $\vec{J_o}$ is the virtual unit current density through the coil and dl is the length of the coil. Note that (46) is similar to the general form given in (35).

3.3 Computational Electromagnetics

Computational electromagnetics (CEM) encompass modelling the electromagnetic fields governed by Maxwell's equations. CEM comprises numerical approaches that partition space into subdomains to solve Maxwell's equations on each entity [125]. Depending on the relevant domain, i.e. time or frequency domains, various methods are available. In this thesis, the electromagnetic measurements are induced by means of a time-harmonic excitation coil; hence the frequency domain is of interest. In the frequency domain, the most relevant methods are the method-of-moments, the finite integration time method, and the FEM [125] [126]. FEM is advantageous for intricate shapes and non-linearities and is preferred for the computation of magnetic problems over other numerical methods [116] [125] [126]. Thus, FEM is the method employed in most commercial packages and is detailed below.

3.3.1 Finite element method (FEM)

FEM is a numerical technique for solving the boundary value problems via approximate solutions. FEM is based on volume discretisation, where the space is subdivided into small mesh elements. The mathematical models that describe the electromagnetic phenomena are also discretised by the FEM.

The resulting partial differential equations describe Maxwell formulation and the boundary conditions, i.e. the boundary value problem together with initial conditions. The discretisation of the mathematical model results in the numerical model of the singular system.

FEM discretises the integral form of Maxwell's equations for all subdomains. The distribution of the unknown parameters within each domain is interpolated from either the values of the nodes or the values of the edges (edge FEM). The interpolation, defined by the shape functions, accounts for a set of polynomials. These polynomials must satisfy three key requirements, i.e. continuity, differentiability, and completeness. Consequently, shape functions must guarantee continuity of the primary unknown quantities across the inter-domain boundaries and accurately characterise the solution in the FE domain [127].

The numerical solution of the problem is obtained after solving the system of linear equations resulting from the governing differential equation and boundary conditions. The system of equations yields a global matrix system that characterises the entire domain of the boundary value problem [127].

The difference between the solution to the numerical and the mathematical models results in residual errors. The accuracy of the computed numerical solution is greater, with the residual error approaching zero, for a larger number of subdivisions [124]. However, despite how small the subdomains are, the residual error cannot vanish at every point in the domain. The weighted residual method, based on the multiplication of the residual error by a weighting function, forces the integral of the weighted expression to become zero [128].

3.3.1.1Weak formulation

The initial step in FEM is the weak formulation of the mathematical model. The weak formulation turns the differential equation into an integral equation, with weight functions defined over each domain [124]. For second-order differential equations, the shape functions, which are used to interpolate the primary unknown variable, need to be twice differentiable. By using integration by parts and distributing the second derivative between the weight and the shape functions, the requirement of differentiability is weakened. This yields shape functions, which need to be only once differentiable. The outlined formulation is called weak formulation.

The selection of the weighted residual technique defines the type of weighting function. Two techniques are normally used to formulate the electromagnetic equations using FE, namely the Rayleigh-Ritz and the Galerkin methods. The former, although mathematically desirable, is difficult to apply, whereas the Galerkin method is guaranteed to integrate the governing equations even when the Rayleigh-Ritz method fails [128]. In the Galerkin method, the weights are set to be equal to the shape functions, yielding a system of linear algebraic equations that satisfies the number of unknown variables [128].

The weak form of the MIT boundary value problem from (45) is given by

$$\int_{\Omega} \left(\left(\nabla \times \left({\mu_0}^{-1} \nabla \times \vec{A} - \vec{M} \right) \right) \cdot \vec{W} + (j\sigma\omega - j\omega^2 \varepsilon_0) \vec{A} \cdot \vec{W} - \left(\sigma \mathbf{v} \times \left(\nabla \times \vec{A} \right) \right) \cdot \vec{W} \right) d\Omega = \int_{\Omega_n} \vec{J_e} \cdot \vec{W} \, d\Omega \tag{47}$$

where $\vec{W}$ is the weight function.

Scalar potentials can be approximated by nodal or edge shape functions. Nodal functions result in spurious solutions and are unable to model field singularities in geometrically thin elements [129]. Conversely, edge elements, also called Nédélec elements, are suitable for modelling complex shapes and discontinuous electromagnetic properties arising from electromagnetic waves propagating through various materials [130]. The shape functions for edge elements (edge FEM) are constructed so that their tangential components are continuous across the inter-element border without imposing conditions on their normal components [131].

3.4 Computation Software

Adopting commercial computation software allows fast model development and multiple scenario evaluation. Due to license availability aspects, two commercial FE software packages were interchanged throughout the various studies performed along this thesis. COMSOL and CST Studio Student Edition were used to solve the Forward Problem of MIT with outputs from both models showing consistency as discussed in Section 3.6.3.

The AC/DC module in COMSOL and the CST EM studio use the FEM to solve the governing electromagnetic problem described in (47) [132] [133]. Alternatively, the RF module in COMSOL, which also solves the full set of Maxwell's equations, was used here for eigenfrequency computation undertaken as part of the MIT sensor design.

3.5 Workflow

FE analysis of the boundary-value problem comprises, in general terms, the following steps: a) domain discretisation; b) selection of shape functions; c) formulation of a system of equations and; d) solution of the global matrix [124]. When using commercial software, this workflow translates to the tasks described below.

3.5.1 Geometry

Prior to developing a domain discretisation, a geometry model needs to be created. FEM simulations entail special geometry considerations since unnecessary short edges or small faces may result in an undesirable concentration of elements. The models here used were simulated in a 3D space and comprised the free space domain, the sensors model, and the electromagnetic shield.

3.5.1.1 Free space

Model accuracy depends on the boundary conditions of the region of interest. One modelling approach is to set the spatial domain to be sufficiently large so that its exterior boundary conditions do not considerably affect the solution. The external boundary conditions that commercial software provide are based on forcing a zero normal component of the field, i.e. $\hat{n} \times \vec{A} = 0$ [134]. Placing the external boundary conditions far away from the electromagnetic source allows a sensible approximation to the decay of the field [116]. However, large domains lead to large and hence expensive computational models.

Alternative methods to limit the extent of the model include imposing an artificial truncation of the domain through coordinate scaling or wave absorption [134]. Replacing the boundary condition, $\hat{n} \times \vec{A} = 0$, for an absorbing boundary condition yields waves to be absorbed into the domain without reflection. A common boundary condition for wave absorption is that of perfectly matched layers (PML), which applies a coordinate scaling to a layer of wave-absorbing virtual elements on the exterior of the domain. PML is not available in the AC/DC module of COMSOL but is available for eigenfrequency studies in the RF module.

Coordinate scaling also allows an adequate description of the field distribution on smaller computational domains. In AC/DC COMSOL, the 'infinite elements' built-in feature was used to model the free space of the MIT problem. Infinite elements use domains that virtually stretch-out towards infinity. In the outer layers surrounding the computational domain, where infinite elements are applied, the dependent variables are forced to vary slowly with radial distance from the centre of the domain.

3.5.1.2 Sensors

The MIT design and the subsequent comprehensive evaluation of the system capabilities required the implementation of various sensor-modelling approaches. These modelling methods range from detailed geometry modelling to simplified geometry approximations with special considerations.

A. Detailed geometry

Sensor design requires finding the fundamental resonance frequency of the coils. In inductors, the geometric characteristics determine the frequency at which the parasitic capacitance resonates with the inductance [135]. This leads to the need to model the detailed features of the sensor geometry by means of an eigenfrequency analysis (see Figure III-1). Other modelling approaches, like the coil-domain approximations, do not account for winding capacity and thus do not exhibit self-resonance as a real coil does.

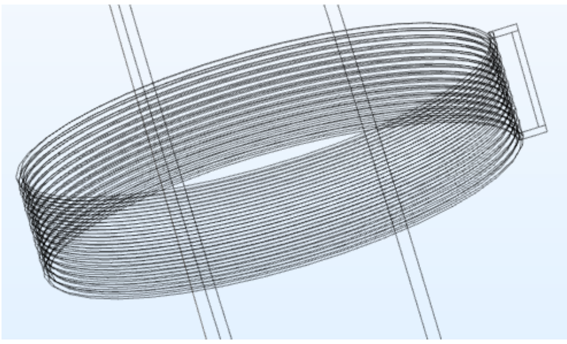

Figure III-1. Exemplary geometric model of circular helix coils in COMSOL-RF module

In the eigenfrequency study, the coil geometry is modelled explicitly, including the winding separation and insulation. The sensor characteristics and domain varied according to the method shown in Figure III-2. Initially, the inductor was considered a perfect conductor, where the tangential part of the magnetic field was zero ($\hat{n} \times \vec{H} = 0 = \hat{n} \times \left(\mu^{-1}\nabla \times \vec{A}\right)$), and the eigenfrequency equation was solved for the electromagnetic waves only in the surrounding air domain. Subsequently, the conductive surface losses were considered by assigning material properties of the copper to the coil domain. Results were contrasted to select the most appropriate modelling approach aiming to tune the maximum number of turns admissible for a given coil profile and dimensions. The results from the evaluated scenarios are shown in Section 3.6.

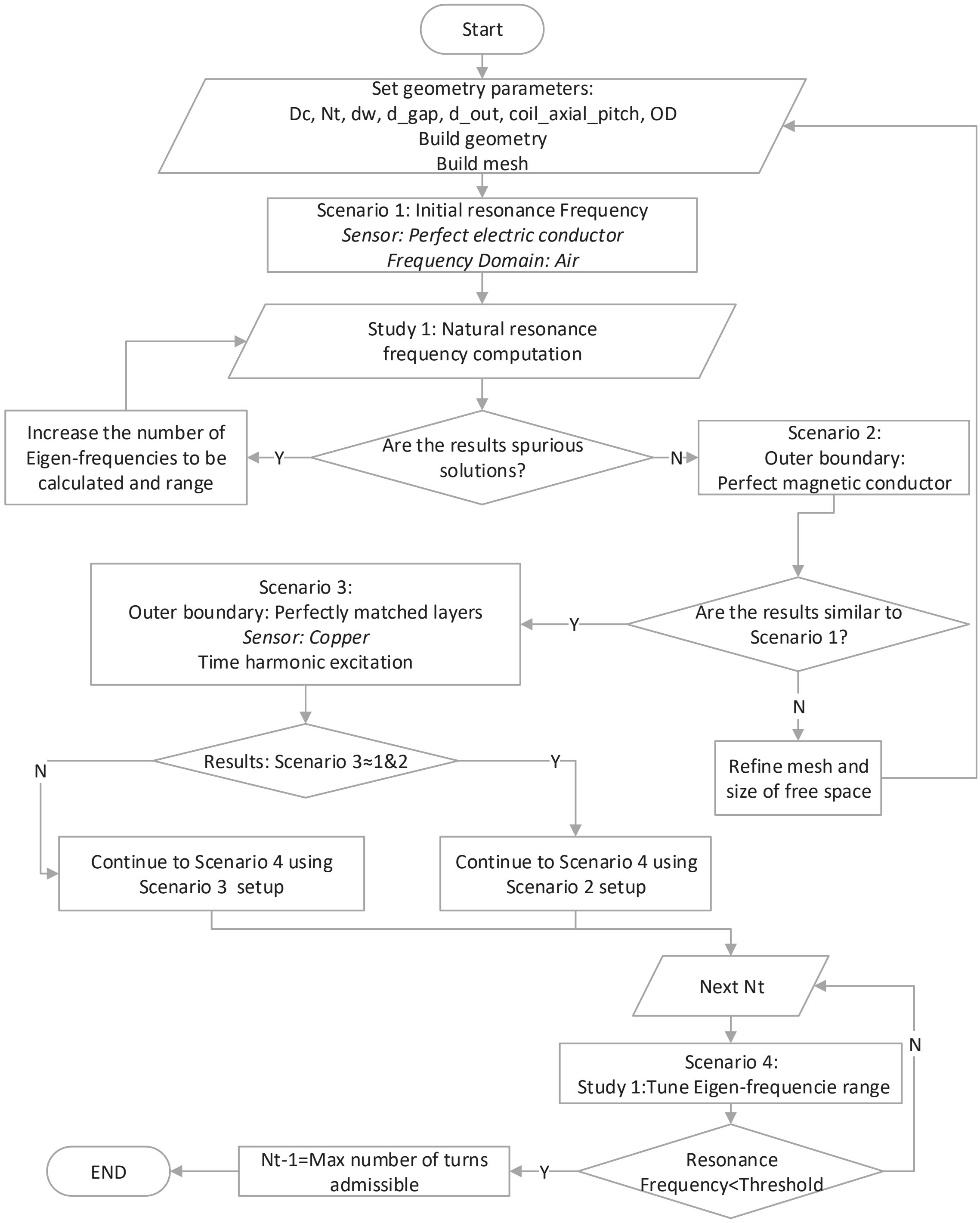

Figure III-2. Flow diagram of resonance frequency simulation in COMSOL for coil design

B. Geometry Approximations

Conversely to the eigenfrequency study, for the solution of the Forward Problem of the MIT system, the coils are modelled as solid blocks (see Figure III-3). This approach makes use of the available software geometry approximations, i.e. coil domain, to reduce the computational cost of the models, which by other means could be prohibitive. The coil-domain-based model ensures a closed current path in agreement with Maxwell’s equations. This condition is satisfied by introducing an excitation source across an infinitesimal cross-sectional slit. The excitation slit alongside the coil domain built-in function assumes that the source is outside the modelling domain and by doing so, it provides the possibility to model alternative features outside the coil array and assign different boundary conditions on the exterior of the modelling domain. The winding characteristics of the coils are specified by using the homogenised multi-turn and stranded functions in COMSOL and CST, respectively. The effective cross-sectional area of the winding considered the skin depth of the winding material at the excitation frequency.

The coil definition entitles specification of the excitation source. The sensing coils were modelled as open circuits with the electromotive force computed from (46) representing the maximum potential difference when no external load is connected. The direction of the current is set so that the magnetomotive force of the coils were joined in series [136].

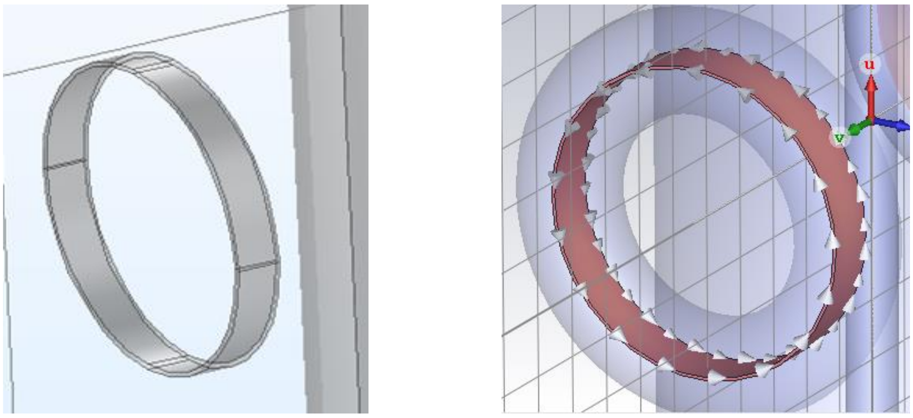

(a) (b)

Figure III-3. Geometric model of circular helix coils in (a) COMSOL-AC/DC module and (b) CST EM Studio

Alternatively, for the evaluation of planar PCB coils geometries, whose thickness is fundamentally smaller than any other dimensions, the layered shell domain introduced in COMSOL v5.4 was used. This feature allows the coil layout to be drawn as flat and on the same plane. In this type of simulation, the current flows in between layers through vertical interconnected access (VIA). The model initially considers an open path for the surface current density computation from Ohm’s law. The computed surface current density is later applied as the source term in the Ampere’s law to compute the magnetic field distribution in the space surrounding the coil.

3.5.1.3 Shield

Similar to the coils, the shield design accounts for various modelling techniques. Investigation of the shielding material, thickness and relative height to the sensor size were performed by discretising the shield as an additional material. In this modelling approach, the electrical properties of the shielding material are considered, and the decay of the magnetic field through the thickness of the barrier can be evaluated. The interface conditions here are imposed by the edge element formulation [137]. The induced and transmitted fields, beyond the shielding material, in the free space region would extend to the truncating boundary.

For the considerably larger model of a MIT Forward Problem, in order to avoid numerous extremely small elements and save significant computational effort, two alternative approaches were evaluated. The first modelling technique comprised truncating the domain at the surface of the shield by imposing the impedance boundary condition (IBC). The IBC models a small permeation of the field inside the shielding material, i.e. small skin depth at high frequencies [134]. This assumes that the currents flow entirely on the surface of the shielding material and avoids solving Maxwell's equations in the interior of the domain.

The second modelling approximation accounts for a geometrically thin shielding material using the transition boundary condition (TBC). The TBC represents a discontinuity in the fields across the boundaries due to the induced current densities arising on the surface of the boundary [134]. Contrary to the IBC, the TBC considers the material properties as well as the thickness of the material as inputs, leading to a drop in the transmitted electric field [134].

3.5.2 Domain discretisation

The division of the computational domain into subdomains or finite elements is key in FEM. In FEM, the distribution of the unknown variable inside every mesh domain is interpolated from the conditions in the edges of the elements. Meshing algorithms built in commercial software provide a variety of 3D element types, namely tetrahedral, bricks, prisms, and pyramids. Tetrahedral elements provide the advantage of being able to mesh any 3D volume, including complex shapes and topologies, with smaller discretisation error than other element types [138]. Furthermore, elements with triangular profiles are advantageous when using edge elements to solve electromagnetic problems [127]. Hence, in this study, tetrahedral edge FE was used to solve the weak form of the problem.

The density and quality of the mesh strongly affect the numerical solution. An increased mesh density leads to more precise results but also results in larger computation time and memory requirements. Furthermore, low regularity of the mesh elements' shapes, i.e. mesh element quality, can lead to convergence issues [139]. The meshing technique must ensure that the meshed domain accurately represents the physical characteristics of the system and that in regions where large field variations are expected, sufficiently small elements are used [127]. Additionally, avoiding elements from overlapping is crucial for solution convergence.

In order to decrease the error induced due to the finiteness of the mesh, i.e. discretisation error, a mesh refinement exercise was performed. All scenarios fulfil the general meshing rule of a minimum of 10 linear elements per wavelength and two linear elements per skin depth where no special boundary conditions are imposed [134]. An accurate mesh discretisation was achieved by empirically evaluating the impact of the mesh element size on the solution. This was done by successively decreasing the size of the mesh elements until the consecutive solutions were virtually the same; that is, the difference between them was less than 1E-3.

The amplitudes and phase from the mesh sensitivity study were assessed using different medium conductivities. Results show that increasing the number of elements beyond 56K does not provide significant improvement to the solution. Setup 2 in Table III-1 was found to provide a small discretisation error and sensible computational cost, hence this meshing configuration was used for the solution of the MIT Forward Problem.

Table III-1. Mesh discretisation exercise using predefined element sizes in COMSOL

Simulation index	**Mesh Size**	**Coils**	**Free space**	**Total tetrahedral elements**
1	Normal	Extra fine	Finer	212,228
2	Normal	Finer	Fine	56,396
3	Normal	Extremely fine	Normal	292,988

3.5.3 Solver setup

The number and order of the elements in the mesh structure dictate the dimension of the linear system of equations to be solved. In a problem with well-defined boundary conditions, different solvers should reach virtually the same solution. However, different solver types lead to dissimilar computation times. The direct solvers provide advantageous computation speed and robustness over the iterative methods [131]. However, direct solvers require significant memory resources and can become prohibitive for large meshing domains, where iterative solvers perform better.

It is a common feature in commercial software to provide built-in default solver settings, based on the characteristics of the problem. The solver selection accounts for the greatest possible robustness and lowest memory usage. AC/DC COMSOL provides various iterative solution techniques. Here, the biconjugate gradient stabilised method (BiCGStab) was used. Using BiCGStab, the memory usage and computation time for every iteration are constant. The speed of convergence was accelerated using a geometric multigrid (GMG) preconditioner. GMG is suitable for electromagnetic models due to its approach of combining speed and memory efficiency [139].

The element type used in the simulations was restricted to only first-order and second-order edge elements. Higher-order elements add additional degrees of freedom in interior mesh elements, which decreases the sparsity of the system and leads to larger memory requirements.

3.6 Benchmark tests

Validation of the numerical models addressed in previous sections, targeting the MIT Forward Problem, was performed through a series of benchmark tests detailed in the following subsections. In all cases, a residual error lower than 1E-3 was achieved.

3.6.1 Boundary conditions for the computational domain

The eigenfrequency study was designed to alternatively account as a benchmark test for boundary condition assessment (see Figure III-2). The setup model comprised modelling the detailed geometry of a circular helix coil of 34 mm diameter and 14 turns wound from a 0.5 mm wire. The coil is placed in the midplane of a spherical domain. The study accounted for two boundary conditions on the computational domain. First, a free space domain sufficiently large was modelled so the outer perfect electric conductor boundary conditions would not affect the numerical solution. The dimension of the spherical free space was set to be three times larger than the coil outer diameter.

Perfect magnetic conductor layers were then added in the exterior face of the domain (see Figure III-4). The objective of this is to corroborate the spatial domain considerations by comparing the results from both approaches.

The eigenfrequency solver was set up to provide four frequencies below 100 MHz, and the results of the first harmonic frequencies for both approaches was compared. The perfect electric conductor boundary conditions (scenario 1 in Figure III-2) returned an eigenfrequency of 49.758 MHz. For the scenario where the perfect magnetic conductor conditions were applied to the outer layers of the domain (scenario 2 in Figure III-2), the computed eigenfrequency was 49.429 MHz. The proximity of both results suggests that the size considered for the free space domain is sufficiently large to confine the extent of the physical effect.

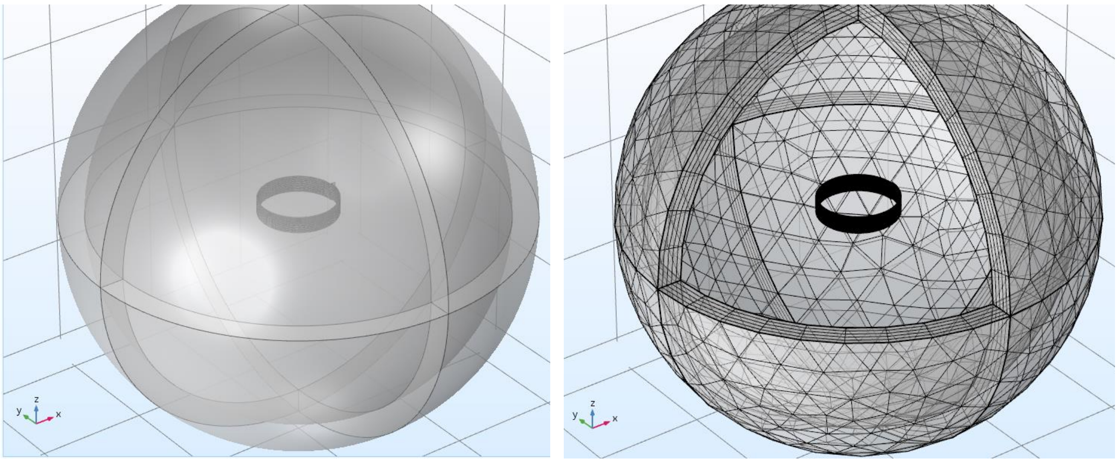

Figure III-4. Model setup and mesh view of perfect magnetic layered computational domain in the detailed coil geometry model

For material parameters (permittivity and conductivity) with sharp interfaces, the field equations are complemented with appropriate interface boundary conditions. This means that at the interface between the two media, the tangential components of the electric and magnetic fields must be continuous, yielding:

$$\hat{n}_2 \times \left(\overrightarrow{E_1} - \overrightarrow{E_2}\right) = 0 \tag{48}$$

$$\hat{n}_2 \times \left(\overrightarrow{H_1} - \overrightarrow{H_2}\right) = J_s \tag{49}$$

where the subscripts 1 and 2 refer to the different mediums.

3.6.2 Boundary conditions for shield design

The benchmark test for shield modelling contrasts the selection of IBC and TBC for the boundaries of the shielding material. The model comprised an array of coils located around a cylindrical imaging area of 110 mm in diameter enclosed in an electromagnetic shield. The model shown in Figure III-5(a) involves IBC assigned to the surface of the shield, as suggested in [132]. Here, the free space is modelled as an air cylinder that envelops the coil array and continues through the shield open ends.

An alternative approach, illustrated in Figure III-5b, assigns a TBC to the shield domain. Conversely to the IBC model, the shield geometry here is contained within the free space domain. The size of the computational domain is three times larger than that of the shield. The cylindrical free space was terminated using infinite domain layered elements. The coil geometries and computational domain height of both setups were kept the same in the interest of model comparison.

The results of the phase angle measured from a receiving coil positioned opposite the transmitting coil are shown in Figure III-6. In the plot, the TBC and IBC models are compared for various coil-to-shield distances, i.e. stand-off distance (sf). Additionally, results from a ‘no shield’ scenario are also included for reference. Results from the TBC model show an increasing trend in the phase shift that plateaus beyond sf=1.5, approximating to the ‘no shield’ case. Notorious dissimilarities can be seen when the TBC results are compared to the IBC case. The difference between the phase angles measured using IBC or TBC increase with increasing stand-off distance. Results suggest that in the IBC model, the field is truncated, which results in a larger damping effect.

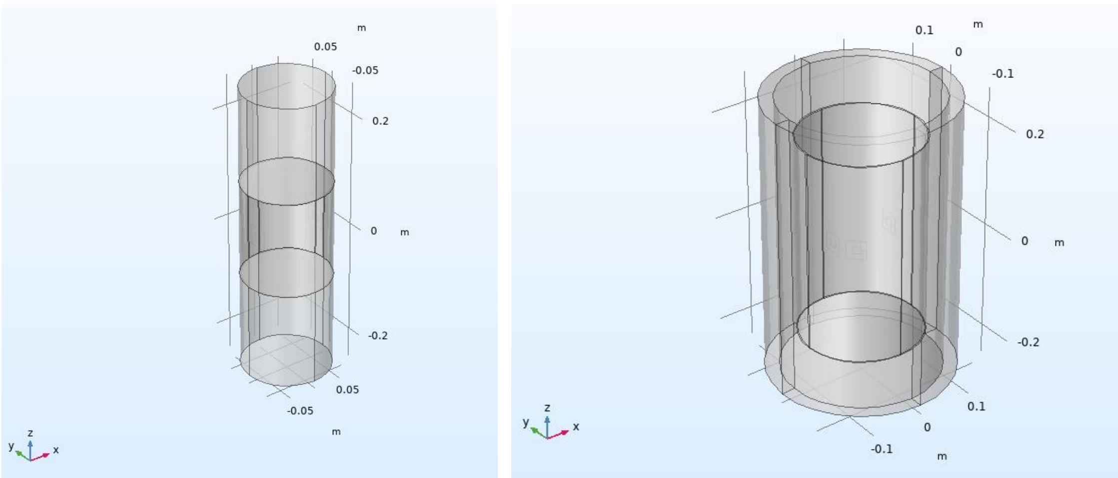

(a) (b)

Figure III-5. Simulation setup showing the modelling approach for an aluminium shield of 165 mm diameter and 1 mm thick using (a) Impedance boundary condition (IBC) and (b) Transition boundary condition (TBC)

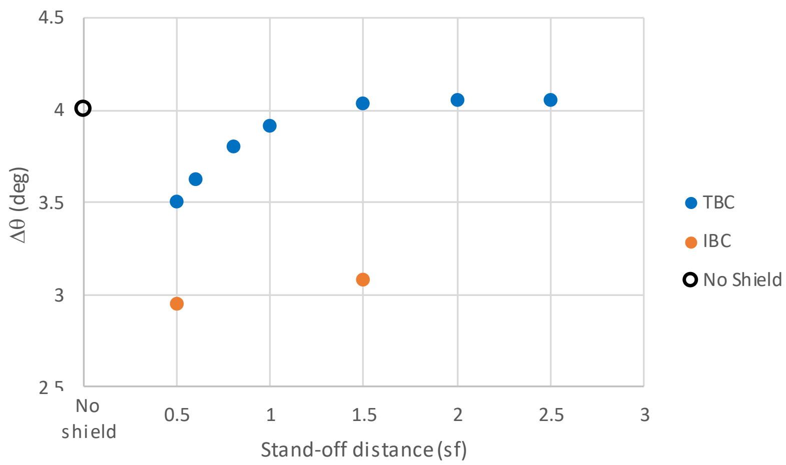

(a)

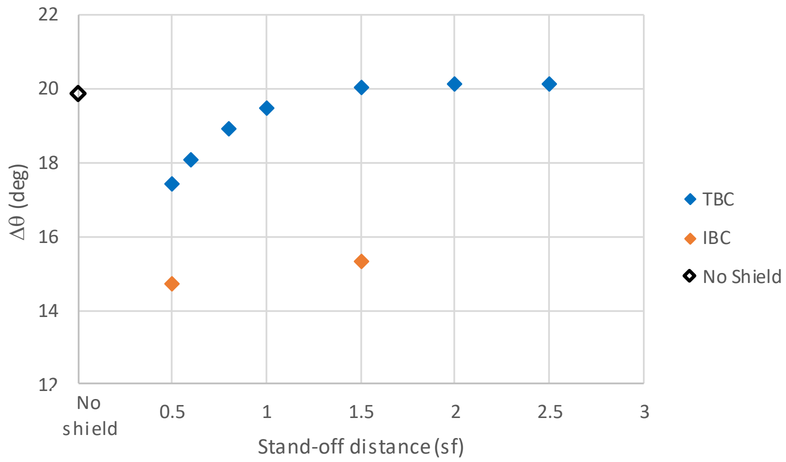

(b)

Figure III-6. Phase shift for IBC and TBC configurations and various stand-off distances for conductivities in the imaging region of (a) 1 Sm^{-1} and (b) 5 Sm^{-1}

3.6.3 Computation software

As previously discussed, the various scenarios of the MIT design were evaluated using two computation packages. In order to ensure consistency among the results, a similar setup was simulated in both software using the same boundary conditions and initial values. The simulation models comprise two identical opposite coils distanced by 110 mm. The coils were modelled as circular rings of 34 mm of diameter. Six scenarios were evaluated, in each the number of turns was increased by four turns at a time, ranging from 2 to 22. The coils were modelled using the coil geometry approximation feature available in both packages. The transmitting coil was current driven at a 0.5 A level and the receiving coil was modelled as an open circuit by specifying a current through the coils of 0 A. The CST student edition license is limited in the number of mesh elements that can be resolved.

To overcome this and improve the numerical solution in the area of interest, the coils were enclosed in dummy toroids, as illustrated in Figure III-7.

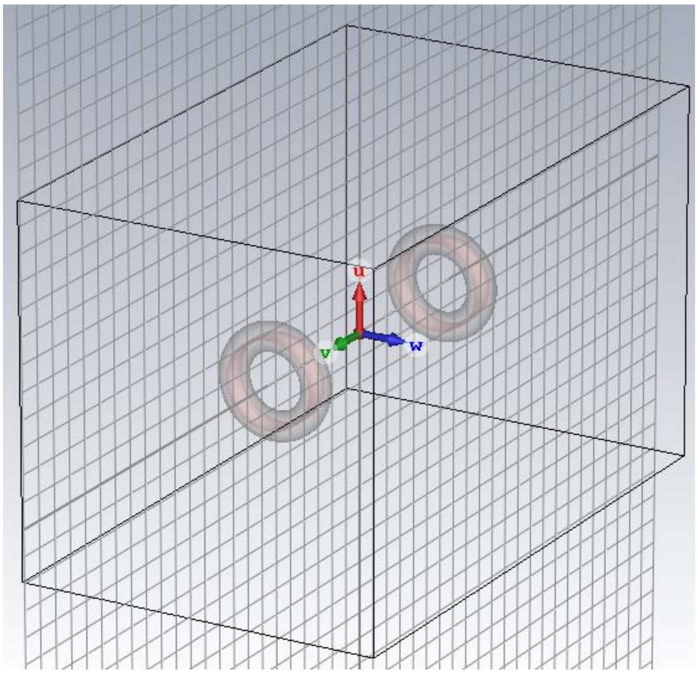

Figure III-7. Bench test model built in CST Student Edition

In Figure III-8, the amplitude dynamic range of both models is compared. It can be seen that the voltage ratio given an increase in the number of turns is consistent between both simulation models.

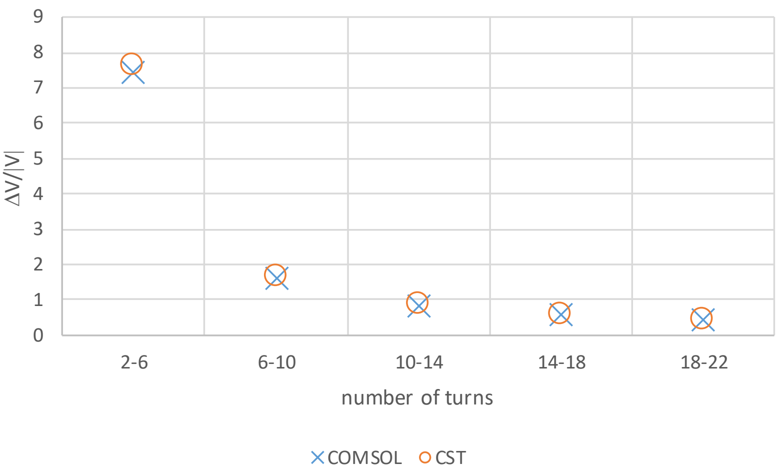

Figure III-8. Results from bench test model comparison

The modelling approach used for PCB coils was validated by comparing the simulated coil inductance of two different coil setups to the manufacturer specification. The specifications of the customised LDC part were exported from the manufacturer design tool, i.e. Webench coil designer [140]. The geometry outlined from Webench was replicated as layered shells in COMSOL. For both coil layouts, accounting for trace widths of 0.4 mm and 0.3 mm, the inductance values between the manufacturer specifications and the simulations are consistent, as shown in Figure III-9. The averaged difference between the reference and the modelled inductances is less than 0.6%.

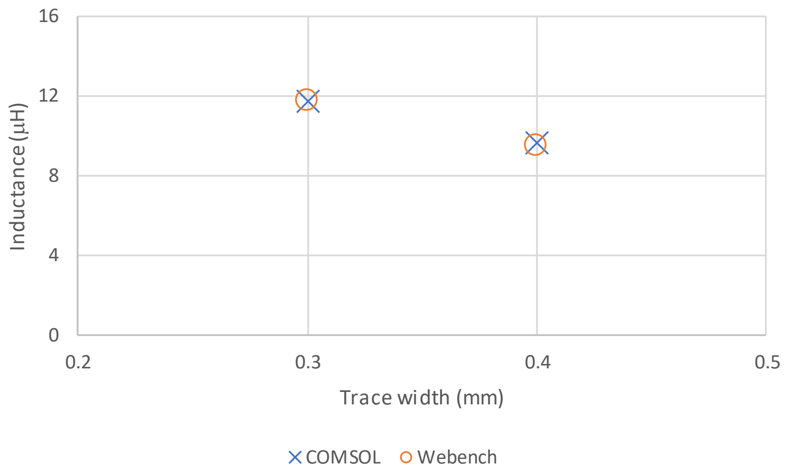

Figure III-9. Coil inductance from planar coils showing result from simulations in COMSOL and from the manufacturer design tool (Webench)

3.6.4 Dual coil approximation

Concerning the computational cost of the MIT Forward Problem solution, for selected scenarios, it is convenient to treat the problem as a dual coil system. Extrapolation of the results from the dual coil model to a full 8-coil MIT system requires equivalent simulation models. In order to validate the scaling approach of the dual coil system, the outputs of the simulation from both models were critically evaluated.

A benchmark test was performed in which results from the system setups shown in Figure III-10 were compared. The investigation involved comparing the received signals from opposite coils from a dual coil system and from a full 8-coil system. The dual coil model comprised one coil acting as transmitting and the other as the receiving sensor. The two coils were located opposite to each other across a cylindrical imaging region of 110 mm diameter (see Figure III-10a).

The full model accounted for eight coils equally distributed around the cylindrical imaging region. In the full coil model, one coil is excited with a time-harmonic current, and the remaining seven coils act as receiving sensors. The coils in both setups were modelled as homogenised multi-turn rings with a varying number of turns, as described in Section 3.5.1.2-B. The computational domain is defined by a cylindrical space, layered with infinite domains in the radial direction, which was proven to be suitable to confine the extent of the physical effect. The background material is air for both models.

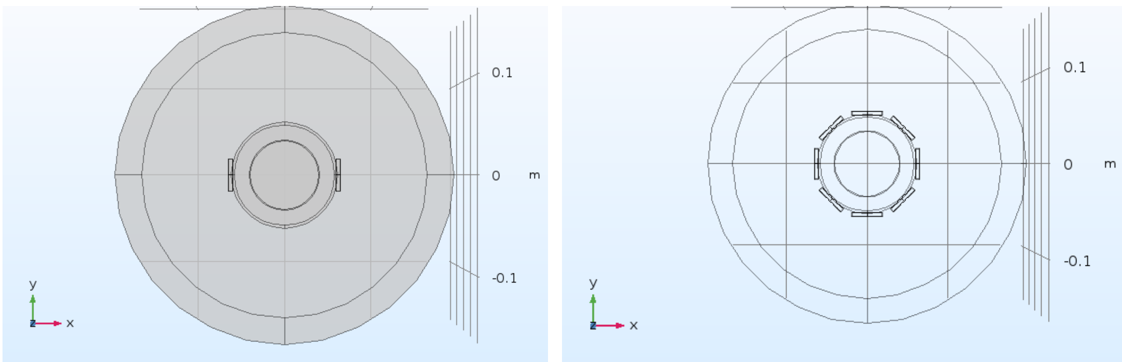

(a) (b)

Figure III-10. Bench test model comparison between (a) dual coil setup and (b) full coil system

The amplitude and phase signals from the opposite receiving coils in both models are shown in Figure III-11. It is evident that both models give a good fit, hence validating the alternative use of dual coil systems for a decreased computational cost.

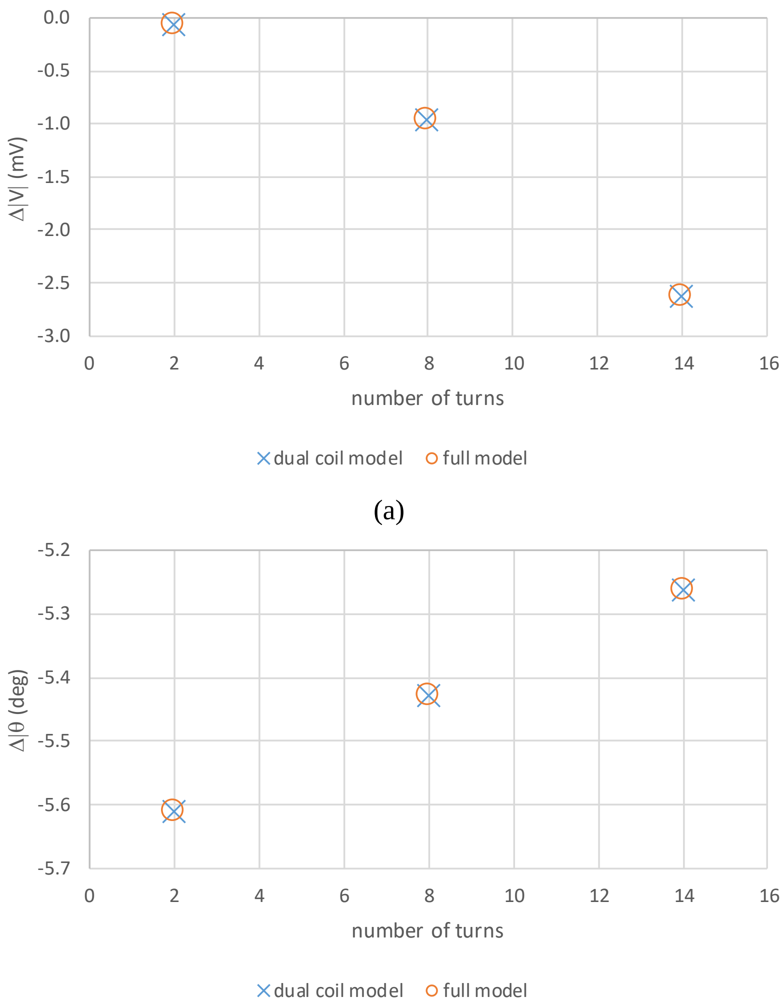

(a)

(b)

Figure III-11. Results from bench tests of dual coil setup and full coil system showing (a) voltage induced and (b) phase angle

3.6.5 Simulated vs measured data

Once the boundary conditions are defined, the FE model can be compared to experimental measurements. Along the MIT design process, the numerical models were compared to available experimental data. In the following subsections, the setups used for experimental studies are reproduced through simulations and their results are critically evaluated.

3.6.5.1 Electromagnetic shielding

Experimental tests to evaluate the shielding capacities of various materials were performed using attenuation barriers of 120 mm ×130 mm (see Chapter V). The evaluation described in this subsection considers results from aluminium sheets of 6.33 mm and 2.1 mm thick as they are suitably representative of the electromagnetic shields commonly used in MIT and the material properties are readily available in the built-in material library of the software. In the study, the experiments were conducted using two coils located opposite to each other under various operating frequencies. First, the reference voltage was measured with the shielding material absent. Subsequently, the shielding material was placed orthogonally between the coils, and the load measurement was acquired.

The same experimental setup was simulated in CST. Recalling from Section 3.5.1.3, discretising the shield as an additional material provides practical means to evaluate the decay of the magnetic field through the thickness of the material.

At frequencies below 20 MHz, the intensity of the transmitted field (H_t) is related to the shielding effectiveness (S_H) and the load to reference voltage ratio (V_i/V_t) by the relationship [17]:

$$S_H = 20\log_{10}(H_i/H_t) = 20\log_{10}(V_i/V_t) \tag{50}$$

Simulated and experimental results are shown in Figure III-12. The simulation outputs of the near-field system at a distance of 15 mm from the shield, for the given aluminium barrier thickness, is shown in Figure III-12a. The numerical solution identifies a narrow difference in the intensity of the magnetic field close to the receiving sensor with varying barrier thicknesses. This slight difference is equally seen in the experimental results shown in Figure III-12b.

The experimental and numerical outputs are in agreement, as both trends provide evidence of the decrease difference between thicknesses as the excitation frequency increases. These tests designed to evaluate the performance of the model under conditions with readily known responses allowed to prove that the simulated measurements are consistent with the laws of physics.

3.6.5.2Coil design

In this section, the results from the numerical simulation of the coils are compared to the experimental study carried on the two coil geometry configurations, i.e. circular helix and square helix. The inductance of coils for both geometry profiles and the number of turns is plotted in Figure III-13. Here, simulated inductance is compared to data measured under the laboratory conditions from coils of 34 mm wound from a copper wire of 0.5 mm. The inductance of the coils was measured using a GW-Instek LCR-817 meter.

The trends observed in the experimental measurements are consistent with those seen in the simulated data, with the square helix geometry (SH) resulting in consistently larger coil inductance than circular coils (CH). Both experiments and simulations agree on an increasing larger difference between the evaluated profiles with an increasing number of turns. However, it can be noted that the absolute measured values are greater than the simulated ones, although within the same order of magnitude. The difference between both figures is attributed to the excitation frequency used in the model. As the frequency increases, the simulation model is able to capture the change in reactance and the skin effect that are not considered in the Alternating Current (AC) measurements [136].

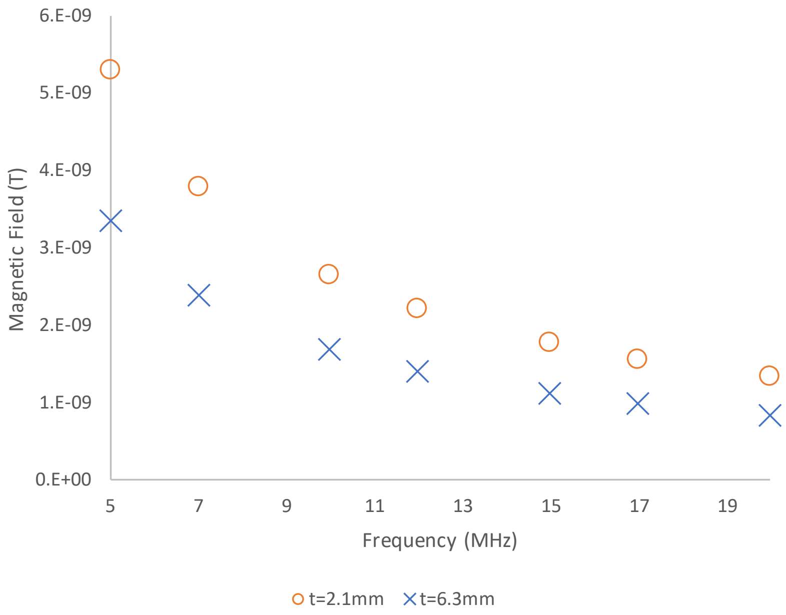

(a)

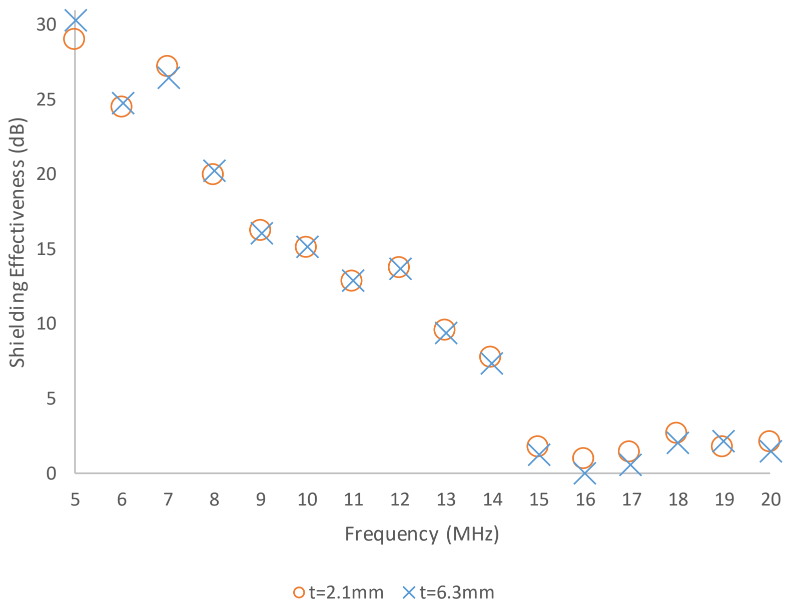

(b)

Figure III-12. Comparison of results from (a) transmitted magnetic field in CST and (b) shielding effectiveness from experiments

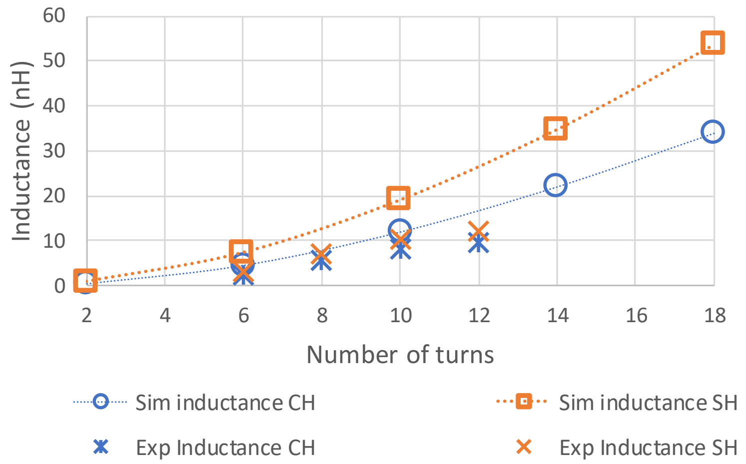

Figure III-13. Coil inductance of circular (CH) and square helix (SH) geometries for various number of turns from simulations in COMSOL (Sim) and bench tests measurements (Exp)

Numerical simulation modelling is used in the remainder of the thesis, and it is core to the MIT sensor and hardware design in Chapter IV and Chapter V, respectively, as well as in the extended MIT measurement capabilities presented in Chapter VII. In this thesis, the MIT models used comprise a selection of the modelling approaches evaluated in this chapter. All the simulation models are based on a close approximation to the actual physical representation detailed in the following chapters.

Table C-1 in Appendix C provides a summary of the main characteristics of the simulation models exploited in the remainder of the thesis and justifies the approach selected based on the evaluations undertaken in this chapter.

3.7 Discussion and Conclusions

A relevant advantage of FEM simulation is its accuracy in dealing with discontinuous electromagnetic properties. The use of commercial packages like CST and of COMSOL for solving the MIT Forward Problem allowed rapid estimates of the signals for feasibility tests and hardware design. CST student edition license provides significant limitations in the size of the model geometry; hence its use was limited to reduced scaled problems. Therefore, when appropriate, CST will be employed for the hardware design based on scaled-down models. COMSOL is employed in the remainder of this thesis for full-scale MIT forward model solution.

For large 3D models, encompassing a full MIT system, more than 50,000 meshing elements are necessary to ensure negligible discretisation errors and accuracy of the numerical solution. A free space of at least three times the instrument dimension terminated in virtually infinite element layers was seen to provide an adequate decay of the electromagnetic field that does not truncate the solution.

Geometry approximations used for multi-turn coils were in good agreement with experimental measurements. However, for sensor design, it is crucial to perform an independent evaluation of the resonance frequency of the coils before using simplified geometry approximations.

Comparison of the FE results with reference values and experimental measurements ensure the validity of the modelling techniques used. Changes in the induced e.m.f and in the distribution of the magnetic field resulted, as expected, in changes in material properties, operating conditions, and barrier dimensions. All the above changes are consistent with the laws of physics. Furthermore, the system responses and trends between the measurements from benchmark tests and simulation result were seen to be in agreement. This enables the use of the results from the simulation models to describe the electromagnetic problem, derive conclusions and make predictions.

Chapter IV MIT Sensor design

4.1 Introduction

Low conductivity imaging requires a high excitation frequency and high-resolution equipment [66] [93]. Recalling from Section 2.5.1, high frequencies yield smaller skin depth. Hence, at high frequencies, the skin depths of the electromagnetic fields are comparable to the target dimensions, and the signal arising from the induced eddy currents is only a fraction of that of the primary magnetic field [73]. The amplitude measurements from a low conductive medium is a few orders of magnitude smaller than the driving input, hence resulting in weak signals. From Maxwell's equations, it is evident that the performance of MIT systems largely depends on the intensity of the induced field and currents (refer to Chapter II).

The inductive coupling between the sensors and the medium is influenced by the hardware design, including the system sensors [90]. Several MIT systems have been designed over the past three decades, most of which rely on sensors built from circular helix coils [11] [81] [91] [95] [141] [142] [143] [144] [145]. The reason for this selection is not well elaborated in the literature, and limited research has addressed the design optimisation for MIT sensors, suggesting the use of alternative geometries and manufacturing techniques [96] [98] [146].

In multiphase flows, the electrical and physical properties of the inclusions vary in both the spatial and the time domain. These variants challenge the definitions of models for non-continuous conductivity distributions, which in order to be representative of the targets of interest must necessarily address a range sufficiently wide as to encompass all possible multiphase flow scenarios. Consequently, the present chapter focuses on the design parameters of MIT sensors. It does so, using a uniformly distributed conductive medium. This approach is valid for homogeneous and steady-state flow, which allows first the assessment of the performance of MIT systems in connection to the overall variations of the electrical properties within the bulk medium and second the design of the system.

The scope of this work focuses on the design and evaluation of air-core coils, which are preferred for MIT systems over ferrite-core solenoids [66] [92]. Air-core coils have a constant permanence that yields a linear behaviour; similarly, the inductance is independent of the current through them [75] [147]. All these characteristics simplify the data processing.

This chapter provides a study of the geometric characteristics of the sensors encompassing the performance of the electromagnetic measurements. The work combines qualitative and quantitative analyses in order to develop algebraic models to predict the overall performance of MIT systems for a given coil setup. The quantitative assessment is based on inferential statistics, which allow the testing of specific hypotheses about the sensor geometry [148]. The two main types of inferential tests have been adopted in this work: the tests of association to describe the relationship between variables and the tests of group differences for data dispersion analysis and correlation validation. The numerical results analysed in Section 4.6 are based on a combination of statistical techniques that comprise bivariate correlations, uniqueness indexes, and multiple regressions. The bivariate association tests can provide a measure of the statistical significance, a measure of association between variables, or both [148]. Spearman test provides a measurement of both significance and association. Spearman correlation coefficient measures the degree of correlation between a pair of combined variables, i.e. ordinal and continuous, irrespective of their linearity or lack thereof [148][149]. On the other hand, the Mann-Whitney test, which is aimed at non-parametric data, is an alternative bivariate test for variable association irrespective of the data distribution shape [150].

Furthermore, the computation of the relative importance of geometric parameters on the overall system performance is achieved through multiple regression analyses. Multiple regression provides the model that best fits the behaviour of the data. Similarly to the correlation approach taken for data processing from experiments in multiphase flow [151], curve fitting coefficients are used to describe the performance of the MIT systems via correlation models.

The present work is based on the author's contribution to the manuscripts on sensor characterisation published in 9WICIPT [16] and in the Journal of Meas. Science Tech [152]. The results disclosed in this chapter were partially included in the patent document GB1810733.4 [15] in which the author and Dr Ma are the co-inventors (see Appendix B). The contribution of the author to the patent document include the qualitative and quantitative analyses of the sensor performance presented in Sections 4.5 and 4.6 of the present chapter.

The main parameters to consider for MIT sensor design are discussed in the following sections, organised as follows. The geometric characteristics and performance parameters relevant to the MIT sensor design, detailed in Sections 4.2 and 4.3, respectively, are empirically assessed in accordance with the experimental setup in Section 4.3. The effects of the changes in the coil geometry are systematically evaluated and compared to simulation results in Section 4.5. Section 4.6 provides a quantification of the sensor performance based on the statistical analysis of the sensor behaviours to various stimuli. Finally, the results discussed in Section 4.7 lead to the concluding remarks in the final subsection of the chapter.

4.2 Sensors characteristics

The selection of the design parameters of interest to assess the performance of MIT systems is based on a probing survey of existing literature. The geometrical parameters comprise coil size, wire gauge, number of turns, and the shape profile, i.e. circular helix and square shaped coils. The dimensions of the coils and the size of the saline inclusion used in the experiments consider the theoretical spatial resolution and skin effect in low conductive fluids.

The geometry variables assessed here account for combinations whose influence on the MIT performance is not straightforwardly inferred. The number of turns, for example, is known to affect the mutual coupling and the parasitic capacitance [95] [136]. However, its combined impact along other geometry parameters requires further quantification. Similar is the effect of the wire gauge on the induced voltage resulting from the secondary magnetic field arising from flow-induced eddy currents. At high frequencies, the current density across the wire cross-section is not uniform, due to the skin effect of the copper, challenging any *a-priori* analysis. The following subsections detail the geometry characteristics assessed in the study.

4.2.1 Coil Profile

In addition to the widely used circular profile, the performance of square coils is also evaluated here. Square helix coils provide a larger core area, for the same outer dimension, while sharing significant similarities with traditional circular coils in terms of winding techniques and ease of construction.

Figure IV-1 exemplifies the profiles evaluated. Other types of coil that have been somewhat addressed in the literature are circular planar coils or pancake coils. The widest application of planar coils is within the kHz spectrum. These coils provide a high-quality factor, i.e. ratio of resistance to inductive reactance; resulting in the magnification of the current which makes them attractive for induction charging. However, in radio frequency applications, such as imaging systems for multiphase flow, this performance is not desirable. Consequently, these types of coils are not addressed in this study.

Figure IV-1. Example models of the profiles of the coils illustrating (a) a circular helix coil and (b) a square-shaped coil

4.2.2 Coil dimensions

The size of the coils in an MIT system targeting flow measurement is restricted by the pipeline dimensions. The outer diameter of the pipe limits the number of sensors that can be accommodated around its perimeter. Furthermore, the number of sensors impacts the resolution of the measuring device, see Equation (51). The spatial resolution of the electromagnetic meter, denoted R, is proportional to the number of independent combinations of transmitting to receiving coils and is given by [86]:

$$R = \frac{1}{\sqrt{\frac{n_c(n_c - 1)}{2}}} \tag{51}$$

where n_c is the number of sensors working either as exciters or receivers.

It is worth noting that the metering resolution cannot be infinitely improved. A large number of independent measurements increases the correlation between the individual data resulting in increased complexity of the Inverse Problem [99]. From (51), for typical multiphase pipelines diameters in the oilfield, below 200 mm [153][154], eight coils provide a sufficient number of measurements, i.e. 28, and a decent theoretical image resolution of approximately 19% of their diameter.

4.2.3 Number of turns

Theoretically, a larger number of turns would result in a greater induced voltage as by Faraday's law, which establishes the proportionality between the induced voltage in an air-core coil and the number of turns. Nevertheless, in MIT systems the induced voltage results from the inductive coupling between the sensors and the conductive medium. The secondary field arising from a flow-induced eddy current is intrinsically dependant on the properties of the fluids contained within the pipe.

An increased number of turns, although resulting in an increased electromotive force, also reduces the self-resonance frequency of the coil. At high operating frequencies, the coil self-resonance frequency becomes a limiting factor of the maximum number of turns. Within the MHz spectrum, the parasitic capacitance resonates with the inductance, altering the ideal behaviour of the coil [11] [13] [95]. Consequently, too few a number of turns fails to provide enough inductance; if on the contrary, there are too many turns, the resonance frequency may overlap the operating frequency creating instabilities.

4.2.4 Wire gauge

The effect of the coil wire diameter in the performance of MIT systems is not straightforward, as evident in Ampere Law. Ampere described the magnetic field inside a solenoid, where the effect of the wire diameter is implicit, affecting both the length of the coil and the current distribution profile. Furthermore, at high frequencies, the current density ceases to be uniform due to the skin effect in the wire material. Within the low MHz range, the skin depth effect causes the current to flow only through the portion nearer the outer surface of the wire. The effects discussed above represent a challenge in accounting for the effect of wire diameter in the performance of MIT systems. Based on commercial wire gauges and information on existing MIT coil designs [11] [81], six different copper core diameters, ranging from 0.4 mm to 0.8 mm, were evaluated.

A summary of the evaluation range for the geometry parameters above is given in Table IV-1. Assessment of the designs parameters in the performance of MIT systems is based on the quantification of the influence of the sensor geometry, which is addressed in the following sections.

Table IV-1. Coil design parameters for evaluation

Parameter	Range
Coil outer dimension - Dc (mm)	[20, 25, 34, 40, 50, 54]
Wire diameter - dw (mm)	[0.4, 0.5, 0.55, 0.60, 0.75, 0.85]
Number of turns - N	[2, 4, 6, 8, 10, 12, 14, 16, 18, 20]
Shape Profile	Circular (CH), Square (SH)

4.3 Performance parameters

The complexity of the electromagnetic phenomena bounds the sensor evaluation not to be restricted to a single governing factor that attempts to quantify the performance of the MIT meter uniquely. Hereafter, the combined effects of geometric parameter sweeping were evaluated and ranked by their impact on the various performance indicators.

The amplitude of the induced voltage given by Equation (46) is proportional to the background field generated by the driving signal, hence affecting the signal-to-noise ratio. The performance factor, designated V_i, accounts for the ratio of induced to driving signal as

$$V_i = \frac{V_{Rxi}}{V_{Txi}} \tag{52}$$

where V_{Rx} and V_{Tx} are the induced and driving voltages respectively for a given set of scenarios i $= \{1,2, \dots, n\}$ for a total of 180 coil configurations ($n = 180$). Note that a large induced voltage, i.e., voltage ratio (V_i) closer to unity, implies a better signal to noise ratio. High signal levels remove the complication of using an extreme amplification circuit, hence, reducing the hardware complexity.

The signal of interest in MIT systems arises from the eddy currents induced in the conductive medium, defined by $\nabla \times \vec{H} = \vec{J}$ where $\vec{J}$ is the induced eddy current within the imaging region, which contains information on the electric properties of the fluids. The size of the signal from the induced field is only a fraction of the full measurement. The scale of the induced currents bounds the sensor design to account for high induction currents and large rate of penetrations, i.e. skin depths. Here, the strength of the conduction current field in the imaging region is evaluated along the central longitudinal axis of the pipe and is compared in every scenario $i = \{1,2, \cdots, n\}$ by (53)

$$J_i = \max_{j \in \{1,2,\cdots,m\}} (J_j) \tag{53}$$

where the magnitude of the induced conduction current J is computed as the maximum scalar registered within all mesh elements indexed by $\{1, \cdots, m\}$ for a total number of elements (m). Note that as for the voltage ratio, the total number of configurations is again $n = 180$.

Equally relevant to the previous parameters is the sensitivity of the system to changes in conductivity within the imaging area. MIT sensitivity is deduced from the Geselowitz relationship by [98] [155] and expressed as:

$$S_i = \frac{\Delta V_{RXi}}{I_i \Delta \sigma_i} \tag{54}$$

where S is the sensitivity of the system for a given change of electrical conductivity ($\Delta\sigma$). I is the current through the transmitting coil. The index $i = \{1,2, \cdots, n\}$ refers to the evaluated scenarios. It is noteworthy that the original relationship derived by [98] considers the variation of the complex conductivity ($\Delta\kappa = \sigma + j\omega\varepsilon_0\varepsilon_r$). Here, the conductivities evaluated are high ($\omega\varepsilon/\sigma \ll 1$), and the eddy-current approximation is used in accordance to [114].

From (52) to (54) it is inferred that the higher the values of the performance parameters V_i, J_i, and S_i, the better the performance of the MIT system is.

Having defined the geometry characteristics of inductors and the performance parameters of interest for MIT systems, the following sections aim to evaluate, both empirically and numerically the correlation between the two.

4.4 Experimental design

An experimental setup composed by a dual coil system was used for empirical assessment of the effects that changing the coil characteristics have on the performance of the MIT system. The coils are positioned opposite to each other across a pipe of 110 mm outer diameter. The transmitting coil (Tx) was excited with a time-harmonic signal at 10 MHz and 5 $V_{p\text{-}p}$. The excitation signal induces a magnetic field that is inductively sensed by the receiving coil (Rx), located at 180º from Tx. A digital oscilloscope connected to Rx measures the induced voltage and phase in the receiving sensor for further data processing. Cylindrical inclusions of various salinities and 70 mm in diameter were used to evaluate the sensitivity of the MIT system to changes in electrical conductivity. The inclusions were individually placed in the centre of the imaging region equidistant from Tx and Rx. The system illustrated in Figure IV-2(a) shows the system setup with generic coils of outer dimension Dc formed with N turns of wires of diameter dw. Figure IV-2(b) shows images of a selection of the coils used for the experiments. The experimental scenarios were selected based on representative geometries that could provide an overall understanding of the system performance. The results from the experiments also served to validate the simulation outputs, which were next extended to a wider range of geometry parameters.

For the determination of the resonance frequency of the coils, a two-turn coil was used as the excitation source. Tx was loosely coupled to the coil under evaluation (Rx) as illustrated in Figure IV-2(c). The gap between Tx and Rx acts as a capacitor and avoids damping the resonance frequency. The excitation signal used was a square wave of 4 $V_{p\text{-}p}$. Square wave input allows for easy identification of the subharmonics represented as sine waves in the oscilloscope. In this regard, the input frequency was swept until the voltage in Rx formed a sine wave and the input frequency to Tx was a fraction of that measured in Rx (third subharmonic). Further tuning of the resonance frequency was performed by sweeping the frequency of a time-harmonic wave around the resonance value and noting the maximum signal from Rx that is observed in the oscilloscope.

4.5 Qualitative analysis of the performance of the sensor

This section qualitatively assesses the effect that varying the geometry parameters of sensors have on the performance of the MIT systems. The assessment combines empirical work and results from simulations which allow a comprehensive assessment over a broad range of parameters.

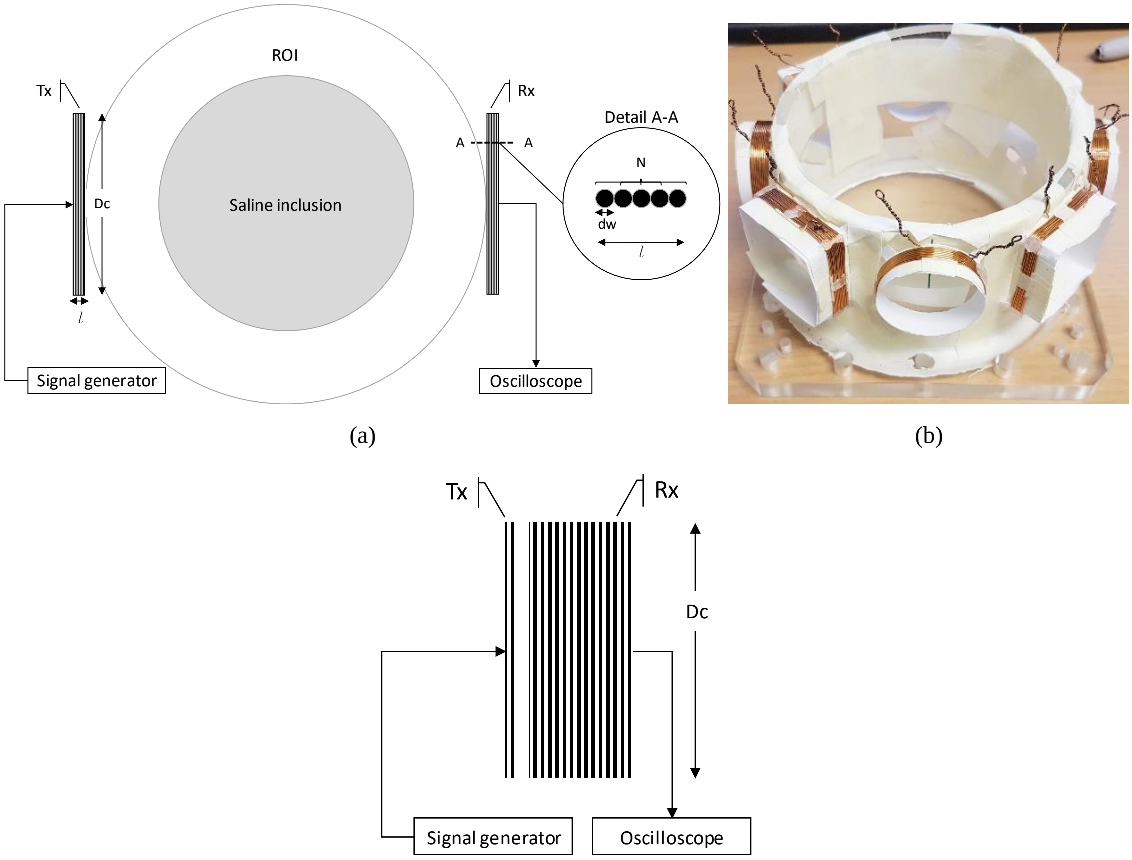

(c)

Figure IV-2. Experimental setup showing (a) the illustration of the receiver (Tx) and receiver (Rx) connection setup for coil characterisation; (b) an image of a selection of coils used for geometry characterisation; and (c) illustration of the experimental setup for resonance frequency measurement

4.5.1 Effect of coil diameter on the signal level

The effect of the geometry parameters on the voltage ratio accounting for variations in the background signal is presented in Figure IV-3. The 95% Confidence Interval (CI) of the voltage ratio is represented as error bars in Figure IV-3. The maximum standard deviation registered in the induced signal (V_{Rxi}) was 1.5E-4 V.

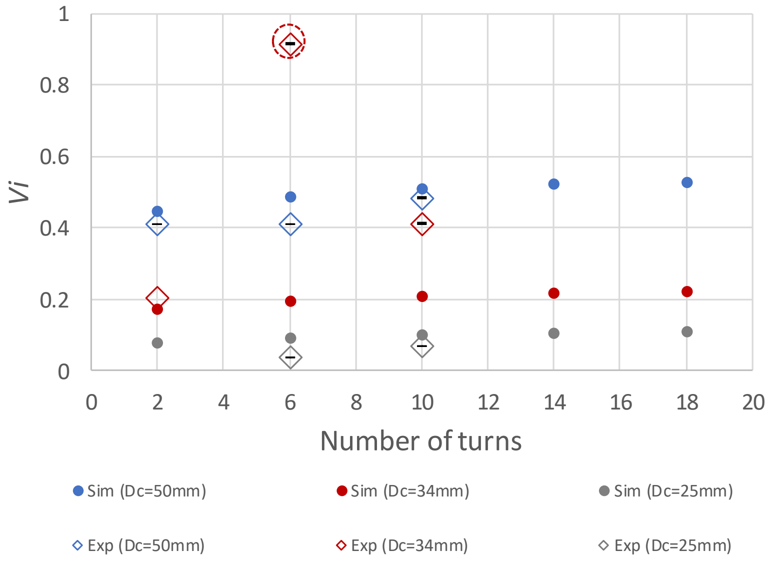

Figure IV-3. Simulated (Sim) and measured (Exp) induced-to-excitation voltage ratio of circular helix coils of various diameters and number of turns wound from 24 AWG copper wire. The black error bars show the 95% Confidence Interval

The results show the ratio of induced to excitation voltage of helix coils with the various number of turns and geometric configurations from simulation and experiments. The overall trends from simulation outputs and experimental voltage ratios are consistent and show that the voltage ratio is related to the coil diameter.

However, results from the test point of the coil with six turns and an outer diameter of 34 mm, highlighted in Figure IV-3, do not follow the trend seen in the remaining data points. This effect is attributed to the proximity of the operating frequency to the circuit resonance frequency, resulting in unrepresentative high induced voltage (more details in Section 4.5.4). This effect on the induced voltage is neglected in the simulations given the numerical approximation used to model the coil domain. Disregarding the outliner, the absolute mean difference between the experimental data points and the simulated voltage ratios is 0.06, which corresponds to a mean per cent difference of 17%.

4.5.2 Effect of wire diameter on the signal level and coil coupling

The electromagnetic field induced at the central longitudinal axis of the imaging region for various geometric parameters is shown in Figure IV-4. The simulation results show that the intensity of the primary field increased with larger coils and wire gauges. Consequently, the induced voltage for all coils sizes increased with increased wire diameter (see Figure IV-5a). The increasing effect seen with increasing wire diameter is smaller than that obtained with changing the coil dimensions.

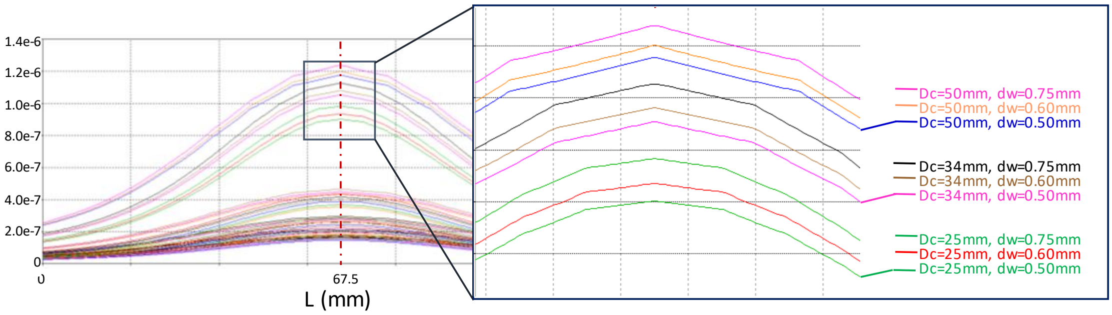

Figure IV-4. Electromagnetic field intensity (A.m^{-2}) induced by circular helix coils of various diameters for a given number of turns measured along the longitudinal axis of the cylindrical imaging region. The vertical red line signalises the position of the centre of the coils

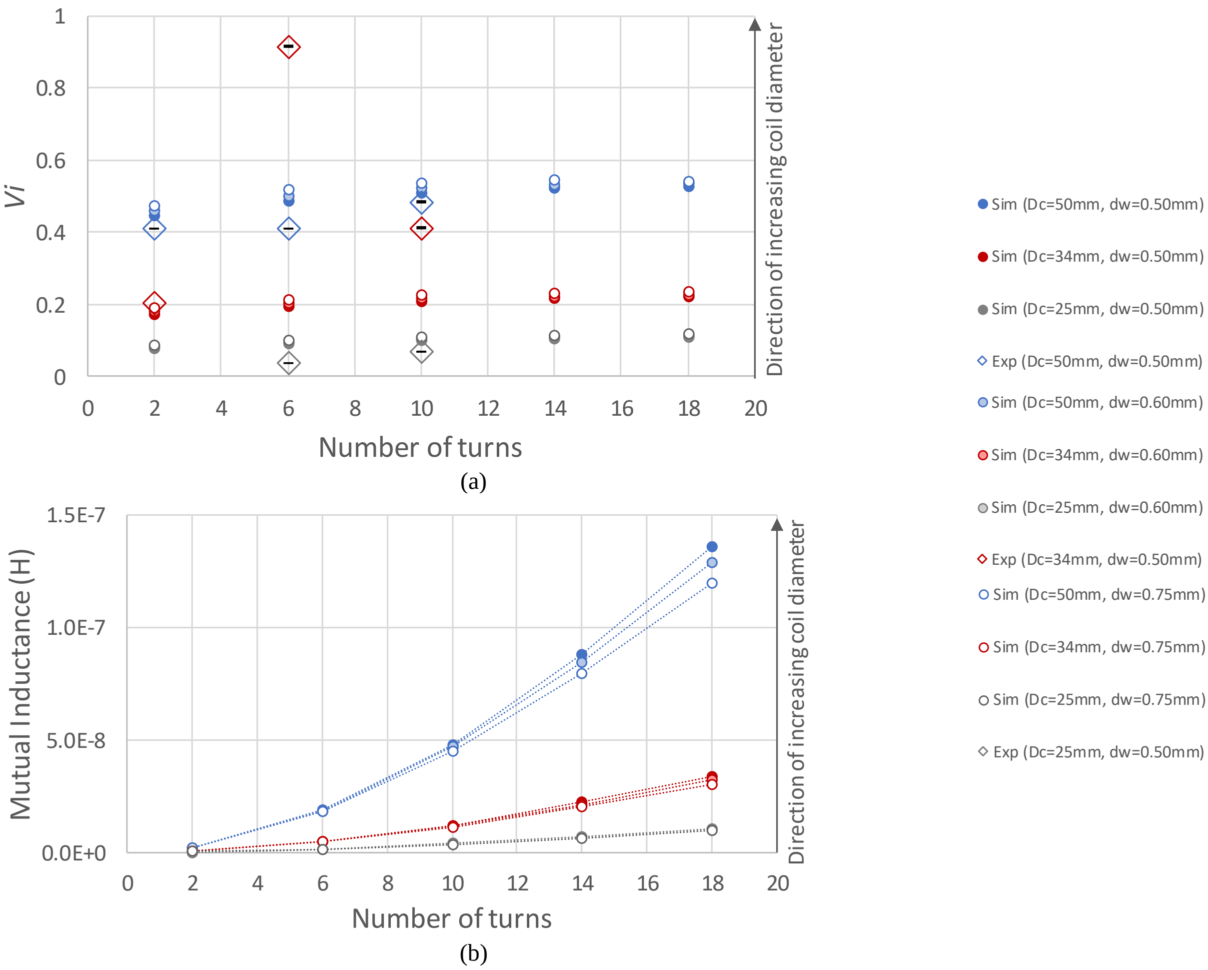

Figure IV-5. Effect of the wire diameter and coil size variations in (a) the induced signal and (b) background coupling for the various number of turns. The error bars in black show the standard deviation in the measurements

Figure IV-5(b) shows the coil coupling for the various number of turns and wire gauges. The results demonstrate that coupling between coils is more significantly affected for a higher number of turns and larger coils. In concordance to the signal level, the effect on the coupling of changing the coil size is greater than that of changing the wire diameter.

4.5.3 *Effect of the geometry on the sensitivity*

Figure IV-6 shows the variation in the voltage ratio for given numbers of turns and coil shapes. Results show that regardless of the inductor profile, there is an increase in signal level with an increasing number of turns. However, square helix coils in Figure IV-6(b) show consistently larger induced amplitude signals than circular helix coils in Figure IV-6(a). The difference between both geometry profiles is more noticeable for a larger number of turns. Similarly, although less apparent than with the number of turns, larger wire diameters also yield larger signal ratios.

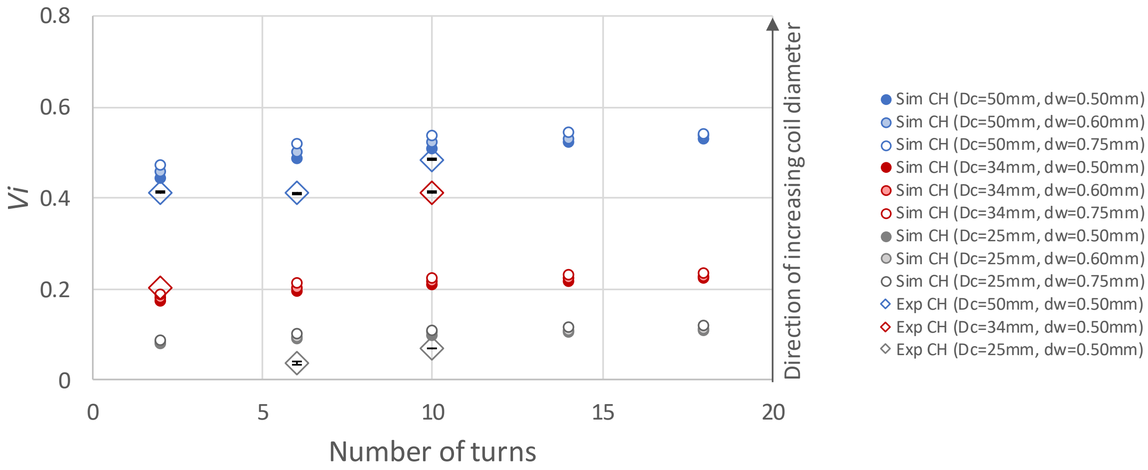

(a)

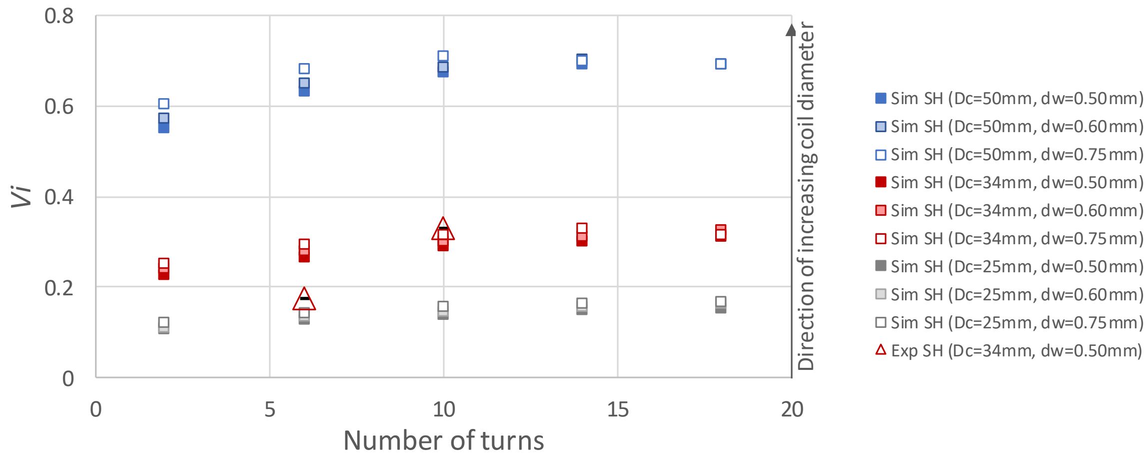

(b)

Figure IV-6. Simulated (Sim) and experimental (Exp) results of induced-to-excitation voltage ratio of (a) circular (CH) and (b) square (SH) helix coils of various coil sizes, wire gauge and number of turns. The error bars in black show the 95% Confidence Interval

The sensitivity of the coils to changes in the conductive properties of the medium for various coil geometries is illustrated in Figure IV-7. For electrical conductivities of the inclusion of 1 Sm^{-1} to 5 Sm^{-1}, results are consistent with those from the voltage ration in Figure IV-6. The system sensitivity increases with an increasing number of turns irrespective of the core area. Conversely, to free space scenarios, results suggest that the larger the wire cross-section, the less sensitive the system is to changes in conductivity.

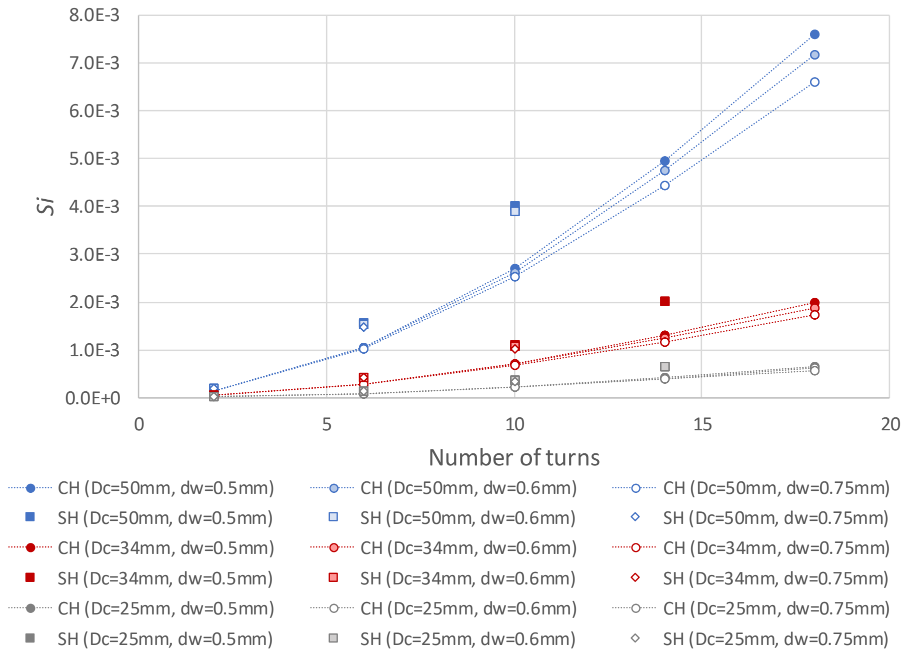

Figure IV-7. Sensitivity of circular (CH) and square (SH) helix coils of various coil sizes, wire gauge and number of turns

4.5.4 *Effect of parasitic capacitance*

The effect of the parasitic capacitance of coils of various geometry configurations was evaluated using an experimental setup based on Figure IV-2(b). The results in Figure IV-7 show the tendency of the coils to respond at greater amplitude when the operating frequency matches the coils resonance frequency than it does at other frequencies.

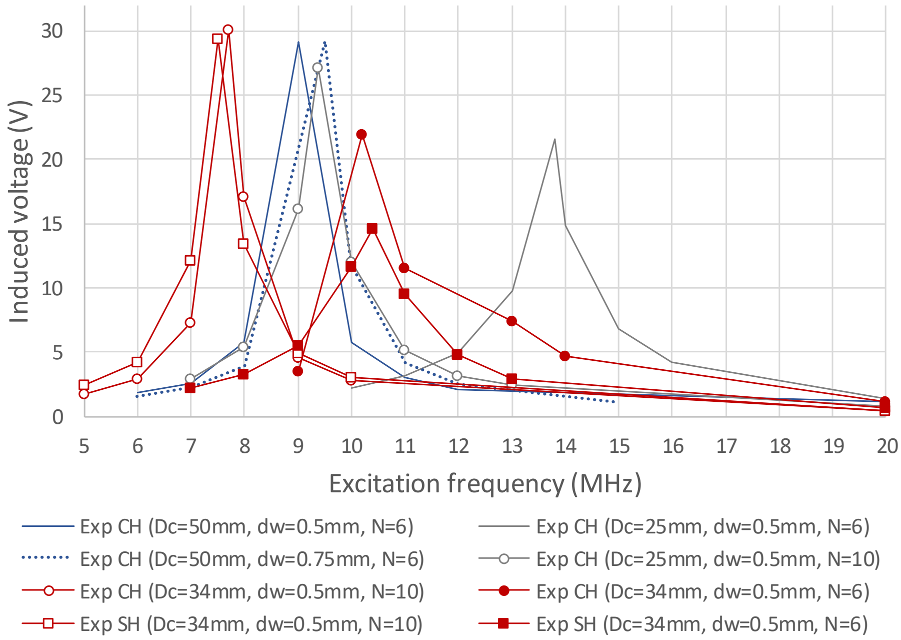

Figure IV-8. Effects of changing coil geometry and dimensions on the inter-turn parasitic capacitance as reflected by the tendency of the coils to respond at greater amplitude when the operating frequency matches the circuit's resonance

As expected, for air-core coils, more turns resulted in higher coil self-inductance and hence lower self-resonance frequency. The self-resonance frequency is intrinsically related to coil geometry characteristics, thus for coils of fixed outer dimensions and wire gauge, the shift in the trends results from the variation in the area of the coil core. There is very little difference between geometries, with the square coils exhibiting a slightly lower self-resonance frequency than the circular geometry. For circular helix coils, increasing the coil diameter reduces the resonance frequency, whereas the wire diameter has little effect on the inter-turn parasitic coupling. Similarly to self-inductance trends, the measured inductance of a selection of coils shows that the resonance frequency is non-linear (see Figure IV-9). Contrasting the inductance of both square helix (SH) and circular coil (CH), it is evident that consistently larger inductances are measured in square-shaped coils. The quadratic trend in the data yields larger differences between both geometries for an increasing number of turns. In this regard, the mean relative change between the square and the circular coils for every variation in the number of turns are in agreement, with ratios of 0.37 and 0.33 for the simulated data and the experimental points, respectively. As discussed in Section 3.6.5.2, the variation evidenced between the measured and simulated inductances is due to the capacity of the simulation model to capture the change in reactance and the skin effect that is not present in the low-frequency AC measurements.

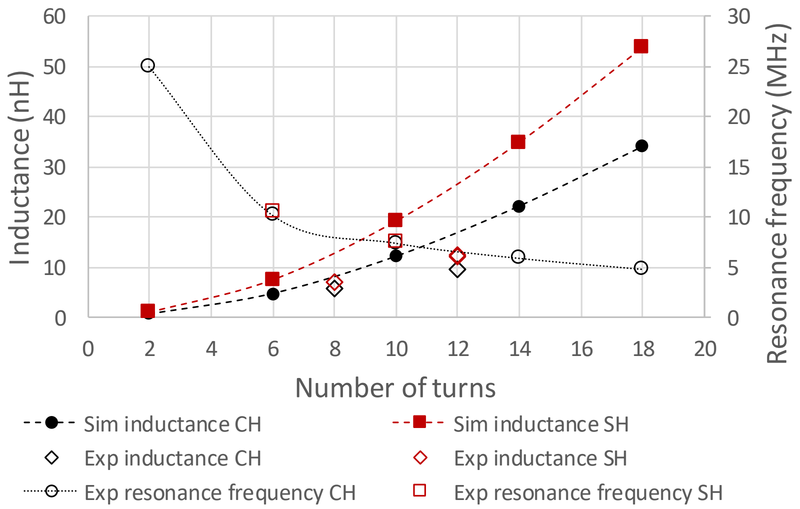

Figure IV-9. Effects of changing coil geometry and dimensions on the self-inductance and resonance frequency based on coils of 34 mm in diameter and 24AWG wire

These results show that the number of turns is the governing factor for self-resonance of the coils with little impact on the other geometric variables. Accordingly, in the subsequent sections, the self-resonance frequency is not considered as a performance parameter but as a limiting factor for the maximum number of turns of the coils.

A summary of the qualitative analysis above is presented in Table IV-2.

Table IV-2. Summary of the qualitative analysis on changes of sensor geometry

Sensor characteristic	Signal Level (V_i)	Sensitivity (S_i)	Coupling (H)	Resonance frequency (f)
Dimension (D_c)	$\uparrow D_c = \uparrow\uparrow V_i$	$\uparrow D_c = \uparrow S_i$	$\uparrow D_c = \uparrow\uparrow \mathrm{H}$	$\uparrow D_c = \downarrow \mathrm{f}$
Wire gauge (d_w)	$\uparrow d_w = \uparrow V_i$	$\uparrow d_w = \downarrow S_i$	$\uparrow d_w = \downarrow \mathrm{H}$	$\uparrow d_w = \uparrow \mathrm{f}$
Number of turns (N)	$\uparrow \mathrm{N} = \uparrow V_i$	$\uparrow \mathrm{N} = \uparrow\uparrow S_i$	$\uparrow \mathrm{N} = \uparrow\uparrow \mathrm{H}$	$\uparrow \mathrm{N} = \downarrow \mathrm{f}$
Profile CH / SH	$V_{SH} > V_{CH}$	$S_{SH} > S_{CH}$		$\mathrm{f}_{SH} \approx \mathrm{f}_{CH}$

where a single arrow, i.e. ↑ indicates the direction of change, two arrows (↑↑) denotes a large magnitude change in comparison with the remaining parameters, a reverse arrow, ↓ indicates a change in the opposite direction.

4.6 Quantitative analysis of the sensor performance

Based on the performance of the sensors evaluated in Section 4.5, the quantification of the effects of the geometric variables on the performance factors V_i, J_i,and S_i and the nature of the predictive relationship is now assessed. In this section, statistic procedures are used to quantitatively assess the relative importance of the geometric variables on the MIT performance.

The performance factors computed for every scenario were grouped as per geometry parameter cluster (see Table IV-3). The covariance (s_{xy}) of the grouped parameters serves to recognise if the relationships among the variables ($s_{xy} \neq 0$) are direct or inverse, i.e., $s_{xy} > 0$ or $s_{xy} < 0$, respectively. Validation of the premise of a linear relationship between the variables is assessed through the coefficient of determination R^2.

Table IV-3 shows the response of the performance parameters to changes in the coil geometry. The coil size influences the induced voltage the most, with a joint positive variability according to both the coefficient of determination and the covariance. The remaining parameter configurations do not follow a linear relation. However, the coil dimension is seen to also influence the measurement sensitivity as by the analysis of the covariance. As for the number of turns, the negative sign of the covariance suggests an inverse effect on the intensity of the induced currents.

A summary of the bivariate analysis is presented in Table IV-4. The degree of association between the continuous variables (Dc, dw, and N) is given by the Spearman correlation coefficient (ρ) and its significance index (sig_s<0.05). The relative correlation between the variables and the nominal predictors (i.e. coil profile) is assessed using Mann-Whitney tests and its significance index (sig_m<0.05). The author corroborated that the ideal unique variance conditions for the bivariate analysis hold: the independent and dependent variables show strong correlations and the independent variables demonstrate a weak correlation with each other (ρ=0.00, sig=1.00).

Table IV-3. Performance variables for various geometry parameters

		V_i			J_i			S_i		
		$\sum V_i$	s_{xy}	R^2	$\sum J_i$	s_{xy}	R^2	$\sum S_i$	s_{xy}	R^2
Dc[a]	20	0.010	1.2E-2	9.6E-1	9.28	4.0E-1	7.2E-3	0.005	2.1E-2	4.1E-1
	25	0.016			14.99			0.008		
	34	0.033			16.85			0.025		
	40	0.048			11.64			0.060		
	50	0.078			18.18			0.097		
	54	0.091			11.92			0.161		
dw[a]	0.40	0.049	-5.7E-4	1.4E-5	10.49	2.5E-3	1.9E-3	0.087	-4.2E-5	1.1E-2
	0.50	0.042			16.34			0.047		
	0.55	0.050			10.89			0.077		
	0.60	0.042			16.62			0.044		
	0.75	0.043			17.06			0.040		
	0.85	0.049			11.47			0.062		
N	2	0.025	4.6E-5	6.0E-5	26.42	-1.8E+0	6.5E-1	0.001	8.5E-3	2.4E-1
	4	0.030			13.61			0.006		
	6	0.026			9.58			0.010		
	8	0.030			7.25			0.021		
	10	0.026			6.05			0.023		
	12	0.030			5.02			0.042		
	14	0.026			4.45			0.040		
	16	0.029			3.85			0.066		
	18	0.025			3.51			0.058		
	20	0.029			3.12			0.091		
Profile	CH[b]	0.135	1.9E-5	1.3E-3	42.87	-7.8E-3	1.7E-3	0.173	2.9E-5	4.7E-4
	SH[c]	0.141			40.00			0.184		

[a]Measured in mm.
[b]Circular helix coils.
[c]Square helix coils.

The system response for the three continuous performance factors in Table IV-4 shows mostly positive correlations with all geometric variables. Inverse relations are seen for induction currents with an increasing number of turns and for sensitivity with increasing wire gauge, i.e. ρ=-0.968 and ρ=-0.065, respectively. The relation among the geometric parameters is given by the Spearman coefficient. Accordingly, a strong relationship between the induced voltage ratio and the coil dimensions is evident (ρ=0.982). Additionally, the analysis shows a large and inverse association between the induction currents and the number of turns in the coils. These outcomes are in agreement with the increase in sensitivity of the metering system with increasing coil size and number of turns. The above correlations are statistically significant at the 0.05 level.

Conversely, the Mann-Whitney test suggests that the performance factors are not statistically different (sig_m>0.05) when compared against coil profiles.

Table IV-4. Analysis of the results using Spearman correlation method for ordinal data and Mann-Whitney test for nominal data

		V_i	J_i	S_i
Dc	ρ	0.982	0.112	0.741
	sig_s	0.000	0.135	0.000
dw	ρ	0.017	0.070	-0.065
	sig_s	0.818	0.349	0.385
N	ρ	0.004	-0.968	0.628
	sig_s	0.960	0.000	0.000
Profile	sig_m	0.344	0.060	0.532

An assessment of the combined influence of the various geometric parameters on the performance factors was performed through multiple regression analyses. The quality of the predictions is given by the ratio of mean squares. R^2-adjusted allows for a comparison among models with different numbers of parameters. The standardised Beta coefficients allow for a comparison of the relative significance of the geometric variables. The results of the multiple regression analysis in Table IV-5 demonstrate that the coil diameters and the number of turns are the parameters with the largest impact on the performance factors. Conversely, the wire gauge is the least relevant variable.

Table IV-5. Multiple regression analysis

	Model V_i			Model J_i			Model S_i		
	Stand. Beta	R^2-adjusted	Std. error of estimate	Stand. Beta	R^2-adjusted	Std. error of estimate	Stand. Beta	R^2-adjusted	Std. error of estimate
Dc	0.993	0.988	0.00149	0.115	0.977	0.04349	0.713	0.989	0.08065
N	0.000			-0.936			0.637		
dw	0.008			0.042			-0.043		
Profile	0.039			-0.1			0.049		

The global equations for every performance factor were obtained by fitting the data with quadratic and logarithm curves. ANOVA tests indicate that the models statistically significantly predict the performance factors (sig ≤ 0.005). The correlations given by (55) to (57) account for a combination of geometric variables that describe over 98% of the variability of the performance models. The derived correlations can be used to enhance sensors design for a wide range of imaging areas and conductivity contrasts.

$$Vi = (a_1 Dc + a_3 N^2 + a_5 N^{0.5} + a_8 G + a_9)^2 \tag{55}$$

$$Log(Ji) = a_1 Dc + a_2 Dc^{0.5} + a_3 N^2 + a_4 N + a_5 N^{0.5} + a_7 dw^{0.5} + a_8 G + a_9 \tag{56}$$

$$Log(Si) = a_1 Dc + a_2 Dc^{0.5} + a_3 N^2 + a_4 N + a_5 N^{0.5} + a_6 dw + a_8 G + a_9 \tag{57}$$

where dw and Dc are expressed in mm, σ in Sm^{-1}, a_i are scalars representing the model parameters (see Table IV-6) and G is the shape index, with nominal values of 1 for CH and 2 for SH.

Table IV-6. Model constants

	V_i model	J_i model	S_i model
a_1	0.001119	-0.015762	-0.060902
a_2	-	0.221681	1.246442
a_3	-6.686246E-6	-0.001315	0.002449
a_4	-	0.123560	-0.262666
a_5	0.000934	-0.860193	1.800712
a_6	-	-	-0.186440
a_7	-	0.117432	-
a_8	0.001540	-0.0484915	0.0852280
a_9	-0.009126	$0.1758\sigma - 0.4643$	-11.639089

The spread data around the composite models are presented in Figure IV-10. The plots show a significant linear relationship between predicted and reference value with an overall fit within the ±15% deviation range.

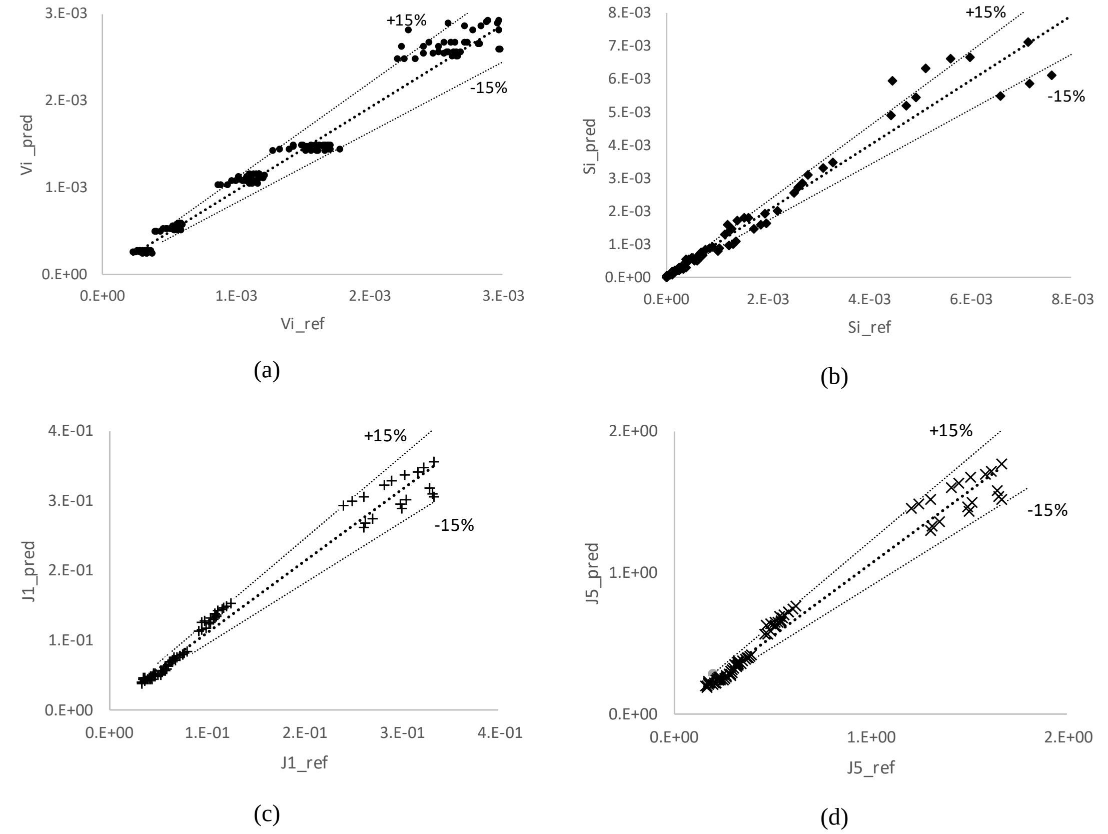

Figure IV-10. Predicted performance parameters against reference values showing data dispersion around (a) V_i, (b) S_i, (c) J_i for medium conductivity of 1 Sm^{-1}, and (d) J_i for medium conductivity of 5 Sm^{-1}

4.6.1 Performance of models

The assertiveness in the prediction of the performance parameters is contrasted via the relative performance factor in (58). The relative performance indicator is a modification of the factor recommended in [156] [157]. The proposed modification obliges the normalisation of the performance factor to correlate the three performance parameters which respond to different scales.

$$\mathrm{F_{rf}} = \frac{|\mathrm{E_1}| - |\mathrm{E_{1\,min}}|}{|\mathrm{E_{1\,max}}| - |\mathrm{E_{1\,min}}|} + \sum_{j=2}^{3} \frac{\mathrm{E_j} - \mathrm{E_{j\,min}}}{\mathrm{E_{j\,max}} - \mathrm{E_{j\,min}}} \tag{58}$$

where $\mathrm{F_{rf}}$ is the relative performance factor and ranges from 0 to 3, 0 being the best relative performance. E refers to the error of the predicted values computed as follows:

$$\mathrm{E_1} = \left[\frac{1}{\mathrm{n}} \sum_{\mathrm{i}=1}^{\mathrm{n}} \frac{(\mathrm{P_i})_{\mathrm{pred}} - (\mathrm{P_i})_{\mathrm{ref}}}{(\mathrm{P_i})_{\mathrm{ref}}}\right] \times 100 \tag{59}$$

$$E_2 = \left[\frac{1}{n}\sum_{i=1}^{n}\left|\frac{(P_i)_{pred} - (P_i)_{ref}}{(P_i)_{ref}}\right|\right] \times 100 \tag{60}$$

$$E_3 = \left[\sqrt{\frac{1}{n-1}\sum_{i=1}^{n}\left(\frac{(P_i)_{pred} - (P_i)_{ref}}{(P_i)_{ref}}\right)^2}\right] \times 100 \tag{61}$$

where P_i are the performance parameters, namely V_i, J_i, or S_i. The suffixes $'\mathrm{pred}'$ and $'\mathrm{ref}'$, refer to the predicted and the reference values, respectively. E_1 is the mean per cent error and measures the bias in the prediction, indicating the degree of over or under prediction. In the absolute mean per cent error (E_2), the sign of the deviations is considered, which is key in the assessment of the prediction capability of the models. E_3 is the root mean square per cent deviation, which indicates the proximity of the predictions to the reference values.

The statistical parameters E_4, E_5, and E_6, given by (62)-(64) are similar to E_1 , E_2 and E_3, respectively, but expressed in absolute magnitude terms non-relative to the reference values.

$$E_4 = \frac{1}{n}\sum_{i=1}^{n}(P_i)_{pred} - (P_i)_{ref} \tag{62}$$

$$E_5 = \frac{1}{n}\sum_{i=1}^{n}\left|(P_i)_{pred} - (P_i)_{ref}\right| \tag{63}$$

$$E_6 = \sqrt{\frac{1}{n-1}\sum_{i=1}^{n}\left((P_i)_{pred} - (P_i)_{ref}\right)^2} \tag{64}$$

E_4 is the mean error and predicts the agreement between predicted and reference measures relative to the reference parameter. E_5 and E_6 are the mean absolute and the root-mean-square errors, respectively.

The variance (s^2) of the difference between the reference and predicted variables is derived for every model from (65).

$$s^2 = \left\{\frac{1}{n}\sum_{i=1}^{n}\left[\frac{(P_i)_{pred} - (P_i)_{ref}}{(P_i)_{ref}} - \left(\frac{1}{n}\sum_{i=1}^{n}\frac{(P_i)_{pred} - (P_i)_{ref}}{(P_i)_{ref}}\right)\right]^2\right\} \times 100 \tag{65}$$

Note that the second term on the right-hand side of the equation is the mean of the predicted variables among all data points for every scenario $i = 1,2,\dots,n \ \therefore n = 90$

4.6.1.1 Overall Evaluation

The global evaluation considers all four geometry parameters and three prediction models in order to study their combined performance. The evaluation is first performed using the numerical results from section 4.5. Subsequently, to validate the models, and make the evaluation unbiased a second database is designed for geometric parameters inside and outside the initial range previously evaluated. The secondary dataset of geometric parameters is detailed in Table IV-7.

Table IV-7**.** Geometric parameters for model performance validation

Dc (mm)	dw (mm)	N	σ (Sm^{-1})	Profile
20	0.4	4	1	CH
40	0.55	8	3	SH
54	0.85	12	5	
		16		
		20		

Table IV-8 shows the accuracy of the predictions for all three models using both datasets. The evaluation using data from Table IV-1 leads to the errors listed in Columns 2 to 5 of Table IV-8. The deviations computed using the dataset from Table IV-7 are shown in Columns 6 to 10 of Table IV-8.

Table IV-8**.** Accuracy of prediction of performance models

	V_i[c]	$J_{i_\sigma=1}$[c]	$J_{i_\sigma=5}$[c]	S_i[c]	V_i[d]	$J_{i_\sigma=1}$[d]	$J_{i_\sigma=3}$[d]	$J_{i_\sigma=5}$[d]	S_i[d]
E_1[a]	0.3455	9.7781	11.1633	0.2879	0.0538	-14.6176	-17.5665	11.3386	0.7569
E_2[a]	5.4276	9.9703	11.2709	5.9772	6.6253	20.7793	17.6337	11.6268	7.9100
E_3[a]	7.1260	11.5848	12.8095	7.7600	9.5109	23.0032	18.5606	13.7733	11.5742
E_4[b]	-1.8194E-6	1.0567E-2	6.0245E-2	-1.2819E-6	1.2375E-5	-1.1866E-2	-3.8499E-2	4.0431E-1	-3.2217E-5
E_5[b]	7.7424E-5	1.1113E-2	6.1959E-2	9.7102E-5	9.6445E-5	1.6517E-2	3.8558E-2	4.0431E-1	2.5331E-4
E_6[b]	1.1771E-4	1.8048E-2	9.7946E-2	2.3962E-4	1.5853E-4	2.1579E-2	4.6450E-2	4.7432E-1	5.7766E-4
s^2	0.5066	0.3752	0.3806	0.6014	0.99045	3.1309	0.3244	0.5970	1.3338
F_{rf}	0.017	1.132	1.373	0.089	0.228	2.832	2.515	1.467	0.482

[a]Figures shown in percentages.
[b]Units: V_i is a ratio, J_i in $A.m^{-2}$ and S_i is dimensionless.
[c]Reference values from Dataset 1.
[d]Reference values from Dataset 2.

The low statistical variances, s^2, seen in all models, i.e. lower than 3.5%, show that the models are consistent. The relative performance factor is systematically larger when the models are validated using the second set of data. The V_i model provided the most precise predictions from the relative performance indicator, followed by the S_i model. Predictions of eddy currents (J_i) result in the largest deviations with an absolute mean percentage error of up to nearly 21%.

4.7 Discussion

The simulated and measured voltage ratios shared common trends. Results showed that large numbers of turns and small wire cross-sections provide enhanced sensitivity and large coil couplings. Furthermore, square helix coils induced larger voltages and increased the system sensitivity in contrast to circular geometries.

The degree of association of the coil geometry characteristics to the system performance parameters was computed following statistical analysis of the numerical outputs. Using multiple regressions, three universal models given by (55) to (57) were computed. The models containing a combination of independent variables accounted for over 98% of the variance observed in all performance factors.

The induced voltage ratio was found to be primarily influenced by the coil size and shape. Smaller amplitude ratios resulted in a higher signal-to-noise ratio in experimental MIT systems. Conversely, a low number of turns results in greater system stability by avoiding parasitic resonance. The developed model for voltage ratio resulted in predictions with a mean absolute error below 7% and a proximity to reference values within a 10% margin.

The sensitivity of the system to changes in conductivity was strongly influenced by the number of turns and the coil size. A negative relationship between the sensitivity model prediction and the wire diameter was reflected in the associated correlation. Experiments performed on coils with a large number of turns and small wire cross-sections provided enhanced sensitivity to changes in conductivity, resulting in higher signal stability.

The induced eddy currents have a close negative interaction to the number of turns as by Spearman coefficient and multiple regression analyses. The J_i models presented the poorest performance with a large mean per cent error and among the highest variance figures recorded, i.e. 21% and 3% for the scenario with the lowest conductivity ($1Sm^{-1}$), respectively.

The developed models resulted in predictions of the performance parameters within a ±15% deviation margin. This accuracy level means that although the models are fit to provide an overall trend of the system performance, specific scenarios of interest would still benefit from solving the Forward Problem.

The evaluated MIT system showed enhanced performance for square coils of a large number of turns, provided that the operating frequency departs from the circuit resonance frequency. The overall error of the predictions is greater for reference values outside the initial database spectrum.

4.8 Conclusions

Knowledge of the effects of varying the geometry of the coils is beneficial to enhance the design of the sensors since comprehensive studies of their effect on MIT system performance are not available in the literature. In this chapter, three performance models based on 90 sensor geometry combinations were derived. The data was processed through both bivariate correlation and multiple regression analyses. The correlation factor among four geometric parameters (coil size, wide diameters, coil profile and number of turns) and three performance factors (voltage ratio, induced eddy currents, and sensitivity) were given.

The correlation models presented in this chapter comprise the best fits to describe the behaviour of the data. These correlations have the potential to help researchers predict the relative overall performance of MIT systems for given coil setups. The proposed models allow enhanced sensor designs without the need to perform extensive experimental tests or simulation work as the models were seen to be consistent in the overall trend of the system performance. The correlation models can be extended to predict the level of the signal to be measured from a particular sensor design and hence provide useful information to developers. The optimisation of the sensor design given a set of design premises is out of the scope of this thesis. However, a case study exemplifying the problem optimisation is given in [152], and further details can be found in [158].

The sensor characteristics evaluated in this chapter are incorporated into several design premises, framed by the intended application, to provide a comprehensive hardware design in Chapter V.

Chapter V MIT apparatus design

5.1 Introduction

The MIT hardware encompasses not only the sensors detailed in Chapter IV, but also the sensor-pipe fastening system and the electromagnetic shield. Existing MIT systems described in the literature have been developed to work under controlled laboratory conditions. Two main approaches for MIT coil positioning around a cylindrical fluid container are found in the literature. One consists of attaching the coil formers to the shield structure [11] [90] [91]. The other approach accounts for fixing cylindrical coil formers to the fluid container [95]. However, the design of a MIT system targeting multiphase flow metering in pipelines involves a different hardware design approach.

The MIT apparatus design, detailed in the following sections, comprises both the external electromagnetic shield and the coil formers structure. Electromagnetic shielding is key for increased MIT accuracy and the elimination of direct capacitive coupling between the sensors. Reports on an overestimation of the induced signal of up to 70%, due to direct capacitive coupling and electromagnetic interference can be found in the literature [73] [95]. Herein, a broad assessment of various shielding alternatives is addressed.

In this chapter, the hardware design of an MIT system for multiphase flow metering is discussed. Shield dimensioning is addressed via experimentation and through computational modelling. This section encompasses the work published in the IEEE Sensors Journal [17] on near-field electromagnetic shielding effectiveness. Details of hardware design are disclosed in the patent document GB1810735.9 [14] in which the author and Dr Ma are the co-inventors (see Appendix C). The contributions to the patent, that derives from this work, comprises the studies of shielding effectiveness of soft and hard shields (Section 5.3.3), shielding effectiveness of hard shields (Section5.3.4), and the sensor structure (Section 5.4).

The chapter is organised into six sections. It starts with a discussion of electromagnetic shielding in the context of MIT design and operation in Section 5.2. The concept of shielding effectiveness is then introduced in Section 5.3, along with the methodology and the numerical and empirical assessment of various attenuation materials. Section 5.4 presents the MIT hardware design and characteristic. The results of the analyses undertaken in this chapter are discussed in Section 5.5 and the conclusions are derived in Section 5.6.

5.2 Electromagnetic shielding

Previous work on MIT design significantly reduced capacitive coupling by installing external radial electromagnetic enclosure around the MIT sensors [11] [66] [88] [91] [93]. Preceding experiences in the use of ferromagnetic shields, with thicknesses that vary between 300 μm to 3 mm, have proven effective electromagnetic shielding properties in the kHz and GHz frequency range [159]. In the context of high frequencies, the greatest losses in electromagnetic fields come from eddy-currents forming within the shield material, which are proportional to the square of the frequency [160].

The principal parameters to consider in the design of the electromagnetic shield are the geometry dimensions, the attenuation material, and the stand-off distance to the coils. Optimum electromagnetic shielding yields from balanced prevention of self-resonance and self-capacitance [96]. Previous studies showed that a coil-screen separation between 60% and 80% of the diameter of the coil provides reasonable suppression of the inter-coil capacitive coupling [161]. Moreover, the capacitive coupling can be further attenuated by increasing the length of the screen [94].

In the following subsections, the effectiveness of various MIT shielding alternatives is addressed. The shield design, which combines simulation and experimental work, is presented following the description of the experimental evaluation methodology. The method used for shielding evaluation is based on free-space measurement of near-field electromagnetics [162].

5.3 Shielding effectiveness

The principle of electromagnetic shielding of MIT systems consists of using an attenuation material that inhibits the radiation of electromagnetic fields from or into the region of interest. The widely accepted principles on electromagnetic shielding are derived from [163]. Shielding theory states that the effectiveness of field attenuation across a barrier comprises three main mechanisms, namely, reflection, absorption, and multiple reflections.

Figure V-1 illustrates the refection mechanism arising at the boundaries of the shielding barrier where a sudden change in the conductivity and permeability of the medium exists. The portion of the incident field that is not reflected at the surface of the material passes through the medium where it is consequently attenuated in proportion to a factor $e^{-z/\delta}$, known as absorption loss.

The field initially transmitted through Wall A becomes the incident field to the second surface (Wall B) and undergoes a similar reflection mechanism as in the former boundary. The section of the wave that is not reflected is transmitted through Wall B. The transmitted signal adds to the total transmitted field to the right-hand side of the material. The signal reflected by wall B is further attenuated by the material before part of it is again reflected by Wall A, repeating the process of multiple reflective losses.

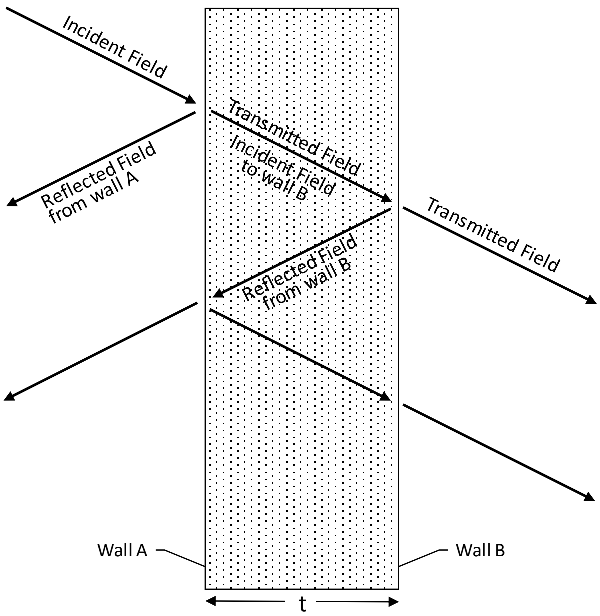

Figure V-1. Illustration of shielding effects of an incident magnetic field within a shielding material of thickness 't'

The overall shielding effectiveness of an attenuation material S_H is the sum of all the different loss mechanisms that an incident wave undergoes [164], i.e.

$$S_H = R_{dB} + A_{dB} + M_{dB} \tag{66}$$

where R_{dB}, A_{dB}, and M_{dB} are the reflection, the absorption, and the multiple reflection losses expressed in dB, respectively.

For shield thicknesses larger than the skin depth of the material, multiple reflection losses are negligible [73] [95], leading to absorption and reflection losses to be the primary shielding mechanisms for near magnetic fields. Absorption is related to the Ohmic losses and material heating arising from the exponential decrease in amplitude of the wave as it passes through a medium [165]. The reflective shielding mechanism is based on the radiation reflected by a shield surface. Reflection losses are typically encountered in metallic materials due to their conductivity and their capacity for charge mobility [166].

Absorption loss is the dominant shielding mechanism for all frequencies of magnetic sources within the near field distance from the shield [167]. For instance, at around 10 MHz operating frequency, the reflective losses in a 0.508 mm copper shield are half of those from absorption mechanisms [164].

The total shielding effectiveness (SE) of a material in free space placed in the plane wave incident region is given by (67) [168]

$$S_H = 20 \log_{10} \frac{H_i}{H_t} \tag{67}$$

where H_i and H_t are the incident magnetic field and the transmitted signal, respectively.

In the time domain, the SE can be computed from the ratio of the electromotive forces (e.m.f) [169]. Equation (67) is equivalent to Equation (68) as follows

$$S_H = 20 \log_{10} \frac{V_1}{V_2} \tag{68}$$

where V_1 is the reference e.m.f without the shield and V_2 is the load measurement of the induced e.m.f with the barrier in place.

The SE of an attenuation material depends predominantly on five aspects: the electric properties of the material; the frequency of the incident wave; the length scale with respect to the wavelength (near or far fields); the continuousness of the material surface and; the thickness of the barrier [112][170].

5.3.1 *Shielding effectiveness modelling*

The simulation model was created in CST Microwave Studio Student Edition. The numerical simulations consider vacuum conditions and disregard the electromagnetic noise and the interference of external sources to which real free-space sensors are subjected. Details of the model setup and the boundary conditions are given in Chapter III and Appendix C. Numerically, the magnetic fields H_i and H_t and the induced e.m.f, V_1 and V_2, are computed by solving the time-harmonic electromagnetic forward problem with and without the attenuation material placed between the coils in the simulation model.

Figure V-2 shows the scenarios modelled. The thickness of the shielding barriers and material properties varied according to the requirements of each set of scenarios. As specified in Chapter III, the attenuation material was fully discretised to evaluate the decay of the magnetic field through the thickness of the barrier. Given the sharp change in electric properties in the air-shield interface, Maxwell's equations were complemented using built-in appropriate interface boundary conditions that ensure continuity of the tangential components of the fields. Figure V-2(a) shows the base model used to account for the effect of the thickness of transversal barriers on the induced signals at various operating frequencies. In the second study, the receiving coil was located inside a radial enclosure. This novel experimental method, where the configuration of the attenuation material resembles MIT shield profiles (see Figure V-2(b)), was proposed by the author and published in [17]. For the final scenario, both evaluation methods are compared at given shield dimensions. Figure V-2(c) exemplifies the change in the height and width for a transversal barrier shield.

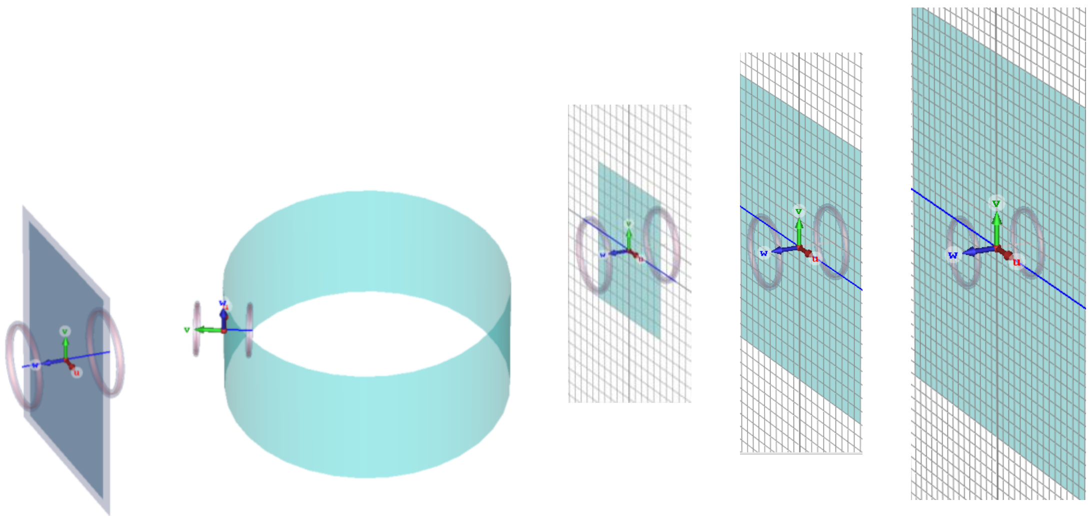

(a) (b) (c)

Figure V-2. Modelling scenarios for shielding effectiveness evaluation showing (a) transversal barrier method, (b) enclosed receiving sensor method and (c) changes in the shield dimensions.

5.3.2 *Experimental method*

The experimental procedures to measure SE aim to quantify the attenuation of an electromagnetic field by a shielding barrier. The reference measurement yields from the background signal detected by the MIT sensor in the absence of the attenuation barrier. The attenuated signal induced in the receiving sensor is proportional to the signal transmitted through the surface of wall B of the shielding barrier (see Figure V-1).

Depending on the intended application, different SE methods are available in the relevant literature. Three main methods exist for the measurement of complex permeability namely, the transmission/reflection line method, the free space method, and the resonant method [169] [171] [172] [173]. Each methodology is limited to specific frequencies, materials, and applications [174]. Considering the intrinsic characteristics of the MIT systems, a free space method using electromagnetic probes was selected for near-field magnetic shielding evaluation [162].

The experimental method comprises the measurement of the shielding effectiveness of seven attenuation materials placed between two interrogating probes. In the setup, MIT sensors were used as electromagnetic probes. The transmitting source (Tx) was excited with a time-harmonic signal that created a magnetic field incident to the surface of the shielding material. The receiving sensor (Rx), located at a fixed distance from the Tx, sensed the magnetic field that permeated the shielding material. From Equation (68), the ratio of the background signal to the attenuated signal gave the material SE.

The following stages were adopted to evaluate the SE of a range of attenuation materials:

- Sample preparation
- Experimental testing using three different setups, namely: no-shield, transversal-barrier shield, radial-enclosure shield.
- Simulation of various geometry profiles to assess their impact on the electromagnetic field distribution.
- Analysis of results.

5.3.2.1 Sample Materials

The evaluation of attenuation materials included experiments on hard, soft, and composite shields. The hard and soft shields were prepared from samples of metals and dust state ferrite, respectively. Seven samples, labelled A1, A2, B, C, X1, X2, and CX2, were prepared for experimental SE measurement. A1 and A2 samples are Aluminium sheets with thicknesses of 6.3 mm and 2.1 mm, respectively. B is a 2.1 mm thick sample of Mild Steel. C is a 0.1 mm Mu-Metal alloy sheet. Perspex (Polymethyl methacrylate, PMMA) receptacles with bulk dimensions of 20 mm and 5 mm filled with

Ferrite Powder were labelled X1 and X2, respectively. A composite shield (CX2) was built by combining Mu-Metal (0.1 mm) and Ferrite Powder (5 mm). The material properties are summarised in Table V-1. All samples used were cut to 120 mm by130 mm in width and height, respectively.

Table V-1. Electrical properties of shielding materials

Sample	**Material**	**Thickness (mm)**	**Relative Conductivity (σ_r)**	**Relative Permeability (μ_r)**	**Type of shield**
A1	Aluminium	6.3	5.87×10^{-1}	1	Hard
A2	Aluminium	2.1			
B	Mild Steel	2.1	1.17×10^{-1}	1.0×10^{2}	Hard
C	Mu-Metal	0.1	2.80×10^{-2}	90×10^{3}	Hard
X1	Ferrite Powder	20	1.68×10^{-1}	N/A	Soft
X2	Ferrite Powder	5			
CX2	Mu-Metal & Ferrite Powder	5.1	N/A	N/A	Composite

A. Experimental setup

Considering typical operation parameters of MIT systems for low conductivity imaging, a frequency spectrum of 5 MHz to 20 MHz is of interest. The selected frequency range ensures wavelengths larger than the characteristic dimensions of the region of interest [7] and sensors operating within the electromagnetic near zone. The experimental frequency range covers a near-zone of at least 2.3 m from the electromagnetic source. Typical pipelines for multiphase transport in the Oil and Gas industry are well within the near-zone [153] [154].

Experiments were carried out at the Fluid and Complex Systems Research Centre, Coventry University, UK. The experimental setup used is illustrated in Figure V-3. The test assembly comprised a dual coil MIT system. The hardware configuration accounts for the excitation of Tx and the measurement of the field perturbations by Rx. Figure V-3(a) illustrates the experimental setup with Tx located opposite to Rx. A fixed distance, equal to the diameter of the coil, separates the coils and the attenuation material to ensure a dimension-to-distance ratio as specified in [169].

The source coil was excited through an alternating wave of 10 $V_{p\text{-}p}$ in amplitude using a function generator. All metallic attenuation materials were grounded. Circular helix air-core coils with six turns and 50 mm in diameter were used. Coils were wound in the same direction, and their terminals were connected so that the magnetomotive force of the coils were joined in series aiding [136]. Experiments were conducted at room temperature.

Reference and load measurements were repeatedly gathered throughout the frequency spectrum. The reference measurements were taken without any attenuation material, as illustrated in Figure V-3(a). The load measurements were taken with the sample surface positioned orthogonally to the incident wave (see Figure V-3(b) and Figure V-3(c)). In the setup shown in Figure V-3(c) the shielding material is not restricted to a one-dimensional barrier flanked by the sensors. Instead, it partially encloses Rx in the XZ direction.

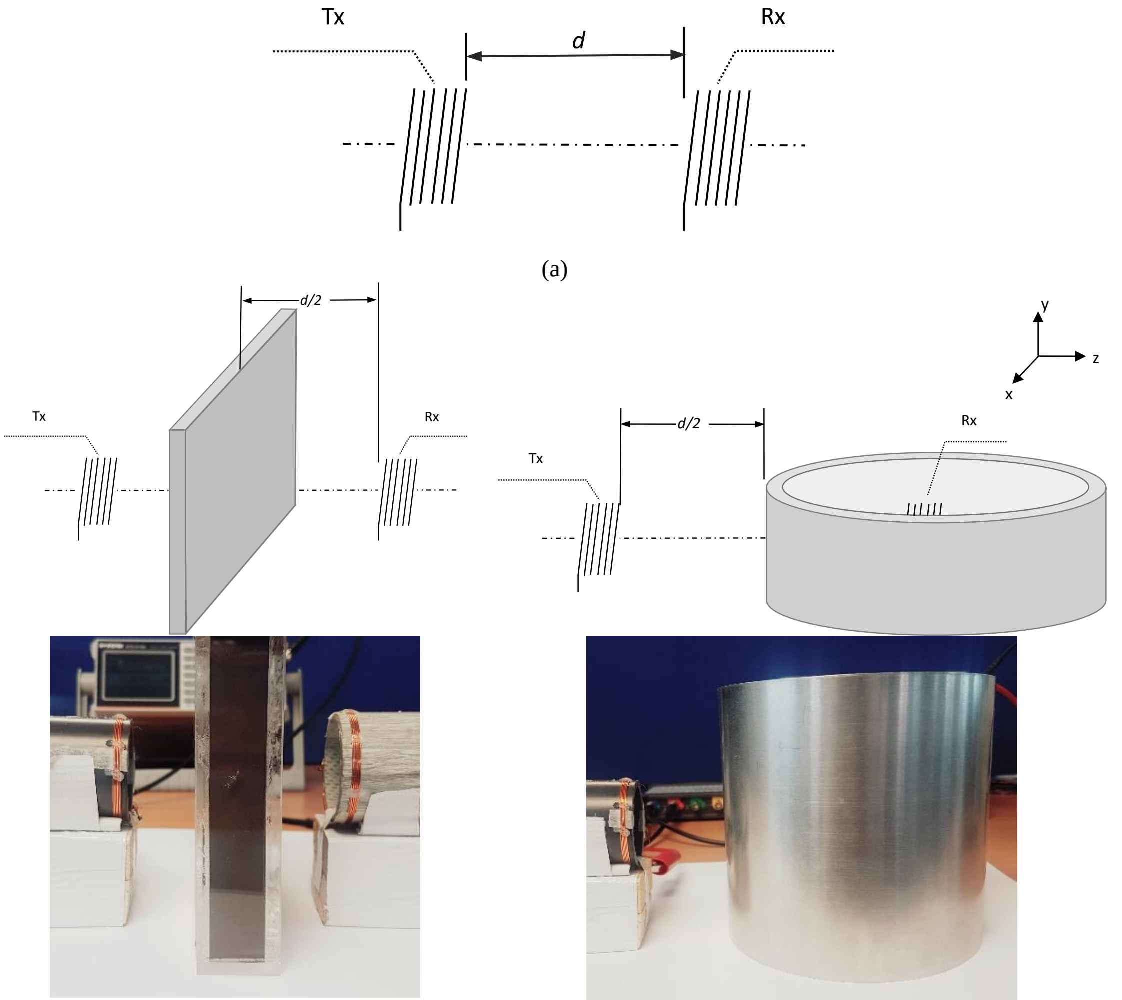

(a)

(b) (c)

Figure V-3. Experimental setup for the shielding effectiveness measurement showing (a) base scenario for reference measurement, (b) load measurement with X2-transversal shielding barrier positioned between the sensors, and (c) load measurement with near-field magnetic measurement method from a partially enclosed sensor (radial enclosure).

5.3.2.2 Statistical analysis of results

Through the statistical analysis, the experimental measurements were assessed to determine the quality of the data and to better understand the relationship among a broad range of parameters. The data dispersion was measured through the standard deviation for every dataset. The mean load and reference measurements were used to calculate the SE for all given operating frequencies. The CI gives the probability that the measurements lie within a particular distance from the mean value [175] [176]. To report SE computation figures, a 95% CI was adopted.

The mean values from SE of all seven materials were further analysed through Analysis of Variances (ANOVA) or Welch tests. Both tests establish the relationship between two dependent variables based on the similarity of the means of two or more groups of independent variables. Verification of the assumptions is key for the reliability of the hypothesis tests to be conducted. In the analysis of variance, the sensitivity of the results obtained for the test statistic is mostly influenced by the heterogeneity of the variances [177]. The Welch test is a robust alternative to ANOVA when the hypothesis of homogeneity of variances is discarded [178]. Homogeneity tests performed on the data determines the validity of the homogeneity hypothesis and hence enable the utilisation of ANOVA tests for analysis of variances; otherwise, the Welch test is used.

ANOVA and Welch tests only allow testing the hypothesis that the compared averages are the same. Rejecting this hypothesis means that the comparative SE of various materials is not equal, but it does not specify precisely where the detected differences lay. In this sense, the significant difference among various data sets is derived from focused comparisons of experimental outcomes performed *a posteriori* [179]. These comparisons are conducted through *post-hoc* tests using the software IBM SPSS Statistics. Tuckey and Games-Howell *post-hoc* analyses were used for homogenous and heterogeneous variances, respectively.

5.3.3 Shielding effectiveness of soft and hard shields

The mean electromagnetic SE of all sample materials tested within the frequency spectrum 5 MHz to 20 MHz is shown in Figure V-4. The total standard deviations of the measurements are 3.05 mV and 0.41 dB for the induced e.m.f and SE, respectively. The 95% CI of the mean SE is represented as error bars in Figure V-4. Overall, the dispersion of the data is small, yet soft shields represent higher dispersions at higher frequencies than other evaluated samples. This effect is related to higher noise-to-signal ratios seen in the induced signal.

Dismissing the equality variance hypothesis, Welch tests yield a significant difference among materials. Games-Howell *post-hoc* tests performed on secluded analyses of hard and soft shields indicate that the SE of X1 was statistically significantly higher than that of X2. There was, however, no statistically significant difference among the different hard samples.

The SE of hard shielding materials decreases with increasing frequency (Figure V-4(a)). The results show little variation regarding the layer thickness in concordance with typical reflection loss behaviour of metals [166]. Among the lowest frequencies (5-8 MHz), the aluminium samples (A1 & A2) provide the highest wave attenuation with a SE of over 20 dB. The Mu-Metal sample (C) shows a slightly better performance within the 9-13 MHz range.

Conversely, Figure V-4(b) shows that soft shields present increasing electromagnetic shielding capacity with increasing frequency and barrier thickness. Above 13 MHz, soft samples (X1 & X2) outperformed hard shields, reaching a maximum SE of 16 dB (X1) at 16 MHz, whereas the shielding capacity of metallic samples was nearly null. Based on results from [100], the composite shield (sample CX2) was expected to provide enhanced shielding effectiveness. On the contrary, CX2 showed similar performance to those of hard shields. This behaviour suggests the generation of a low reluctance path of the transmitted signal in the soft shield layer, which results in a higher concentration of the transmitted electromagnetic field and hence a lower SE.

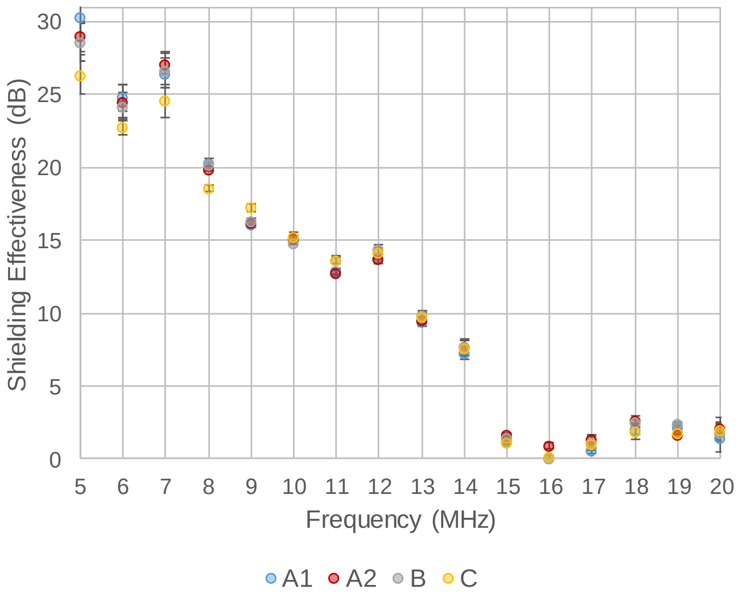

(a)

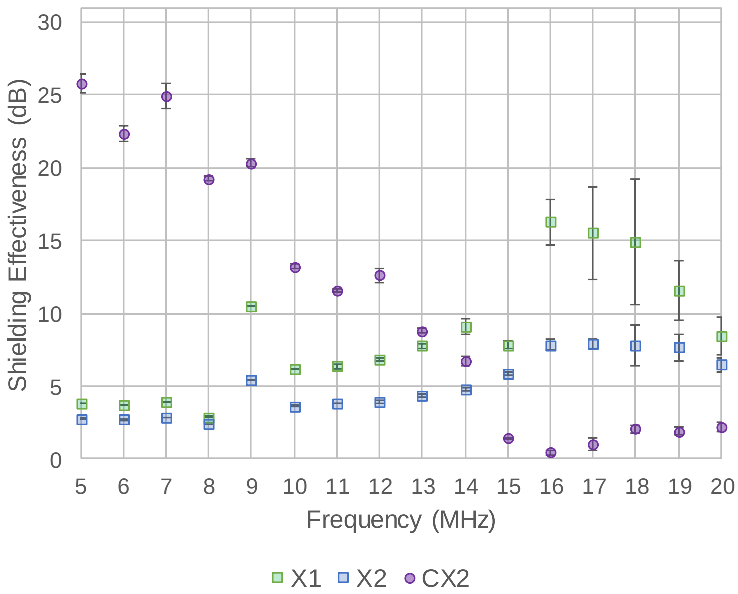

(b)

Figure V-4. Experimental results of (a) hard shields and (b) soft shields and composite shields showing error bars for the 95% Confidence Interval

Figure V-5 compares results from Mu-metal and composite barriers under the transversal barrier method and the new radial-enclosure setup shown in Figure V-3(b) and Figure V-3(c), respectively. Results showed an average increase of 5 dB in shielding effectiveness of both Mu-Metal (Figure V-5(a)) and dual shielding CX2 (Figure V-5(b)) when the radial-enclosure setup was used. The observed shielding capacity of the partial enclosure is attributed to the geometry of the shield, which eliminates the effect of one dimensional variable in the XY plane (see Figure V-3).

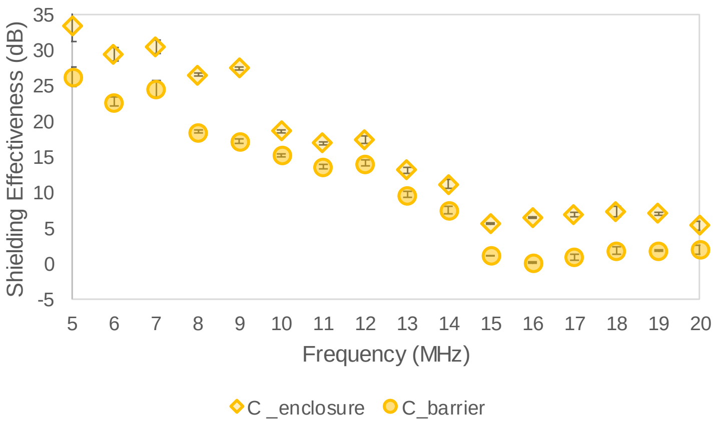

(a)

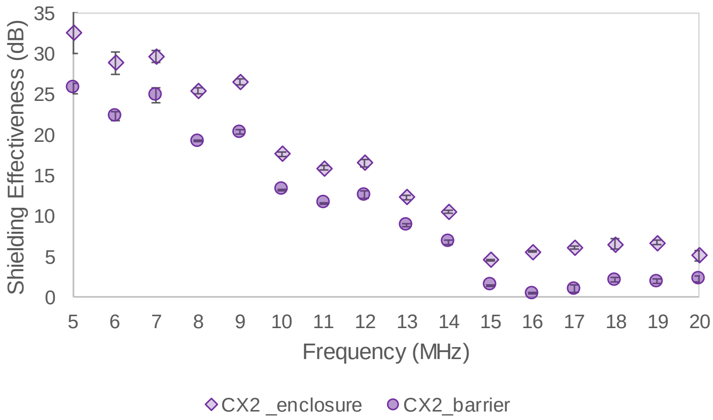

(b)

Figure V-5. Experimental results of shielding effectiveness showing the signal attenuation of (a) Mu-metal and (b) C2X composite for the transversal barrier (see Figure V-3 b) and the radial enclosure (see Figure V-3 c) setups. The error bars show the 95% Confidence Interval

5.3.3.1 Shielding effectiveness measurements methods

Simulation allows for a comparison of the electromagnetic field distribution around the two shielding measurement methods. Figure V-6 illustrates the electromagnetic field distribution around the experimental setup. The magnitude of the field on the side of the shielding material opposite from the transmitting coil (Tx) is several orders of magnitude lower than in the area surrounding the source, showing the blocking effect of the barrier on the incident wave.

The magnetic field distribution around Rx for both experimental setups, i.e. transversal-barrier method and radial-enclosure method, is shown in Figure V-6(a) and Figure V-6(b), respectively. Numerical outputs show the generation of a fringe field on the edges of the metallic barriers. The radial enclosure method provides a 50% decrease in the electromagnetic field distribution inside the enclosure and in the fringe field intensity on the top barrier when compared to the transversal barrier setup.

These results prove that hard shields provided enhanced SE around the operating frequency of the MIT system (10 MHz). The following sections focus on the evaluation of hard shields.

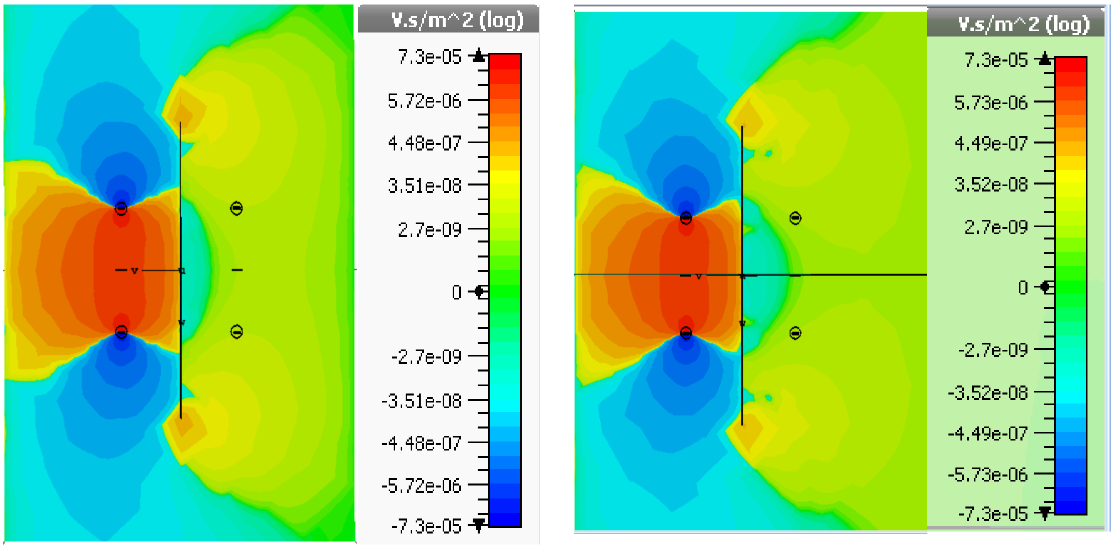

(a) (b)

Figure V-6. Side view (YZ plane – see Figure V-3) of the magnetic field distribution and fringe field at 10 MHz around (a) C sample sheet (Mu-Metal) simulating the transversal measurement setup and (b) Mu-Metal shield radial enclosure

5.3.4 *Shielding effectiveness of hard shields*

Load measurements, and consequently shield effectiveness computation, is largely dependent on the dimensions of the material attenuation samples. Numerical simulations below allow quantifying the effect that geometry and dimensions of the barrier have on SE measurements.

5.3.4.1 Barrier thickness

Five different thicknesses were modelled and the effects on the magnetic field, at a point located 15 mm from the barrier, are shown in Figure V-7. Numerical results show a slight variation in the intensity of the magnetic field for different barrier thicknesses. This difference decreases with increasing operating frequency. These results support the experimental outcomes in Figure V-4(a), which illustrates that the SE of the hard shields differs marginally irrespective of their thickness. This is converse to soft shield for which the impact of varying the barrier thickness is increasingly larger at higher frequencies.

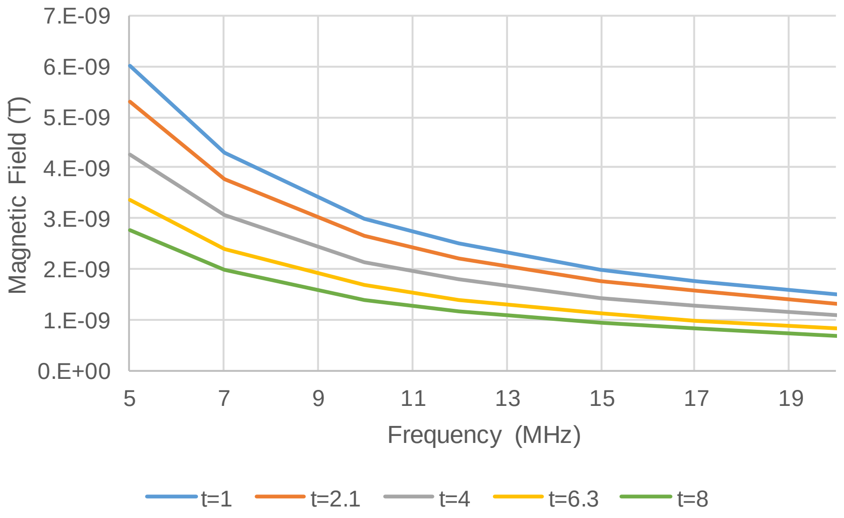

Figure V-7. Simulation outputs on the effect of barrier thickness on the transmitted magnetic field intensity. Thicknesses are given in mm

5.3.4.2 Effects of barrier height

Figure V-8 shows the intensity of the electromagnetic field at the edges of the shield for various shield heights. The radial-enclosure method is seen to provide enhanced field attenuation. Accordingly, the radial-enclosure SE method results in a more precise SE estimation. For the experimental setup used, a shield height to coil diameter ratio of 6 provided a sufficient height to attenuate the gross of the incident field, hence removing the fringe effect at the top and bottom edges.

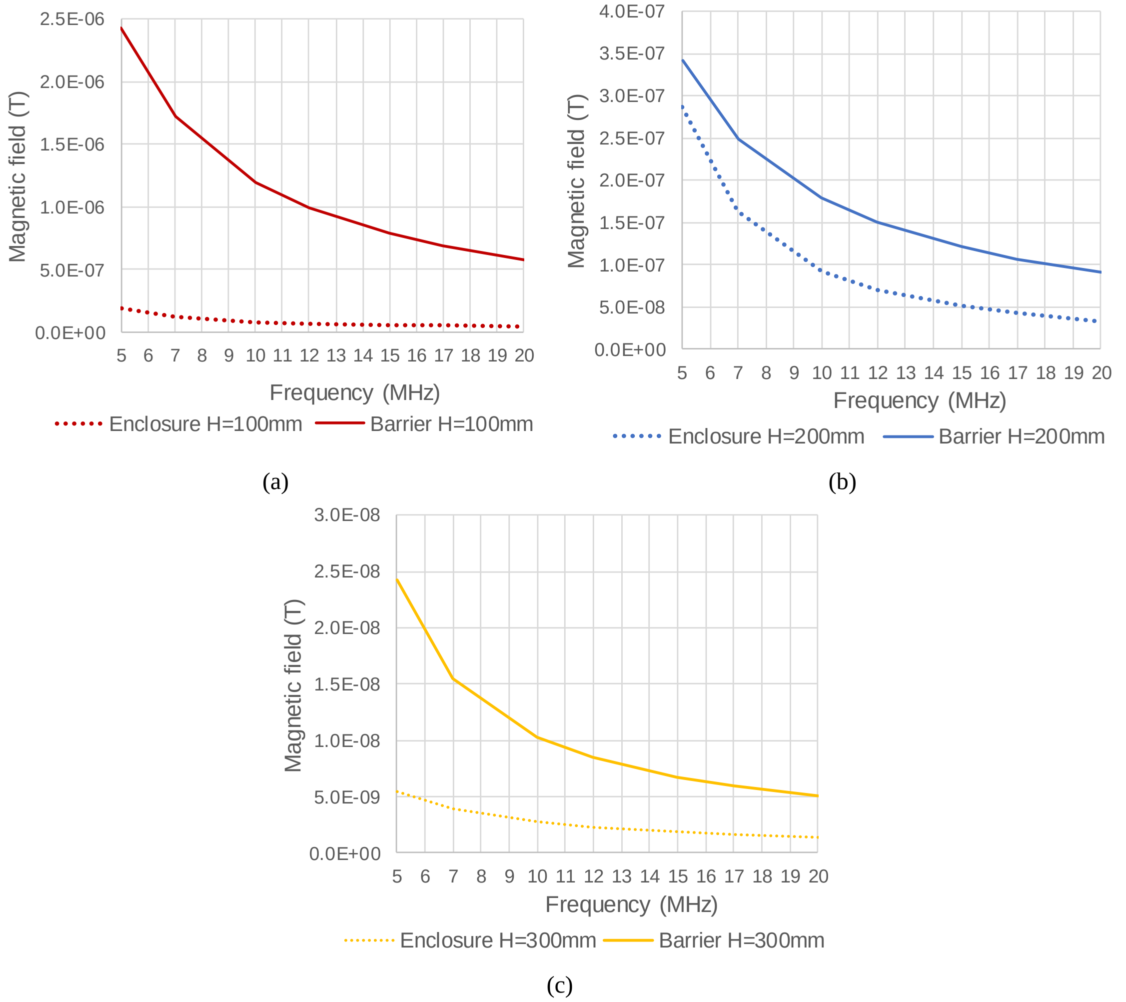

Figure V-8. Simulation results showing the effect of the fringe field on Mu-metal barriers of various heights (a) 100 mm, (b) 200 mm, and (c) 300 mm. The continuous lines correspond to the transversal barrier method (Figure V-3b). The dotted curves represent the radial enclosure setup (Figure V-3c)

5.3.4.3 Stand-off distance

The separation of the attenuation material to the inductive sensors affect their performance. In [94], it was demonstrated that eddy currents formed in the screen form a magnetic dipole which results in a less far-reaching field. The smaller the coil-shield separation, the more affected the more distant coils become. Furthermore, the greater the separation, the less efficient the shields are in eliminating capacitive coupling. Numerical simulations performed on an 8-coil system show that the effects described in [94] are non-linear (Figure V-9).

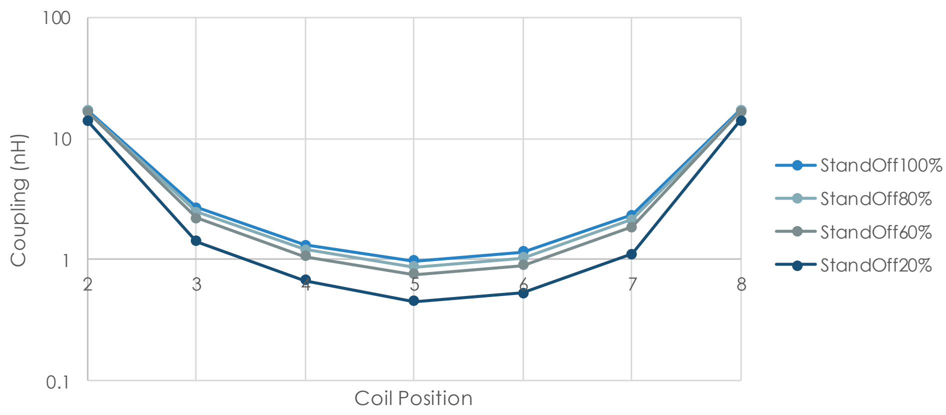

Figure V-9. Simulation results showing the coupling between coil pairs for stand-off distance of 20% to 100% the coil diameter

Further modelling alloweds to identify that the shielding effect reaches a plateau, approximating the no-shield scenario, when the gap between the shield and the coils, i.e. stand-off distance, is greater than 1.5 times the coil diameter (See Figure III-6).

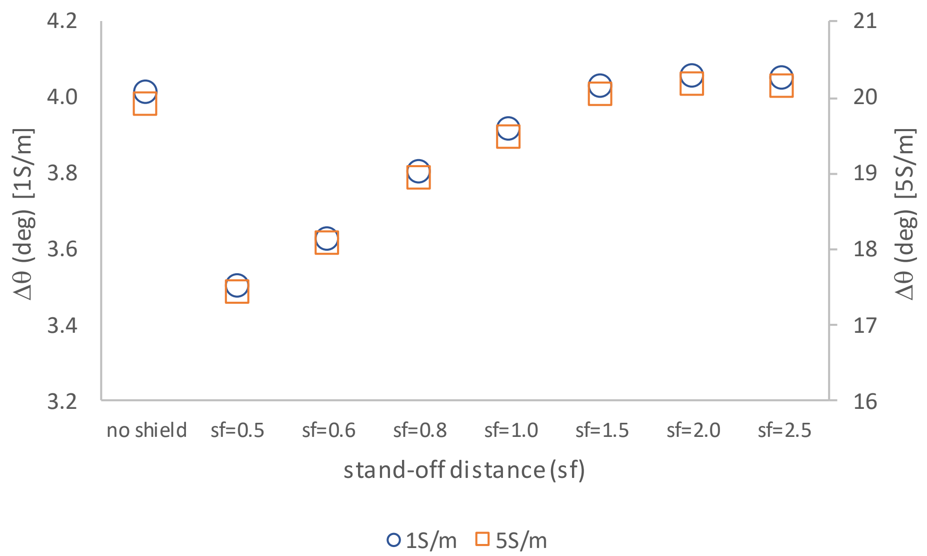

Figure V-10. Phase shift for various stand-off distances and conductivities in the imaging region of 1 Sm^{-1} and 5 Sm^{-1}

5.4 Sensor structure

Existing MIT systems account for separate bodies for the coil former, the shield structure and the fluid container. Although these solutions comply with the measurement requirements for laboratory environments in terms of functionality and repeatability, their mechanical design does not provide the necessary flexibility for pipeline metering.

The MIT prototype here developed encompasses the following design premises: ease of installation and assembly, portability, and equidistant sensor fixation. The following subsection provides the general hardware features. Detailed drawings of the apparatus can be found in the publicly available information included the patent application GB1810735.9 [14].

5.4.1 General features

The novel MIT prototype presented in this section considers a comprehensive design with a clamp-on mechanism and exchangeable pieces to account for limited pipe diameter reduction and an outer electromagnetic shield. The prototype assembly combines the coil formers and the clamp-on mechanism in a single unit. This single structure design ensures a rigorous and repeatable measurement. During data interpretation, the relative position of the sensors to flow structures can be back-traced given the angular position of the unit to the pipe configuration. Figure V-11 illustrates the unit with eight square formers for helix coils mounted on a horizontal pipe. The design of the square-shaped formers are in agreement with the enhanced performance from square coils demonstrated in Chapter IV.

The hardware geometry combines an inner cylindrical geometry with an outer octagonal profile. The outer planar surfaces avoid the deformation of the coil profiles and ensure orthogonality of the coil face. The cylindrical inner feature ensures direct tight coupling to the pipe walls or to exchangeable artefacts that could allow its installation on smaller geometries. Furthermore, the mounting mechanism provides installation flexibility on pipes of various orientations (vertical, horizontal, or inclined).

The manufacturing material of the sensor unit must necessarily be non-conductive to avoid signal interference. The prototype used for the experiments was 3D printed with Polylactic acid (PLA) filaments of 2.85 mm in diameter to account for a filling density of 20%. The electromagnetic shield was built from industrial aluminium, which, as seen above, presents similar shielding effectiveness to that of Mu-metal at 10 MHz, with reduced costs. The 2 mm shield is located at a stand-off distance from the coils of 1.5 times the coil diameter and was fixed to the unit through friction-fit.

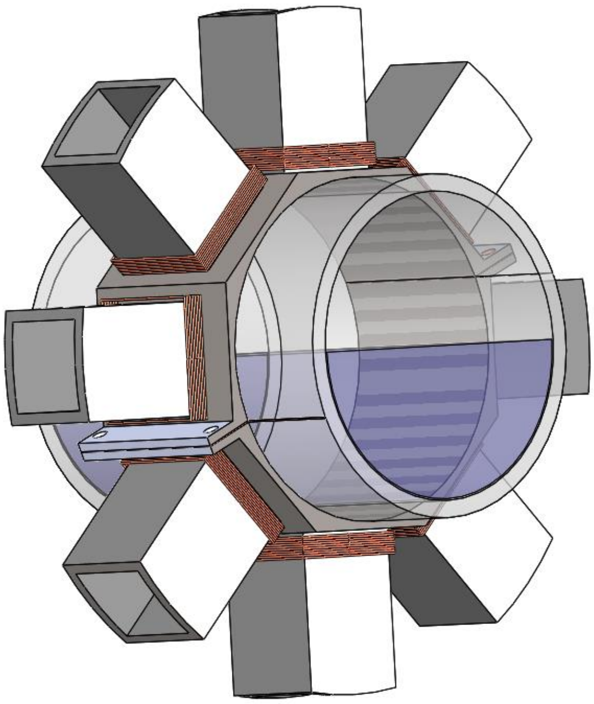

Figure V-11. MIT hardware clamp-on structure

5.5 Discussion

The study of shielding effectiveness of various attenuation materials within the frequency spectrum [5-20] MHz resulted in statistically significant differences between soft and hard shields. The shielding effectiveness of metallic barriers decreases with increasing frequency and is independent of the barrier thickness, so long it is larger than the material skin depth at the operating frequency. Among the evaluated materials, hard shields showed a consistent superior wave attenuation performance for frequencies below 13 MHz.

The dimensions of the material barriers have a significant impact on the load measurement accuracy. Dimensioning of the external shield requires a compromise on the stand-off distance. In this regard, a smaller stand-off distance, i.e. more proximity between the shield and the sensors, was seen to maximise the electrical coupling to ground and minimise external interference. On the other hand, a larger stand-off distance avoids the reduction in sensitivity due to the induced eddy currents in the screen, which create an opposing field that cancel the primary field produced by the coils.

The MIT apparatus for flow measurement provides enhanced design features for flow metering through pipes compared to systems described in the literature. The hardware considers sensors positioned equidistantly and symmetrically around the pipe perimeter with enhanced flexibility in terms of manufacturing, installation, and maintenance. There is, however, a need to perform a trace calibration of the prototype design and assess the prototype capabilities and operability. This is addressed in the following chapter.

5.6 Conclusions

This Chapter evaluated various attenuation materials and shielding mechanisms for a range to RF frequencies of interest. The results presented are key in the design of MIT prototypes. The effects on material selection and shield dimensioning were seen to be of significance at frequencies typical of MIT systems for low-conductivity samples. For the excitation frequency of the MIT prototype (10 MHz), metal shields showed improved attenuation capacity over the soft and composite shield.

The results indicated that the dimensions of the material barriers have a significant impact on the load measurement accuracy of near-field, free-space methods. The proposed semi-enclosed Rx measurement method provided a more accurate representation of the material isolation properties as the load measurement is corrected by eliminating the fringe effect at the side boundaries of the barrier. Moreover, the radial enclosure-based method proved to decrease the intensity of the fringe effect at the top and bottom of the barrier, for an enclosure of equal height than the transversal screen.

The analyses presented in this chapter and in Chapter IV set the basis for the design of the MIT model used in Chapter VII and for the manufacturing of the prototype tested in Chapter VI. Details of the sensors, shield design, and clamp-on structure are protected under the patent applications GB1810735.9 [14] and GB1810733.4 [15].

Chapter VI Measurement traceability

6.1 Introduction

The hardware design of the MIT prototype was addressed in Chapter IV and Chapter V. At this stage, we have an electromagnetic instrument, whose performance is intended to be assessed in the present chapter. To do so a traceable chain calibration was designed. In this regard, the International Dictionary of Metrology [180] defines metrological traceability as a property of a measurement result by means of which it is possible to relate it with a standard measurement unit or measurement procedure through documental confirmation of a continuous chain of calibrations. This chapter presents a chain of measurement calibration in which the performance of the instrument is assessed by means of comparison to reference measurements. A series of steps are taken here to ensure instrument accuracy and prove the capabilities of the metering systems relating the measurements from the instruments to reference quantities.

The chain calibration aims to provide certainty on the precision and accuracy of the measurement results. The instrument is assessed against legacy meters having recognised valid performance, which grants traceability of the measurement results. In this sense, the MIT prototype is tested and compared to a commercial ECT system detailed in [59]. The ECT sensor used in the experiments reported here are fully guarded, in that on each side of the ring of measurement electrodes there is another ring of electrodes driven at the same potential as the measurement set but unused in the measurement. Thus, the axial sensitivity of the measurement electrodes is well-constrained to the physical length of the electrodes in the flow direction, avoiding the electric field fringing out into the flow in either direction in an undefined manner.

The MIT measurements are made using the hardware prototype assembled following the characteristics discussed in Chapter IV and Chapter V and detailed in the patent documents [14] [15]. Unless otherwise specified, the MIT sensor head was coupled to electronics loaned by iPhase Ltd, manufactured based on the principles described in [8]. The commercial ECT meter used in this chapter, in turn, was calibrated against phantom tests and its performance is validated against a Gamma-ray densitometer designed by the University of Bergen (UiB).

The results on instrument capability and operational envelope detailed below were presented at the 18th Flow Measurement Conference [181]. The concentration calibration results presented in this chapter are published in 2020 IEEE International Instrumentation & Measurement Technology Conference Proceedings [18].

The following sections intend to prove that the accuracy of the instruments is good enough to allow the desired conclusions to be drawn from the measurements. Firstly, the traceability methodology is established in Section 6.2, following which the performance of the instruments is assessed by means of a series of bench tests and comparison to a legacy measurement system in Section 6.3. Later, the capabilities and operational envelopes of MIT and ECT are investigated in Section 6.4. Finally, in Section 6.5, the results are discussed and conclusions are provided.

6.2 Measurement traceability method

The stages illustrated in Figure IV-1 define the methodology adopted for traceability of the measurements. At the top of the pyramid, we have the underlying physics governing the measurement principles. This was sufficiently addressed in Chapter II and Chapter III; hence only the following steps are addressed in this chapter.

Stages II and III of the methodology aim to establish the instrument accuracy and to validate the capability and operational envelope of the meters. In this regard, the accuracies of MIT and ECT are assessed from bench tests and through comparison to reference measurements. The capability of the meters is established based on reference measurements from legacy instruments under static and dynamic conditions.

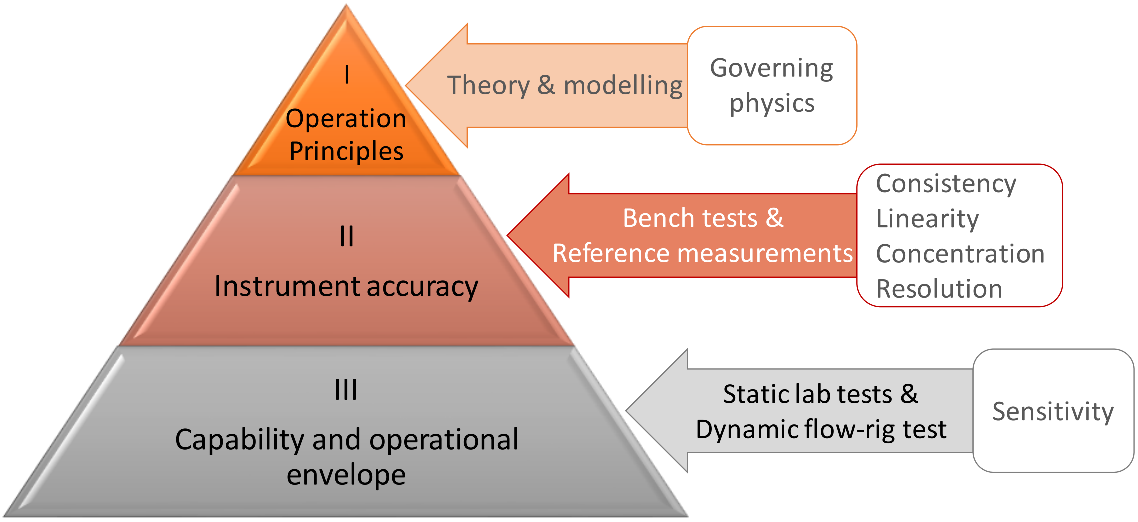

Figure VI-1. Measurement traceability methodology

6.3 Instrument accuracy

The accuracy of both MIT and ECT meters were compared to reference quantities. Static bench tests were designed to assess the quality of the measurements of the systems targeting their particular operational principles. Details of the test design and experimental results are provided in this section.

6.3.1 MIT sensor performance

The performance of MIT sensors under controlled laboratory conditions is assessed in the following subsections. The performance tests were conducted at iPhase facilities in Basingstoke, UK, where the author collaborated in the assembly setup described below, undertook the experimental work and performed the data analysis. The assessment aims to verify the quality of the measurements by correlating the electromagnetic induced signal to known electric conductivity input conditions. The tests here described are barely conducted to proof of principles that the sensors work. The comprehensive operation of the MIT system is assessed later in Section 6.4.

6.3.1.1Experimental assembly

The MIT bench tests were designed to assess the performance of the system in terms of repeatability and conductivity detection capability. The experiments were performed by clamping the MIT sensor head on a 110 mm polyethylene pipe section. Tx was excited through a 10 MHz time-harmonic signal that induced a magnetic field inside the pipe. The induced signal was measured by seven sensing coils (Rx) located in the perimeter of the pipe. The measured signal is proportional to the strength of the primary magnetic field, the conductivity of the medium and the volume of the conductive fluid [72].

For this set of bench tests, the pipe was alternatively filled with five water-NaCl mixtures yielding conductivities ranging from 1.10 Sm^{-1} to 5.30 Sm^{-1}. In the setup the receiving coils were connected to a digital oscilloscope (PicoScope 5444B) for data acquisition. The use of a built-in scope tool entitles offline data processing, given the tool inherent limitations.

Figure VI-2 illustrates the system setup. The coils, designated ‘L’, were sequentially numbered anticlockwise from 1 to 8. Coils ‘L1’ and ‘L2’ were successively used as transmitting coils in two separate measurement cycles. During each measurement cycle, the primary and secondary magnetic fields were measured from the remaining seven coils. The sensor array setup for cycle 1 and cycle 2 are illustrated in Figure VI-2(a) and Figure VI-2(b), respectively.

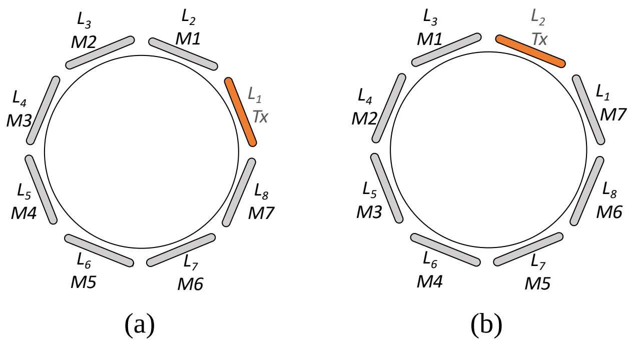

Figure VI-2. Illustration of the sensor array around the pipe highlighting the positions of the transmitter (Tx in orange) and receiving (Rx in grey) inductors for (a) measuring cycle 1 and (b) measuring cycle 2

6.3.1.2 Induced measurements

Figure VI-3 shows the phase difference between the primary and secondary signals from all receiving coils and for both measurement cycles. The results provide evidence of the symmetry of the measurements toward both sides of the axis formed by the transmitting coil and the opposite receiving coil in position M4. This symmetry, as well as that evident between both measuring cycles, shows consistency among the measurement from Rx coils that share the same relative position to Tx, i.e. measurements from M1 and M7, from M2 and M6 and from M3 and M5.

The repeatability of the measurements is indicated by the standard deviation of the data. A comparison of the data from both cycles, for the same conductivity and measurement position, resulted in a maximum standard deviation of 4.1%, made evident in position M2-M6. However, at higher signal levels, e.g. position M4, the standard deviation falls to values below 0.7%.

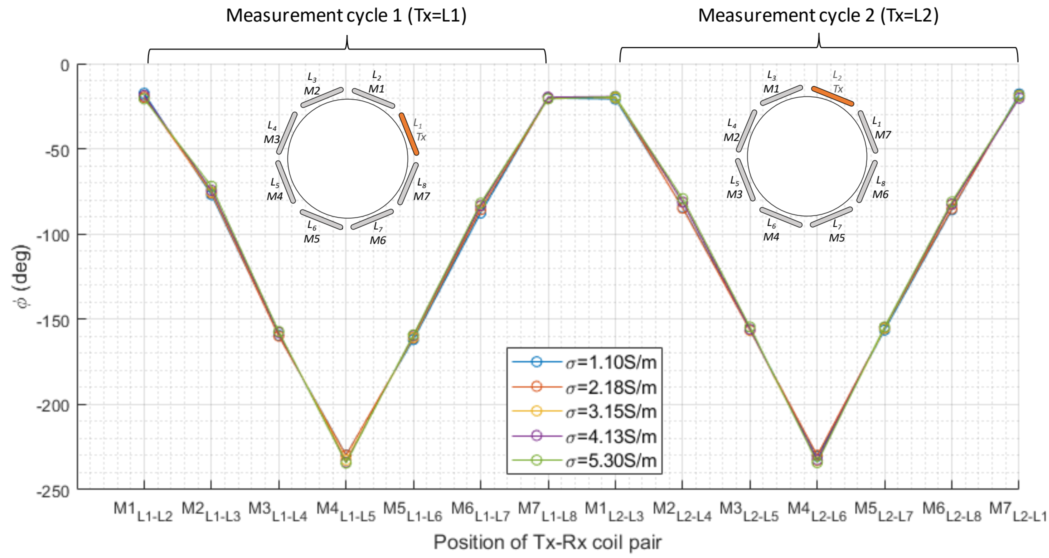

Figure VI-3. Phase measured from seven coils located in the perimeter of the pipe accounting for two measurement cycles where the transmitting coils were alternated from L1 to L2 in cycles 1 and 2, respectively

6.3.1.3Linearity

The mean phase angle measurement from the coil opposite to the transmitting coil is plotted against the conductivity of the medium in Figure VI-4. The results show the susceptibility of the meter to changes in the medium conductivity. The phase measurements exhibit a linear trend for the various water conductivities evaluated, which is expected theoretically from Equation (2) (see detailed discussion in Chapter VII). However, improved linearity is expected with enhanced data acquisition electronics.

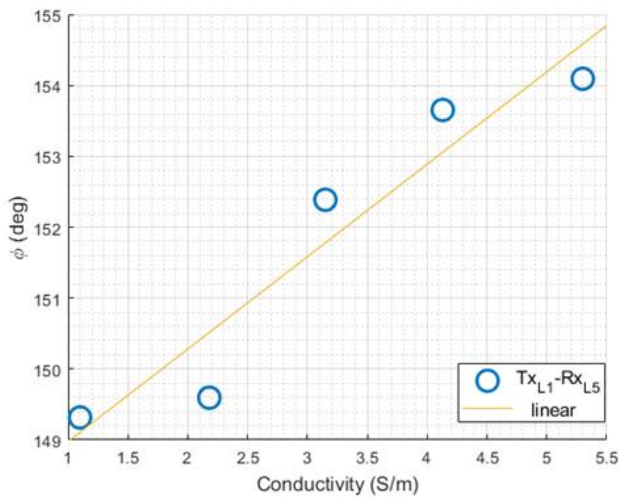

Figure VI-4. Phase angle measured from coil L5, opposite to transmitting coil L1 for different water conductivities

6.3.2 *ECT performance*

This subsection assesses the performance of ECT under controlled laboratory conditions. It is noteworthy that for the image reconstruction assessment (Section 6.3.3.3), because of the physical length of the electrodes along the flow direction, each pixel in the image plane is actually an average along the sensitivity length of the electrode pair. The axial resolution achievable with the given sensor array will be approximately equal to the axial length of the measuring sensor. This means an average along 0.035 m of the flow, given that the electrodes are fully guarded. Based on the Taylor hypothesis [182], it is assumed that in the time interval of a single frame of measurement the flow pattern translates along the pipe in a 'frozen' manner without significant evolution. Thus, the equivalent time averaging of this sensor length is u/L which varies from 0.1 s for $u=$0.35 m/s to 0.001 s for $u=$35 m/s. The sampling rate used, of approximately 500 frames per second, gives an averaging time of 0.02 s. Hence, the 3-D averaging due to the physical length of the sensor is comparable to the time averaging due to sampling rate.

Acquisition or analysis of data at higher rates can be regarded as oversampling. Flow structures significantly smaller than these time or physical scales will be hidden. Improved imaging reconstruction methods cannot improve on that resolution without extra knowledge of the flow or assumptions about the flow that are made in [122], for example. However, these 'hidden' structures are fully represented in the measured permittivity and hence volume fraction measurements. Estimates of flow-scale parameters such as mixture density are unaffected by the fact that the structures are hidden in the images. Comparison with experimental data in the following subsections as well as in Chapter VIII are therefore primarily based on flow-scale values as well as images. For the following ECT performance assessment, the capacitance measurements and reconstructed images are compared to *a-priori* known volume fractions and velocities. A series of static and dynamic tests were performed at UiB, making use of phantom rods that simulate flow spatial distributions of interest. The author designed the tests, undertook the experimental work, and analysed the data. The experimental setup was assembled in collaborated with Dr R.Ahmed and S. Stavland from UiB. The data presented in Section 6.3.2.2 and 6.3.2.3 was processed in collaboration with Dr Hunt.

6.3.2.1Experimental assembly

In order to provide quantitative measures of the performance of the ECT metering capacities, concerning its ability to compute volume fractions and visualize the flow components for different flow conditions, static physical models, i.e. phantoms, were used to simulate the physical properties of the flow. The ECT measurements were compared to theoretical computations, *a-priori* known quantities, and reference measurements. The volume and distribution of the phantoms are known;

hence the measurements and the reconstructed images were compared to that of the physical model to obtain a quantitative measure of the actual system performance.

The static phantom rods used during the characterisation work were made of polypropylene with drilled through-holes along the z-axis. Table VI-1 summarizes the density and dielectric properties of the phantoms for reference.

Table VI-1. Density and relative permittivity of phantom materials

Element	Density (Kg/cm^3)	ε_r
Polypropylene	946	2.20-2.36
Air	1.2	1

A set of four different phantoms were used in the static tests. The phantoms provide a combination of artificial patterns intended to characterise the features and constraints of the imaging systems. The cross-section structures of phantoms are illustrated in Figure VI-5.

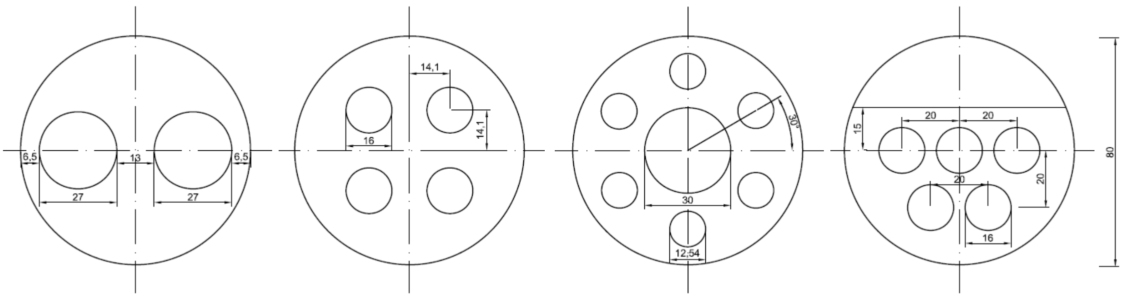

Phantom 1 Phantom 2 Phantom 3 Phantom 4

Figure VI-5. Experimental phantoms used for static tests. Dimensions are given in millimetres

The ECT used was the APL-S-SL-110-01 model provided by ATOUT Ltd [59]. The sensor head in Figure VI-6(a) comprised 16 electrodes arranged in two measurement planes of 8 sensors each. All unique capacitance pairs were measured. The total length of the sensors was 225 mm with a distance between the measurement planes of 65 mm. The sensor head was installed on a peek pipe of 100 mm OD, as illustrated in Figure VI-6(b). The phantoms were alternatively positioned in the interior of the pipe, and the measurements were taken for a period of 2 min for each inclusion. The experimental setup was designed to replicate the experimental conditions of the dynamic tests conducted in Section 6.3.3.2.

6.3.2.2Concentration calibration

The measured permittivity distribution allows the direct computation of the volumetric concentration of the different materials along the pipe cross-section [183]. For the ECT calibration, the volume fraction is calculated, from the permittivity measured within each reconstructed pixel, using the Series Capacitance Model in (69).

$$\alpha = \frac{\varepsilon_2(\varepsilon_m - \varepsilon_1)}{\varepsilon_m(\varepsilon_2 - \varepsilon_1)} \tag{69}$$

where, for the present exercise, α is the concentration of the higher permittivity material, i.e. polypropylene, ε_m is the effective mixture permittivity, ε_2 is the permittivity of the rod, and ε_1 is the permittivity of the air.

The Series model agrees with the experimental setup, as the high permittivity rod located at the centre of the sensor is treated like an equivalent circuit where the background medium and phantom are in series composition [107] [184].

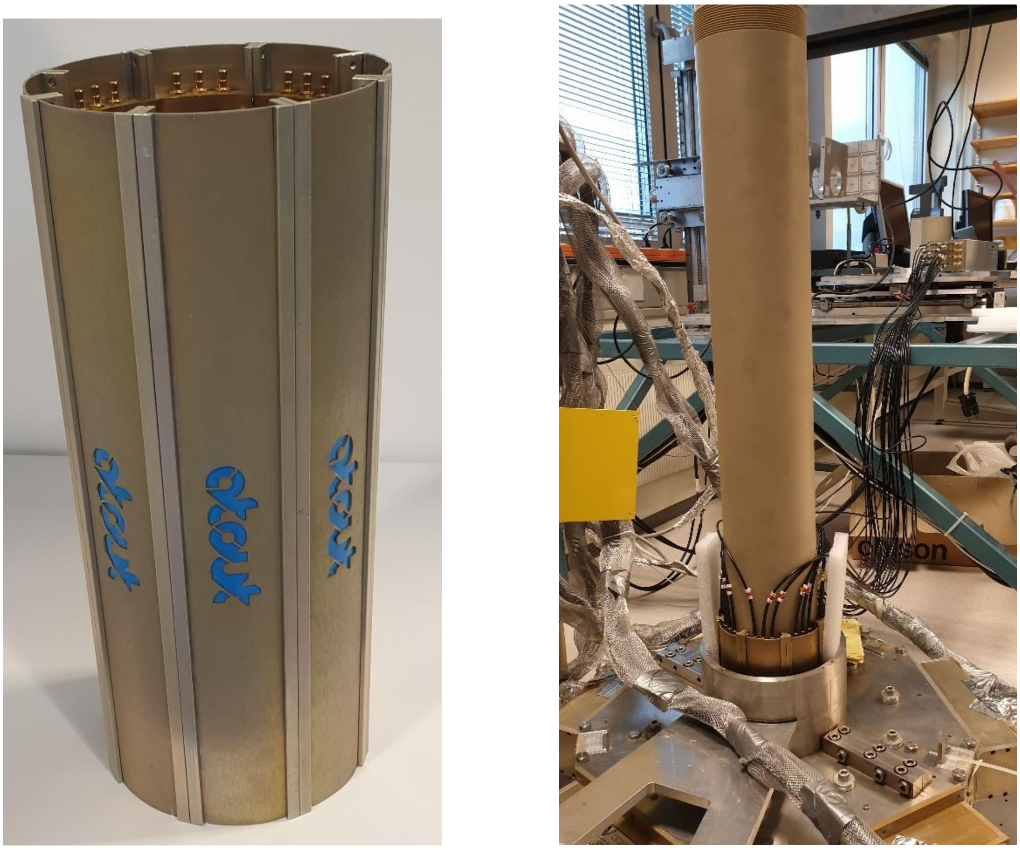

(a) (b)

Figure VI-6. Experimental setup showing (a) ATOUT APL-C-110 ECT sensor head details and (b) Connected assembly of the ECT clamped on a peek pipe at the Instrumentering Test-lab 432 of UiB

In Table VI-2 and Figure VI-7 the volume fractions estimated from the permittivity measurement (α_{ECT}), relative to the phantom cross-section, are compared to the reference ratios (α_{ref}) computed from the dimensions of the inclusions.

Table VI-2. Volume fractions of phantoms from measurements of ECT

Phantom	$\boldsymbol{\alpha_{ref}}$	$\boldsymbol{\alpha_{ECT}}$	**Accuracy**
1	0.772	0.793	97.5 %
2	0.840	0.826	98.5%
3	0.712	0.737	96.5%
4	0.533	0.499	96.5%

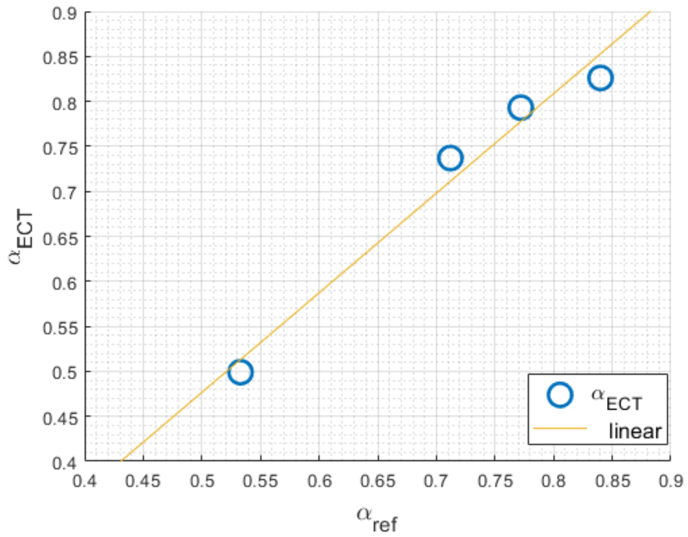

Figure VI-7. Volume fraction from ECT and reference values of phantom tests

From the results above, it is evident that the volumetric fractions from ECT are in agreement with the references values, with an overall mean accuracy of 96.4% and a maximum standard deviation of 2.4%. These values are within the generally agreed uncertainty range for production systems (±2-±5) [3].

6.3.2.3 Image resolution of phantom rods

Image reconstruction of ECT measurements was performed using LBP. Because the side-by-side measurements were found to remain unchanged between low and high permittivity calibration measurements, the ‘wsm8_32’ sensitivity map built-in the Flowan™ software was chosen. This sensitivity map ignores the side-by-side measurements, and considers a cross-section discretisation matrix of 32x32 pixels [107].

The image reconstruction method assumes that all pixels which have a non-zero sensitivity coefficient contribute equally to the measured change in capacitance between the electrode pairs. This results in that for each electrode pair measurement, each pixel which has a non-zero sensitivity coefficient is allocated an elemental value which is proportional to the measured change in the normalised capacitance between these electrodes. Then, the elemental values for the pixel for all of the electrode-pair capacitance measurements are added up to obtain the value of the pixel permittivity.

The reconstructed images for the phantom tests are shown in Figure VI-8. The images provide a gross character of the phantoms, particularly the ‘stratified’ case of phantom 4. However, a poor spatial resolution for the void geometries is evident, regardless of the high accuracy of the mean volume fractions reported in Table VI-2. The effects of the LBP image blurring discussed in Section 2.5.1.3B are clearly visible in Figure VI-8. It was not possible to improve these images through iterative techniques, due to the challenges imposed by the geometry setup, i.e. the thickness of the pipe used for the bench tests (10 mm), in addition to an extra 10 mm difference between the pipe ID and the rods OD; which decreases even more the already compromised orthogonal resolution of the ECT sensors in the central region. Further image resolution tests are presented in Section 6.3.3.3.

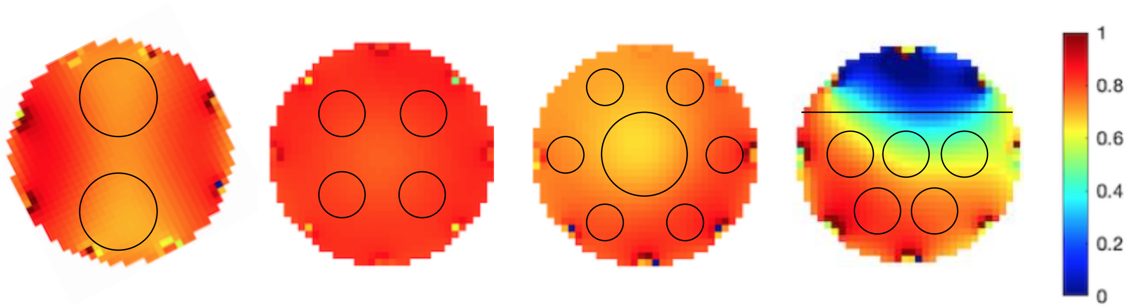

Figure VI-8. Image reconstruction from phantom tests showing the reference phantom patterns and a scale of the colour code for permittivity concentration from 0 to 1

6.3.2.4Dual plane measurements

A drop test was designed to evaluate the dynamic capabilities of ECT through cross-correlation of the dual-plane measurements. The tests comprise the comparison of ECT measurements to known quantities, i.e. cross-correlation velocity and cumulative transit volume. The test used a polypropylene phantom free falling through the vertically positioned pipe shown in Figure VI-6(b), for this, a solid cylinder of 56 mm diameter and 100 mm long was used.

The time difference of the features measured by the two measurement planes allows for cross-correlation of the object velocity. In ECT, the mean velocities are computed considering the transit time of the dynamic structures between the twin measurement planes. The velocity within the pipe cross-section at each point in time is calculated by correlating the instantaneous concentration of one plane with that in the other plane. It is noteworthy that the cross-correlation velocity is not necessarily the in-situ flow velocity. The scientific challenge at the moment is to understand that relationship. In order to represent physically appropriate areas of the pipe and perform a comprehensive analysis of the velocities, the measurements are grouped into zones containing a number of pixels. The time shift between the signals from both sensors corresponds to the time it takes the structures to travel the known distance that separate the sensors. The cross-correlation velocity function ($R_{xy,i}$) is expressed as

$$R_{xy,i}(\tau) = \lim_{T\to\infty} \frac{1}{T} \int_0^T C_{1,i}(t) C_{2,i}(t+\tau) dt \tag{70}$$

where $C_{1,i}(t)$ and $C_{2,i}(t)$ are the instantaneous concentrations in zone i in measurement planes 1 and 2, respectively. T is the averaging time.

The free-fall test was undertaken twice for validation purposes. Figure VI-9 shows the volume fraction of both drop tests over the period the phantom traversed both measurement planes.

The time difference between the peaks from the measurement planes was 20.9 ms and 19.7 ms for the first and second drop test, respectively. The theoretical time difference considering free fall from the top end of the pipe, located at 920 mm from the bottom measurement plane, was computed in 20.49 ms yielding a terminal velocity of 4.25 m/s. The cross-correlated ECT average velocities for the drop tests are 4.98 and 3.40 m/s, in agreement with the theoretical figure.

Using trapezoidal integration of the volume fraction curves allows for an estimation of the phantom total volume. The cumulative volume of polypropylene passing through the measurements planes was estimated by combining the total area below the curves in Figure VI-9 with *a-priori* knowledge of the pipe cross-section and the mean phantom velocities computed above. From the drop tests, the mean total phantom volume computed from the ECT measurements was 0.26 cm^3, which when compared to the actual measured volume (0.25 cm^3), results in a deviation of less than 5%.

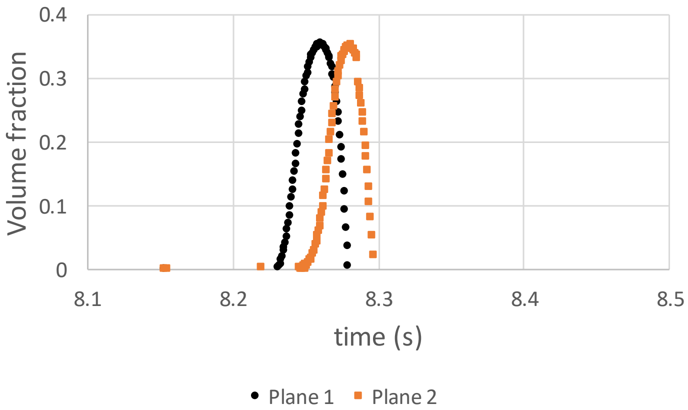

(a)

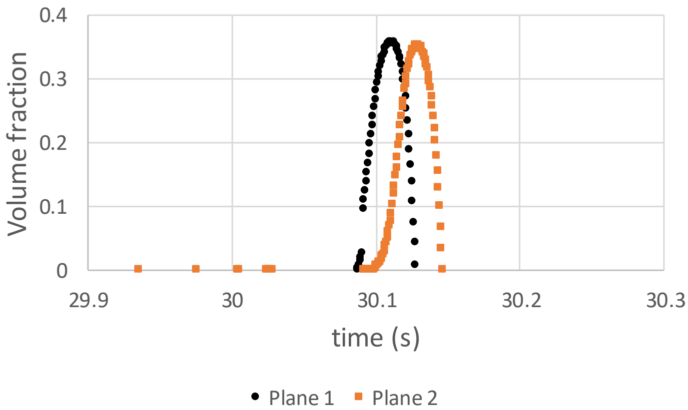

(b)

Figure VI-9. Measurements of ECT showing the phantom volume crossing the measurement planes 1 and 2 for the first and second drop tests shown in (a) and (b), respectively

6.3.3 Reference measurements

The present subsection correlates two-phase flow measurements from combined hard and soft tomographic metering technologies. The performance of ECT was contrasted to reference measurements of a Gamma-ray tomography (GRT) system. Gamma-ray based tomography is a well-established method for the determination of the gas fraction distribution in stratified gas-oil flows, and gas-solid flows [47] [48].

This study aims to assess the dynamic measurement capabilities of ECT for determination of volumetric fractions of oil-gas flow by comparison to a legacy GRT. It also explores the use of the multimodal approach for measurement of dynamic multiphase flow patterns which departs from previous experiences restricted to static structures [185].

The experiments were conducted by the NORCE team at their flow rig in Bergen, Norway as part of the MultiflowMett II project. The author undertook the tasks related to assembly and data collection of the ECT system. The GRT was simultaneously operated by the team from UiB. The data presented in Section 6.3.3.2 and Section 6.3.3.3 was processed in collaboration with S. Stavland from UiB. An extended analysis of the collected data is available in the work published in [18].

6.3.3.1Experimental facilities

A schematic of the NORCE flow loop is shown in Figure VI-10(a). The test facility comprises a recirculating three-phase pressurised flow loop with a gravimetric separator. In the tests, diesel fuel oil was recirculated around the test facility using centrifugal pumps. The laboratory reference liquid flow rate was measured downstream of the pump using a Coriolis flow meter. Nitrogen was supplied into the experimental section through a standard tee connection. The gas flow rate was also measured using Coriolis flowmeters. A horizontal experimental section of 3” SCH160 was used. The loop was operated at nominal 30 Sm^3/h and 30 m^3/h of gas and liquid, respectively, which resulted in mean superficial velocities of 1.83 m/s and a mixture velocity of 3.66 m/s.

The diagram of the test section in Figure VI-10 (a) illustrates the relative positions of the GRT unit and the ECT sensors. The metering devices were located in the same horizontal section with the ECT sensor placed 1.2 m downstream the GRT measuring plane, as shown in Figure VI-10(b).

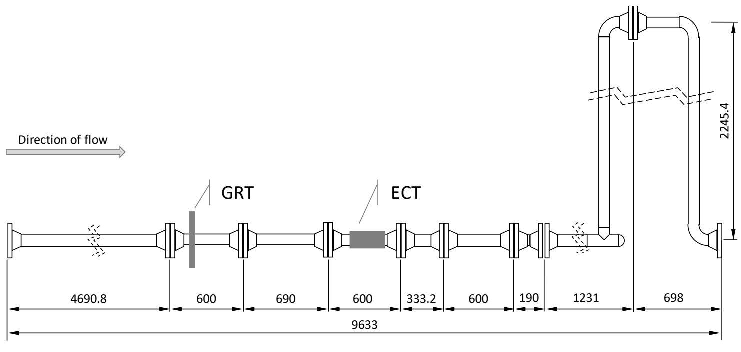

(a)

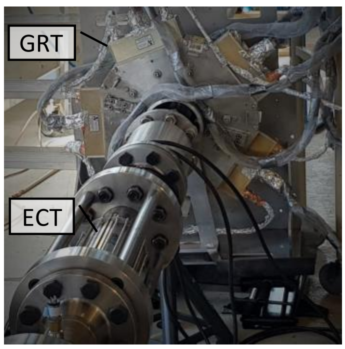

(b)

Figure VI-10. Relative position of the instruments in (a) schematic diagram of the test section at NORCE and (b) photographic record
(a)Modified from: Test Protocol for Multiphase Intercomparison Roxar 2600 ID67mm Transfer Package, p5

The ECT sensor head used for this test was the APL-C-900-104 model provided by ATOUT Ltd [59]. The sensors in Figure VI-10(b) were installed on a Perspex pipe of 100 mm OD, on the horizontal test section of the rig, as illustrated in Figure VI-6(b). The sensor head of 16 electrodes and two measurement planes is very similar to the one described in Section 6.3.2.1 but of a smaller diameter. All unique capacitance pairs were measured yielding a full set of measurements. The calibration of the ECT meter used single-phase flow of diesel oil and gas in the pipe for reference measurements. The excitation signal was a 24 V peak to peak square wave at 2.5 MHz.

The GRT was designed and prototyped at the Department of Physics and Technology, UiB, Norway. The design is based on five gamma-ray sources symmetrically mounted around the pipe. The five radiation sources and the five detector arrays, each consisting of 17 detectors, are mounted on the opposite side of the pipe. GRT measurement is based on measuring the attenuation of the radiation through the media. In the gamma-ray energy range, the linear attenuation is approximately proportional to the density of the matter for monochromatic radiation. More details of the GRT design and assembly can be found in [186] and [50].

6.3.3.2Concentration from permittivity vs concentration from weight

The oil volumetric fractions from ECT were calculated from the permittivity measurements using the extended Maxwell-Wagner-Sillars model described in [64] as in (71)

$$\varepsilon_m = \varepsilon_c[1 + n\alpha(\varepsilon_i - \varepsilon_c)/(\varepsilon_i + (n-1)\varepsilon_c - \alpha(\varepsilon_i - \varepsilon_c)] \quad (71)$$

where the ε_m is the effective mixture permittivity, ε_c is the permittivity of the continuous material, ε_i is the permittivity of the inclusions, α is the volumetric fraction occupied by the inclusions, and the coefficient n is a function of the eccentricity of the inclusions, taking a value of 3 for spheres [186] and greater than 3 for prolate spheroids [64].

For two-phase mixtures, GRT component fractions are computed by normalizing the measured intensity to that of the calibrated measured intensity of the single components, as shown in (72).

$$\alpha_1 = \ln\frac{I_2}{I_m}\Big/\ln\frac{I_2}{I_1} \quad (72)$$

where I_1 and I_2 are the measured intensities for the single components, α_1 is the volume fraction of the first component and I_m the measured intensity of the mixture.

The oil volumetric fractions from ECT and the mean measurement of the fractions measured through the five GRT views are presented in Figure VI-11. The correlation between the measurements is readily evident. The pattern is identifiable as intermittent structures. Some differences are obvious, i.e. the length and shape of structures, which reflects the evolution of the dynamic structures over the distance separating the metering systems. Differences in the time delay between the metering systems are also observable and is a result of varying flow velocity. However, the overall difference between the mean measurements of ECT and those from GRT is 3.4%. The accuracy of the measurements, which is well within the agreed uncertainty range [3] regardless of the setup-induced differences, demonstrates the capabilities of ECT for accurate determination of the volumetric fraction distribution for non-conductive species.

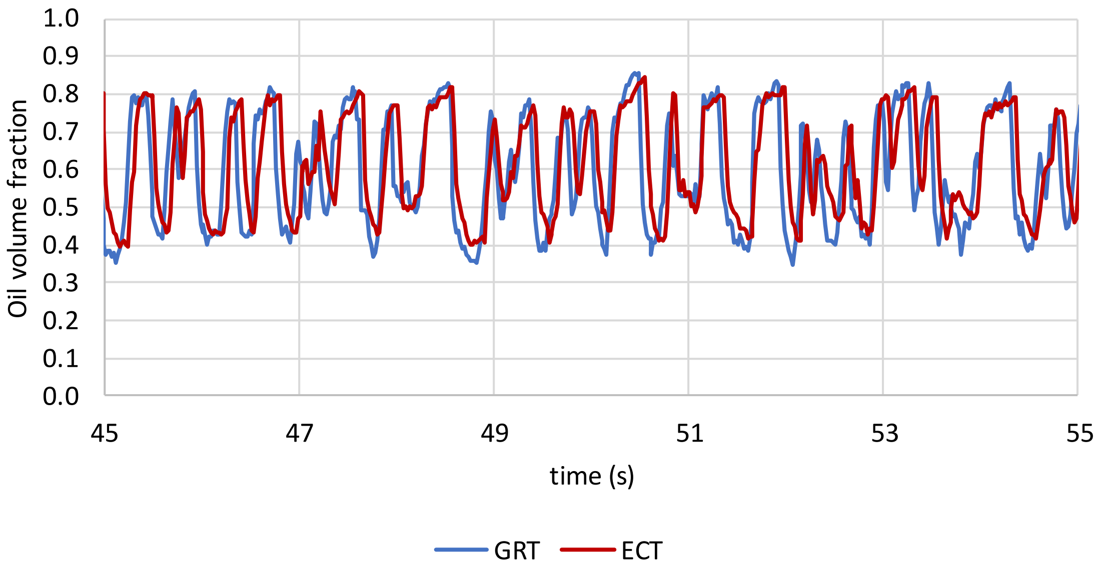

Figure VI-11. Oil volume fractions measured from the GRT compared to the relative permittivity measured with ECT

Further computation of the mean volumetric flowrates of these intermittent flow structures can be computed by combining the measured volume fractions and cross-correlating the velocity of the flow structures as discussed in Section 6.3.2.4. As reported in [18] ECT and GRT measurements can be combined following (73), and then used to estimate the gas and liquid flow rates across the pipe cross section.

$$Q_i = \sum_{k=1}^{K} Q_{ik} = \sum_{k=1}^{K} \alpha_{ik} v_{ik} A_k \tag{73}$$

where Q_i is i[th] component volume flow rate, α_{ik} and v_{ik} are the i[th] component fraction and velocity in the k[th] zone, respectively and A_k is the area of the kth zone. The component fractions are estimated from the GRT measurements and the velocities from the transit time between the ECT measurement planes.

In order to perform a comprehensive analysis of the measured velocities, in [18] the measurement were grouped into zones. The flow rate of the i[th] component within each zone is a linear combination of the zonal velocity, the component fraction, and the area. Therefore, the relative uncertainty contribution to the zonal flow rate from each variable is the same as the relative uncertainty of the variable. A full quantification of the uncertainty is beyond the scope of this work. However, it is relevant to understand the uncertainty contribution from the individual measurements. When combining the uncertainties from individual zones it is probable that some of these are correlated. Neglecting the area uncertainties, the combined uncertainties can be expressed as in (74) [18] [187].

$$\sigma_{Q_i}{}^2 = \sum_{k=1}^{N}\sum_{m=1}^{N} A_k A_m \Big(\alpha_{ik}\alpha_{im}\sigma_{v_{ik}}\sigma_{v_{im}} r(v_{ik}, v_{im}) + v_{ik} v_{im}\sigma_{\alpha_{ik}}\sigma_{\alpha_{im}} r(\alpha_{ik}, \alpha_{im}) + \alpha_{ik} v_{im}\sigma_{v_{ik}}\sigma_{\alpha_{im}} r(v_{ik}, \alpha_{im})\Big) \quad (74)$$

where r are the correlation factors between the measurements from different zones 'm' and 'k'.

This type of computations is, however, strongly influenced by the dynamicity of the flow regimes. Temporal steady-state flow, e.g. smooth stratified flow, can significantly limit the accuracy of the flowrate measurement due to the induced errors derived from the intrinsic dependency of the cross-correlation method to dynamic temporal structures.

6.3.3.3Image reconstruction of dynamic structures

The reconstructed images from ECT in Figure VI-12 (a) are consistent with those from the GRT in Figure VI-12 (b). In both sets of images, the variable flow with gas plugs at the top of the pipe are identifiable and consistent with the time structures observed in Figure VI-11. These results serve to validate the capabilities of the built-in ECT image reconstruction algorithm (see Section 2.5.1.3B) for dynamic flow structures.

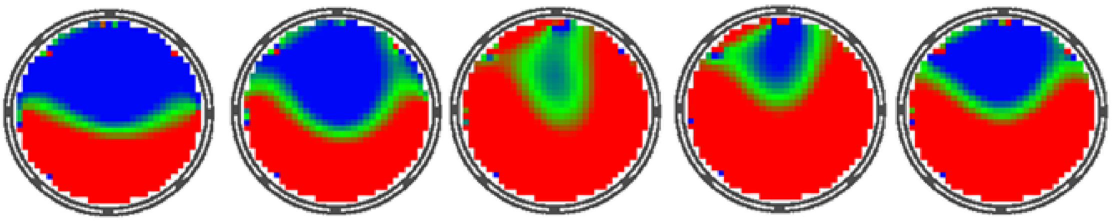

(a)

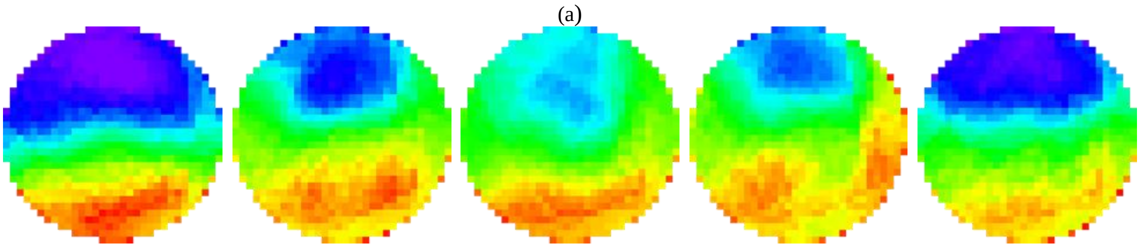

(b)

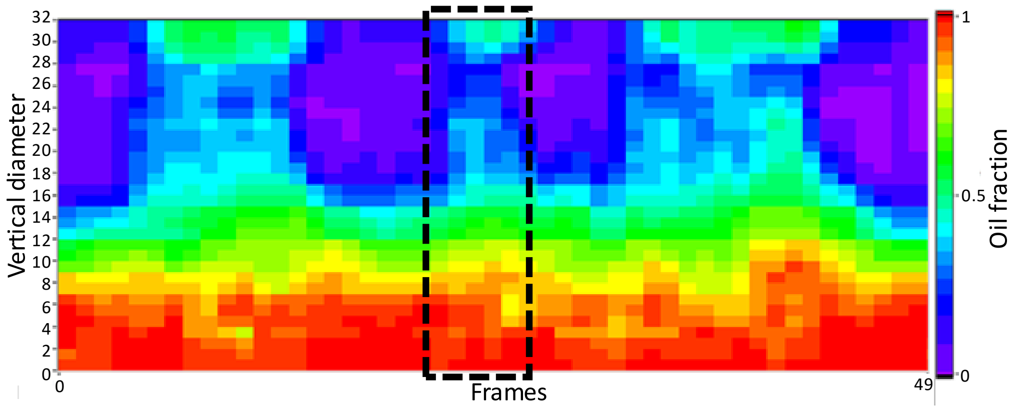

(c)

Figure VI-12. Reconstructed images of flow structures from (a) cross-section permittivity measurements through ECT and; (b) cross-section oil distribution from GRT measurements, and (c) transient GRT oil fraction with highlighted section corresponding to the ECT and GRT reconstruction sequences above

6.4 Instrument capability and operational envelope

A combination of dielectric and electromagnetic measurements are assessed here in order to determine the capabilities and operational limits of the ECT and MIT meter. The capabilities of ECT for measurement of non-conductive materials in static and dynamic conditions were established in Sections 6.3.2.2, 6.3.2.4, and 6.3.3.2. The correlation between eddy-current measurements and single-phase water mixtures of various conductivities was demonstrated in Section 6.3.1.3. In order to explore the capabilities of the MIT and ECT instruments for MFM, an experimental plan was designed, where the capacitance measurements from ECT and phase measurements from MIT are combined for various oil-water mixtures. The instruments infer the fluid concentrations based on measurements of the electric or dielectric properties of the fluids flowing through the pipes.

6.4.1 *Experimental facilities*

The experiments were conducted at the iPhase multiphase flow loop in Basingstoke, UK. The experimental campaign was designed by iPhase ltd. The author was invited to collaborate in the operation of the flow loop and to undertake the MIT measurements. The ECT equipment was simultaneously operated by a Coventry University colleague, L. Tom. The data were analysed by the author.

The experimental loop, illustrated in Figure VI-13, comprises a recirculation rig that uses gravimetric separation of the fluids in continuous operation. The liquid flows are recirculated around the test facility using centrifugal pumps. The injection rates are controlled by an automated circuit led by turbine flow meters located at the separation vessel outlet. The three-phase gravity separator, with a capacity to segregate the water and oil phases, also serves as a liquid storage tank. The horizontal experimental segment comprised a clear acrylic section of 100 mm inner diameter and 3 m (30D) long that allows visualisation of the flow prior to metering. Experiments were conducted under controlled laboratory conditions at a temperature of 20°C. The working liquids used in the loop were Ultramax10 oil and saline water. The experimental matrix and flow conditions are summarised in Table VI-3.

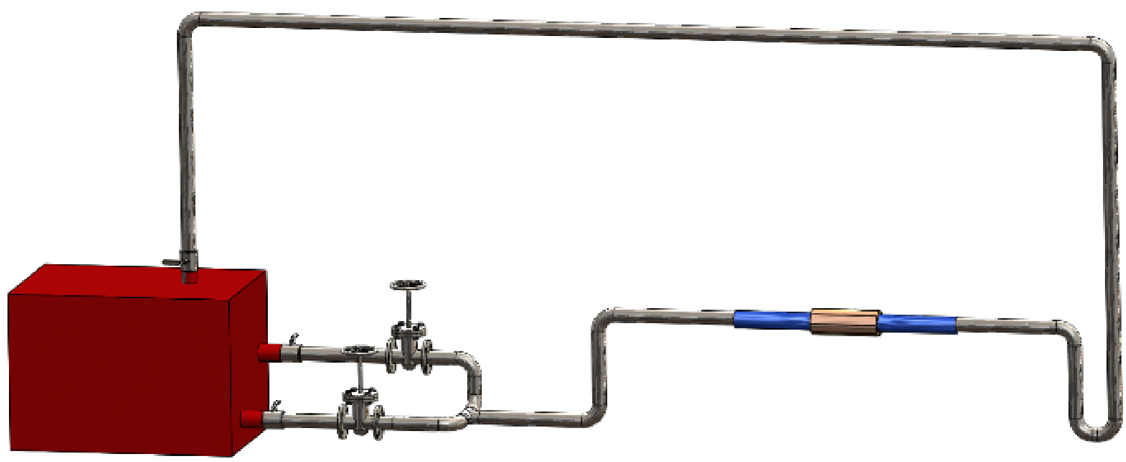

Figure VI-13 iPhase flow rig diagram showing the metering system on the horizontal test section

Table VI-3. Experimental setup for liquid-liquid flow measurement

Water cut	(%)	{0,25,30,35,40,45,50,55,60,65,70,75,100}
Pressure	(psi)	3
Temperature	°C	20
U_{os}	(m.s^{-1})	0.11 – 0.32
U_{ws}	(m.s^{-1})	0.11 – 0.32
Oil type		Exol Ultramax10
Oil density (kg.m^{-3})	(kg.m^{-3})	851
Oil relative permittivity		2.156 – 2.224
Water conductivity	(S.m^{-1})	1.05

The volumetric flowrates and density of the single-phase oil and water are measured using turbine meters and a differential pressure transmitter as reference measurements. The turbine meters, differential pressure transmitter, as well as the control valves are calibrated at UKAS accredited laboratories and traceable to various national and international recognised standards. The uncertainties of the turbine meter and differential pressure transmitter at full scale are $\pm 0.5\%$ at 95% confidence level, $\pm 0.1\%$ at 95% confidence level.

6.4.2 Instrument assembly

The tests accounted for the metering of electric and dielectric properties using three meters, i.e. an 8-sensor ECT (ECT-8), a 2-sensor ECT (ECT-2) and a 2-sensor MIT, as illustrated in Figure VI-14. The sensors of ECT-8 and ECT-2 are identical and measure the flow-induced capacitance changes through independent data acquisition systems. The sensor head used for these sets of tests comprised 16 electrodes of 15.2 cm long arranged in two measurement planes and were designed following the same principles from Atout's system [59]. The full set of measurements from ECT-8 account for the measurement of all unique capacitance pairs. These measurements were simultaneously taken between all pairs of electrodes and two measuring planes. The data acquisition system used is the same capacitance measurement unit (CMU) provided by Atout, Ltd for the tests in the previous sections. Secluded single sensor-pair data was collected for every test point by ECT-2 and MIT using iPhase data acquisition system.

For both ECT instruments, the excitation signal used consisted of 24 $V_{p\text{-}p}$ square wave at a frequency of 2.5 MHz. The calibration of the ECT meters used oil and air as reference fluids. When water is present, the value of the average mixture permittivity may exceed the calibration range, in which case simple extrapolation is used.

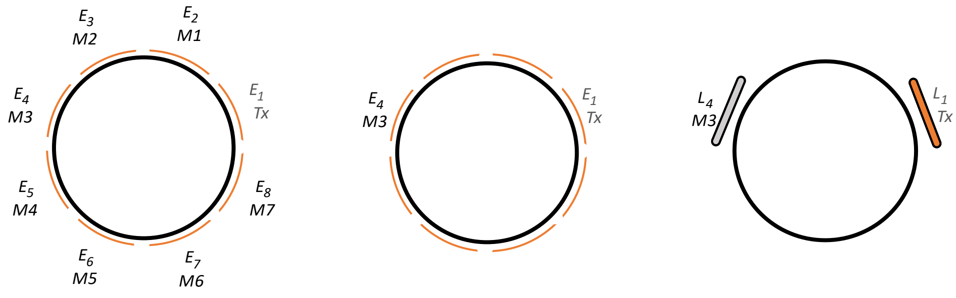

Figure VI-14 Diagram representation of the sensors used for data acquisition showing (a) the 8-sensor ECT, denominated ECT-8, with all electrodes E_1 to E_8 enabled, (b) the 2-sensor ECT or ECT-2 with only electrodes E_1 and E_4 enabled, and (c) the 2-sensor MIT with the coils L_1 and L_4 enabled

The electromagnetic meter consists of a dual-sensor device that detects field perturbations caused by eddy currents in the conductive medium. The experimental assembly is equivalent to a dual-coil MIT system [102]. The principle of operation of the MIT allows for a correlation of the measured signals with the water content, which is key for validation and interpretation of the electric capacitance measurements at high water contents.

The MIT sensors were located downstream of the ECT-2 instrument, sharing the same relative positions. The sensors were located at the top section of the pipe, with Rx at 135 deg from the Tx, (see measurement position M3 in Figure VI-14). In the MIT, the transmitting coil (L1) was excited through a 0.5 A current at 10 MHz. All three instruments were placed in the horizontal test section of the flow rig.

6.4.3 MIT measurements

Single-phase measurements are shown in Figure VI-15. The induced eddy currents arising from changes in the bulk conductivity of the medium are shown by the angle (θ) measurements for the oil and water flows plotted. Results in Figure VI-15 show two different signal levels for a pipe full of oil and full of water, respectively, showing the sensibility of the system to changes in the bulk conductivity of the medium.

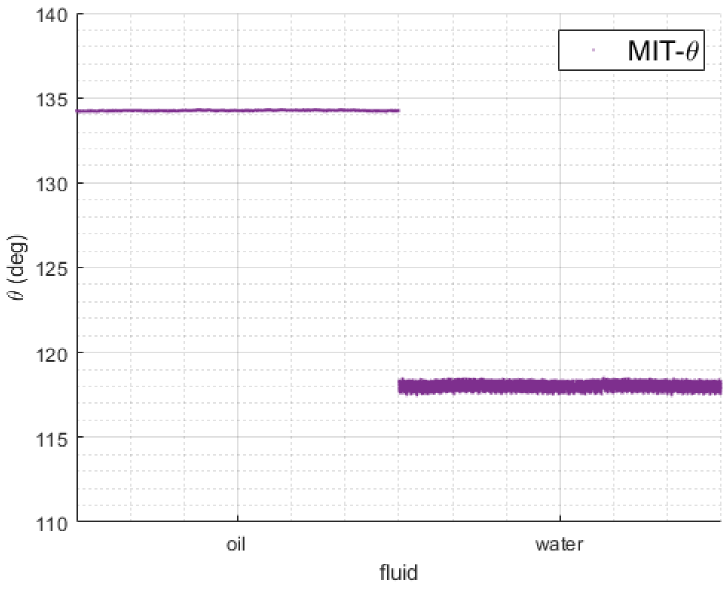

Figure VI-15. Measurements from a dual-sensor MIT instrument for single phase horizontal flows

The angle measurements from the multiphase flow are plotted in Figure VI-16. The variation of the signal for water cuts below 40% is significantly higher than for higher water cuts. This variation is not noise but a reflection of the flow conditions. A point of inflexion when the water cut reaches 40% is observed. At this point, the declining trajectory of the phase trend with increasing water cut changes, evidencing from that point onwards a linear phase increase with increasing water content, as expected from Figure VI-4.

The inflexion in the phase measurement is consistent with the simulation results in Figure VI-17(a) and is a result of the position of the selected sensor pair with regards to the fluid interface. Extended simulation results considering different sensor pairs show that the position of the sensors to that of the interface has a significant effect on the linearity of phase measurements (see Figure VI-18).

It is evident, however, that in the experimental measurements, the inflexion takes place at lower water concentrations than simulated. This is attributed to the differences in the flow structures seen in the experiments and those simulated. That is, the simulation model accounts for stratified materials with a sharp oil-water interface, whereas the flow pattern arising in the actual experiments is more complex, including bubbly and wavy stratified flow [31].

The accuracy of the phase measurements for water cuts above 40% is ±2.5%. Further accuracy computation for lower water cuts requires collection of data different from pairs of sensors as evidenced in the simulation results.

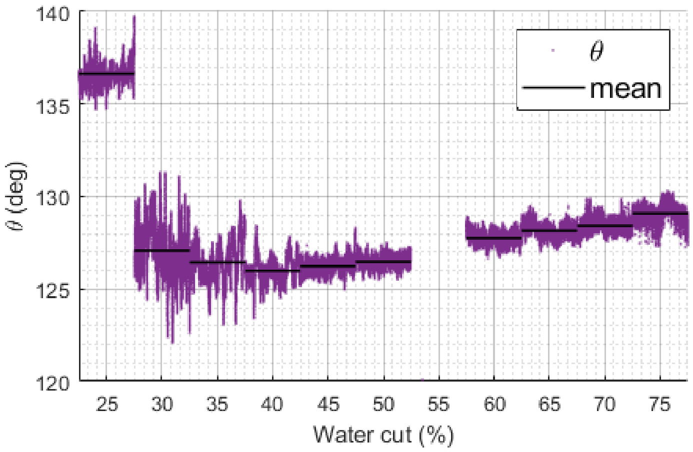

Figure VI-16. Variation of oil-water concentrations in a horizontal pipe showing the phase induced measurements from a dual electromagnetic metering system (MIT)

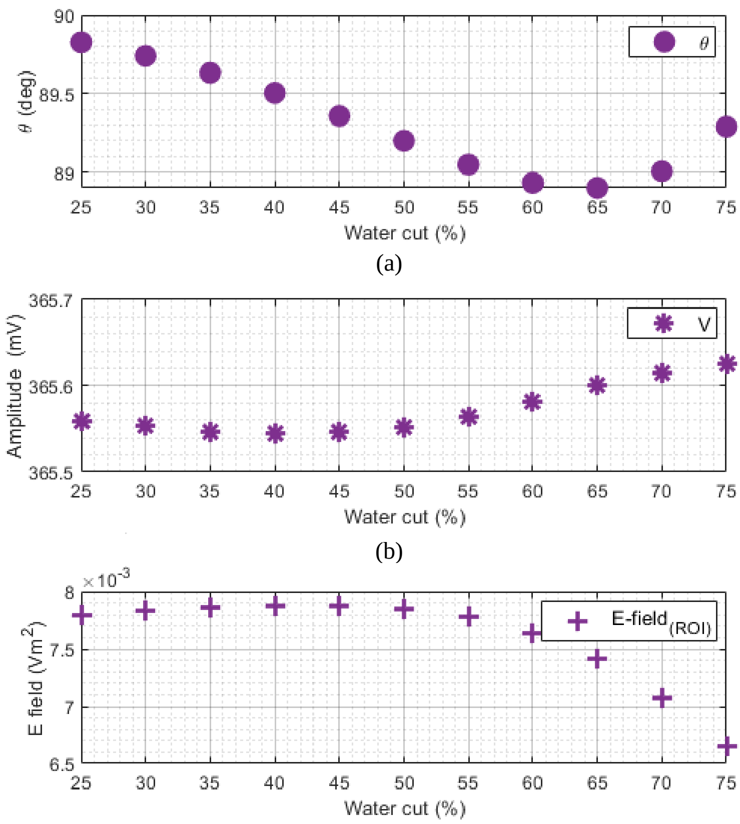

(c)

Figure VI-17. Variation of oil-water concentrations in a horizontal pipe showing simulation results of (a) phase angle; (b) signal amplitude and; (c) electric field in the imaging region from static stratified oil-water model

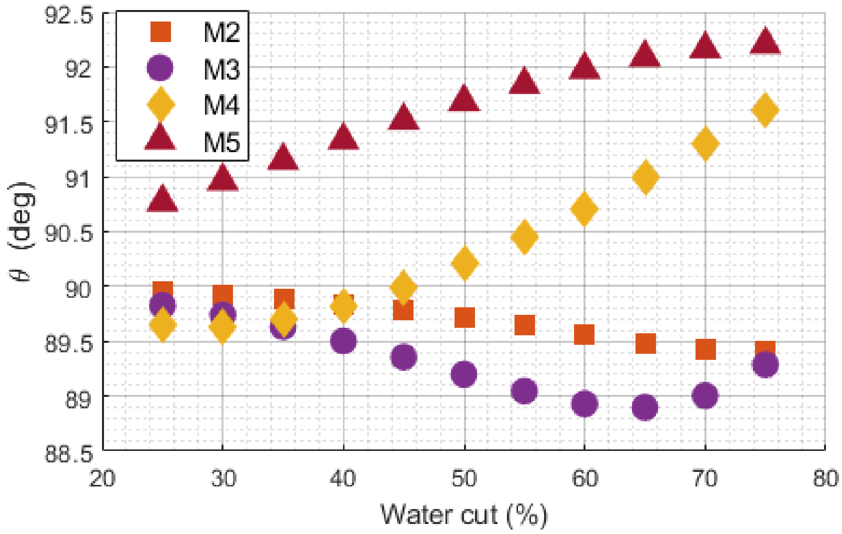

Figure VI-18. Extended simulation results showing the phase angle of horizontal stratified fluids measured from receiving coils at positions M2, M3, M4 and M5

6.4.4 *ECT operational envelope*

The relative permittivity of single-phase horizontal flows and low water contents is plotted in Figure VI-19. The mean permittivity, computed by averaging 30,000 data points, is also plotted along with the complete set of measurements. The results show two different levels of relative permittivity for single-phase flows, namely air and oil. The measurements of both single phases are slightly higher than the reference values in Table VI-3 due to traces of water at the bottom of the horizontal test section, which could not be removed prior to the start of the tests.

During the experiments, as the water content was increased in the oil-water mixture, from 25% to 35%, the measured relative permittivity also increased (see Figure VI-19). As expected, when water flows through the sensor, the capacitance measurements are larger than for the single-phase flows, due to the increased relative permittivity of water.

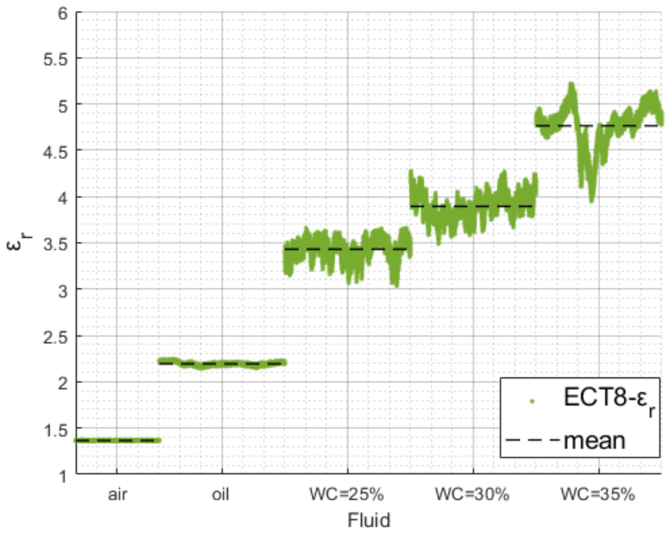

Figure VI-19. Measurement of mean relative permittivity in the pipe for two single-phase flows (air-low permittivity and oil-high permittivity) and multiphase flow with low water cuts (25% to 35%)

Figure VI-20 contrasts the inter-electrode capacitance measured between the electrode pair E_1-E_4 (M3 in Figure VI-14) with the ECT-8 and the ECT-2. For both systems, the capacitance measurements show a broader dynamic for low water content. The results of both instruments are consistent for low water cuts. However, for water contents above 45%, the trend of ECT-8 and ECT-2 are different and the full 8-sensor ECT fails to accurately predict the relative permittivity when the conductive phase inundates the pipe cross-section. This is in agreement with published literature that restricts the use of ECT to mixtures with low water cuts [59].

Comparing the measurements of the ECT-8 and ECT-2 systems, it is readily evident that the ECT-2 measurements show a larger data dispersion, which affects the measurement repeatability. However, the single pair capacitance meter (ECT-2) shows an overall quasilinear trend of the capacitance measurement with increasing water cut. This linearity suggests that by secluding individual electrode pairs, the inherent signal compensation that occurs during the solution of the Inverse Problem of the full ECT is avoided. These results create opportunities to expand the envelope of the operation of ECT systems with and overcome inversion in the coupling mechanism of the electrodes as the conductive phase becomes more dominant in the liquid-liquid mixtures.

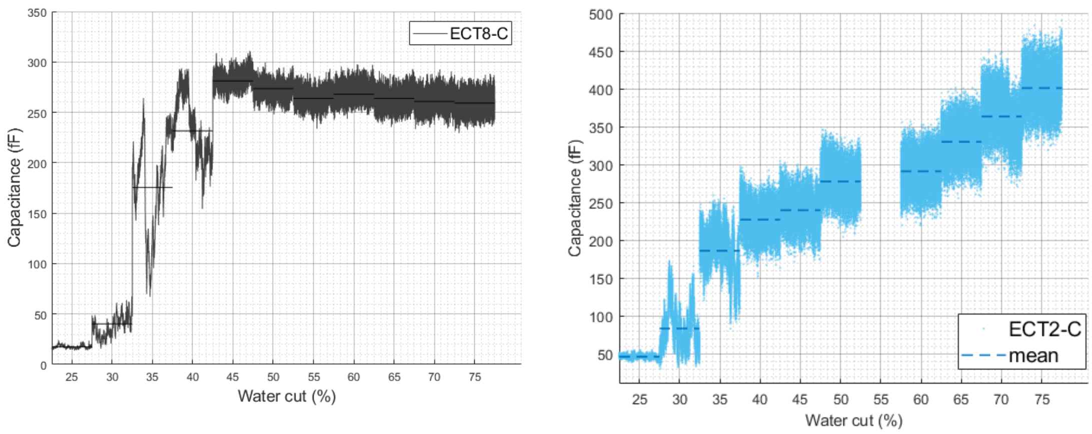

(a) (b)

Figure VI-20. Capacitance measurements from electrode pair at position M3 for various multiphase mixtures from (a) full 8-sensor ECT instrument (ECT-8) and b) single electrode-pair ECT (ECT-2)

6.4.5 ECT vs MIT

Figure VI-21 contrasts the experimental results from the single-pair ECT meter (ECT-2) and the MIT meter. The primary and secondary vertical axes show the phase measurements from the electromagnetic sensors and the capacitance from the ECT, respectively. For water concentrations above 40%, both metering systems follow the same trend of increasing phase and capacitance with increasing water cut, i.e. increasing mixture conductivity and permittivity. From the simulation results in Figure VI-18 and previous bench tests (see Figure VI-4) it is evident that selecting a different MIT sensor-pair, would result in a linear trend and hence a better match with the capacitance measurement below 40% water cut.

As expected, the MIT shows enhanced signal-to-noise ratios for high water cuts, i.e. more intense eddy-currents, whereas the capacitance measurements from the dual ECT shows improved performance for low water contents.

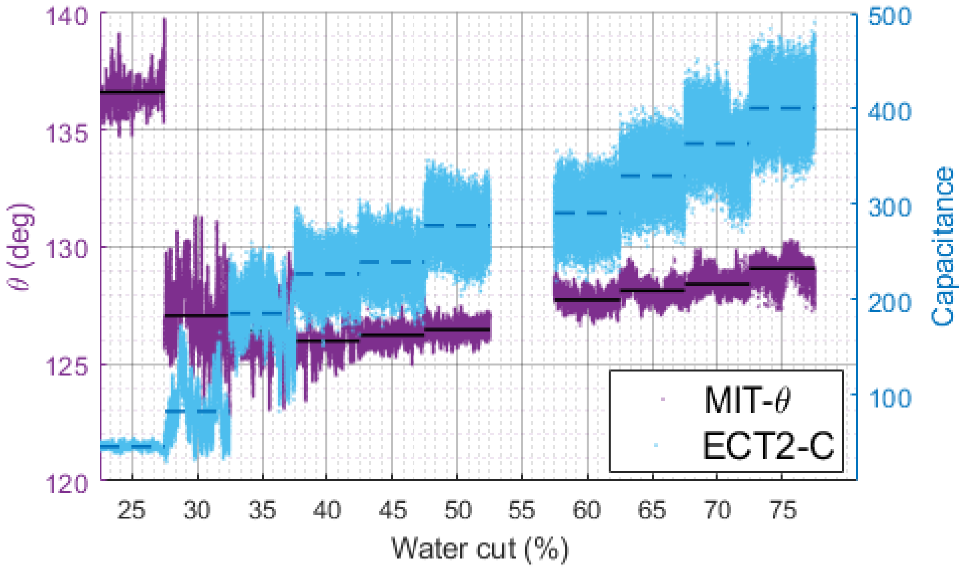

Figure VI-21. Measurement from the induced signal phase from the MIT, and measured capacitance from the single electrode-pair ECT (ECT2) for various oil-water mixtures

6.5 Discussion and Conclusions

A measurement calibration chain was performed. The MIT and ECT accuracy and operational capabilities were assessed from bench tests and flow tests. Comparisons were presented between the test measurements and standard quantities as well as reference measurements from legacy instruments.

Bench test measurements from the MIT prototype showed consistency, repeatability, and linearity with changes in the conductivity of the medium. In multiphase stratified flow, however, this linearity was shown to be highly affected by the relative position of the sensors to that of the interface as demonstrated by cross-correlating experimental measurements and simulated results. MIT sensors showed a repeatability of 4% for static bulk conductivities ranging from 1 S/m to 5 S/m. Limited experiments performed with a single pair of sensors showed measurement accuracy of ±2.5% for water cuts above 40% in stratified two-phase oil-water flows. Accuracy estimation for other flow patterns requires further experimentation with data collection from a number of pairs of electrodes, which was not available at the time at which the tests were conducted.

ECT proved highly accurate in permittivity measurement and inter-plane velocity computation for non-conducive materials. It also exhibited good image reconstruction and volumetric fraction derivation for intermittent oil-gas flows.

A key outcome of this work results from the secluded electrode-pairs measurement, which challenges the generally accepted theory that ECT is restricted to low-water contents. This provides opportunities to broaden the operational envelope of this technology, provided that the signal-to-noise ratio for high water cuts is improved.

Further comparison between electrical capacitance measurements and electromagnetic measurements showed that ECT provides enhanced performance for water contents below 35%, whereas MIT provided good linearity for water contents above 40%. This brings opportunities for the use of multimodal metering systems based on the combination of ECT and MIT for multiphase flow measurement over a wide range of operating conditions than they would under stand-alone configurations. Combining ECT and MIT, based on the operational envelopes assessed, is technically feasible and would be beneficial for multiphase mixtures of conductive and non-conductive fluids of different relative permittivities, i.e. gas-water or oil-water flow. This approach would benefit from the ECT capabilities (±4% uncertainty) to measure relative permittivity for close-to-non-conductive mixtures, i.e. low water cuts, and MIT accuracy (±2.5%) for conductivity measurements when electrically conducting water is the dominant phase.

At this stage, the multiphase flow meter designed has been calibrated and assessed through various laboratory tests. The remaining of the thesis focuses on exploiting the measurement capabilities of the instruments for multiphase flow characteristics readily found in the industry.

Chapter VII Three-phase detection

7.1 Introduction

It is well known in the ‘art’ to use two separate systems to measure the various fluids in multiphase flow regimes, with the two separate systems usually operating at two different frequencies. The previous chapter explored the combined use of ECT and GRT and proved the feasibility of combining ECT and MIT to measure the concentrations of one conductive and one non-conductive fluid for a broad concentration range. This multimodal technique, however, suffers from the problem of both temporal and spatial lags between two sets of measurements, as made evident in Section 6.3.3.2. There is a need in the measurement art for an improved monitoring method that challenges the existing multiphase data processing approach and extends the use of MIT systems beyond the measurement of solely electric properties.

Traditionally, applications for MIT account for the imaging of low conductivity contracts of two-phase mixtures, one of which is conductive and the other one non-conductive [11] [12] [66]. These experiences are based on either analytical or numerical solutions [132] [188] [189], static experimental verification [7] [11] [12] [65] [66] [67] [68] [69] [71] [88] [190], or quasi-static experimental verification [8]. In the present chapter, the former approach is used to evaluate the feasibility of broadening the niche of MIT systems for the measurement of multiphase flows containing more than one non-conductive phase. This is achieved by assessing the signal response of a dual MIT system to changes in the dielectric and electric properties of the medium via the numerical solution of the electromagnetic Forward Problem. Results from simulations are used here to identify the response of the measured signal to changes in both the conductivity and the relative permittivity properties of the medium that could potentially lead to enhanced three-phase measurement capabilities.

The approach proposed here departs from that used in existing electromagnetic meters, which measure conductivity contrasts solely. Most MIT applications for low conductivity measurements have focused on the conduction currents induced in the imaging region, neglecting the displacements currents. Displacement currents account for the effect of permittivity, which, in hand with conduction currents, give rise to the measured secondary field. However, for cases where $\varepsilon\omega/\sigma \ll 1$ (ε is the permittivity, σ is the conductivity and ω is the angular frequency), the displacements currents are traditionally neglected. This approach is referred to as the eddy-current approximation.

In multiphase flow, the mean permittivity and conductivity of the flow vary in both the temporal and the spatial domain. Both the displacement and eddy currents contribute to the induced magnetic field that results in the change of the measured signal. Therefore, the effect of the displacement currents should not be ignored. Only a few studies have addressed the effect of permittivity in electromagnetic measurements, all of which are limited to the biomedical field [11] [188] [190] [191] [192] [193]. Previous work demonstrated the feasibility of deriving the permittivity from electromagnetic measurements using inclusions of skin depth much larger than the sample dimensions [88]. In these studies, the components of the signal are de-multiplexed, and the effect of the properties are evaluated separately for the imaginary and real components. It was reported that when the skin depth of the sample is comparable with the thickness of the inclusions, the measured signals departed widely from the theory. This results in the need for a more detailed analysis of the effect of the permittivity on the induced signal.

The present study aims, at least partially, to meet the need in the art, particularly in the field of oil and gas exploration and production, to provide enhanced analytical data in real-time on the phase composition of the multiphase flow. This chapter addresses the measurement of non-conductive contrast solely through MIT. In this regard, Section 7.2 sets the basis of the study by discussing the electromagnetic premises considered in this work. Section 7.3 assesses the feasibility of using a single magnetic induction tomography system to measure both the phase shift and amplitudes of the complex voltages and by doing so, measure the phase fraction of conductive and non-conductive fluids in a multiphase flow. The main aim is to prove that by combining the phase and amplitude measurements, it is possible to account for electric and dielectric changes in pipelines arising from the flow of water, hydrocarbon, and sand. Subsequently, in Section 7.4, a thorough evaluation of the electromagnetic signals induced by various fluids and phase fraction distributions is presented. The electromagnetic signal response to changes in the electric and dielectric properties of the medium is evaluated using the numerical model detailed in Table C-1 of Appendix C.

The results from the solution of the Forward Problem presented in this chapter are published in [19].

7.2 Electromagnetic considerations

The governing equations of MIT within the imaging region are given by the set of Maxwell's equations. The simplified eddy-current problem, which has been broadly used in low-conductivity imaging, is a quasi-static approximation of the full electromagnetic problem. This approximation is considered valid for small inclusion dimensions and high conductivities ($\varepsilon\omega/\sigma \ll 1$). However, more information can be retrieved from MIT measurements, which account for the effect that characteristic hydrocarbon mixtures have on the MIT signal. This requires the solution of an accurate relationship between the dielectric properties and the measured signals by avoiding the intrinsic inaccuracies of the eddy-current approximation [194] [195] via retaining the displacement currents term as in equations (78) and (79). Considering the effect of the current source, Equation (7) is rewritten as

$$\vec{J} = \sigma\vec{E} + \vec{J_s} \tag{75}$$

Recalling from Equation (6) Ampere-Maxwell's law can be expressed as

$$\nabla \times \vec{H} = \vec{J} + j\omega\vec{D} \tag{76}$$

Substituting $\vec{J}$ in (76) yields

$$\vec{E} = \frac{\nabla \times \vec{H}}{\sigma + j\omega\varepsilon} \tag{77}$$

Combining Faraday's law of induction and the magnetic field constitutive relation in (6), yields

$$\nabla \times \left[(\sigma + j\omega\varepsilon_0\varepsilon_r)^{-1}\left(\nabla \times \left(\mu^{-1}\vec{B}\right)\right)\right] = -j\omega\vec{B} \tag{78}$$

$$\nabla \cdot \vec{B} = 0 \tag{79}$$

where the properties of the materials are defined by the electrical conductivity (σ), the magnetic permeability (μ) the permittivity (ε), with $\vec{B}$ being the magnetic field distribution, and ω is the angular frequency of the applied magnetic field.

The measured MIT signal combines information from the conduction and the displacement currents within the imaging region. For lossless coils, the background voltage (v_0) measured by the receiving coil, in the absence of an inclusion, lags 90 deg from the driving current (i_s). When an inhomogeneity is placed between the sensors, the measured signals change to (v_1) (see (80) to (82)) as illustrated in Figure VII-1.

$$i_s(t) = I_0 \cos(\omega t) \tag{80}$$

$$v_0 = A_0 \cos(\omega t + \theta) \tag{81}$$

$$v_1 = A_1 \cos(\omega t + (\theta - \Delta\theta) \tag{82}$$

where I_0 is the excitation current, A is the amplitude of the measured voltage, and θ is the phase shift of the induced signal with respect to the excitation current.

In phasor representation, we have:

$$V_0 = A_0 e^{j\theta} = V_{0,Re} + jV_{0,Im} \tag{83}$$

$$\therefore \theta = 90° \Rightarrow V_0 = jV_{0,Im} \tag{84}$$

$$V_1 = A_1 e^{j(\theta - \Delta\theta)} = V_{1,Re} + jV_{1,Im} \tag{85}$$

where V is the induced voltage, the subscripts Re and Im are the real and imaginary components of the induced voltage, respectively. Subscript 0 refers to measurements from the background signal and 1 to measurements with an inclusion in place.

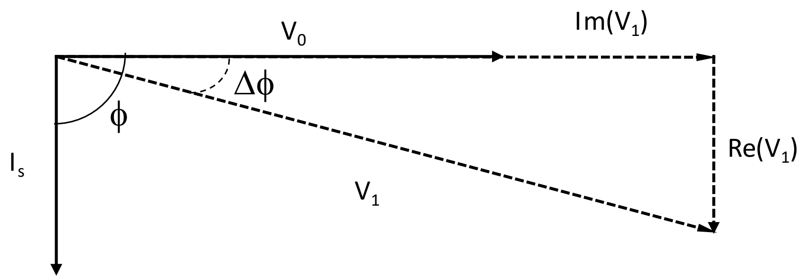

Figure VII-1. Signal phasor diagram of a current-driven MIT system

Deriving Maxwell's equations through the introduction of the combined magnetic and electric scalar potentials, and using the temporal gauge yields (86)

$$\nabla \times \left(\mu^{-1} \nabla \times \vec{A}\right) + (j\sigma + \omega\varepsilon_0\varepsilon_r)\omega\vec{A} = \vec{J_s} \tag{86}$$

where $\overrightarrow{J_s}$ is the current density of the source, and ε is the absolute permittivity ($\varepsilon = \varepsilon_0\varepsilon_r$). $\vec{A}$ is the magnetic vector potential used for converting the governing equations into second-order differential equations.

In Equation (86) the term $j\sigma + \omega\varepsilon_0\varepsilon_r$ is the complex conductivity, which comprises the residual static conductivity and the polarisation losses due to dispersion. The relative permittivity is directly related to the macroscopic properties of the materials, such as polarisation or capacitance. The inclusion of the dielectric properties in (86) reflects the contribution of the fluid properties to their polarisation when subjected to an electric field.

There are a number of sources that generate the material polarisation at different frequencies. The frequency dependence of the relative permittivity contributes to the observation that, in any given material, several polarisation sources will activate at different frequencies [196]. Considering that the electronic and atomic effects do not change significantly, dipolar, space charge, and ionic effects are the main contributors to the polarisation mechanism arising at RF frequencies of interest [197].

The following sections address the effect of the macroscopic effective dielectric permittivity distribution of hydrocarbon mixtures in electromagnetic signals. Due to the inherent complexity of the multiphase flow phenomena, i.e. the complex interfacial polarisation arising from multiple fluids in contact, in addition to the presence of conductive materials, the present work focuses on the macroscopic electromagnetic behaviour of multiphase mixtures. The concept of macroscopic effective permittivity assumes that a heterogeneous mixture interacts with electromagnetic excitations as if it were a homogeneous medium [198]. This concept is valid, from an electromagnetic perspective, only if the particles inside the mixture are small compared to the wavelength of the excitation field, which is the case of the present study.

7.3 Electromagnetic measurements of dielectric properties

An assessment of the dielectric properties of fluids on MIT measurements incorporates the solution of the full electromagnetic Forward Problem via finite element discretisation to evaluate the combined effect of permittivity and conductivity on the induced signals. Further assessment of the variation of the excitation frequency on the induced conduction and displacement currents was also performed to characterise the complex hydrocarbon mixtures cohesively.

For the numerical model built in COMSOL AC/DC, a cylindrical imaging region of 110 mm diameter was used. The 3D model accounts for a dual coil system built using a current-driven coil domain at the transmitter coil and open-circuit approach for the receiving coil (see Section 3.5.1.2). The sensors were located opposite to each other across the circular cross-section.

Three scenarios were modelled for which the conductivity and permittivity of the medium were swept over the values summarised in Table VII-1. The listed values of the dielectric constants reflect a range of fluids readily available in multiphase flow transport, e.g. air (ε_r=1), natural gas (ε_r=1.2), octane (ε_r=2), oil (ε_r=2.8), water (ε_r=80), dry sand (ε_r=6), and dry limestone (ε_r=7) [199] [200] [201]. The resulting 99 conductivity-permittivity combinations accounted for various ratios of water, hydrocarbon and sand content. The volume fraction of the fluids in the imaging region were also varied by changing the size of the cylindrical inclusion to account for segregated annular flow configurations.

Table VII-1. Conductivity and relative permittivity values

Property / fluid	Gas	Oil	Sand	Water
Conductivity (Sm^{-1})	[0]	[0]	[0]	[0.5, 0.15, 0.25, 0.35, 0.45, 0.55, 1, 5]
Dielectric constant ($\boldsymbol{\varepsilon/\varepsilon_0}$)	[1]	[2, 2.8, 3, 3.2, 4]	[5, 6.03, 7.4,10]	[80]

The assessed scenarios cover a broad range of $\sigma/\omega\varepsilon_0\varepsilon_r$ relationships, ranging from 1.12E-1 to 8.99E4 for excitation frequencies between 1 Mz and 100 MHz. This would allow proving the hypothesis that even for low $\sigma/\omega\varepsilon_0\varepsilon_r$ ratios (below 1E3), the displacement currents have a significant effect in the electromagnetic measurements.

In the following subsections, the macroscopic electromagnetic behaviour of various materials usually found in oil transport systems is assessed.

7.3.1 Frequency dependence of induction currents

The effects of excitation frequency on the intensity of the induced currents are evaluated here. The relationship of the MIT measurements for various excitation frequencies comprised a combination of the scenarios summarised in Table VII-2.

Table VII-2. Simulation parameters for evaluation of excitation and displacement currents

Conductivity (Sm^{-1})	[0.55,1,3,5]
Dielectric Constant ($\boldsymbol{\varepsilon/\varepsilon_0}$)	[2,7.4,70, 75, 80]
Operating Frequency (Hz)	[1E6, 5E6, 1E7, 2E7, 1E8]

The induced currents were calculated within the imaging region by integrating the amplitude of the current density over the fluid volume. Figure VII-2 shows the effect of varying the excitation frequency on the displacement and conduction current densities.

Results show that for frequencies below 20 MHz, the amplitude of the conduction currents is linearly proportional to the excitation frequency and it is not affected by the permittivity of the medium (see Figure VI-21(a)). Conversely, changes in permittivity are reflected in the displacement current density, which is proportional to the frequency squared. There is virtually no change in the displacement current density due to variations in conductivity, although a slight difference for larger permittivity values is observed as the frequency increases (see Figure VI-21 (b)).

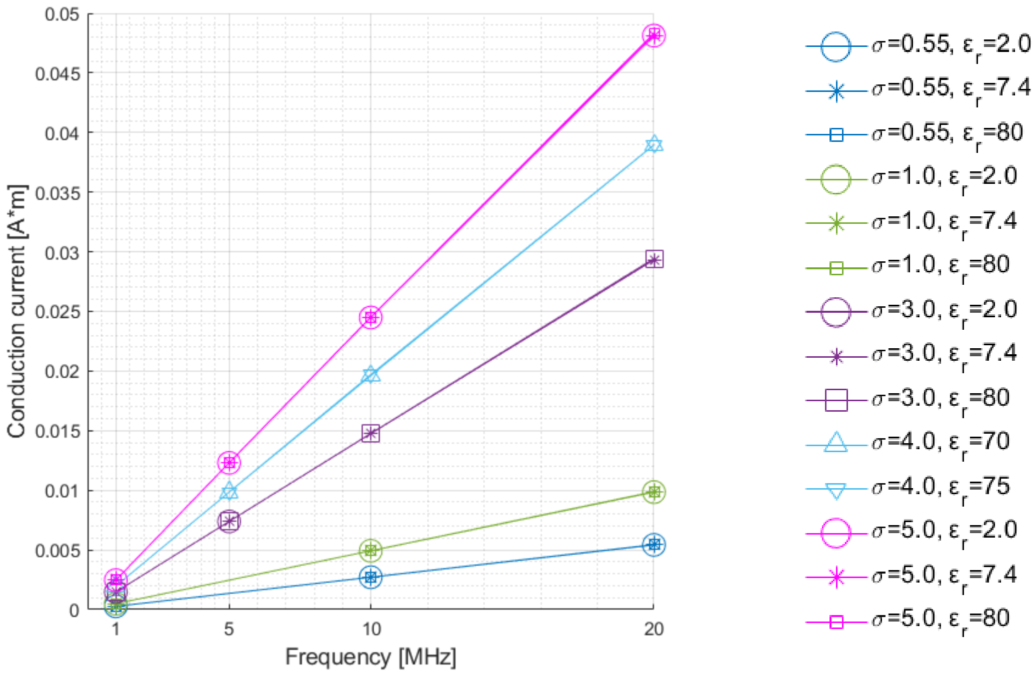

(a)

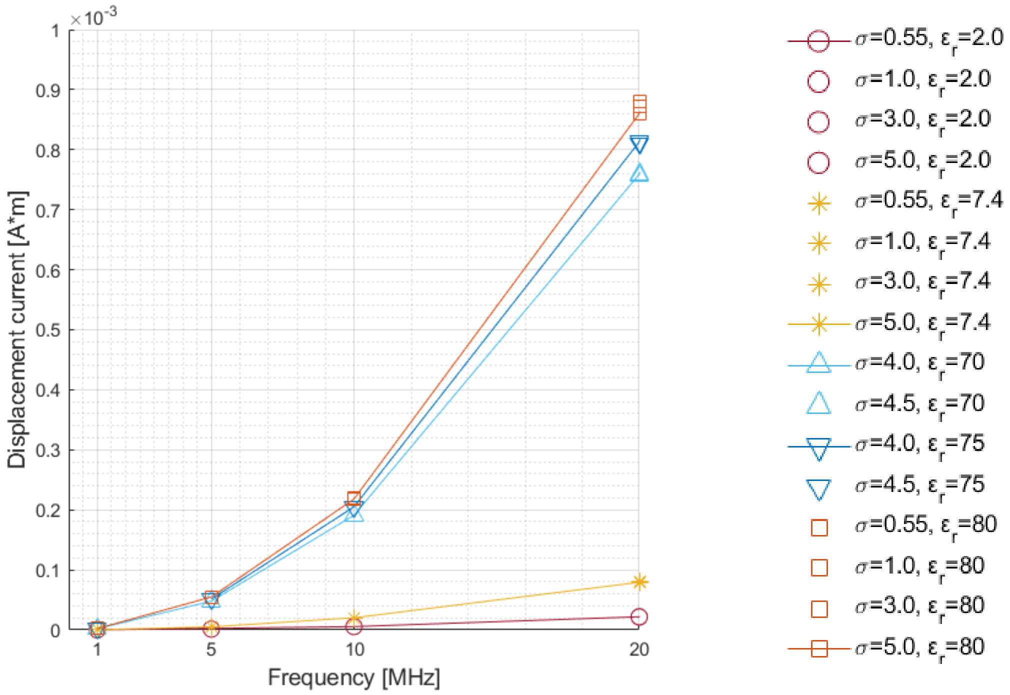

(b)

Figure VII-2. Effect of the frequency in (a) conduction currents and (b) displacement currents of phases of various conductivities and permittivities for excitation frequencies of 1 to 20 MHz

Traditional measurements of conductivity contrast through MIT typically use excitation frequencies between 1 and 30 MHz. However, in order to investigate the frequency dependence of the induced currents, an extended analysis was performed in which an excitation frequency of 1E8 Hz was included in the scenarios. At such a high frequency, both the permittivity and the conductivity have a combined effect on the induction and conduction currents (see Figure VII-3). This is attributed to the change in the polarisation mechanism, which would preclude any direct correlation between the electric and dielectric properties of the medium and the measured signals.

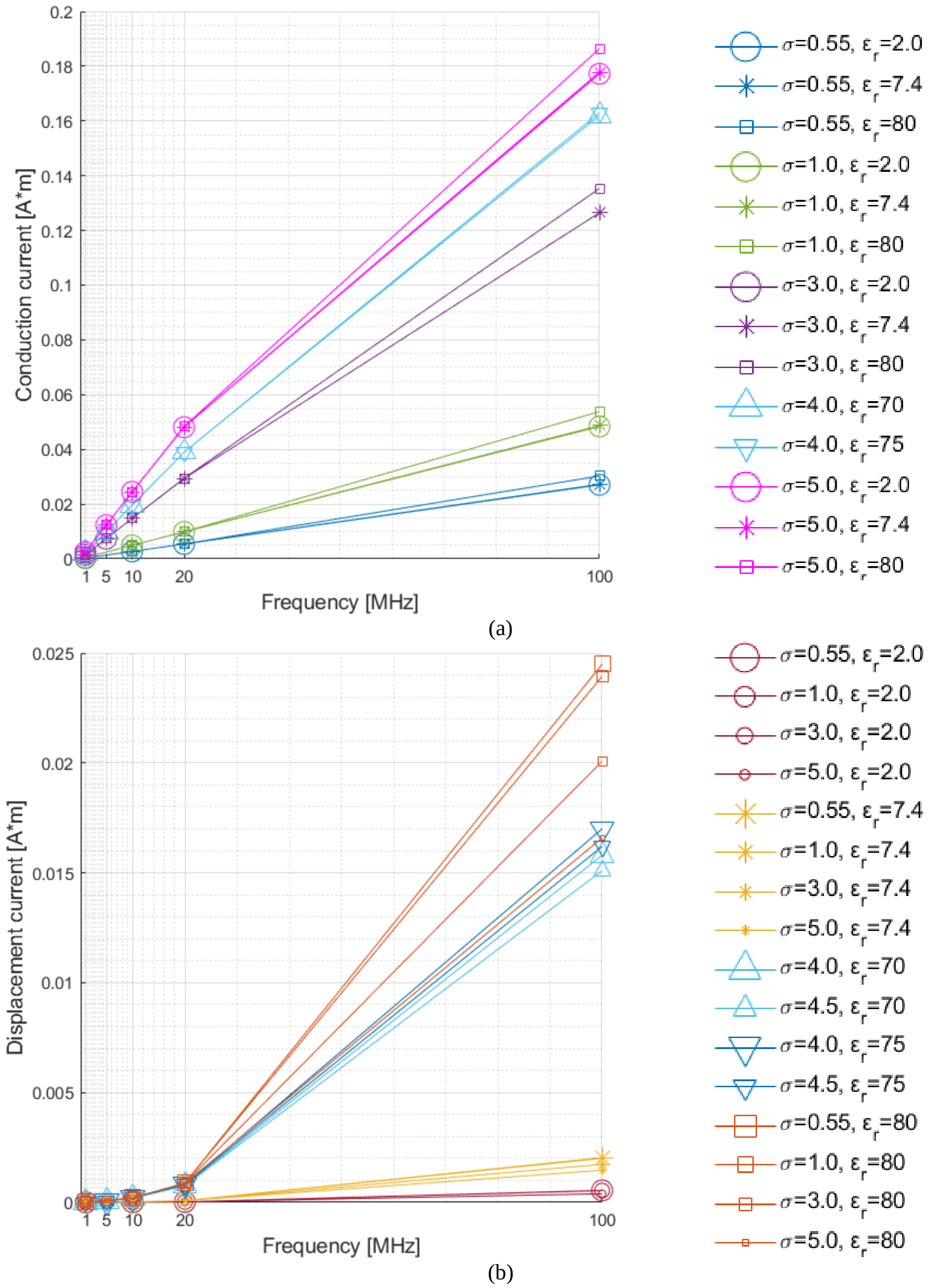

Figure VII-3. Variation of (a) conduction currents and (b) displacement currents of phases of various conductivities and permitivities for excitation frequencies of 1 to 100 MHz

7.3.2 *Induced currents dependence on changes in the spatial domain*

Multiphase flow accounts for a high complexity in the spatial and temporal distributions of the phases. Here, the assessment of the effect of non-uniform distributions on the received signals comprised changes in the spatial domain of the modelled flow mixtures. These spatial changes considered a cylindrical inclusion of various lengths located in the middle of the imaging region yielding various water-air ratios. The water volumetric fractions (α) assessed comprise the following range α= [0.3, 0.5, 0.7, 0.8, 0.9, 1.0].

The induced displacement and conduction currents for the volume fractions above are presented in Figure VII-4. Results show that, at a given excitation frequency of 10 MHz, the displacement and conduction current densities are affected by changes in volume for scenarios involving fixed permittivity and conductivity.

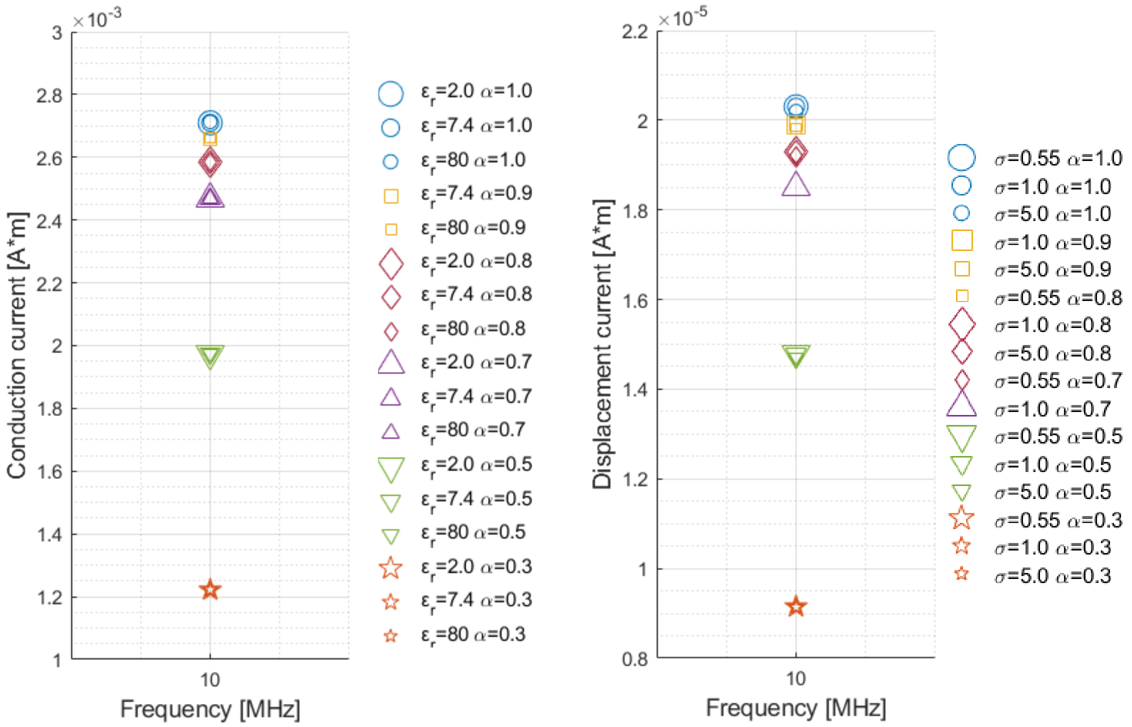

(a) (b)

Figure VII-4. Effect of changes in volume fraction with variations in (a) conduction currents for a mixture conductivity of 0.55 Sm^{-1} and (b) displacements currents for a mixture relative permittivity of 7.4

Figure VII-5 contrasts the changes in the current densities due to variations in volume for various bulk conductivities and permittivities. The differences in the induced current densities are relatively linear with the volumetric changes. The variation of the induced currents per volumetric fraction change is quadratic, as represented by the trends in the inner boxes. The shift in the slope of the induced currents shows that, given the model setup, the received signals are highly sensitive to changes of volume fractions in the vicinity of the sensor array.

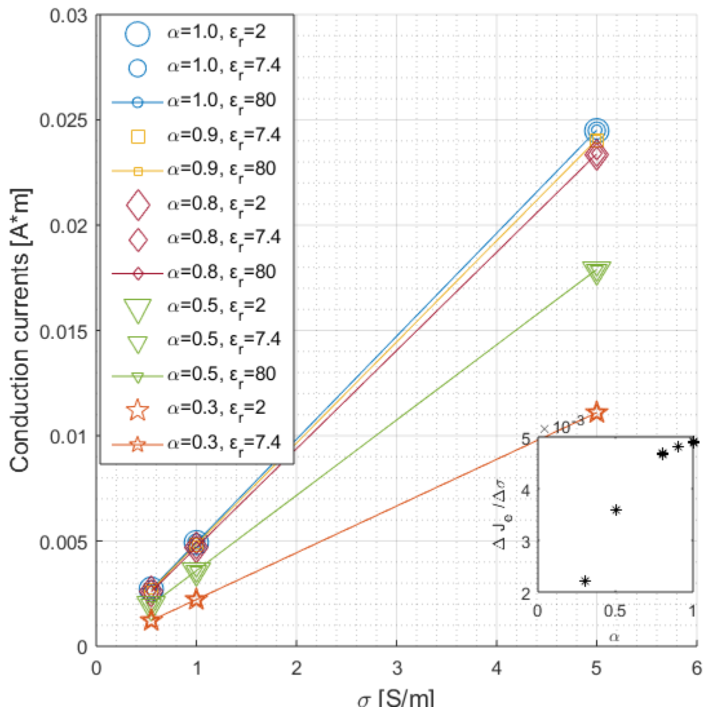

(a)

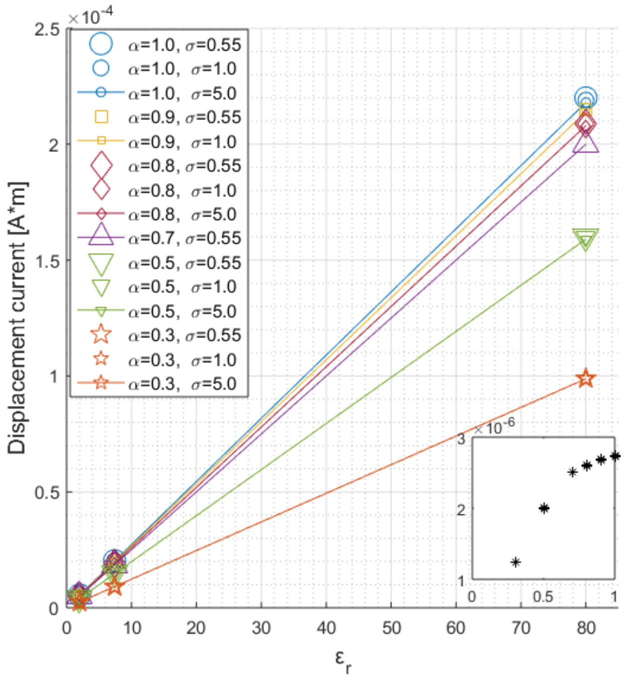

(b)

Figure VII-5. Effect of changes in volume fraction on (a) induced conduction and (b) displacement currents

7.3.3 *Electromagnetic measurement dependence on changes in permittivity and conductivity*

An analysis of the MIT response to changes in the electric and dielectric properties of the fluids is presented below. The influence of the fluid conductivity on the induced amplitude and the phase angle of the signal measured at the opposite receiving coil is shown in Figure VII-6.

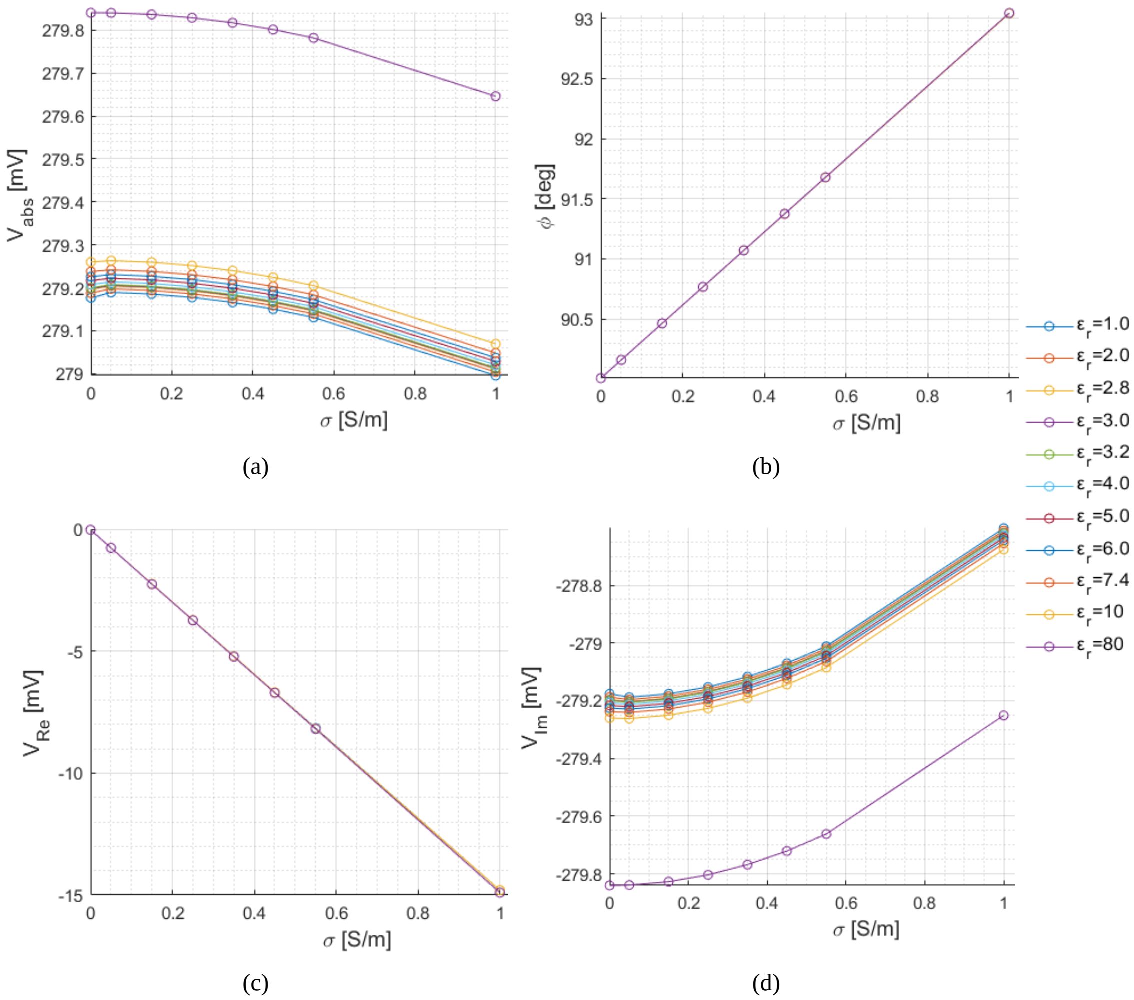

Figure VII-6. Effect of variations of conductivity on (a) absolute amplitude, (b) phase angle, (c) real component of amplitude, and (d) imaginary component of amplitude

It is evident that the conductivity has a significant impact on all measured signals. Particularly, the phase angle measurements prove that angle deviation arises from the eddy-current induced within the conductive phase, with negligible effect from changes in the relative permittivity of the mixture (see Figure VII-6(b)). The same response is seen in the real component of the magnitude in Figure VII-6(c).

Conversely, the dielectric constant is mainly reflected on the absolute amplitude signal and on its imaginary component signal, see Figure VII-6(a) and (d), respectively. These complex amplitude signals encompass combined information regarding the displacement currents induced by the dielectric medium and the conductive currents induced in the conductive phase. Such a complex measurement is reflected in the boxes within Figure VII-7 (a) and (b).

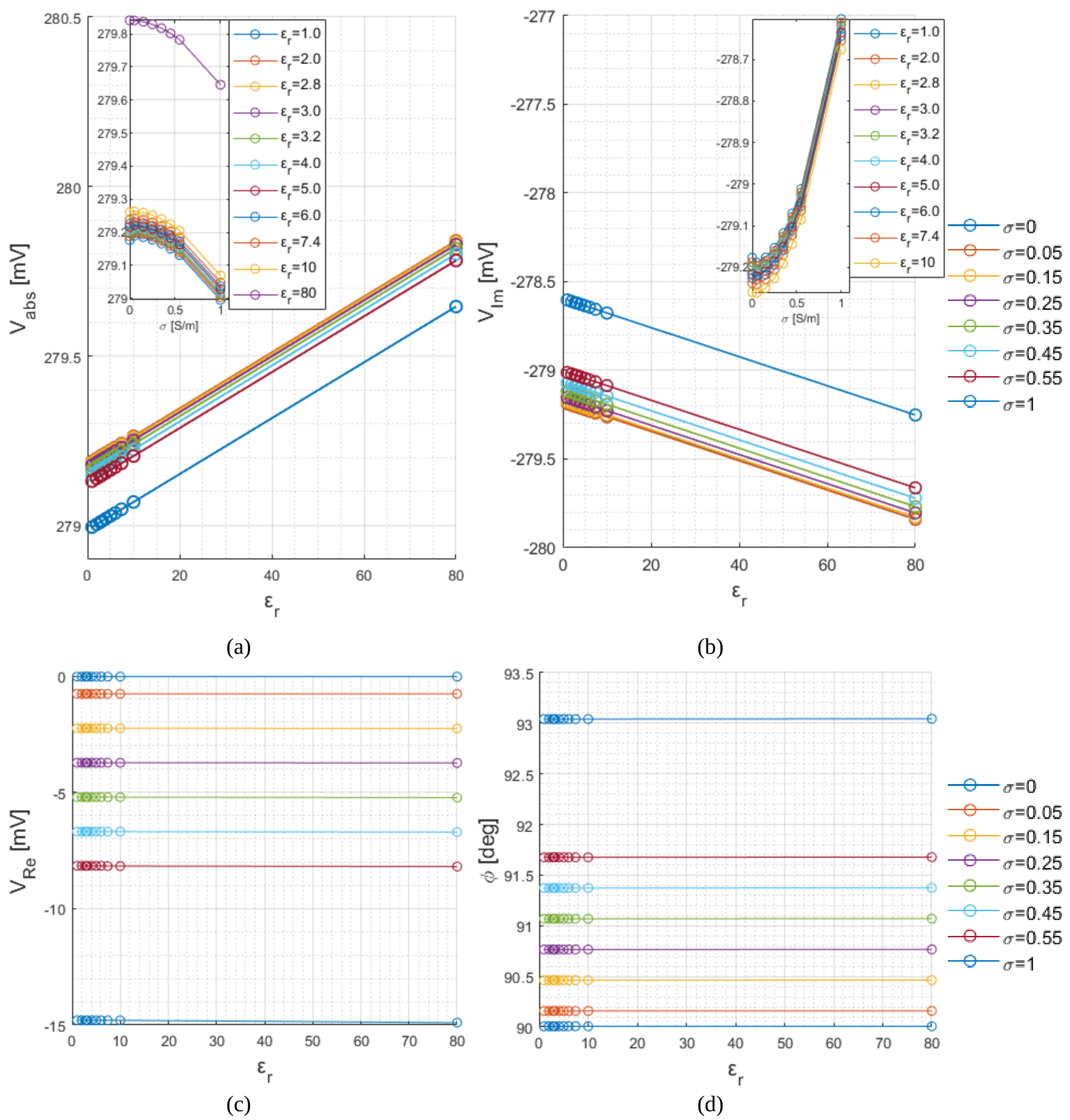

Figure VII-7. Effect of variations of permittivity (and conductivity in inner boxes) on (a) absolute amplitude, (b) imaginary component of amplitude (c) real component of amplitude, and (d) phase angle

7.4 Hydrocarbon mixture characterisation through complex conductivity measurement

7.4.1 Electromagnetic signal dependence on changes in the spatial domain

A characterisation of the susceptibility of the system to the intrinsic properties of the hydrocarbons, sand, and water is presented below. The simulation approach accounts for mixed fluids, equivalent to distributed bubble or slurry, forming a core bulk mixture with changing relative permittivity. The fraction of the mixture occupying the pipe was varied systematically. Figure VII-8 (a) shows that variations on the amplitude signal due to changes in volume fraction (α) of both sand (ε_r=7.4) and gas (ε_r=1) in the non-conductive mixture are linear and in the order of 1.5 μV per every 10% increase. The changes in amplitude due to variations in the permittivity of the mixture are also linear but much smaller than those seen for changes in volume fraction (see Figure VII-8(b)).

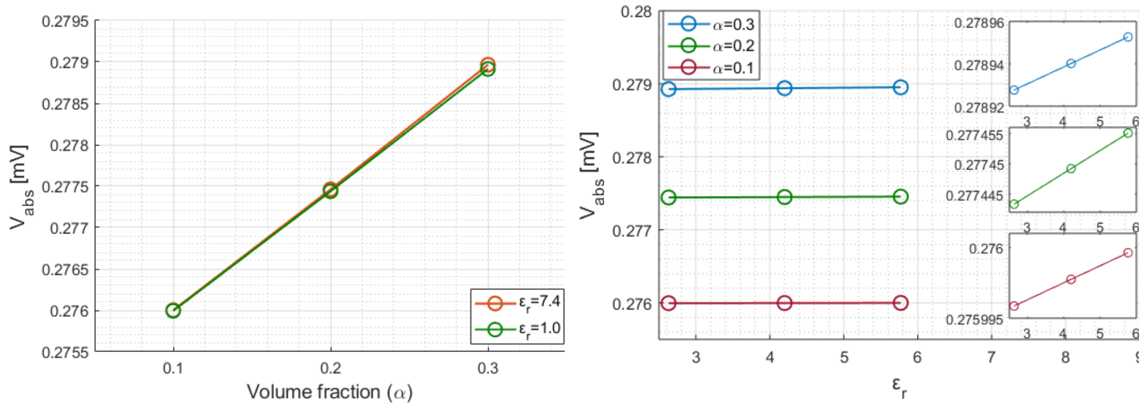

(a) (b)

Figure VII-8. Results of induced absolute amplitude from (a) sand (ε_r=7.4) and gas (ε_r=1) and (b) various permittivity mixtures

The ratio of the change of amplitude to that of the variation of permittivity is shown in Figure VII-9. The trend is non-linear and accounts for variations in the microVolts range per every permittivity shift, which constitutes a challenge to currently available data acquisition systems.

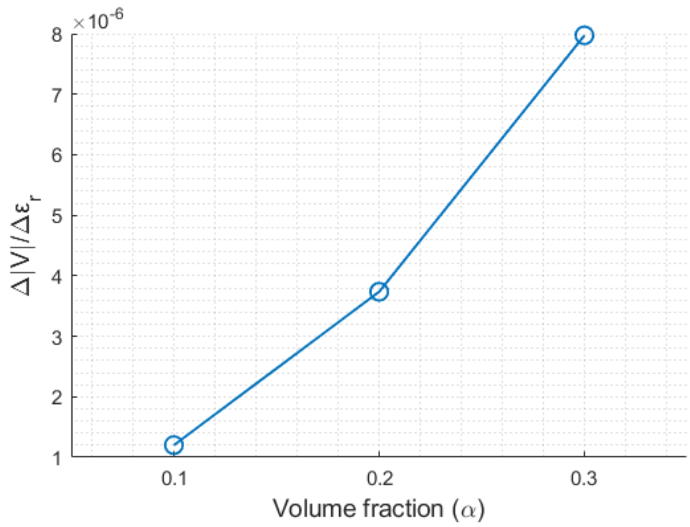

Figure VII-9. Amplitude dynamic range for changes in permittivity and volume

7.4.2 *Electromagnetic signal characterisation for multiphase flow in pipelines*

By using extensive computational models, the weighting of the conductivity and permittivity to the measured signals has been assessed to gain a better understanding as to which electrical properties the voltage measurements stem from, at any given condition. Figure VII-7 (a) showed that for mixed flows with low conductivity, typical of low water contents, the change in amplitude of the induced voltage has a linear relationship with relative permittivity of the mixed flow. Figure VII-10(a) displays the induced amplitude from three two-phase systems within low bulk conductive environments, i.e., conductivity less than 0.6 Sm^{-1}. The evaluated mixtures comprise water-oil, water-gas, and water-sand flow with relative permittivity of 2, 1, and 7.4, respectively. The difference among the received voltages is constant throughout the bulk conductivity range.

Results in Figure VII-10(a) allow further contrasting of the three-phase flow scenarios containing both oil and water combined with either gas or sand. Figure VII-10(b) illustrates that the change in the signals is solely due to the change in the relative permittivity of the gas and the sand. The influence in the receiving signal of the water-oil-sand flow to that of the water-oil-gas flow is given by a 4.4:1 ratio.

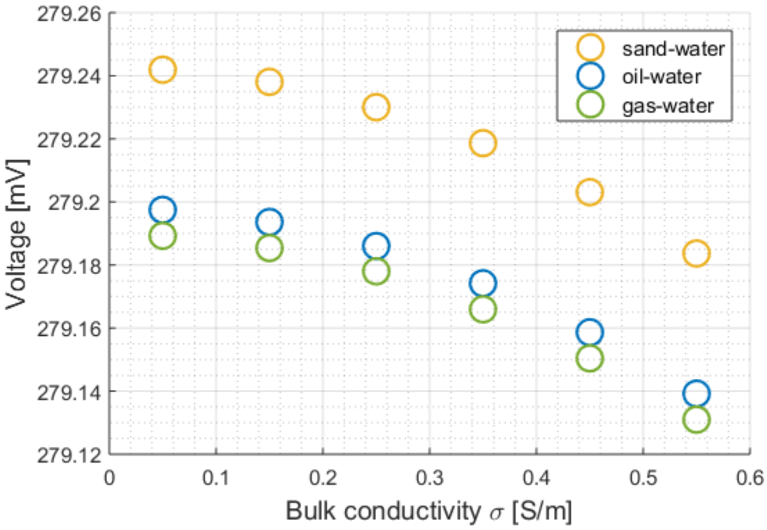

(a)

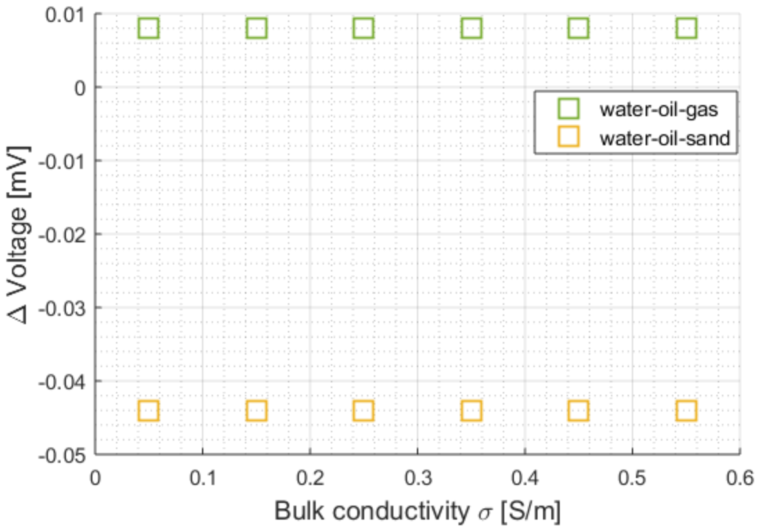

(b)

Figure VII-10. Induced voltage from (a) a trio of two-phase flows of water-oil, water-gas, and water sand, and (b) the signal difference between the water-oil and the water-gas flows (labelled water-oil-gas) and the water-oil and the water-sand flows (labelled water-oil-sand) in low conductive environments (σ=0.05-0.5 Sm^{-1})

Figure VII-11 presents the amplitude of the induced voltage for variations of the relative permittivity in various conductive environments. For a given bulk conductivity below 1 Sm^{-1}, the change in amplitude of the induced voltage increases as the relative permittivity of the mixed flow increases (see box in Figure VII-11(a) and in Figure VII-11(b)). In contrast, as the water content increases creating a mixture conductivity of 1 Sm^{-1} or greater, the change in amplitude of the induced voltages is dominated by the conductivity increase (also evident in Figure VII-7(b)). This behaviour is more pronounced when the conductivity difference of the mixed flow is beyond 4 Sm^{-1}, similar to that of formation water and slurries.

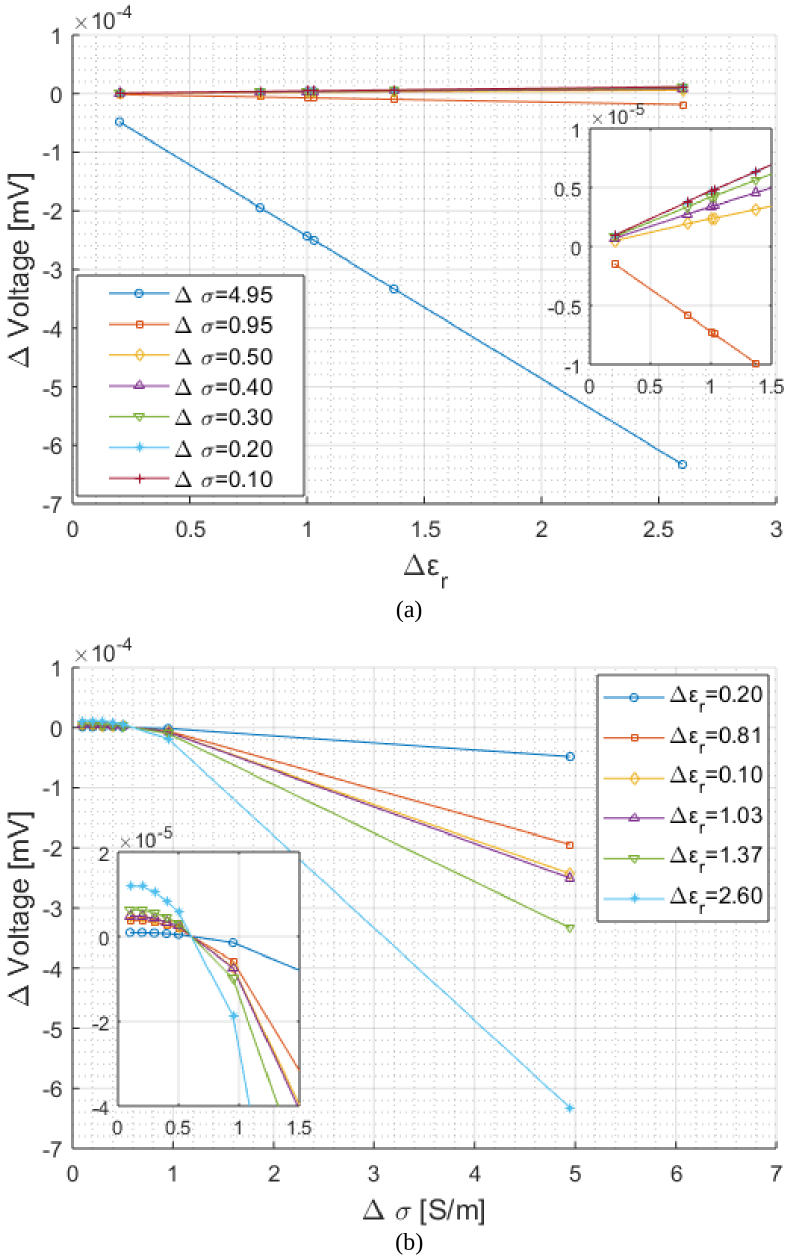

Figure VII-11. Changes in the amplitude of the induced voltage for various mixed relative permittivity and bulk electric conductivities

7.5 Discussion and Conclusions

The feasibility of deriving the permittivity from electromagnetic measurements using inclusions of skin depth much larger than the sample dimensions has been addressed. The range of electric properties that are relevant to the intended application was derived, and the degree of correlation between the measurements and the electric properties was evaluated. Results show a correlation between the simultaneous responses from the system to changes in permittivity and conductivity.

A key contribution from the study resides in the demonstration that for a given three-phase flow of water-oil-sand or water-oil-gas with low water contents (bulk conductivity ranging from 0.05 to 0.6 Sm^{-1}), the change in amplitude of the induced voltage is influenced by the permittivity of the fluids. Hence, electromagnetic induction could be used to measure both the phase shift and amplitudes of the complex voltages to continuously monitor and measure the phase fraction of conductive and non-conductive phases. Furthermore, it was verified that the effect of permittivity in the absolute amplitude signal is at least one order of magnitude greater than that observed on the real and imaginary components disjointedly. These results provide improvements to previous approaches where electromagnetic signals were de-multiplexed for measurements in low conductive environments.

The use of amplitude signals that provide information related to the dielectric properties of non-conductive fluids allows multiphase measurement over the same cross-section. By doing so, it enhances the measurement accuracy and broadens the application spectrum of electromagnetic based imaging technologies for in-situ flow pattern imaging.

The results presented are of particular interest for low conductive mixtures, where the measured signal is predominantly dominated by the permittivity, i.e. the volumetric fractions of the oil, gas, and sand. This novel approach yields a real-time derivation and verification of the conductive and non-conductive phase volumetrics using a single apparatus, hence, removing the need, and expense, of co-locating two separate metering systems.

Chapter VIII Flow pattern identification

8.1 Introduction

The present chapter describes the hydrodynamic phenomena of multiphase flow configurations derived from tomography images. Flow pattern maps are typically derived from experimental observations via optical methods under controlled conditions. The visual characterisation of flow configuration offers an insight into the distribution of fluid species inside a pipeline for given operational conditions.

The identification of dynamic flow regimes in the literature is mainly based on visual observation of the flow structures. The visual characterisation is time-consuming, and observations are limited to structures externally identifiable. The drawback of optical techniques is that complex flow configurations, or the presence of opaque fluids such as oil, can lead to pattern misclassifications [30].

In this chapter, the benefits of tomography techniques for flow pattern characterisation are exploited and in doing so, the two drawbacks of optical methods, i.e. visual limitations and slowness, are addressed. The approach used here departs from traditional methods for the classification of volumetric concentrations in pipelines by exploiting the information available from intrinsic dielectric measurements. The experimental outputs were analysed via an automated algorithm that compared the spatial and temporal flow characteristics arising at various experimental conditions. The analysis performed on the experimental data leads to the understanding of the transition boundaries between the flow regimes and their relationship with dimensionless quantities.

The derived improvements to non-dimensional maps encompassing a broader flow characterisation can be of significant impact for oil field operators, and facilities' designers given the enhanced accuracy of flow pattern prediction maps and its impact on the costs associated with transport and production handling.

This chapter contains some excerpts from the following journal article (currently in press): "*On the life and habits of gas-core slugs: Two-phase gas-liquid intermittent structures in co-current horizontal flow"* in *Journal of Natural Gas Science and Engineering* [20]. The chapter is organised as follows. Section 8.2 describes typical horizontal gas-liquid spatial distributions. Section 8.3 proposes a unified horizontal gas-liquid flow pattern characterisation based on published literature. Section 8.4 details the experimental facilities where the tests were conducted. In Section 8.5, the flow regimes inside the pipe during every experiment are characterised based on the ECT measurements and specific flow-related key parameters. Section 8.6 exploits the capabilities of ECT for automatic flow pattern identification by combining the mean concentration from reconstructed images and a logic-based algorithm applied to intermittent structures. The characterisation of the flow structures serves to propose changes to existing flow pattern maps in Section 8.7. Finally, in Section 8.8, the results are discussed, and the final remarks are drawn.

8.2 Horizontal gas-liquid flow

The spatial distributions of the flow species within a horizontal pipe can be described as an evolution of flow patterns. Let us assume an initial condition where the gas and liquid velocities are low. At low flow velocities, the fluids tend to segregate and flow in separate strata, denoted stratified flow. In stratified flow, gravity effects yield the denser phase, i.e. oil, to flow at the bottom section of the pipe while the gas occupies the top section. As the gas velocity increases, the shear forces dominate over viscous forces, and waves are formed in the interphase, yielding stratified wavy flow. This waves, known as Jeffrey waves, take place when the following condition occurs [202]:

$$U_{gs}{}^{2} \geq \frac{4\mu_L g(\rho_L - \rho_g)}{s_j \rho_L \rho_g} \tag{87}$$

where U_{gs} is the gas superficial velocity, μ_L is the liquid dynamic viscosity, g is the acceleration of gravity, ρ_L and ρ_g are the liquid and gas densities, respectively and s_j is a sheltering coefficient with a value of 0.01[202].

As the gas velocity increases further, so do the waves height, hence reducing the available area for gas flow. This area reduction increases even more the gas velocity and causes an instant pressure drop. This phenomenon yields large irregular waves that can reach the top of the pipe resulting in intermittent slug patterns. Depending on the conditions of the liquid, segregated stratified flow can alternatively transition to segregated annular flow or to distributed flow [33] [32] [203] [204].

These transitions between stratified, intermittent, and annular flow has not been sufficiently addressed in the literature. In [205], the authors refer to this transition zone as a pseudo-slug area. However, there is no general agreement on the characteristics of a ‘pseudo-slug’. A recent study in air-water horizontal flow demonstrates that two flow regimes coexist in that pseudo-slug zone [206]. In one regime the air penetrates through the water forming a two-phase mixture in the core of the slug “with no clear boundary between the phases”, and in the other, the air forces the water to the pipe perimeter with a gas-continuous core. The latter regime will be addressed in detail in the following sections. The aim of the study is to gain more knowledge on this recently studied sub-flow pattern by extending the analysis to fluids of interest for hydrocarbon transport.

For consistency, in the remainder of this chapter, the pseudo-slug with a maintained gas core is referred to as ‘*gas-core slug*’, as denoted by [207]. Although it is believed to be consistent with structures previously reported as ‘ghost’ or ‘huge waves’ [208] [206].

8.3 Horizontal gas-liquid characterisation

In the literature, there are numerous regime classifications for gas-liquid mixtures. Following a comprehensive review, three main flow patterns are recurrent in the literature encompassing horizontal gas-liquid flows, namely: (1) segregated flow where both phases are separated into separate layers, i.e. stratified or annular; (2) disperse flow where droplets of liquids or gas bubbles travel through the matrix of the continuous phase and; (3) intermittent flow.

As a result of the abundant maps available, a large number of different definitions arise, which makes the comparison of the performance of existing regime maps difficult. An integrated flow pattern classification would enable cross-correlation among different studies, hence the unified classification proposed in Table VIII-1. The proposed classification is based on a detailed review of relevant literature and constitutes the initial basis for the present study.

The generalisations used for the pattern map characterisation in the literature are based on correction factors for given fluid properties [203], the ratio of superficial velocities [209] [210] [211], or the use of dimensionless numbers [32] [212] [213]. The majority of the maps published were developed by correlating the dimensional quantities of the experimental data and visual observations. The use of dimensional quantities limits the applicability of the maps to conditions similar to those at which they were derived, i.e., pipe dimensions and flow properties [31]. Conversely, the use of dimensionless numbers, which correlate the governing forces and the effect of variations in the fluid properties, for prediction of flow pattern distribution is believed to provide the opportunity of extending the applicability to a wider range of conditions [31].

Table VIII-1 Unified horizontal gas-liquid flow pattern classification

Flow Pattern	Characteristics	Representation
Distributed – Bubble	-The liquid forms a continuous phase with dispersed bubbles of gas.	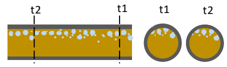
Distributed – Mist	- Most or all of the liquid is entrained by the gas phase.	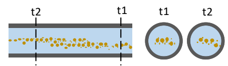
Intermittent – Slug	-Periodic waves reach the top of the pipe. -The flow consists of slugs of liquids alternated with segregated flows.	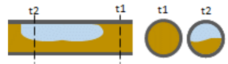
Intermittent – Plug	-Alternate plugs of liquid and gas move along the upper section of the pipe.	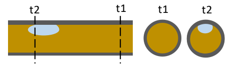
Intermittent – Gas-core Slug	- Liquid film envelops the wall of the pipe. -The flow consists of gas-core slugs of liquids alternated with segregated flows.	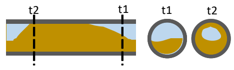
Segregated – Stratified	- Flow in separate layers. The liquid flows at the bottom of the pipe. - The gas flows at the top of the pipe. - The interface is flat	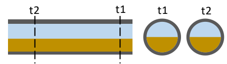
Segregated – Wavy	- Flow in separate layers. The liquid flows at the bottom of the pipe. - The gas flows at the top of the pipe. - Visible waves in the interface.	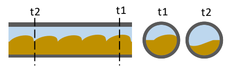
Segregated – Annular	- The gas flows through the pipe core. -The liquid forms film layer around the pipe walls. Due to gravity, the film at the top of the pipe is thinner than at the bottom.	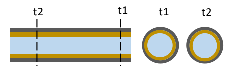

In this study, the prediction accuracy of eight flow pattern maps on the experimental measurements is evaluated. The map selection comprise those derived by Beggs and Brill [33], Beggs and Brill modified [33], Shell [212], Eaton [32] Baker [203], Taitel-Dukler [202], Barnea [204], Lin and Hanratty [205], and NEL [214]; the latter corresponds to the map from their experimental facility. The maps were selected considering (a) proven extrapolation to different data sets; (b) broad industrial use; (c) applicability to the experimental conditions of our data; and (d) existing sub-classification of intermittent slug structures. In this sense, the assortment of selected maps accounts for the above consideration and all three generalisations detailed before.

The maps from Beggs and Brill, Beggs and Brill modified, and Eaton combine dimensionless quantities and the Froude number. The Froude number is highly representative of the behaviour of wave structures and hence the regime transition between segregated and intermittent flow. The maps from Shell, Lin and Hanratty, and Beggs and Brill, do not consider the effects of the fluid properties in the flow regime transitions. On the other hand, the maps from Baker and that of Eaton take into account the density, viscosity, and surface tension of the phases. To complement the study, the semitheoretical map from Taitel-Dukler, which do not follow any of the generalisations above, is also included.

8.4 Experimental facility

Experiments were conducted by the NEL team and Dr Hunt at the multiphase flow loop at TUV-NEL in East Kilbride, UK [215]. The experimental facility comprises a recirculation flow loop that uses gravimetric separation of the fluids (oil, gas, and water) in a continuous operation. A schematic of the loop showing the position of key components is given in Figure VIII-1. The liquid flows are recirculated around the test facility using variable-speed centrifugal pumps. The dry nitrogen is delivered from the storage tank at 12 bar at the injection point. After passing through the test section, the gas is vented to the atmosphere from the separator. The flow rate of the gas in the test section is a function of the differential pressure between the testing section and the storage line.

At the centre of the facility is a three-phase gravity separator with a capacity to separate 35 m^3 and 25 m^3 of water and oil, respectively. The separator acts as a storage vessel for the liquids undergoing test and also helps to separate fluids for recirculation. The liquid used for the experiments was a refined oil, Paraflex HT9 (see properties in Table VIII-2). The reference measurements for both liquid and gas flows are determined using turbine flowmeters after exit from the separation vessel.

The test section consisted of a clear acrylic pipe of 8.5 m long and 100 mm inner diameter, preceded by a development length of over 30 m (>300 pipe diameters). The flow can therefore be considered well-developed, though slug flows in particular are known to continue to develop over longer lengths [216][217], so there can be no assumption of stabilised flow patterns in a general sense. All experiments were conducted under controlled laboratory conditions at a temperature of 20°C.

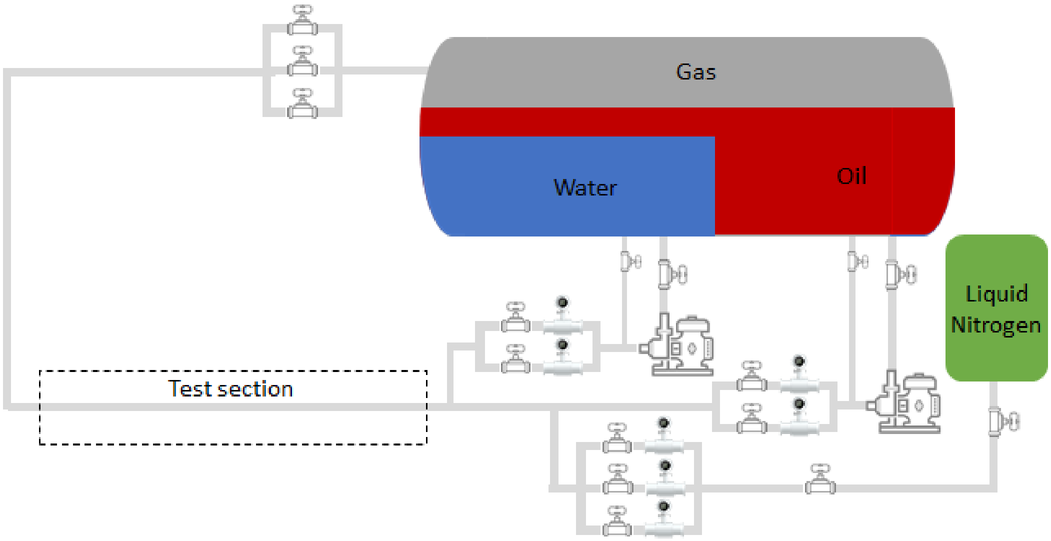

Figure VIII-1. Schematic of the NEL multiphase flow facility.

Table VIII-2 Experimental setup for gas-liquid flow measurement

Pressure (bar)	2-10 bar
Temperature (C)	20 C
U_{os} (m/s)	0.10 – 4.8
U_{gs} (m/s)	0.25 – 8.9
Oil type	Paraflex HT9
Oil density (kg/m^3)	830 to 831
Oil viscosity (cP)	15.9-17.9
Gas type	Nitrogen
Gas density (kg/m^3)	3.4-13.8
Surface tension (dyna/cm)*	20.8-24.2

*calculated from Baker & Swerdloff equation with pressure correction $\gamma = \left(37.5 - 0.2571\left(\frac{141}{\rho_o/\rho_w} - 131.5\right)\right)(1 - 0.024P^{0.45})$

8.5 Flow diagnostic techniques

Characterisation of volumetric concentrations in pipelines can be achieved by a variety of methods. Some of the most commonly used methods comprise techniques and elements that are either intrusive or contain nuclear sources, such as quick-closing valves [218], wire-mesh sensors (WMS) [206], and Gamma-ray densitometers [208]. Intrusive techniques interact with the process and can perturb the flow yielding to misleading observations.

Available processing techniques include statistical analysis of traditional sensor data; statistical analysis of image data and; combined statistical and structure analysis of image data. These techniques, while valuable in studying the flows, are often frequency limited with non-specific sensitivity [219]. Furthermore, they are non-physical where the link to conventional patterns is not clear. Although the combined analysis can identify key physical parameters and apply statistical techniques, showing great promise, standard procedures are not currently agreed [220].

In this chapter, non-invasive tomography combined with an automated pattern detection algorithm is proposed to characterise the different flow patterns. Although the method applied here can be extended to measurements from any high-speed tomography system, ECT is selected due to its suitability regarding the nature of the multiphase gas-oil mixture. In this regard, ECT has been widely used to obtain images of the distribution of permittivity inside pipelines transporting non-conductive flows [57] [58] [59] [62] [63] [64] [45] and has been proven accurate for gas-oil flow measurement when compared to weighing systems (see Chapter VI).

In the following subsections, the premises for pattern characterisation of the overall dominant flow scheme using ECT alongside the prediction accuracy of existing maps is presented. Subsequently, an automated algorithm is used for detailed analysis and characterisation of the measured intermittent structures.

8.5.1 ECT measurements for characterisation of the dominant flow regime

By combining the mean concentration in the cross-section of the pipe and the reconstructed images, the flow regimes can be characterised. Specific flow-related parameters, that can be used for flow characterisation are available from electrical imaging. The key indicators of a horizontal flow structure can be classified into spatial and temporal parameters, as follows.

The spatial indicators are:

- average concentrations of the liquid phase (holdup),
- spatial distribution of the concentration over the pipe cross-section,
- fluid level,
- range and balance of the probability density function of average concentration, e.g. (a) primarily liquid with gas bubbles present; (b) primarily gas with liquid structures passing or; (c) fully intermittent slugs or waves.

The temporal parameters comprise:

- frequency distribution – number of structures passing in a given period,
- the primary structure velocity, and
- the length-scale of the primary structure.

Based on the parameters above and the unified flow pattern classification in Table VIII-1, the ECT measurements of the experimental tests was characterised according to Table VIII-3.

Table VIII-3 ECT parameters for flow characterisation

Parameter	(a) Single-phase	(b) Segregated-Stratified	(c) Segregated-Wavy	(d) Intermittent - Slug	(e) Intermittent-Plug
Holdup	0% or 100%	Low	Low	High	High
Spatial distribution	Homogeneous	Segregated	Segregated	Segregated	Segregated
Interface	No interphase	Steady interface	Varying interface	Fully intermittent	Fully intermittent
Frequency	N/A	Low	Medium	High	Very high
Velocity	N/A	Low	Low	High	High
Length scale	N/A	N/A	High	Medium	Low

The characterisation of the experimental data for the superficial velocities of the given phase is shown in Figure VIII-2. The data presented correspond to the characterisation of the dominating flow pattern of each of the 33 test points. The classification, based on ECT measurements, follows the parameters listed in Table VIII-3. Note that gas-core slug is not listed in Table VIII-3 as it has not been included in the available maps in the literature, with the only exception of the pseudo-slug zone described in [205].

Figure VIII-2 plots the characterisation of the test points and relates the predominant flow structures to the superficial velocities of the gas and liquid phases. The flow regime transitions between distributed, intermittent, and segregated, are primarily influenced by the oil volumetric fraction. Conversely, the transitions among the intermittent flows, including that to gas-core slug, are predominantly driven by the velocity of the gas phase.

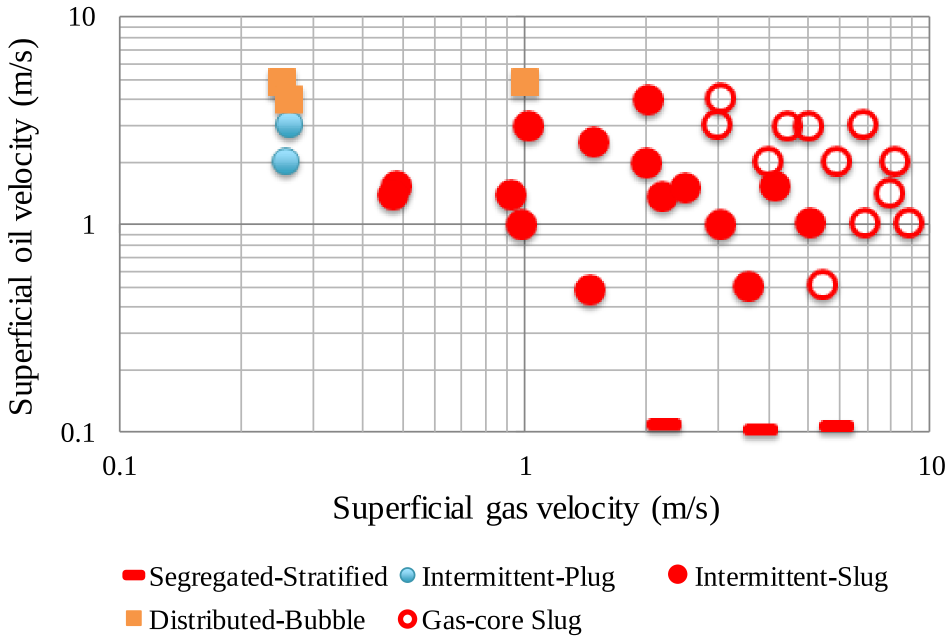

Figure VIII-2. Flow pattern classification of the dataset over the range of superficial velocities of the phases

8.5.2 Prediction accuracy of flow pattern maps

The accuracy of existing maps to predict the development of the flow regimes, as identified per the ECT signal indicators above, is evaluated through the juxtaposition of the experimental data with existing regime maps.

The dimensionless functions presented in Table VIII-4 were used to compare the ECT-based characterisation to the regime-specific zones within the pattern maps. The dimensionless quantities used are: the Reynolds number, the Weber number, and the Froude number. The Reynolds number correlates the inertial and viscous forces, which is relevant for the characterisation of segregated-distributed flow transitions. The Weber number is useful for analysing the phase interface through the correlation between the inertial forces and the surface tension. The Froude number, derived from the ratio of inertia to gravity forces, is strongly relevant for the analysis of wave evolution.

Table VIII-4. Dimensionless quantities for flow regime characterisation

Eaton et al. [32]	Two-phase Reynold's function	$(\boldsymbol{N_{Re}})_t = \dfrac{\boldsymbol{W_t H_L}^{\boldsymbol{2}}}{\boldsymbol{D\mu_t}}$
	Two-phase Weber function	$(N_{We})_t = \dfrac{\rho_L v_L H_L^{\frac{1}{2}}}{\gamma} + \dfrac{\rho_g v_s (1-H_L)^{\frac{1}{2}}}{\gamma}$
Beggs and Brill [33]	Froude Number	$Fr = \dfrac{u_m}{\sqrt{gD}}$
	Non-slip holdup	$\lambda = \dfrac{Q_L}{Q_L + Q_g}$
Baker [203]	Baker's gas mass multiplier	$\tau = \sqrt{\dfrac{\rho_g}{\rho_a}\dfrac{\rho_w}{\rho_L}}$
	Baker's liquid-gas ratio multiplier	$\psi = \dfrac{\gamma_w}{\gamma_L}\left(\dfrac{\mu_L}{\mu_w} + \left(\dfrac{\rho_w}{\rho_L}\right)^2\right)^{\frac{1}{3}}$
Taitel-Dukler [202]	Lockhart and Martinelli parameter (Abscissa axis)	$X = \left[\dfrac{\frac{4C_L}{D}\left(\frac{U_{Ls}D}{v_L}\right)^{-n}\left(\frac{\rho_L\,(U_{Ls})^2}{2}\right)}{\frac{4C_G}{D}\left(\frac{U_{gs}D}{v_g}\right)^{-m}\left(\frac{\rho_g\,(U_{gs})^2}{2}\right)}\right]^{\frac{1}{2}}$
	Ordinate of the frontier between (a)S-Wavy & annular (b) S-Wavy & Intermittent (c) S-Wavy & S-Smooth	$F = \sqrt{\dfrac{\rho_g}{\rho_L - \rho_g}}\dfrac{U_{gs}}{\sqrt{Gg\cos\alpha}}$
	Ordinate of the frontier between Intermittent & Distributed Bubble	$T = \left[\dfrac{\frac{4C_L}{D}\left(\frac{U_{Ls}D}{v_L}\right)^{-n}\left(\frac{\rho_L\,(U_{Ls})^2}{2}\right)}{(\rho_L - \rho_g)g\cos\varphi}\right]^{\frac{1}{2}}$
	Ordinate of frontier between Segregated Stratified / Wavy	$K = \left[\dfrac{\rho_g U_{Ls} U_{gs}{}^2}{(\rho_L - \rho_g)g\ v_L\cos\varphi}\right]^{\frac{1}{2}}$

where W_t is the total mass ratio, H_L is the liquid holdup, D is the pipe diameter, μ_t is the total viscosity given by $\mu_t = \mu_L{}^{H_L}\mu_g{}^{(1-H_L)}$, ρ_L and ρ_g are the liquid and gas densities, respectively, v_L is the liquid velocity, $v_s$is the slip velocity given by $v_s = v_g - v_L$, U_{Ls} and U_{gs} are the superficial velocities of the liquid and gas phases, γ is the interface superficial tension, Q_L is the liquid flowrate, and Q_g is the gas flowrate. The subscripts a and w refer to the reference properties of air and water, respectively. γ is the interfacial tension, and φ is the inclination of the pipe. Taitel-Dukler coefficients for turbulent flow are $C_L = C_G = 0.046$ and $n = m = 0.2$.

Using the dimensionless numbers above, the experimental data was compared to the flow patterns of existing maps yielding the distributions in Figure VIII-3 to Figure VIII-6. The dimensionless maps derived by Beggs and Brill, Shell, and Eaton in Figure VIII-3(a) and (b), and in Figure VIII-4(a), respectively, combine dimensionless quantities and the Froude number. The maps from Shell and Beggs and Brill, do not consider the effect of the fluid properties in the flow regime transitions. By contrast, the maps from Eaton and Baker (Figure VIII-4) consider the density, viscosity and surface tension of the phases. The maps from Barnea in Figure VII-5(b), and those from NEL and from Lin and Hanratty in Figure VII-6 (a) and (b), respectively, are based on the inflow quantities of the gas and liquid phases. The regime transitions in Taitel-Dukler map, in Figure VII-5(a), originate from theoretical grounds avoiding the constraints of empirical charts.

The data distribution presented in Figure VIII-3(a), Figure VIII-4(a), Figure VIII-4(b), and Figure VII-5 (a) shows that, as expected, the transition from stratified to intermittent flow has a downward trend with increasing liquid content. Figure VIII-3(a), Figure VIII-4(a), Figure VII-5(a), and Figure VII-5(b) show a well-defined transition between distributed, intermittent, and segregated flows.

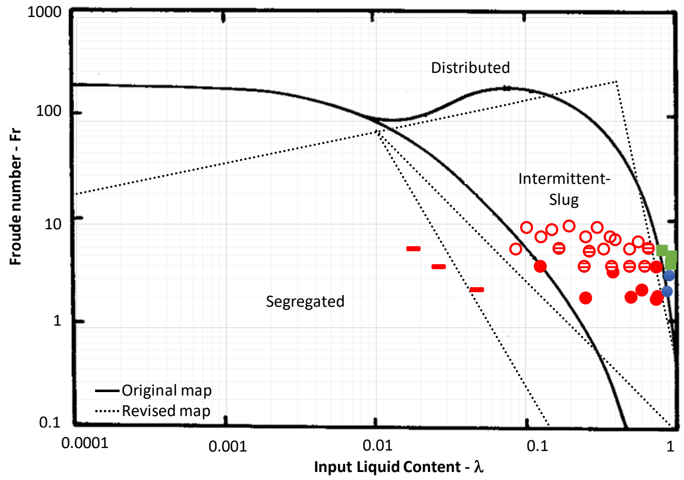

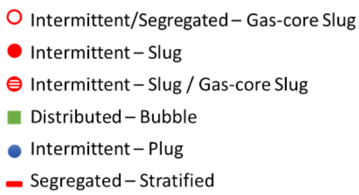

Beggs and Brill (1973) and Beggs and Brill revised (1977) modified from [33], p612

(a)

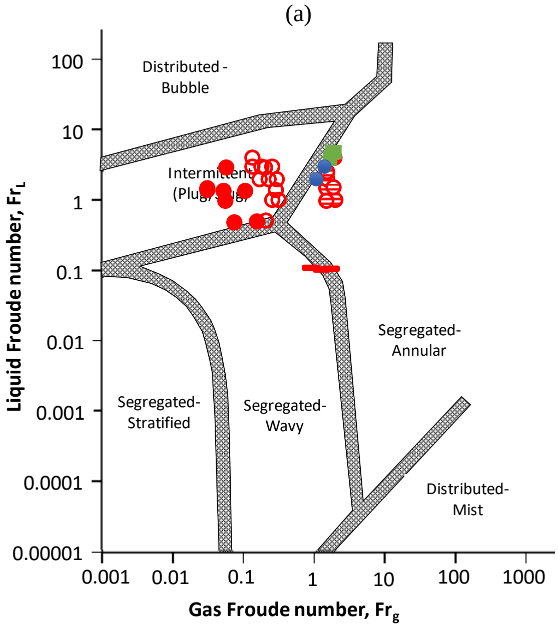

Shell (2007) modified from [212], p77

(b)

Figure VIII-3. Experimental data classification from ECT measurements adjoined with existing flow pattern maps showing the relationship between (a) non-slip holdup and Froude number, (b) gas and liquid Froude numbers

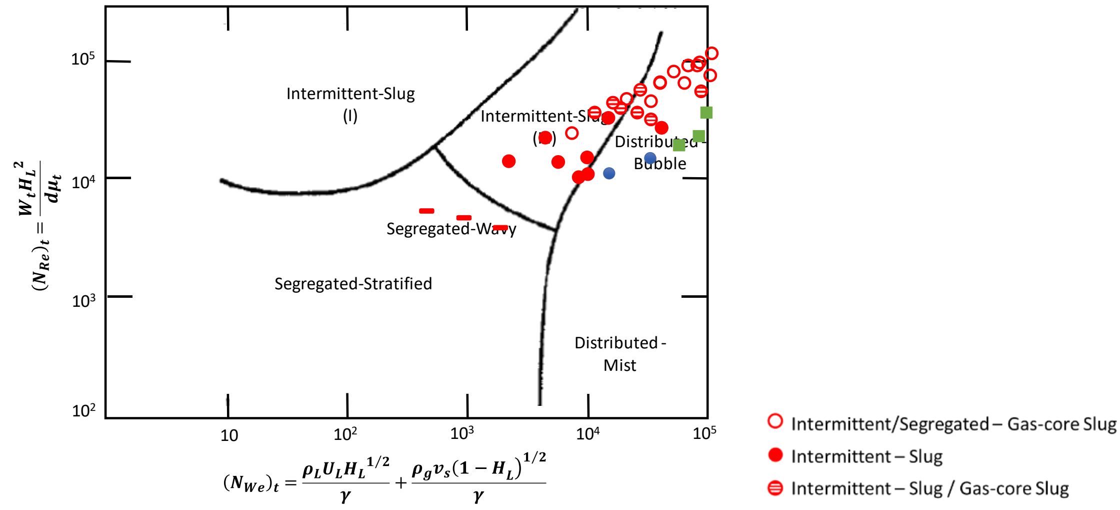

Eaton (1967) modified from[32], p823

(a)

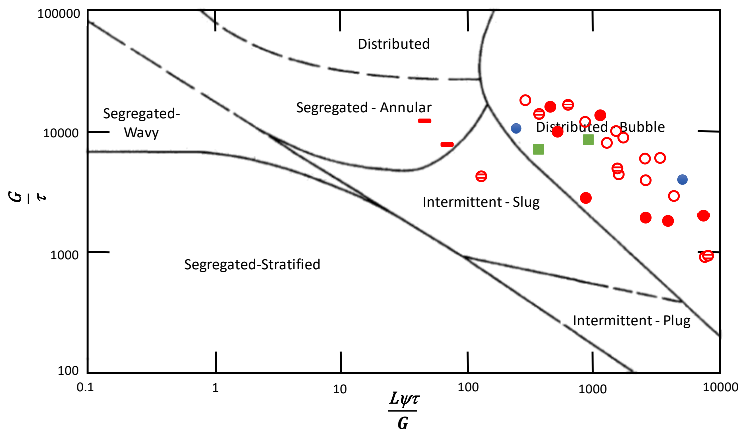

Baker (1953) modified from [203], p12

(b)

Figure VIII-4. Experimental data classification from ECT measurements adjoined with existing flow pattern maps showing the relationship between (a) Two-phase Weber function and Reynolds number, and (b) Gas-mass and Gas-liquid ratios

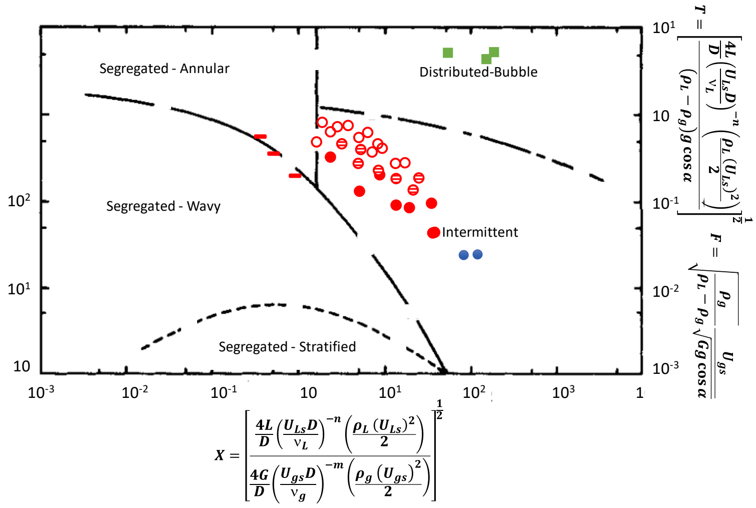

Taitel-Dukler (1976) modified from[202], p51

(a)

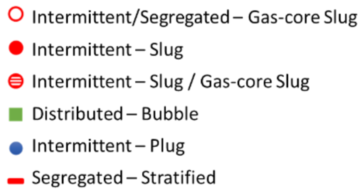

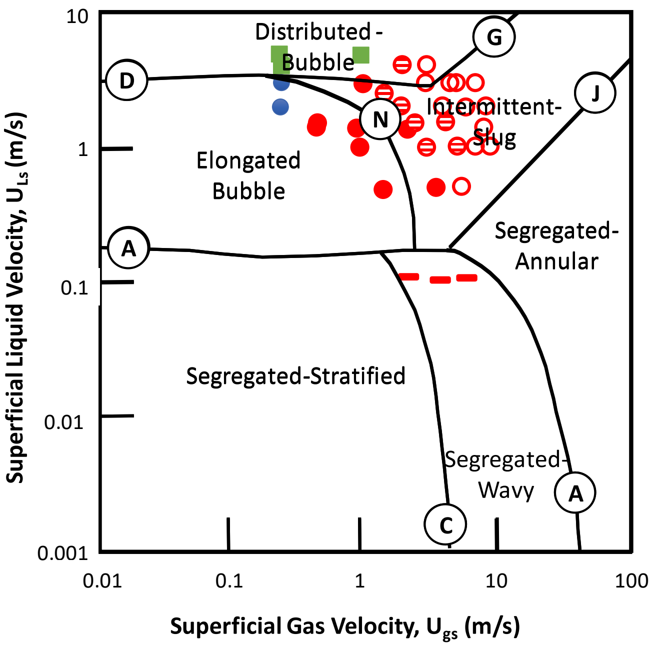

Barnea (1986) modified from [204], p4

(b)

Figure VIII-5. Experimental data classification from ECT measurements adjoined with existing flow pattern maps showing the relationship between (a) Lockhart and Martinelli and Taitel-Dukler transition parameters, and (b) gas and oil superficial velocities

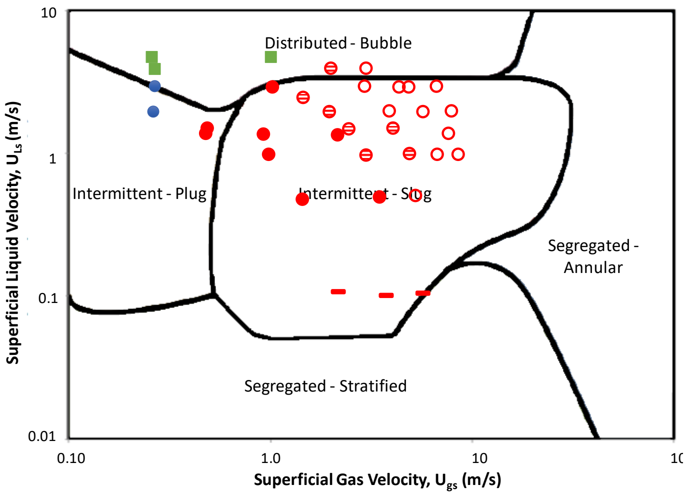

NEL map (1996) modified from [214], p62

(a)

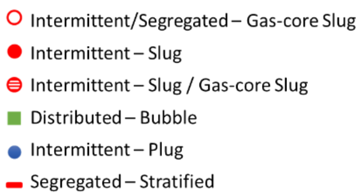

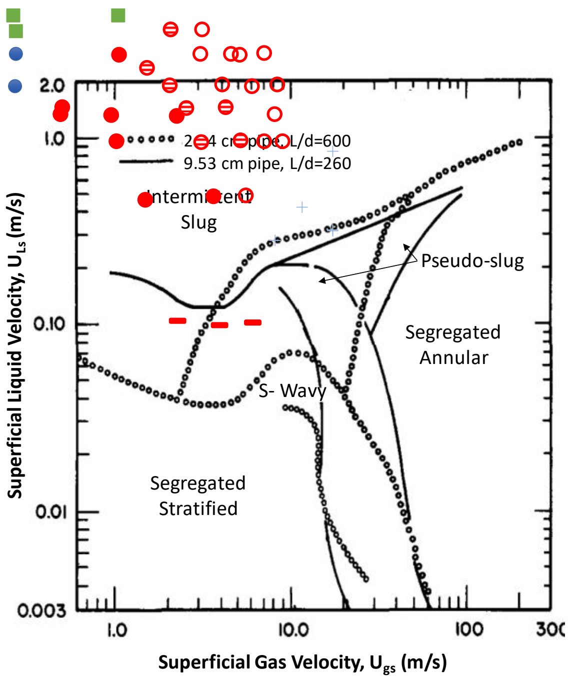

Lin and Hanratty map (1987) modified from [205], p555

(b)

Figure VIII-6. Experimental data classification from ECT measurements adjoined with existing flow pattern maps showing the relationship between gas and oil superficial velocities

The quantification of the accuracy of the prediction of the experimental flow patterns is summarised in Table VIII-5. Considering the similar outer features of the gas-core slugs and the traditional slugs, in addition to the fact that gas-core slug regime has not been previously classified in the literature, the summary in Table VIII-5 combines all experimental points dominated by both gas-core slug and full slug flow under the 'Intermittent-Slug' label.

Table VIII-5. Predictive success of flow pattern maps

Map		Segregated-Stratified	Intermittent-Slug	Intermittent-Plug	Distributed-Bubble	Total
Taitel-Dukler	☑	2	27	2	3	34
	☒	1	0	0	0	1
Predictive success		66.7%	100.0%	100.0%	100.0%	97.1%
Beggs & Brill	☑	3	26	0	3	32
	☒	0	1	2	0	3
Predictive success		100.0%	96.3%	0.0%	100.0%	91.4%
Beggs & Brill-mod	☑	3	24	0	3	30
	☒	0	3	2	0	5
Predictive success		100.0%	88.9%	0.0%	100.0%	85.7%
NEL	☑	1	23	2	3	29
	☒	2	4	0	0	6
Predictive success		33.3%	85.2%	100.0%	100.0%	82.9%
Barnea	☑	3	19	0	3	25
	☒	0	8	2	0	10
Predictive success		100.0%	70.4%	0.0%	100.0%	71.4%
Shell	☑	0	18	0	0	18
	☒	3	9	2	3	17
Predictive success		0.0%	66.7%	0.0%	0.0%	51.4%
Eaton	☑	3	9	0	3	15
	☒	0	18	2	0	20
Predictive success		100.0%	33.3%	0.0%	100.0%	42.9%
Baker Mod	☑	0	0	0	3	3
	☒	3	27	2	0	32
Predictive success		0.0%	0.0%	0.0%	100.0%	8.6%
Lin & Hanratty	☑	0	0	0	0	0
	☒	3	27	2	3	35
Predictive success		0.0%	0.0%	0.0%	0.0%	0.0%

From Table VIII-5, Figure VIII-3(a), and Figure VIII-5(a) it is evident that the ECT characterisation fits well with the predictions from Beggs and Brill and Taitel-Dukler, whereas Baker and Lin and Hanratty show significant discrepancies or no match at all as seen in Figure VIII-4(b) and Figure VIII-6(b), respectively.

The Reynolds function used by various other authors was seen to be insignificant once the flow phases are in a turbulent state yielding a negligible effect from the viscous forces. Contrasting the accuracy of Beggs and Brill and those from Eaton and Baker, it is apparent that the variations of the fluid properties are also non-relevant for the conditions assessed. This is attributed to the significant difference between the physical properties of the gas and liquid phases. The consistent behaviour of gas-liquid flows in pipes contributes to the model having acceptable results over a large range of conditions. This, however, may not be the case for mixtures of fluids with comparable properties, i.e. liquid-liquid flows, where the effect of the properties of the fluids cannot be neglected.

8.6 Gas-core slug flow pattern

The reconstructed structures of the gas-core slugs from ECT measurements are consistent with those reported in [206] using WMS. Gas-core slugs have similar outer features to intermittent slugs but with a sustained central core structure. Figure VIII-7 shows reconstructed images from slugs and gas-core slugs together with the transient volumetric fraction. Gas-core slugs are characterised by the liquid (red) wrapping up around the pipe from an initial stratified state followed by a sustained gas core (blue). The full slug structure is characterised by the rise of the fluid’s interface (green), remaining roughly horizontal, as if cross-section is being filled from below. Full slugs may have gas-core entries or tails, as described in [221].

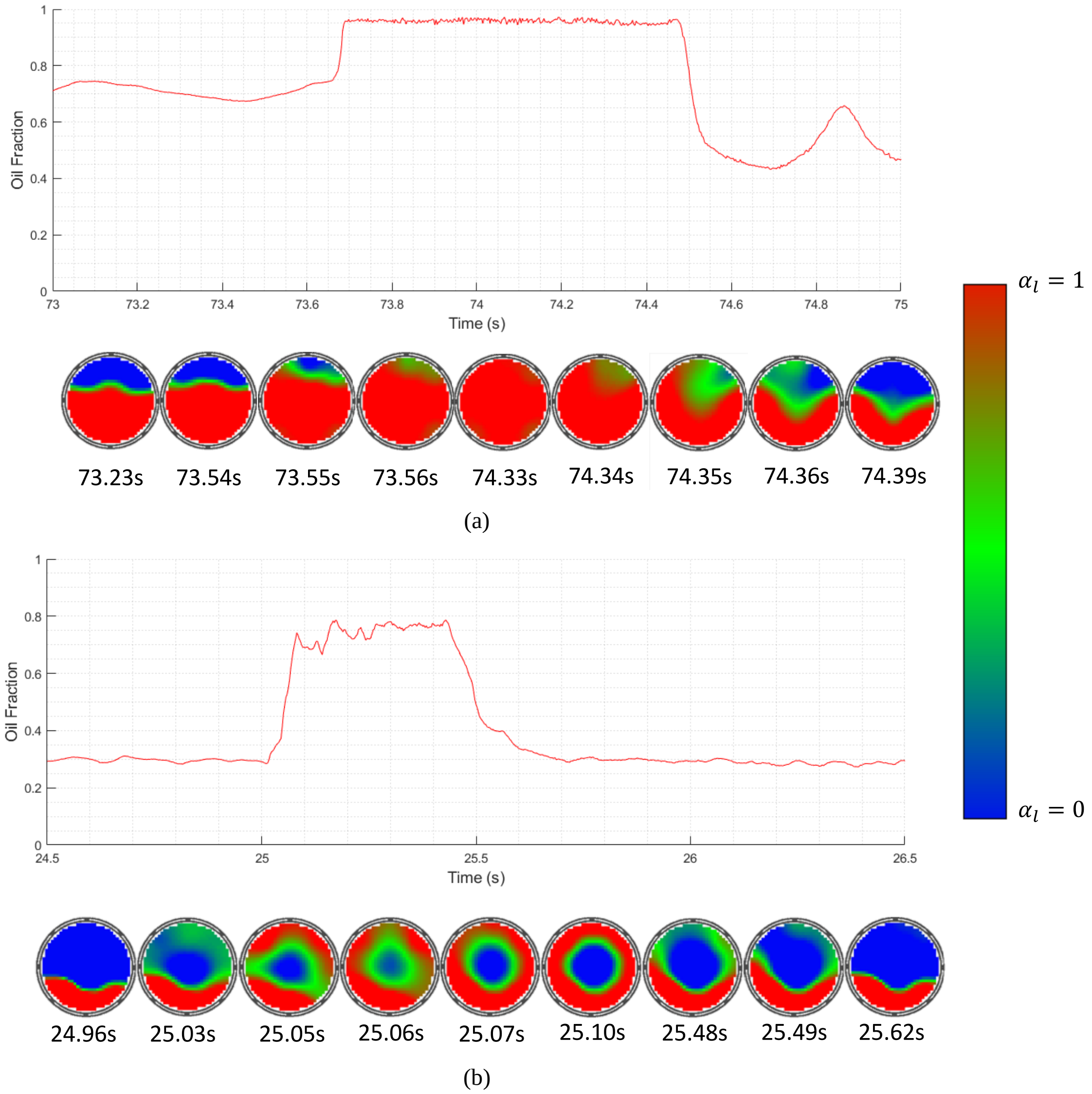

Figure VIII-7. Illustration of the evolution of the liquid volumetric fraction (α_l) of (a) a full slug and (b) a gas-core slug at different times

8.6.1 Intermittent regime sub-categorisation

An automatic flow regime characterisation algorithm developed by iPhase ltd was applied to the experimental data to differentiate between gas-core slugs and full slug structures. The outcomes, analysed by the author, resulted in the characterisation of 4875 intermittent structures, of which 3393 met the logic consistent with GCS and 1482 with that of full slug structures.

The algorithm assigns, at every time frame, an oil volume fraction to each pixel within the virtual 32x32 pixel-matrix across the cross-section. This volume fraction is proportional to the pixel permittivity derived from the capacitance measured by the inter-electrode pairs as by Equation (71).

The slug identification methodology relies on contrasting key parameters measured in different areas of the pipe cross-section to identify and differentiate among various spatial phase distributions automatically. This approach avoids comparisons of averaged cross-section fractions, which allows correct characterisation of the structures that coexist at the same conditions, like the pseudo-slugs discussed in [206]. The flow pattern recognition algorithm groups the cross-section pixels into 13 zones, as illustrated in Figure VIII-8. This discretisation follows the Nyquist–Shannon sampling theorem [222], which, when applied to image processing, limits the dimensions of the zones to at least two times the size of the structures to be characterised. The zonal discretisation is suitable for velocity distribution calculation given that it is highly unlikely that the velocity of the fluid varies on a pixel-by-pixel basis in gas-liquid flow, yet it ensures that no actual information is lost in the analyses process.

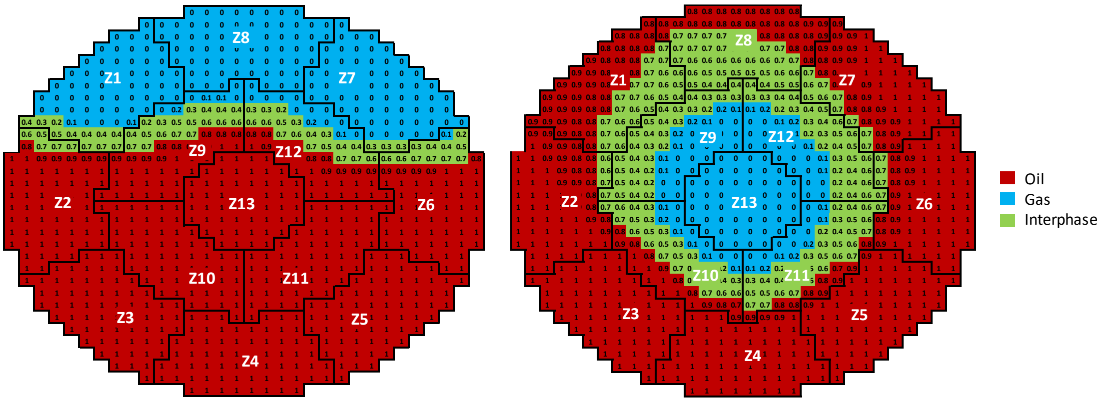

(a) (b)

Figure VIII-8. The zonal discretisation of the pipe cross-section showing the oil volume fraction in every pixel for (a) a developing slug corresponding to t=73.23s in Fig. 3a, and (b) a gas-core slug corresponding to t=25.07s in Fig. 3b. Note that Z1 refers to Zone 1, etc.

Contrasting the volume fractions of the intermittent structures, derived from the reconstructed permittivity distributions, allows the differentiation of gas-core slug flow from full slug flow. The comparison considers the phase fractions measurements at different zones of the cross-section, i.e. at the centre of the pipe and at various zones in the vicinity of the core. The rationale behind this zonal analysis is based on the spatial differences of the two types of slugs, where the gas-core slug flow accommodates a large void fraction in the centre of the pipe, zones 9 to 13, which corresponds to a lower permittivity measurement. Thus, pattern identification is feasible if the measurements from the zones of interest are secluded.

Figure VIII-9 illustrates the parameters used for characterising the flow regimes for further analysis of the flow dynamics using ECT measurements. The premise of the automated flow pattern differentiation between the full slug and the gas-core slug flow are shown in Figure VIII-10, in accordance to the detailed steps given at the end of this subsection.

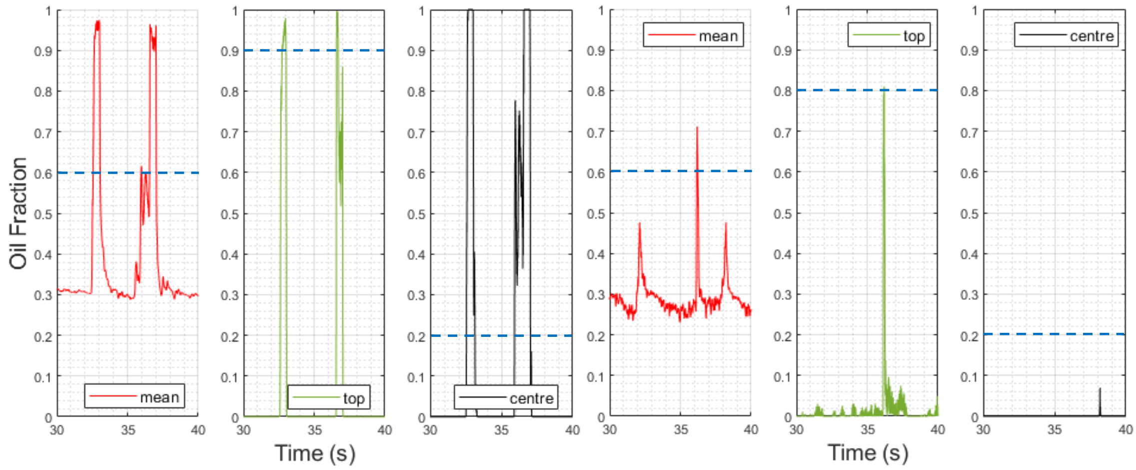

(a) (b) (c) (d) (e) (f)

Figure VIII-9. Illustration of the principles of the algorithm for flow pattern detection showing the measurements of volume fraction from a full slug (a, b, and c) and a gas-core slugs (d, e, and f) registered in the entire cross-section (mean), the top of the pipe (Zone8) and the centre of the pipe (zone 13)

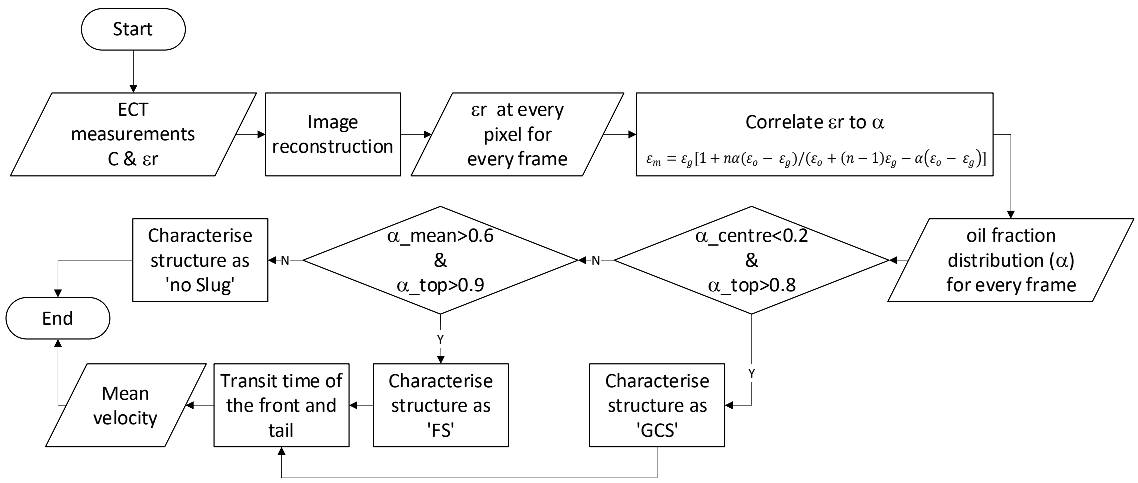

Figure VIII-10. Flowchart of the workflow of the algorithm for flow regime characterisation showing the decision rules. The variable C in the first input block refers to the measured inter-electrode capacitance and ε_r is the relative permittivity. The variable α is the liquid fraction and the terms 'mean' 'centre' and 'top' refers to the selected zone locations within the pipe cross section (see Figure VIII-8 and Figure VIII-9)

a) Measure the capacitance (C) between every electrode pair;

b) Solve the inverse problem and reconstruct a frame-by-frame image showing the relative permittivity (ε_r) distribution in every pixel via capacitance measurements over a given test period;

c) Determine the frame-by-frame volumetric fraction (α) image from the reconstructed permittivity distribution over a given test period, via Equation (71). This is illustrated in Figure VIII-8, where for a given frame -selected from the data in Figure VIII-7- the oil volumetric fraction in every pixel is populated across the entire cross-section;

d) Deduce the occurrence of a gas-core slug or a full slug based on a set of rules relating to the fraction of oil and gas in selected zones of interest, e.g.:

- A low volumetric fraction of oil ($\alpha < 0.2$) in the pipe centre (this can be zone 13, a subsection of zone 13, or zone13 with subsections of adjacent zones-see Figure VIII-9(f)) combined with a high volumetric fraction of the oil ($\alpha > 0.8$) in the near vicinity zones wrapping around the gas core (see Figure VIII-9(e)) indicates the occurrence of a gas-core slug;
- A consistent overall high value of the mean volumetric fraction of oil across all the imaging zones ($\alpha > 0.6$) (see Figure VIII-9(a)) combined with a high volumetric fraction of oil ($\alpha > 0.9$) in at least a subsection of zone 8 (see Figure VIII-9(b)) over a number of the frames indicate an occurrence of the full slug.
- If none of the conditions above are met the algorithm discards the existence of the intermittent slug flow patterns considered.

e) Compute the mean cross-correlation velocity for every structure considering the transit time of the front and tail between the measurement planes. The slug length accounts for the time gap between triggers.

The results from the classification algorithm were validated through blind tests. For verification purposes the algorithm outputs, i.e. number of structures, time of occurrence and length, from three different test points were compared to transient measurements and reconstructed images.

The results of the algorithm are exploited in the remainder of this chapter to evaluate in detail the characteristics and evolution of the intermittent flow structures.

8.6.2 Slug characterisation

During the data analysis, a particular phenomenon was observed in which two types of gas-core slugs, i.e. fully developed gas-core slugs and developing slugs, occurred throughout the experimental campaign. At certain conditions, the gas-core slugs may evolve into regular full slugs or decay over time without further transition. For the purpose of the analysis presented below, all structures are assessed.

8.6.2.1Number of structures

Figure VIII-11 shows the number of gas-core slugs, designated GCS and full slugs, FS, with oil velocity for all test points, each measured throughout 120 s. The relationship between the number of structures and the mixture velocity is evident in Figure VIII-11(a). At low velocities, the intermittent structures are dominated by full liquid slugs. When the velocity increases above 6 $m.s^{-1}$, as a result of increasing gas velocity, only gas-core slugs develop. Results suggest that for high mixture velocities gas-core slugs are not likely to transition to full slugs.

From Figure VIII-11(b), it is apparent that increasing the gas velocity decreases the number of FS structures, but there is no evidence of the influence of the superficial gas velocity on the number of GCS, as suggested in [206]. This discrepancy can be explained by the overall variation of the mixture velocity, which, while not considered in [206], is determinant in the occurrence of FS.

Contrary to the effect of the superficial gas velocity on the intermittent structures, results in Figure VIII-11(c) show a clear relation between the oil superficial velocity and the increasing number of structures, both FS and GCS. The upward trend indicates that as the velocity of the oil increases, a larger number of structures develop, with predominantly more GCS structures for oil velocities beyond 2 $m.s^{-1}$.

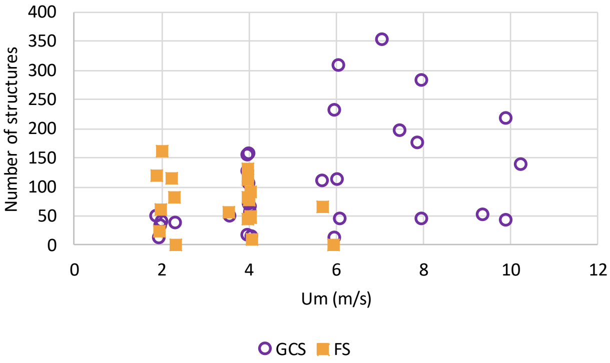

(a)

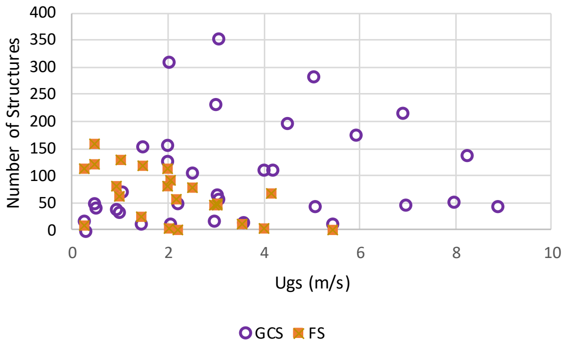

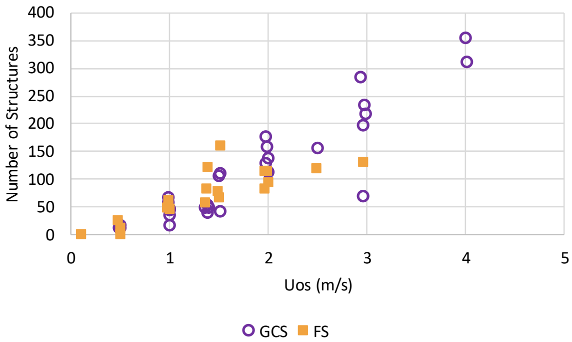

(b) (c)

Figure VIII-11. Correlation between the number of intermittent structures and (a) the mean flow velocity; (b) the mean gas superficial velocity; and (c) the mean oil superficial velocity over a testing period of 120 s

8.6.2.2Structure span

The relationship between the time span of the slug structures and the mean flow velocity is presented in Figure VIII-12(a). The span of GCS structures remained under 0.4 s for all test points. Furthermore, the gas-core slug transition time is consistently lower than 0.2 s for the same condition at which full slugs transition time reaches up to 1 s.

Figure VIII-12(b) and (c) show the evolution of the span of the GCS and FS structures with increasing superficial velocities. Results show that for a given mixture velocity, where both structures co-exist, the length of the CGS increases with increasing gas velocity and that of the FS increases with increasing oil velocity.

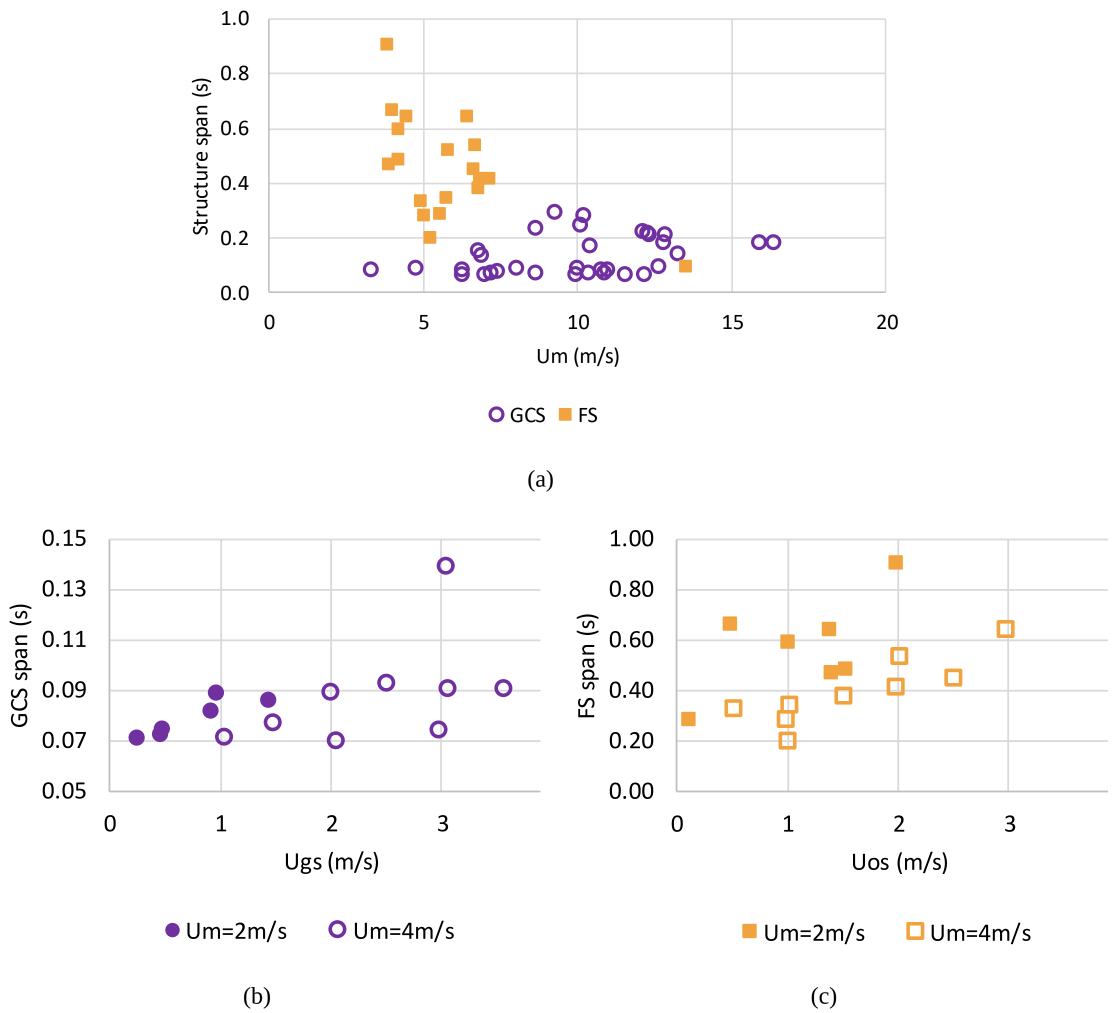

Figure VIII-12. Correlation between (a) the mean duration of the structures and the flow velocity; (b) duration of the gas-core slugs and the gas superficial velocities and; (c) the duration of the full-slugs and the superficial velocity of the oil phase

8.6.2.3Slip velocity

Figure VIII-13 contrasts the oil fraction of a gas-core structure and the velocities of the phases in selected cross-section zones. In gas-core slugs, the central region, denoted Zone 13, contains mainly gas, with an enveloping oil film around the perimeter of the pipe, represented by Zones 1 to 8. The oil velocities at the bottom and top of the pipe, are plotted together the gas velocity in the central region. The velocities shown are the effective phase velocity (V) in the zone given by:

$$\mathrm{V}_{p\_Zi} = \frac{Q_{p\_Zi}}{A_{Zi}} \text{ for } i = \{1,2,\cdots,m\}\ (m = 13) \qquad (88)$$

where the subscript p refers to the phase, i.e. gas or oil, and i is the index of the cross-section zone in accordance with the discretisation shown in Figure VIII-8. A_{Zi} is the area of the Zone 'Z_i' and Q_{p_Zi} is the fraction of the phase 'p' in the respective zone computed from (89).

$$Q_{p\_Zi} = Q_p \alpha_{p\_Zi} \text{ for } i = \{1,2,\cdots,m\}\ (m = 13) \tag{89}$$

where Q_p is the total inlet flowrate of the phase 'p' for each test point conditions, and α_{p_Zi} is the volumetric fraction occupied by the phase 'p' in the zone 'Z_i'.

It is evident that as the structure evolves, the liquid forms a film adhering to the pipe perimeter and enveloping the central region, the velocity at the bottom (V_{o_Z4}) and top (V_{o_Z8}) tend to the same value while the GCS passes, whereas the velocity of the central zone (V_{g_Z13}) rises as a result of the decreased area of gas flow. As the structure decays, and gas-core breaks, the gas velocity decreases to its initial value.

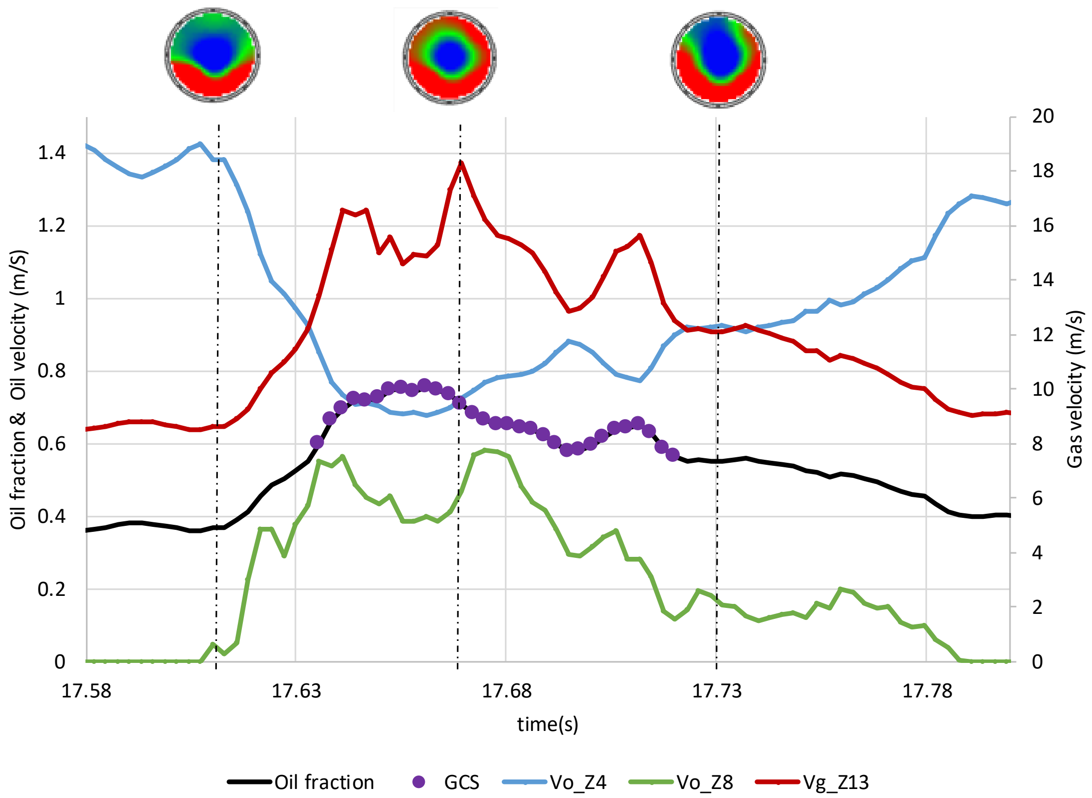

Figure VIII-13. Evolution a gas-core slug showing the liquid fraction and the liquid velocities at the bottom (zone4, Vo_Z4) and top of the pipe (zone8, Vo_Z8), alongside with the gas velocity in the central region (zone 13, Vg_Z13). Note that the colour pattern of the cross-section reconstructed images at the top of the graph refers to the liquid volumetric fraction (α_l) range given in Figure VIII-7

Figure VIII-14 shows the evolution of a gas-core slug into a full slug structure. The slip velocities between the gas and the oil phases are large for the gas-core slug but decrease substantially when the structure evolves to a full slug structure. This is made evident in the slip velocity between the oil and gas phases occupying the somewhat central zone 11.

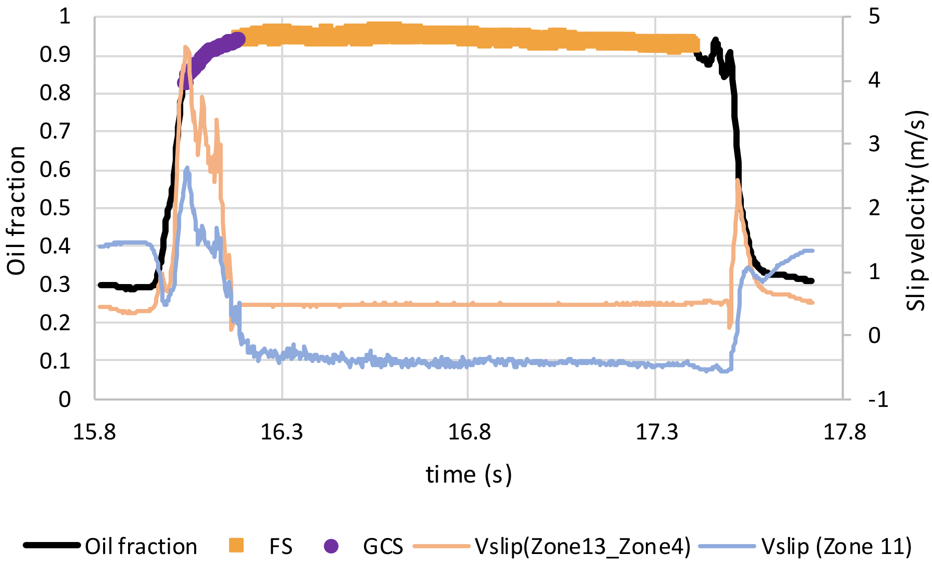

Figure VIII-14. Oil fraction of a gas-core slug evolving into a full slug. The slip velocities between the core and the bottom of the pipe- Zone13 and Zone4, respectively- and the gas and oil fractions occupying Zone 11 are shown

The slip velocities between the oil and gas phases in full slugs and gas-core slugs are compared for two datasets in Figure VIII-15. The flow in the dataset 1 is dominated by full slugs; however, the occurrence of several gas-core slugs throughout the test allows comparison of the slip velocities for the same input conditions. It is evident that the slip velocities in gas-core slugs structures are much larger than in full slug flow, as proposed in [207].

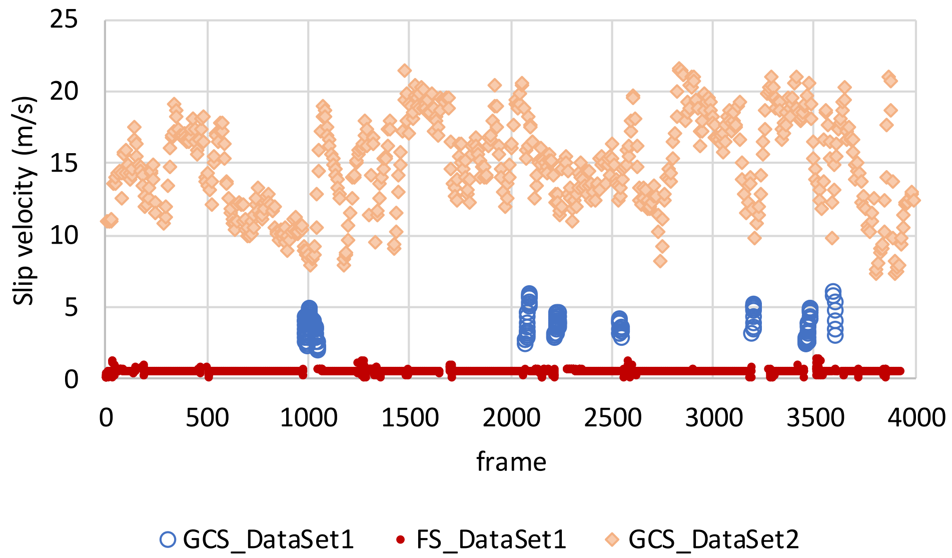

Figure VIII-15. Slip velocity in gas-core slug and full slug flow

8.6.3 Gas-core slug prediction

8.6.3.1Beggs and Brill-based transition model

The gas-core slug flow, evidenced under the experimental conditions evaluated, is well defined by the Froude-holdup relationships as a subgroup within the intermittent region, as shown in Figure VIII-3(a). Hence, the Froude number and input liquid content are suggested here for gas-core slug flow characterisation. The relationship between these variables, supports the characterisation of the gas-core slug flow based on the Beggs and Brill map.

The transition between the full slug flow and the gas-core slug was seen to occur for large liquid inflow and high inertial to gravity forces ratios, see Figure VIII-3(a). From the Beggs and Brill map, the transition to gas-core slug flow is given by a straight line, of the form:

$$Fr = 4\lambda^{0.0021}, \qquad \lambda \in [0.0595, 0.6909] \tag{90}$$

An extended analysis on the suitability of the transition model in (90) comprised the evaluation of all 4875 intermittent structures grouped into 33 data sets. The data are plotted in Figure VIII-16, along with the transition criteria above.

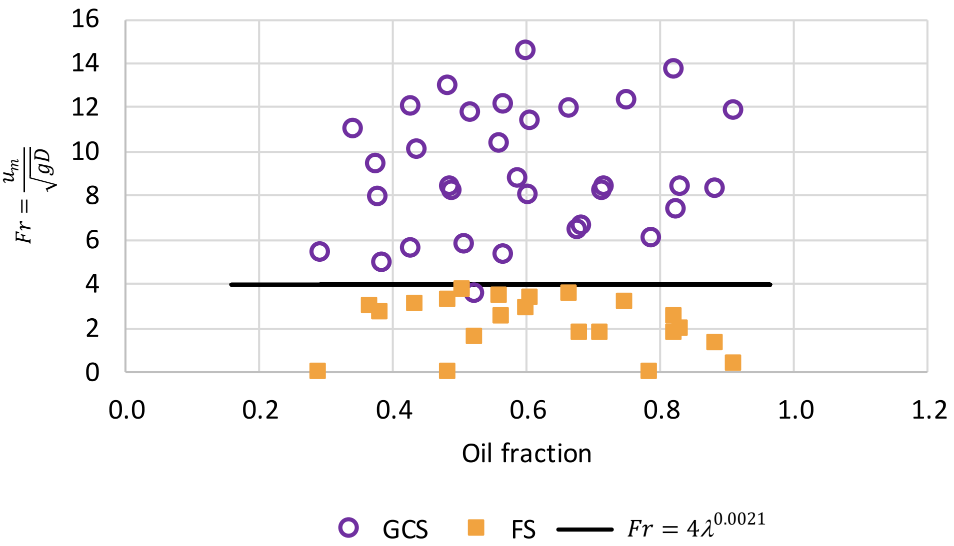

Figure VIII-16. Transition model between full-slug and gas-core slug-dominated flow, based on Beggs and Brill modified map, showing the correlation between the Froude number (Fr) and the flow pattern transition for the given range of non-slip liquid holdup (λ)

8.6.3.2Taitel and Barnea combined prediction criterion

Departing from the purely empirical approach adopted by Beggs and Brill, the mechanistic work from Taitel and Dukler and Barnea is addressed following. In [202] Taitel suggests that the equilibrium liquid level in stratified flow is broken when the interphase surpasses the pipe centre. For a given liquid input, decreasing the liquid velocity results in an insufficient liquid flow to maintain the liquid slug, and so the liquid in the wave is swept up and around the pipe to form a gas core in the slug body.

Barnea [204], stablished that the transition mechanism from dispersed bubbles to intermittent slug flow is defined by (91). From [205] and Figure VIII-5, it is readily evident that the GCS occupies a region of transition between the distributed bubble and intermittent slugs. It is then logical to assume that, depending on the mixture velocity, when the bubble size is large enough they coalescence forming larger gas structures that could derive into gas-core slug or full slugs.

$$d_c \geq \left[0.725 + 4.15\left(\frac{U_{gs}}{U_m}\right)^{\frac{1}{2}}\right]\left(\frac{\gamma}{\rho_L}\right)^{\frac{3}{5}}\left(\frac{2f_M}{D}U_m{}^3\right)^{\frac{-2}{5}} \tag{91}$$

where f_M refers to the friction factor, and d_c is the maximum diameter for stable disperse flow. The remaining terms are defined after Table VIII-4.

The transition criterion in (91) was tested on the experimental data. Gas-core slug flow was found to occur when the critical bubble diameter, above which bubbles are deformed, is greater than the criteria defined by (91). Hence, unifying the Taitel and Barnea transition mechanisms, gas-core slug flow arises when the inequality in (92) is true.

$$2\left(\frac{0.4\gamma}{(\rho_L-\rho_g)g}\right)^{\frac{1}{2}} > \left[0.725+4.15\left(\frac{U_{gs}}{U_m}\right)^{\frac{1}{2}}\right]\left(\frac{\gamma}{\rho_L}\right)^{\frac{3}{5}}\left(\frac{2f_M}{D}U_m{}^3\right)^{\frac{-2}{5}} \tag{92}$$

The prediction model in (92) was tested on the experimental dataset using the mean velocities and volume fractions measured for 2833 intermittent structures. The resulting classification was compared to the results from the algorithm detailed in Section 8.6.1. The data was classified using the algorithm and the structure predictions from the model in (92). The agreement between the number of gas-core slugs and non-gas-core slugs, i.e. full-slugs in this case, is shown in Figure VIII-17. Overall, the model coincided with the algorithm classification in 2630 structures, which corresponds to a 93% match. It is noteworthy that the quality of the prediction is greater than the predictive accuracy reported using the most recently developed semi-analytical algorithms, which is around 80%, and is within the same range as those using machine learning techniques (90-96%) [223].

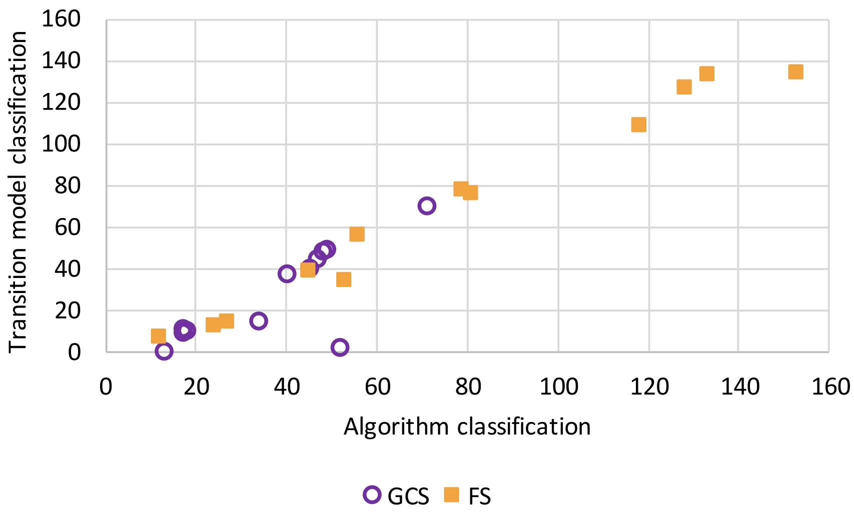

Figure VIII-17. Accuracy of the Taitel-Barnea transition criteria compared to reference slug classification from the automated algorithm

Equations (90) and (92) define the occurrence of gas-core slug structures. The transition models allow the discretisation of the zones where, for given flow conditions, the gas-core-slug flow takes place.

8.7 Flow pattern maps

This section presents two pattern charts, that would allow engineers and operators to predict gas core slug flow, as identified in this work, based on the knowledge of flow variables. Original maps do not account for gas-core slug flow, hence it is of interest to introduce this flow pattern explicitly. The zonal boundaries within these charts represent transitions between the observable flow patterns. The proposed transitions respond to the equations (90) and (92).

In Figure VIII-18, the Beggs and Brill map is reproduced, incorporating modifications to improve the agreement with the recent data and include the gas-core slug flow. The intermittent flow area remains the same size, but a sub-region is created where full slugs transition to gas-core ones. This transition is correlated to the Froude number for a constrained range of liquid input rates.

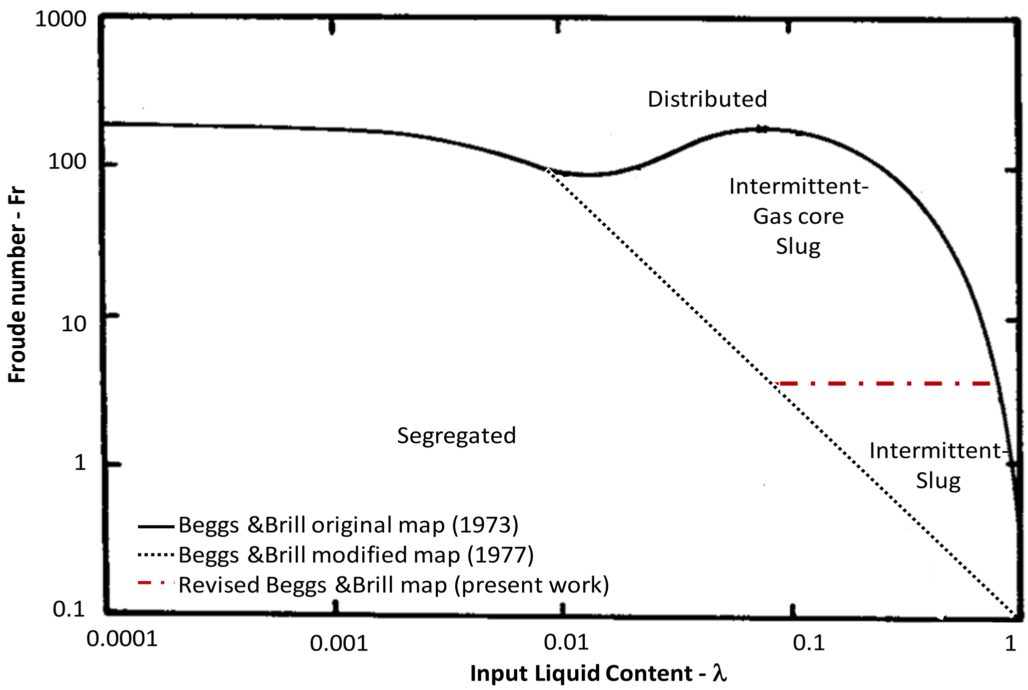

Figure VIII-18. Suggested flow pattern map for horizontal co-current flow showing the transition zones of Beggs and Brill original (1973), Beggs and Brill modified (1977) and the gas-core-slug transition proposed in the present chapter

Figure VIII-19 proposes a modification to the Taitel-Dukler map. This revision includes the gas-core slug prediction according to (92). The transition zone between the liquid slug and gas-core slug flow is defined by a red line of the form $F = -0.126\ \ln X + 0.5767,\ X \in [2, 90]$.

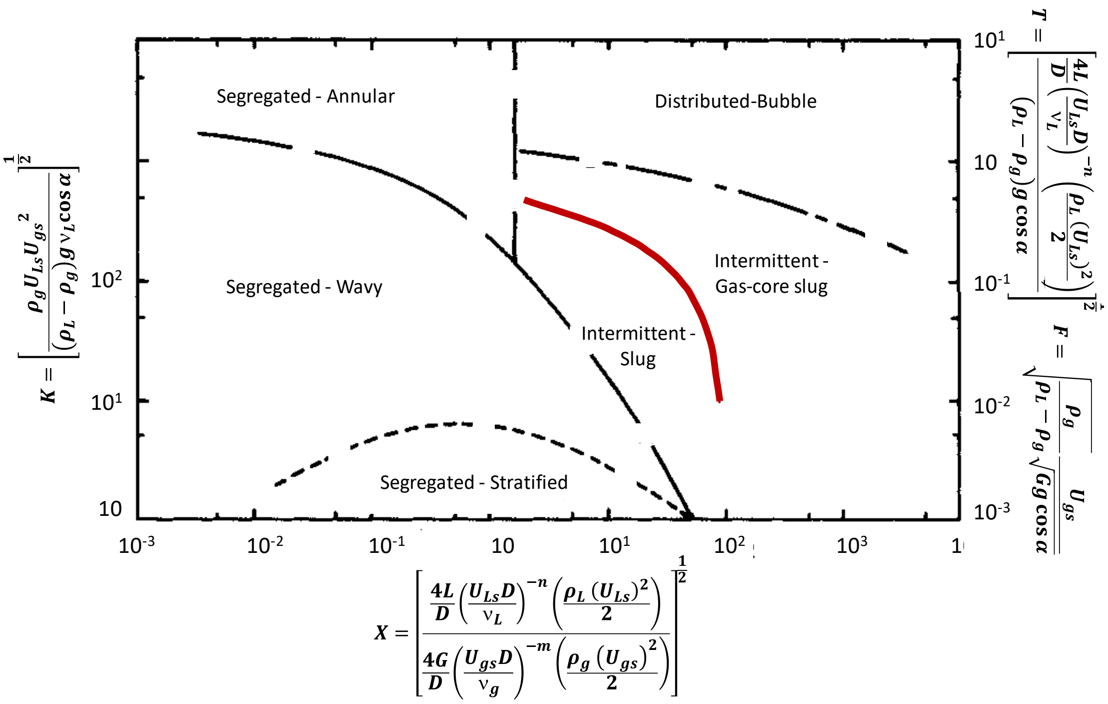

Figure VIII-19. Suggested flow pattern map modified from Taitel-Dukler for horizontal co-current flow, showing the transition between intermittent flows with a red line

8.8 Discussion and Conclusions

In this chapter, a unified flow regime classification is proposed combining published literature and the recently studied flow structure detailed in this chapter, i.e., gas-core slug. Gas-core slugs are believed to have not been differentiated in the vast majority of existing regime maps due to the difficulty in identifying the inner structure of the slug by means of traditional optical methods.

A reconstructed permittivity distribution of two-phase gas-liquid flow, using high-speed electrical capacitance tomography, enabled the identification of intermittent flow patterns in a pipeline without prior knowledge of the flow characteristics.

ECT characterisation of the experimental data was seen to fit well the predictions from Beggs and Brill and Taitel-Dukler. For flow phases in a turbulent state, the effect from the viscous forces was found negligible, and the Reynold number fails to predict flow pattern transitions. However, the Froude number was seen to provide a fair representation of the transition to dispersed flow and between intermittent flows for the given experimental conditions.

Experimental results are consistent with published literature and show that increasing the velocity of the mixture for low liquid contents results in transitions from segregated to disperse flows. Dispersion of bubbles of gas in oil only occurs at low gas velocities and high liquid ratios. Intermittent flows are observed for liquid holdups above 10%. At these conditions, a transition between the slug and the gas-core slug is observed as the Froude number increases. This phenomenon is attributed to the increase in the velocity of the gas phase.

An automated slug differentiation algorithm was used to determine the volumetric fractions within specific zones of the cross-section. The assessment of the intermittent structures allowed characterisation of the gas-core slug flow. Full slug flow decays above 6 $m.s^{-1}$, whereas gas-core slugs dominate intermittent flow for mixture velocities between 6 $m.s^{-1}$ and 10 $m.s^{-1}$. Gas-core slugs are typically shorter than full slug structures but more frequent for the same given period. Gas-core slugs showed a transition time in the order of 0.05 seconds while for full slugs, it is between 0.5 and 1 seconds. The gas-core structures exhibit large gas-oil slip velocities when compared to full slugs. This is particularly evident in cases where gas-core slug flow evolves into full slug flow.

Two revised flow pattern maps that include the gas-core slug region are provided. One transition model to gas-core slug was derived and further validated. The transition model is based on an empirical approach, with a good match to the Beggs and Brill map. A gas-core slug prediction criterion that combines the mechanistic transition mechanisms of Taitel and Barnea was tested in our dataset. Validation of the criteria resulted in an adequate accuracy of prediction in 93% of the cases.

Chapter IX Conclusions

The work presented in this thesis regarding multiphase flow measurement through electric tomography highlighted the potentials and benefits of imaging techniques to monitor multiphase flow. It has identified and addressed a gap in the literature in terms of the design and applications of MIT targeting measurement of dynamic flow structures and identification of non-conductive fluids. This chapter presents the key findings from the present work, which used numerical modelling and empirical testing for gaining a better understanding of the capabilities of tomography technology for hydrocarbon transport. Additionally, recommendations for future work are included at the end of the chapter in order to improve and expand the applicability of the findings of this study.

9.1 Conclusions

The present thesis studied the feasibility and capability of electrical tomography for multiphase flow measurement. The main scientific contribution of this work is the demonstration that electromagnetic signals can be used to characterise three-phase flow. This demonstration was underpinned by the simulation work undertaken in Chapter VII. It was shown that the amplitude signals were correlated to changes in dielectric properties of the medium, which, in combination with phase measurement, allowed differentiation of three-phase components over the same cross-section. The analyses presented suggest that it is feasible to broaden the application niche of MIT technology to non-conductive phase differentiation, which could ultimately lead to enhanced measurement accuracy by eliminating the need for a separate measurement system.

A key technical contribution is the exploitation of tomography techniques for flow pattern recognition presented in Chapter VIII. The results of this study led to new knowledge of intermittent gas-liquid structures and transitions. The work undertaken consisted of comparing the mean concentration of various cross-section sectors to characterise the flow regimes inside the pipe according to specific flow-related key parameters. The analysis focused on a potentially new intermittent flow pattern, with similar outer features to full slugs, but with a sustained central gas core. This flow pattern, designated gas-core slug in this work, was characterised in detail in Section 8.6.2. Gas-core slugs were observed to be shorter and more frequent than full slugs. Transition between full slugs and gas core slugs was seen to be determined almost entirely by the ratio of inertial to gravity forces given by the Froude number. This work led to a mechanistic-based prediction criterion for future gas-core slug flow development.

The experimental work in Chapter VI presents another contribution to new knowledge by challenging the present ECT operational envelope, which suggests enhanced opportunities to use ECT for higher water contents than used traditionally. Furthermore, in Chapter VI, the capability of the MIT prototype was assessed through comparison to an ECT legacy meter, whose measurements were in turn compared to a GRT reference system. The experimental results from Section 6.4.5 and Section 6.3.3.2 highlighted opportunities for the use of multimodal metering systems based on the combination of ECT and MIT, and ECT and GRT, respectively.

Coupled with the above contributions, the work undertaken in this thesis and developed through the different chapters aimed to address a series of fundamental questions. The research questions, designed to gain a better understanding of tomography systems for hydrocarbon transport, were first introduced in Section 1.3. Details of how the questions were conveyed within the thesis embodiment are given below, following the same order in which they were formulated.

In Chapter II, the challenges that the petroleum industry faces in regards to multiphase flow measurement in the fields were addressed and contextualised within the current research trends and MFM market. It was seen that 73% of readily available MFM technologies in the market are either based on intrusive pressure drop techniques or are associated with nucleonic density measurements, which fail to address some of the industry challenges in terms of non-intrusiveness, accuracy, costs and environmental impact. With this in mind, the industry requirements for MFM in terms of flexibility and robustness were incorporated into the prototype hardware design ensuing a single-unit meter with no moving parts and fixed sensor position (see Chapter V). The resulting clamp-on mechanism designed provides portability, ease of installation and maintenance, and low manufacturing costs, given available 3D printing techniques. Furthermore, the meter principle of operation does not rely on nucleonic measurement methods. This decreases costs, ease deployment, and meets the industry demands for cleaner energy production.

The effects of the changes in the physical characteristics of the sensing system and the fluid properties on the MIT measured signals were systematically assessed in Chapter IV and Chapter V. As part of the study, an MIT hardware design that enabled detection, recognition and identification of key properties typically found in hydrocarbon multiphase transport was presented. From the analysis of the key sensor design parameters, i.e. dimension, profile, winding gauge, and number or turns; three performance models were provided which support extended applicability of the characterisation presented. It was demonstrated that square coils provide MIT with enhanced measurement capabilities and that the sensor dimensions and number of turns are key in to enable improved sensitivity. The dimensions and material of the electromagnetic shield was seen to have a significant impact on the electromagnetic induced measurements. Metallic shields show a superior wave attenuation capacity for the MIT operating frequencies of interest.

The operational envelopes of MIT and ECT were evaluated by using alternative data acquisition and processing approaches through simulation and empirical work in Chapter VI and Chapter VII. In accordance with published results, ECT experiments conducted using the traditional data acquisition approach failed to predict the relative permittivity of the flow for water cuts above 45%. However, ECT measurements from a secluded measurement pair showed a quasilinear trend of the capacitance measurement with increasing water content, for mixtures of up to 75% of water cut. Furthermore, it was demonstrated that MIT is able to capture changes in permittivity, in addition to the customary conductivity changes. These results offer possibilities to continuously monitor and measure three-phase flow for mixtures of bulk conductivity below 1 S/m using a single apparatus. The above results challenge the existing limitations of both measurement technologies and open the opportunity to broaden their applications. Moreover, the work in the preceding chapters not only demonstrates the enhanced performance of each meter on extended fluid configurations but also validates the benefits of the multimodal measurement approach. The multimodal approach explored in Chapter VI encompasses measurements of electric and dielectric properties leveraging the experience on the combination of ECT and GRT.

A thorough instrument calibration methodology was undertaken in Chapter VI to assess the accuracy of the measurements and the operability of the instruments. The MIT and ECT instruments were chain calibrated. Measurements from the MIT prototype showed consistency and linearity with a repeatability of 4% for static bulk conductivities ranging from 1 S/m to 5 S/m and an accuracy of ±2.5% for water cuts above 40% in stratified two-phase oil-water flows. Permittivity detection from ECT proved accurate (over 4%) for both phantom tests and for gas-oil flow as by comparison with a reference GRT.

This thesis exploited the benefits of tomography techniques for flow pattern characterisation. The analysis of the experimental data led to a better understanding of the transition boundaries between the flow regimes and their relationship with dimensionless quantities. The proposed application of tomography techniques proved to be an improvement over traditional flow pattern identification methods and provides a possible new future direction of the technology and MFM in general.

9.2 Recommendations for future work

The work presented in this study can be further extended based on the following suggestions categorised in terms of numerical modelling, experimental methodology and key findings that impact the understanding of the fundamentals of electromagnetic induced metering for multiphase flows.

9.2.1 Numerical Modelling

The numerical modelling approach used to solve the electromagnetic Forward Problem treated the field-fluids interaction considering static materials. The limitations of this approach were made evident in Chapter VI, as the interface dynamics observed during the tests, which were not considered by the simulation model, lead to discrepancies between the simulated and measured trends. It may be useful to combine electromagnetic solvers with fluid mechanics modules, i.e. CFD. Using a multi-physics approach would provide an integral solution, which would enable the characterisation of the electromagnetic measurements with the varying spatial fluid distribution.

9.2.2 MIT design

The present study focused on the optimisation of the sensor array and shielding by exploring different possibilities for the sensor geometrical design and attenuation materials. Although a thorough study was performed to optimise the hardware of the MIT prototype for multiphase flow, an optimised meter requires extended work on other components. Following the results in Figure VI 4, which were the very first from the MIT prototype, it was found that the electronics interface have a significant impact on the system capabilities. The prototype electronics should be carefully designed to ensure it is stable and robust to meet the demanding field deployment requirements. MIT meter optimisation should include the electronic circuitry, the computing unit and its software components for image reconstruction and data acquisition protocol.

9.2.3 Sensor optimisation models

The developed optimisation sensor models fitted adequately to the experimental data for the setup used. The models could be extended to automatically predict the performance of a given set of sensor designs without the need to solve the entire Forward Problem. The incorporation of the developed correlations into optimisation techniques with different weights for each derived model will require the use of global optimisation algorithms, increasing the overall computational complexity yet allowing the automation of the sensor design process.

9.2.4 Permittivity measurements through MIT

The absolute MIT amplitude signal provides information on the flow permittivity, which can be traced back to different non-conductive fluids. Although this signal is at least one order of magnitude greater than that observed on the real and imaginary components disjointedly, it is still a few orders of magnitudes smaller than the background signal. There is an opportunity to prove this concept experimentally, provided sophisticated data acquisition equipment is available.

9.2.5 Flow pattern maps

A comprehensive analysis was conducted to characterise gas-core slugs. More research needs to be undertaken to characterise these intermittent structures fully. The decay of gas-core slugs to full slugs is not yet fully understood. An extensive study focused on interfacial phenomena would assist with developing a thorough understanding of the transition mechanisms. Furthermore, accurate closure relationships need to be determined to improve current multiphase flow models to accommodate this novel flow regime.

Finally, the proposed modifications to flow regime transition map and transition criteria to gas-core slugs can be further extended to a wider range of flow conditions, fluid properties, and pipe configurations by including additional sets of experimental data.

References

[1] M. Hermann, T. Pentek, and B. Otto, "Design principles for industrie 4.0 scenarios," *Proc. Annu. Hawaii Int. Conf. Syst. Sci.*, vol. 2016–March, pp. 3928–3937, 2016.

[2] F. Todd, "What are the pros and cons of automation in the oil and gas industry?," *NS Energy*, 2019. [Online]. Available: https://www.nsenergybusiness.com/features/oil-and-gas-automation/. [Accessed: 17-May-2020].

[3] G. Falcone, G. F. Hewitt, C. Alimonti, and B. Harrison, "Multiphase Flow Metering: Current Trends and Future Developments," *Proc. SPE Annu. Tech. Conf. Exhib.*, 2001.

[4] D. Haverkamp, "Development costs of non-associated gas reserves in selected countries," *Soc. Pet. Eng.*, no. 1, pp. 1–30, 1993.

[5] H. Abdel-Aal, M. Aggour, and M. Fahim, *Petroleum and Gas Field Processing*. New York: Marcel Dekker, Inc, 2003.

[6] J. M. Campbell, *Gas Conditioning and Processing Vol. 2: The Equipment Modules*, 7th ed. Oklahoma: Campbell Petroleum Series, 1992.

[7] A. Peyton, "Mutual inductance tomography," in *Process Tomography: Principles, Techniques and Applications*, R. A. Williams and M. S. Beck, Eds. Oxford: Butterworth Heinemann, 1995, pp. 85–100.

[8] L. Ma, A. Hunt, and M. Soleimani, "Experimental evaluation of conductive flow imaging using magnetic induction tomography," *Int. J. Multiph. Flow*, vol. 72, pp. 198–209, 2015.

[9] E. Toskey and A. Hunt, "Clamp-on Subsea Multiphase Measurement," in *Offshore Technology Conference*, 2015, no. May, pp. 1–11.

[10] M. Zhang, L. Ma, and M. Soleimani, "Magnetic induction tomography guided electrical capacitance tomography imaging with grounded conductors," *Meas. J. Int. Meas. Confed.*, vol. 53, pp. 171–181, 2014.

[11] S. Watson, R. J. Williams, W. Gough, and H. Griffiths, "A magnetic induction tomography system for samples with conductivities below 10 S/m," *Meas. Sci. Technol.*, vol. 19, no. 1, pp. 1–11, 2008.

[12] R. A. Albrechtsen, Z. Z. Yu, and A. J. Peyton, "Preliminary Experiments on the Investigation of

the Inductive Technique for Measuring Water Cotent in Muti-Phase Flow.” Proc. ECAPT, Bergen, pp. 205–2013, 1995.

[13] H. Wei and M. Soleimani, “Two-Phase Low Conductivity Flow Imaging Using magnetic Induction Tomography,” *Prog. Electromagn. Res.*, vol. 131, no. May, pp. 99–115, 2012.

[14] Y. Arellano and L. Ma, “Apparatus for monitoring of the multiphase flow in a pipe,” GB1810735.9, 2018.

[15] L. Ma and Y. Arellano, “Method and apparatus for monitoring of the multiphase fluid in a pipe,” GB1810733.4, 2018.

[16] Y. Arellano, L. Ma, A. Hunt, and O. Haas, “Characterisation of the Effects of Sensor Geometry on the Performance of Magnetic Induction Tomography Systems,” in *9th World Congress on Industrial Process Tomography*, 2018, pp. 373–381.

[17] Y. Arellano, A. Hunt, and O. C. L. Haas, “Evaluation of Near-Field Electromagnetic Shielding Effectiveness at Low Frequencies,” *IEEE Sens. J.*, vol. 19, no. 1, pp. 121–128, 2019.

[18] S. H. Stavland, Y. Arellano, A. Hunt, R. Maad, and B. T. Hjertaker, “Multimodal analysis of gas-oil intermittent structures in co-current horizontal flow,” in *2020 IEEE International Instrumentation and Measurement Technology Conference (I2MTC)*, 2020, pp. 1–6.

[19] Y. Arellano, A. Hunt, and L. U. Ma, “Electromagnetic Technique for Hydrocarbon and Sand Transport Monitoring : Proof of Concept,” *IEEE Access*, vol. 8, pp. 1–12, 2020.

[20] Y. Arellano, A. Hunt, O. Haas, and L. Ma, “On the life and habits of gas-core slugs: characterisation of an intermittent horizontal two-phase flow,” *J. Nat. Gas Sci. Eng.*, 2020.

[21] Y. Arellano, O. Haas, H. Ahmed, A. Hunt, and L. Ma, “If cheap and easy oil is over, what now?,” in *International conference on rnergy and sustainable future*, 2019.

[22] U.S. Energy Information Administration, “Annual Energy Outlook 2019 with projections to 2050,” 2019.

[23] A. Michael, “Economic Implications Of The Current Geopolitical Forces Vis-à-vis Hydrocarbons On Global Energy Markets,” 2014.

[24] R. Priddle, “The development of world energy markets,” in *World Petroleum Congress*, 1997, pp. 77–84.

[25] U.S. Energy Information Administration, “WTI Spot Price FOB (dollars per Barrel),” 2019. .

[26] International Energy Agency, "Global oil discoveries and new projects fell to historic lows in 2016," 2017. .

[27] J.-P. Rodrigue, "World annueal oil production (1900-2016) and peak oil (2005-2020)," *The Geography of Transport Systems*, 2019. .

[28] BP, "BP Statistical Review of World Energy 2018," 2018.

[29] Ministry of Petroleum and Energy of Norway, "OG21 - Oil and Gas in the 21st Century," 2016. .

[30] L. S. Hansen, S. Pedersen, and P. Durdevic, "Multi-Phase Flow Metering in Offshore Oil and Gas Transportation Pipelines : Trends and Perspectives," *Sensors*, vol. 19, no. 2184, pp. 1–26, 2019.

[31] R. Ibarra, I. Zadrazil, C. N. Markides, and O. K. Matar, "Towards a universal dimensionless map of flow regime transitions in horizontal liquid-liquid flows," in *11th International Conference on Heat Transfer, Fluid Mechanics and Thermodynamis*, 2015.

[32] B. Eaton, D. Andrews, C. Knowles, I. Silberberg, and K. Brown, "The Prediction of Flow Patterns, Liquid Holdup and Pressure Losses Occurring During Continuous Two-Phase Flow In Horizontal Pipelines," *J. Pet. Technol.*, 1967.

[33] D. Beggs and J. Brill, "A study of Two-Phase flow in inclined pipes," *J. Pet. Technol.*, 1973.

[34] M. Sadri, S. Shariatipour, and A. Hunt, "Effects of flow measurement errors on oil and gas production forecasts," in *WIT Transactions on Engineering Sciences*, 2017, vol. 115, pp. 133–142.

[35] G. Falcone and B. Harrison, "Forecast expects continued multiphase flowmeter growth," *Oil Gas J.*, vol. 109, no. 10, pp. 25–34, 2011.

[36] R. Thorn, G. a Johansen, and B. T. Hjertaker, "Three-phase flow measurement in the petroleum industry," *Meas. Sci. Technol.*, vol. 24, pp. 1–17, 2012.

[37] Quest offshore, "Quest Deepwater Market Insight," Sugar Land, 2015.

[38] EMERSON, "Micro Motion ® Technical Overview and Specification Summary," 2019. [Online]. Available: https://www.emerson.com/documents/automation/product-data-sheet-technical-overview-specification-summary-micro-motion-en-66168.pdf. [Accessed: 10-Jun-2020].

[39] kbv research, "Global Flow Meters Market By Product Type (Magnetic, Positive Displacement, Differential Pressure, Ultrasonic, Coriolis, Turbine, Vortex), Application (Water & Wastewater, Power Generation, Pulp & Paper, Chemicals, Oil & Gas, Food & Beverages)," 2018.

[40] IPhaseflow Ltd., "iPhaseflow Flow Metering Technology," 2020. [Online]. Available:

http://iphaseflow.com/. [Accessed: 06-Feb-2020].

[41] LeEngSTAR, "Shenzhen Leengstar Technology Co., LTD," 2020. [Online]. Available: http://www.leengstar.com/. [Accessed: 06-Feb-2020].

[42] G. Falcone, G. F. Hewitt, C. Alimonti, and B. Harrison, "Multiphase Flow Metering : Current Trends and Future Developments," *Soc. Pet. Eng.*, no. Distinguisehd author series, 2002.

[43] M. S. Beck and R. A. Williams, "Process tomography: a European innovation and its applications," *Meas. Sci. Technol*, vol. 7, pp. 215–224, 1996.

[44] R. Johansen, T. G. Østby, A. Dupré, and S. Mylvaganam, "Long Short-Term Memory Neural Networks for Flow Regime Identification using ECT," in *9th World Congress on Industrial Process Tomography*, 2018, pp. 135–141.

[45] R. Yan and S. Mylvaganma, "Flow Regime Identification with Single Plane ECT Using Deep Learning," in *9th World Congress on Industrial Process Tomography*, 2018, pp. 289–297.

[46] F. J. Dickin, B. S. Hoyle, A. Hunt, S. M. Huang, O. Ilyas, C. Lenn, R. C. Waterfall, R. A. Williams, C. G. Xie, and M. S. Beck, "Tomographic imaging of industrial process equipment: techniques and applications," in *IEE Proceedings G (Circuits, Devices and Systems)*, 1992, vol. 139, no. I, pp. 72–82.

[47] T. Dyakowski, G. A. Johansen, B. T. Hjertaker, D. Sankowski, V. Mosorov, and J. Wlodarczyk, "A Dual Modality Tomography System for Imaging Gas/Solids Flows," *Part. Part. Syst. Charact*, vol. 23, pp. 260–265, 2006.

[48] A. Hunt, J. Pendleton, and Y. Ladam, "Visualisation of two-phase gas-liquid pipe flows using electrical capacitance tomography," in *ESDA2004*, 2004, no. January 2004.

[49] J. C. Hebden, "Evaluating the Spatial Resolution Performance of a Time-Resolved Optical Imaging System," *Med Phys*, vol. 19, no. 4, pp. 1081–1087, 1992.

[50] S. H. Stavland, C. Sætre, B. T. Hjertaker, S.-A. Tjugum, A. Hallanger, and R. Maad, "Gas Fraction Measurements using Single and Dual Beam Gamma-Densitometry for Two Phase Gas- Liquid Pipe Flow," in *2019 IEEE International Instrumentation and Measurement Technology Conference (I2MTC)*, 2019, pp. 1–6.

[51] H. Xue, P. Kellman, G. Larocca, A. E. Arai, and M. S. Hansen, "High spatial and temporal resolution retrospective cine cardiovascular magnetic resonance from shortened free breathing real-time acquisitions," *J. Cardiovasc. Magn. Reson.*, vol. 15, no. 102, pp. 1–15, 2013.

[52] G. Liang, S. Ren, and F. Dong, "An Inclusion Boundary Reconstruction Method Using Electrical Impedance and Ultrasound Reflection Dual-Modality Tomography," in *9th World Congress on Industrial Process Tomography*, 2018, pp. 11–19.

[53] L. Ma, D. Mccann, and A. Hunt, "Combining Magnetic Induction Tomography and Electromagnetic Velocity Tomography for Water Continuous Multiphase Flows," *IEEE Sens. J.*, vol. 17, no. 24, pp. 8271–8281, 2017.

[54] Y. D. Jiang and M. Soleimani, "Capacitively Coupled Impedance Imaging Based on Wideband Phase Measurement," in *9th World Congress on Industrial Process Tomography*, 2018, pp. 3–9.

[55] Q. Wang and M. Wang, "Thresholding Values and Fuzzy Logic Fusion in Visualisation of Gas-Oil-Water Horizontal Flow using Dual-Modality Electrical Tomography," in *9th World Congress on Industrial Process Tomography*, 2018, pp. 749–758.

[56] R. A. Williams and M. S. Beck, "Process Tomography: Principles, Techniques and Applications," p. 565, 2012.

[57] M. Zhang, Y. Li, and M. Soleimani, "Experimental Study of Complex-valued ECT," in *9th World Congress on Industrial Process Tomography*, 2018, pp. 19–24.

[58] X. Zhu, P. Dong, and Z. Zhu, "Gas-solids Flow Measurement in Cyclone Dipleg by Dual-plane Electrical Capacitance Tomography Sensor," in *9th World Congress on Industrial Process Tomography*, 2018, pp. 203–209.

[59] A. Hunt, "Industrial Applications of High-speed Electrical Capacitance Tomography," in *9th World Congress on Industrial Process Tomography*, 2018, pp. 857–864.

[60] W. Yanga, T. Nguyen, M. Bettingc, A. Chondronasios, S. Nattrass, F. Okimotoc, and H. Mccanna, "Imaging wet gas separation process by capacitance tomography," in *SPIE*, 2002, vol. 4665, pp. 347–358.

[61] S. F. A. Bukhari, I. Ismail, and W. Q. Yang, "Visualising Oil Separator Vessel and Decision-Making for Control," in *4th World Congress on Industrial Process Tomography*, 2004, pp. 855–860.

[62] R. Deloughry, M. Young, E. Pickup, and L. Barratt, "Cost Effective Loading of Road Tankers Using Process Tomography," in *2nd World Congress on Industrial Process Tomography*, 2001, no. August, pp. 565–572.

[63] D. Pacho and G. Davies, "Application of Electrical Capacitance Measurements to Study the Collapse of Oil Foams," in *2nd World Congress on Industrial Process Tomography*, 2001, no.

August, pp. 618–627.

[64] A. Hunt, L. A. Abdulkareem, and B. J. Azzopardi, “Measurement of Dynamic Properties of Vertical Gas-Liquid Flow,” *7th Int. Conf. Multiph. Flow*, pp. 1–10, 2010.

[65] Z. Z. Yu, a. T. Peyton, M. S. Beck, W. F. Conway, and L. a. Xu, “Imaging system based on electromagnetic tomography (EMT),” *Electron. Lett.*, vol. 29, no. 7, p. 625, 1993.

[66] A. J. Peyton, Z. Z. Yu, G. Lyon, S. Al-Zeibak, J. Ferreira, J. Velez, F. Linhares, A. R. Borges, H. L. Xiong, N. H. Saunders, and M. S. Beck, “An overview of electromagnetic inductance tomography: description of three different systems,” *Meas. Sci. & Technol.*, vol. 7, no. 3, pp. 261–271, 1996.

[67] R. Binns, a R. a Lyons, a J. Peyton, and W. D. N. Pritchard, “Imaging molten steel flow profiles,” *Meas. Sci. Technol.*, vol. 12, no. 8, pp. 1132–1138, 2001.

[68] M. H. Pham, Y. Hua, and N. B. Gray, “Eddy Current Tomography for Metal Solidification Imaging,” in *1st. World Congress on Industrial Process Tomography*, 1999, no. April, pp. 451–458.

[69] S. Ramli and a. J. Peyton, “Feasibility study of planar-array electromagnetic inductance tomography (EMT).,” *1st World Congr. Ind. Process Tomogr. Buxton, Gt. Manchester*, 1999.

[70] Z. Xiao, C. Tan, and F. Dong, “Multi-frequency difference method for intracranial hemorrhage detection by magnetic induction tomography,” *Physiol. Meas.*, vol. 39, p. 14, 2018.

[71] S. Al-Zeibak and N. Saunders, “A feasibility study of in vivo electromagnetic imaging.,” *Phys. Med. Biol.*, vol. 38, no. 1, pp. 151–160, 1993.

[72] H. Griffiths, “Magnetic induction tomography,” in *Electrical Impedance Tomography*, D. Holder, Ed. London: IOP Publishing Ltd., 2005.

[73] H. Griffits, W. R. Stewart, and W. Gough, “Magnetic Induction Tomography A measuring System for Biological Tissues.” Annals New York Academy of Sciences, 1999.

[74] Z. Liu, M. He, and H. Xiong, “Simulation study of the sensing field in electromagnetic tomography for two-phase flow measurement,” *Flow Meas. Instrum.*, vol. 16, no. 2–3, pp. 199–204, 2005.

[75] H.-Y. Wei and M. Soleimani, “Hardware and software design for a National Instrument-based magnetic induction tomography system for prospective biomedical applications.,” *Physiol. Meas.*, vol. 33, no. 5, pp. 863–79, 2012.

[76] I. L. Freeston and R. C. Tozer, "Impedance imaging using induced currents," *Phys. Med. Biol.*, vol. 16, pp. A257–A266, 1995.

[77] N. G. Genqer, Y. Z. Ider, and S. J. Williamson, "Electrical Impedance Tomography : Induced-Current Imaging Achieved with a Multiple Coil System," *IEEE Trans. Biomed. Eng.*, vol. 43, no. 2, pp. 139–149, 1996.

[78] C. L. Goh, R. Abdul Rahim, and M. H. Fazalul Rahiman, "Process tomography of gas-liquid flow in a vessel: a review," *Sens. Rev.*, vol. 36, no. 3, pp. 287–302, 2016.

[79] S. Kanshio, H. Yeung, and L. Liyun, "The Experimental Study of Liquid Holdup in Gas-Liquid Pipe Cyclonic Separator using Electrical Resistance Tomography and Wire Mesh Sensor," in *17th International Conference Multiphase Production Technology*, 2015, pp. 185–195.

[80] A. Koksal, M. Eyuboglu, and M. Demirbilek, "A Quasi-Static Analysis for a Class of Induced-Current EIT Systems Using Discrete Coils," *IEEE Trans. Biomed. Eng.*, vol. 21, no. 6, pp. 688–694, 2002.

[81] H. C. Wee, S. Watson, R. Patz, H. Griffiths, and R. J. Williams, "A magnetic induction tomography system with sub-millidegree phase noise and high long-term phase stability," *IFMBE Proc.*, vol. 22, pp. 744–747, 2008.

[82] H.-Y. Wei and M. Soleimani, "Electromagnetic tomography for medical and industrial applications: Challenges and opportunities [Point of View]," *Proc. IEEE*, vol. 101, no. 3, pp. 559–565, 2013.

[83] A. Hunt and M. Zhang, "Oilfield metering workshop." Coventry, p. 2020, 2019.

[84] B. Hoyle, "Sandpit Workshop - Real-time State and Performance from IPT Data for Process Control," 2017.

[85] R. Serway and J. Jewett, *Physics for Scientists and Engineers with Modern Physics*, 8th ed. Belmont: Raymond A. Serway, 2010.

[86] H. Griffits, "Magnetic induction tomography," *Meas. Sci. Technol*, vol. 12, no. 2001, pp. 1126–1131, 2001.

[87] Z. Z. Yu and A. J. Peyton, "Development of sensor arrays for electromagnetic inductive tomography: Compensation of large background signal values," *Trans. Inst. Meas. Control*, vol. 20, no. 4, pp. 195–202, 1998.

[88] H. Griffiths, W. Gough, S. Watson, and R. J. Williams, "Residual capacitive coupling and the

measurement of permittivity in magnetic induction tomography.," *Physiol. Meas.*, vol. 28, no. 7, pp. S301–S311, 2007.

[89] P. P. Tarjan and R. McFee, "Electrodeless measurements of the effective resistivity of the human torso and head by magnetic induction.," *IEEE Trans. Biomed. Eng.*, vol. 15, no. 4, pp. 266–278, 1968.

[90] D. Goss, R. O. Mackin, E. Crescenco, H. S. Tapp, and A. J. Peyton, "Understanding the coupling mechanisms in high frequency EMT," *3rd World Congr. Ind. Process Tomogr.*, pp. 364–369, 2003.

[91] a Korjenevsky, V. Cherepenin, and S. Sapetsky, "Magnetic induction tomography: experimental realization," *Physiol. Meas.*, vol. 21, no. 1, pp. 89–94, 2000.

[92] A. Peyton, M. Beck, A. Borges, J. de Oliveira, G. Lyon, Z. Yu, M. Brown, and J. Ferrera, "Development of electromagnetic tomography (EMT) for industrial application: part 2: image reconstruction and software framework.," *World Congr. Ind. Process Tomogr.*, vol. 2, no. 2, pp. 219–225, 1999.

[93] G. M. Lyon, Z. Z. Yu, A. J. Peyton, and M. S. Beck, "Development in electro-magnetic tomography instrumentation," *IEE Colloguium Adv. Electr. Tomogr.*, p. 12/1-12/4, 1996.

[94] A. J. Peyton, S. Watson, R. J. Williams, H. Griffiths, and W. Gough, "Characterising the effects of the external electromagnetic shield on a magnetic induction tomography sensor.," *3rd World Congr. Ind. Process Tomogr.*, pp. 1–6, 2003.

[95] H. Y. Wei and A. J. Wilkinson, "Design of a sensor coil and measurement electronics for magnetic induction tomography," *IEEE Trans. Instrum. Meas.*, vol. 60, no. 12, pp. 3853–3859, 2011.

[96] D. Goss, R. O. Mackin, E. Crescenco, H. S. Tapp, and A. J. Peyton, "Development of electromagnetic induction tomography (EMT) hardware for determining human body composition," *Proc. World Congr. Ind. Process Tomogr.*, pp. 377–383, 2003.

[97] R. Merwa and H. Scharfetter, "Magnetic InductionTomography: The influence of the coil configuration on the spatial resolution," *IFMBE Proc.*, vol. 17, pp. 456–459, 2007.

[98] Z. Zhang, H. Lei, P. Liu, and D. Zhou, "Sensitivity Study for Improved Magnetic Induction Tomography (MIT) Coil System," *Minist. Educ. People's Repub. China.*, vol. 1, no. 1, pp. 1317–1320, 2013.

[99] D. Gürsoy and H. Scharfetter, "Optimum receiver array design for magnetic induction tomography," *IEEE Trans. Biomed. Eng.*, vol. 56, no. 5, pp. 1435–1441, 2009.

[100] Z. Yu, P. Worthington, S. Stone, and A. Peyton, "Electromagnetic screening of inductive tomographiuc sensor," in *Proc. ECAPT*, 1995, pp. 300–310.

[101] H. K. Wei, "Magnetic Induction Tomography for Medical and Industrial Imaging : Hardware and Software Development," 2012.

[102] L. Ma and M. Soleimani, "Magnetic induction tomography methods and aplications: a review," *Meas. Sci. Technol*, vol. 28, 2017.

[103] R. Patz, S. Watson, C. Ktistis, M. Hamsch, and A. J. Peyton, "Performance of a FPGA-based Direct Digitising Signal Measurement module for MIT," *J. Phys. Conf. Ser.*, vol. 224, 2010.

[104] S. Watson, H. C. Wee, R. Patz, R. J. Williams, and H. Griffiths, "A method for increasing the phase-measurement stability of Magnetic Induction Tomography systems," pp. 748–751, 2009.

[105] B. Dekdouk, W. Yin, S. Member, C. Ktistis, D. W. Armitage, and A. J. Peyton, "A Method to Solve the Forward Problem in Magnetic Induction Tomography Based on the Weakly Coupled Field Approximation," *IEEE Trans. Biomed. Eng.*, vol. 57, no. 4, pp. 914–921, 2010.

[106] M. Soleimani and W. R. B. Lionheart, "Absolute Conductivity Reconstruction in Magnetic Induction Tomography Using a Nonlinear Method," *IEEE Trans. Med. Imaging*, vol. 25, no. 12, pp. 1521–1530, 2006.

[107] Process Tomography LTD, "Electrical capacitance tomography system type PTL300E volume 4. Application notes," 2008.

[108] D. N. Dyck and D. A. Lowther, "A Method of Computing the Sensitivity of Electromagnetic Quantities to Changes in Materials and Sources," *IEEE Trans. Magn.*, vol. 30, no. 5, pp. 3415–3418, 1994.

[109] L. Ma, "Magnetic Induction Tomography for Non-destructive Evaluation and Process Tomography," University of Bath, 2014.

[110] O. Biro, "Edge element formulations of eddy current problems," *Comput. Methods Appl. Mech. Eng.*, vol. 169, pp. 391–405, 1999.

[111] O. Biro and K. Preis, "On the Use of the Magnetic Vector Potential in the FInite Element Analysis of Three-Dimensional Eddy Currents," *IEEE Trans. Magn.*, vol. 25, no. 4, pp. 3149–3159, 1989.

[112] H. Haus and J. Melcher, *Electromagnetic fields and energy*. Prentice Hall Books, 1989.

[113] H. Igarashi and T. Honma, "On Convergence of ICCG Applied to Finite-Element Equation for

Quasi-Static Fields," *IEEE Trans. Magn.*, vol. 38, 2002.

[114] A. Bossavit, *Computational Electromagnetism: Variational Formulations, Complementarity, Edge Elements*. Academic Press, 1997.

[115] A. Osiadacz, *Simulation and analysis of gas networks*. Gulf Publishing Company, 1987.

[116] M. Zolgharni, "Magnetic Induction Tomography for Imaging Cerebral Stroke," Swansea University, 2010.

[117] P. Ledger and K. Morgan, "The application of the hp – Finite Element Method to electromagnetic problems," *Arch. Comput. Methods Eng.*, vol. 12, no. September 2004, pp. 235–302, 2005.

[118] S. Chapra and R. Canale, *Metodos numericos para ingenieros*, 5th ed. Mexico D.F.: Mc Graw Hill, 2006.

[119] A. Fraguela, S. Gomez, and J. Oliveros, "A new method for the solution of the inverse problem of Electrical Capacticane Tomography and its application to image reconstruction of multiphase flows," in *Proceedings of the 5th International Conference on Inverse Problems in Engineering: Theory and Practice*, 2005, no. July.

[120] R. A. Brooks and G. Di Chiro, "Principles of Computer Assisted Tomography (CAT) in Radiographic and Radioisotopic Imaging," *Phys. Med. Biol.*, vol. 21, no. 5, pp. 689–732, 1976.

[121] A. V Korjenevsky and S. A. Sapetsky, "Feasibility of backprojection method for reconstruction of low contrast perturbations in a conducting background in magnetic induction tomography," *Physiol. Meas.*, vol. 38, no. 6, 2017.

[122] Q. Wang, X. Jia, and M. Wang, "Bubble mapping : three-dimensional visualisation of gas – liquid flow regimes using electrical tomography," *Meas. Sci. Technol.*, vol. 30, p. 13, 2019.

[123] PROCESS TOMOGRAPHY Ltd., "Electrical Capacotance Tomography system Type PTL300E Operating Manual," vol. 4, no. 6. Wimslow, 2008.

[124] J. Jin, *The Finite Element Method in Electromagnetics*, 2nd. New York: John Wiley & Sons, Inc, 2002.

[125] P. Sumithra and D. Thiripurasundari, "A review on computational electromagnetics methods," *Adv. Electromagn.*, vol. 6, no. 1, 2017.

[126] T. Weiland, M. Timm, and I. Munteanu, "A practical guide to 3-D simulation," *IEEE Microwave Magazine*, no. December, pp. 62–75, 2008.

[127] A. Polycarpou, *Introduction to the Finite Element Method in Electromagnetics*, First. Morgan & Carpool Publishers, 2006.

[128] D. Pepper and J. Heinrich, *The finite element method*, 2nd ed. Taylor & Francis, 2006.

[129] P. Jacobsson, "Nedelec elements for computational electromagnetics," 2007. .

[130] P. Monk, *Finite element methods for maxwell's equations*. Oxford: Oxford Sciece Publications, 2003.

[131] G. Mur, "The finite-element modelling of three-dimensional time-harmonic electromagnetic fields," in *Second International Conference on Computation in Electromagnetics*, 1994, pp. 1–4.

[132] M. Zolgharni, P. Ledger, D. Armitage, D. Holder, and H. Griffiths, "Imaging cerebral haemorrhage with magnetic induction tomography : Numerical modelling," *Physiol. Meas.*, vol. 2, no. July, pp. 187–200, 2009.

[133] C. Mcgowan, "Optimization of Inductively Coupled Coils using CST Microwave Studio," Royal institute of technology, 2009.

[134] COMSOL, "AC / DC Module User's Guide v.5.3." p. 330, 2017.

[135] Z. Yang, G. Wang, and W. Liu, "Analytical Calculation of the Self-Resonant Frequency of Biomedical Telemetry Coils," no. 1, pp. 5880–5883, 2006.

[136] F. W. Grover, *Inductance calculations: working formulas and tables*. New York: D. Van Nostrand Co., 1973.

[137] M. Zolgharni, P. D. Ledger, and H. Griffiths, "Forward modelling of magnetic induction tomography: a sensitivity study for detecting haemorrhagic cerebral stroke," *Med. Biol. Eng. Comput.*, vol. 47, no. 12, pp. 1301–1313, 2009.

[138] W. Frei, "Meshing your geometry: when to use the various element types," *COMSOL BLOG*, 2013. .

[139] COMSOL, "COMSOL Multiphysics Reference Manual v5.3." COMSOL, 2017.

[140] Texas Instruments, "Webench Coil Designer," *Texas Instruments*, 2019. .

[141] H. Scharfetter, A. Köstinger, and S. Issa, "Spectroscopic 16 channel magnetic induction tomograph : The new Graz MIT system," in *IFMBE Proceedings, vol 17.*, 2007, pp. 452–455.

[142] M. Hamsch, C. H. Igney, and M. Vauhkonen, "16 Channel Magnetic Induction Tomography

System Featuring Parallel Readout," in *IFMBE Proceedings, vol 17.*, 2007, pp. 484–487.

[143] M. Vauhkonen, M. Hamsch, and C. H. Igney, "A measurement system and image reconstruction in magnetic induction tomography," *Physiol. Meas.*, vol. 29, no. July, pp. S445–S454, 2008.

[144] H. K. Wei, "Magnetic Induction Tomography for Medical and Industrial Imaging : Hardware and Software Development," University of Bath, 2012.

[145] S. Lyons, K. Wei, and M. Soleimani, "Wideband precision phase detection for magnetic induction spectroscopy," *Measurement*, vol. 115, no. June 2017, pp. 45–51, 2018.

[146] H. Scharfetter, H. Lackner, and J. Rosell, "Magnetic induction tomography : Hardware for multi-frequency measurements in biological tissues," *Physiol. Meas.*, vol. 22, no. March, pp. 131–146, 2001.

[147] J. Nilsson and S. Riedel, *Electric Circuits*, 9th ed. New Jersey: Pearson Prentice Hall, 2011.

[148] M. Panik, *Statistica inference: A short course*. John Wiley & Sons, Inc, 2012.

[149] G. Corder and D. Foreman, *Nonparametric Statistics for Non-Statisticians*. New Jersey: John Wiley & Sons, Inc, 2009.

[150] M. Qualls, D. J. Pallin, and J. D. Schuur, "Parametric Versus Nonparametric Statistical Tests : The Length of Stay Example," *Acad. Emerg. Med.*, vol. 17, pp. 1113–1121, 2010.

[151] R. Ruiz, A. Brito, and J. Marquez, "Evaluation of Multiphase Flow Models To Predict Pressure Gradient in Vertical Pipes With Highly Viscous Liquids," in *Society of Petroleum Engineers*, 2014, pp. 1–8.

[152] Y. Arellano, A. Hunt, O. Haas, H. Ahmed, and L. Ma, "Multiple regression based prediction correlations for enhanced sensor design of magnetic induction tomography systems," *Meas. Sci. Technol.*, vol. 31, no. 2, 2019.

[153] The Canadian Association of Petroleum Producers (CAAP), "Use of reinforced composite pipe (non-metallic pipelines)." CAPP, Calgary, 2017.

[154] Shawcor, "Linepipe products," 2018. [Online]. Available: https://www.shawcor.com/about. [Accessed: 22-Jun-2018].

[155] J. R. Mortarelli, "A geberalization of the Geselowitz relationship useful in Impedance Plethysmographic Field calculations," *IEEE Trans. Biomed. Eng.*, vol. BME-27, no. 11, pp. 665–667, 1980.

[156] A. M. Ansari, N. D. Sylvester, C. Sarica, O. Shonham, and J. P. Brill, “A Comprehensive Mechanistic Model for Upward Two-Phase Flow in Wellbores,” *SPE Prod. Facil.*, no. May, pp. 143–152, 1990.

[157] F. Garcia, R. Garcia, J. C. Padrino, C. Mata, J. L. Trallero, and D. D. Joseph, “Power law and composite power law friction factor correlations for laminar and turbulent gas-liquid flow in horizontal pipelines,” *Int. J. Multiph. Flow*, vol. 29, no. 2, pp. 1605–1624, 2003.

[158] G. Corliss, C. Faure, A. Griewank, L. Hascoet, and U. Naumann, Eds., *Automatic Differentiation of Algoritms: From simulation to optimization*. Springer, 2002.

[159] C. Morari, I. Balan, J. Pintea, E. Chitanu, and I. Iordache, “ELECTRICAL CONDUCTIVITY AND ELECTROMAG- NETIC SHIELDING EFFECTIVENESS OF SILICONE RUBBER FILLED WITH FERRITE AND GRAPHITE POWDERS,” *Prog. Electromagn. Res.*, vol. 21, no. September, pp. 93–104, 2011.

[160] M. Getzlaff, *Fundamentals of Magnetism*. Springer, 2008.

[161] H. Griffiths, M. Zolgharni, P. D. Ledger, and S. Watson, “The cardiff Mk2b MIT head array: Optimising the coil configuration,” *J. Phys. Conf. Ser.*, vol. 224, p. 012046, 2010.

[162] C. Morari and I. Balan, “Methods for determining shielding effectiveness of materials,” *Electroteh. Electron. Autom.*, vol. 63, no. 126–136, 2015.

[163] S. A. Schelkunoff, *Electromagnetic waves*. Boston: D. Van Nostrand Company, Inc., 1945.

[164] C. Paul, *Introduction to Electromagnetic Compatibility*, Second. John Wiley & Sons, Inc, 2006.

[165] R. Kotnala and J. Shah, “Chapter 4 - Ferrite Materials: Nano to Spintronics Regime,” in *Handbook of Magnetic Materials*, K. Buschow, Ed. Amsterdam: Elseiver, 2015.

[166] D. D. L. Chung, “Materials for Electromagnetic Interference Shielding,” *J. Mater. Eng. Perform.*, vol. 9, no. October 1999, pp. 350–354, 2000.

[167] E. S. C. of W. M. IEEE, “Shielding Tutorial,” 2015. [Online]. Available: http://www.westmichigan-emc.org/archive/. [Accessed: 01-Nov-2017].

[168] R. Schulz, V. Plantz, and D. Brush, “Shielding Theory and Practice,” *IEEE Trans. Electromagn. Compat.*, vol. 30, no. 3, pp. 187–201, 1988.

[169] IEEE Standards Committee, “IEEE Standard Method for Measuring the Effectiveness of Electromagnetic Shielding Enclosures,” vol. 1997. The Institute of Electrical and Electronics

Engineers, Inc., 1997.

[170] L. Jin, Z. Haiyan, L. Ping, Y. Xijiang, and Z. Guoxun, "The electromagnetic shielding effectiveness of a low-cost and transparent stainless steel fiber/silicone resin composite," *IEEE Trans. Electromagn. Compat.*, vol. 56, no. 2, pp. 328–334, 2014.

[171] K. C. Yaw, "Measurement of dielectric material properties." Rohde&Schwarz, pp. 1–36, 2012.

[172] V. Voicu, I. P. Ă. Tru, P. Nicolae, S. M. Ieee, and L. Dina, "Analyzing the Attenuation of Electromagnetic Shielding Materials for Frequencies under 1 GHz," in *Advanced Topics in Electrical Engineering (ATEE)*, 2017, pp. 336–339.

[173] C. A. Feickert, M. K. McInerney, and W. . Croisant, "Resonant eddy current analysis: A selective screening method for electromagnetic shielding materials," in *1993 International Symposium on Electromagnetic Compatibility*, 1993, pp. 160–163.

[174] A. Tamburrano, D. Desideri, A. Maschio, and M. S. Sarto, "Coaxial waveguide methods for shielding effectiveness measurement of planar materials up to 18 GHz," *IEEE Trans. Electromagn. Compat.*, vol. 56, no. 6, pp. 1386–1395, 2014.

[175] D. Putra, O. C. L. Haas, J. A. Mills, and K. Burnham, "A multiple model approach to respiratory motion prediction for real-time IGRT," *Phys. Med. Biol.*, no. April, 2008.

[176] Graphpad Statistics Software, "GraphPad Statistics Guide," 2017. [Online]. Available: https://www.graphpad.com/guides/prism/7/statistics/stat_confidence_interval_of_a_stand.htm?toc=0&printWindow. [Accessed: 23-Jan-2018].

[177] K. Baydili and D. Sigirli, "Comparison of Variance Homogenity Tests for Different Distributions," *Turkiye Klin. J Biostat*, vol. 9, no. 3, pp. 197–212, 2017.

[178] J. Clinch and H. J. Keselman, "PARAMETRIC ALTERNATIVES TO THE ANALYSIS OF VARIANCE," *J. Educ. Stat.*, vol. 7, no. 3, pp. 207–214, 1982.

[179] L. Williams and A. Herve, "Post-Hoc Comparisons," in *Encyclopedia of Research Design*, 2010, pp. 1060–1067.

[180] ISO/IEC, "JCGM 200:2012 International vocabulary of metrology – Basic and general concepts and associated terms (VIM)." JCGM, 2012.

[181] Y. Arellano, A. Hunt, O. Haas, H. Ahmed, and L. Ma, "Water cut determination in co-current liquid-liquid flow using electrical capacitance metering," in *18th International Flow Measurment Conference*, 2019.

[182] P. Moin, "Revisiting Taylor's hypothesis," *J. Flui Mech.*, vol. 640, pp. 1–4, 2009.

[183] A. Hunt, "Weighing without Touching : Applying Electrical Capacitance Tomography to Mass Flowrate Measurement in Multiphase Flows," *Meas. Control*, vol. 47, no. 1, pp. 19–25, 2014.

[184] M. R. Baidillah and M. Takei, "Exponential model normalisation of electrical capacitance tomography," in *8th world congress on industrial process tomography*, 2016, pp. 1–7.

[185] B. T. Hjertaker, R. Maad, and G. A. Johansen, "Dual-mode capacitance and gamma-ray tomography using the Landweber reconstruction algorithm," *Meas. Sci. Technol*, vol. 22, no. 104002, 2011.

[186] R. W. Sillars, "The properties of a dielectric containing semiconducting particles of various shapes," *Inst. Electr. Eng. - Proc. Wirel. Sect. Inst.*, vol. 12, no. 35, pp. 139–155, 1937.

[187] GUM, "Evaluation of measurement data — Guide to the expression of uncertainty in measurement," 2008.

[188] H. Scharfetter, R. Casañas, and J. Rosell, "Biological Tissue Characterization by Magnetic Induction Spectroscopy (MIS): Requirements and Limitations," *IEEE Trans. Biomed. Eng.*, vol. 50, no. 7, pp. 870–880, 2003.

[189] S. Zlochiver, M. M. Radai, S. Abboud, M. Rosenfeld, X. Z. Dong, R. G. Liu, F. S. You, H. Y. Xiang, and X. . Shi, "Induced current electrical impedance tomography system: experimental results and numerical simulations," *Physiol. Meas.*, vol. 25, no. 1, p. 239, 2004.

[190] H. Yazdanian and R. Jafari, "Improvement on Conductivity Image Reconstruction in Magnetic Induction Tomography," in *IEEE Transactions on Instrumentation and Measurement*, 2018, vol. 0, no. 1, pp. 1–5.

[191] R. Casañas, H. Scharfetter, A. Altes, A. Remacha, P. Sarda, J. Sierra, R. Merwa, K. Hollauss, and J. Rosell, "Measurement of liver iron overload by magnetic induction using a planar gradiometer: Preliminary human results," *Physiol. Meas.*, vol. 25, no. 1, pp. 315–323, 2004.

[192] L. Ma and M. Soleimani, "Magnetic Induction Spectroscopy for Permeability Imaging," vol. 8, no. 1, pp. 1–8, 2018.

[193] E. Michel, D. Hernandez, and S. Y. Lee, "Electrical conductivity and permittivity maps of brain tissues derived from water content based on T1-weighted acquisition," *Magn. Reson. Med.*, vol. 77, no. 3, pp. 1094–1103, 2017.

[194] H. Ammari, A. Buffa, and J.-C. Nedelec, "A justification of eddy current model for the maxwell

equations," *SIAM J. Appl. Math.*, vol. 60, no. 5, pp. 1805–1823, 2000.

[195] K. Schmidt, O. Sterz, and R. Hiptmair, "Estimating the eddy-current modeling error," *IEEE Trans. Magn.*, vol. 44, no. 6, pp. 686–689, 2008.

[196] B. Lambert, "Dielectric Spectroscopy," *The University of Southern Mississippi*, 2018. [Online]. Available: https://web.archive.org/web20060118002845/http://psrc.usm.edu/mauritz/dilect.html. [Accessed: 14-Nov-2018].

[197] R. Dorey, *Ceramic thick firlms for MEMS and Microdeviced*. Elseiver, 2012.

[198] M. Wang, *Industrial Tomography: Systems and Applications*. Elseiver, 2015.

[199] E. F. May, T. J. Edwards, A. G. Mann, and D. K. Manning, "Density, dielectric constant and PVT measurements of a gas condensate fluid," *J. Pet. Sci. Eng.*, vol. 41, no. 4, pp. 297–308, 2004.

[200] Engineering ToolBox, "Dielectric Constants of Liquids," *Engineering ToolBox*, 2008. [Online]. Available: https://www.engineeringtoolbox.com/liquid-dielectric-constants-d_1263.html. [Accessed: 12-Sep-2019].

[201] W. P. Clement, "Dielectric Constants for Earth materials," 1999. .

[202] Y. Taitel and A. Dukler, "A model for predicting flow regime transitions in horizontal and near horizontal gas-liquid flow," *AIChE*, vol. 22, no. 1, pp. 47–55, 1976.

[203] O. Baker, "Design Of Pipelines For The Simultaneous Flow Of Oil And Gas," *Soc. Pet. Eng.*, 1953.

[204] D. Barnea, "A unified model for predicting flow -pattern transitions for the whole range of pipe inclinations," *Int. J. Multiph. Flow*, vol. 13, no. 1, pp. 1–12, 1987.

[205] P. Y. Lin and T. J. Hanratty, "Effect of pipe diameter on flow patterns for air-water flow in horizontal pipes," *Int. J. Multiph. Flow*, vol. 13, no. 4, pp. 549–563, 1987.

[206] M. Parsi, B. J. Azzopardi, A. Al-sarkhi, N. R. Kesana, R. E. Vieira, C. F. Torres, B. S. Mclaury, and S. A. Shirazi, "Do huge waves exist in horizontal gas-liquid pipe flow ?," *Int. J. Multiph. Flow*, vol. 96, pp. 1–23, 2017.

[207] A. Hunt and D. Millington, "Multiphase Flow Measurement through Next-Generation tomographic visualisation technology," in *Upstream Production Measurement Forum*, 2016, no. UPM 16030.

[208] A. Hunt, J. Pendleton, and Y. Ladam, "Visualisation of Two-Phase Gas-Liquid pipe flows using electrical capacitance tomography," in *7th Biennial ASME Conference on Engineering Systems Design and Analysis*, 2004.

[209] L. P. Golan and A. H. Stenning, “Two-phase vertical flow maps,” *Proc Instn Mech Engnrs*, vol. 184, no. 3, pp. 108–114, 1969.

[210] J. M. Manhandle, G. A. Gregory, and K. Aziz, “A flow pattern map for gas-liquid flow in horizontal pipes,” *Int. J. Multiph. Flow*, vol. 1, pp. 537–553, 1974.

[211] J. L. Trallero, C. Sarica, and J. P. Brill, “A Study of Oil / Water Flow Patterns in Horizontal Pipes,” *SPE Prod. Facil.*, no. August, pp. 165–172, 1997.

[212] Shell Global Solutions International B.V., “Gas-Liquid separators- Type selection and design rules,” no. December. Shell, pp. 1–100, 2007.

[213] D. Beggs and J. Brill, “A Study of Two-Phase flow in Inclined Pipes,” *J. Pet. Technol.*, vol. 25, no. 05, 1973.

[214] M. Macdonald and T. Leonard, “ENG58 Multiphase flow metrology in oil and gas production critical review of multiphase flow patter data,” 2015.

[215] NEL, “Multiphase Flow Meassurment Test Facility.” [Online]. Available: https://www.tuv-sud.co.uk/uk-en/about-tuev-sued/tuev-sued-in-the-uk/nel/our-services/activities/calibration-testing/multiphase-flow-meter-testing-and-calibration/advanced-multiphase-facility-amf. [Accessed: 04-May-2019].

[216] J. Chidamoio, L. Akanji, and R. Rafati, “Effect of length-to-diameter ratio on axial velocity and hydrodynamic entrance length in air-water two-phase flow in vertical pipes,” *J. Oil, Gas Petrochemical Sci.*, vol. 1, pp. 1–7, 2017.

[217] M. Milan, N. Borhani, and J. R. Thome, “Adiabatic vertical downward air – water flow pattern map : Influence of inlet device , flow development length and hysteresis effects,” *Int. J. Multiph. Flow*, vol. 56, pp. 126–137, 2013.

[218] L. P. M. Colombo, M. Guilizzoni, G. m Sotgia, S. Bortolotti, and L. Pavan, “Measurement of the oil holdup for a two-phase oil-water flow through a sudden contraction in a horizontal pipe,” *J. Phys.*, 2014.

[219] S. Zou, L. Guo, and C. Xie, “Fast recognition of global flow regime in pipeline-riser system by spatial correlation of differential pressures,” *Int. J. Multiph. Flow*, vol. 88, pp. 222–237, 2017.

[220] J. Polansky and M. Wang, “Proper Orthogonal Decomposition as a technique for identifying two-phase flow pattern based on electrical impedance tomography,” *Flow Meas. Instrum.*, vol. 53, pp. 126–132, 2017.

[221] R. Drury, A. Hunt, and J. Brusey, “Identification of horizontal slug flow structures for application in selective cross-correlation metering,” *Flow Meas. Instrum.*, vol. 66, no. June 2018, pp. 141–149, 2019.

[222] M. I. Robert J., *Introduction to Shannon Sampling and Interpolation Theory*. New York: Springer-Verlag, 1991.

[223] G. Mask, X. Wu, and K. Ling, “An improved model for gas-liquid flow pattern prediction based on machine learning,” *J. Pet. Sci. Eng.*, vol. 183, 2019.

Appendix A List of publications

Peer-reviewed journal articles:

1. **Y. Arellano**, A. Hunt, and O. Haas. "Evaluation of near-field electromagnetic shielding effectiveness at low frequencies" in *IEEE Sensors Journal*, vol. 19, no. 1, pp. 121-128, 1 Jan.1, 2019.
Impact: The results of the study demonstrate that the shielding mechanism that prevails at low frequencies is that of reflection. Consequently, hard shields such as metals show superior wave attenuation performance for MIT systems. The study also explores the limitations of traditional testing geometry for shielding effectiveness and proposes an alternative approach to near-field, free-space measurement using MIT sensors. The proposed approach shows enhanced shielding effectiveness measurements compared to the traditional method.
2. **Y. Arellano**, A. Hunt, O. Haas, H. Ahmed, and L. Ma. "Multiple regression-based prediction correlations for enhanced sensor design of magnetic induction tomography systems" in *Meas. Science Tech*, vol. 31, no 2, Nov. 13, 2019.
Impact: Three correlation models are derived to help developers predict the relative performance of MIT systems for a given set of coil characteristics. These correlations have the potential to help researchers predict the relative overall performance of MIT systems for given coil setups. The proposed models allow enhanced sensor designs without the need to perform extensive experimental tests or simulation work.
3. S. H. Stavland, **Y. Arellano**, A. Hunt, R. Maad, and B. T. Hjertaker. "Multimodal analysis of gas-oil intermittent structures in co-current horizontal flow". 2020 IEEE International Instrumentation & Measurement conference proceedings " in *2020 IEEE International Instrumentation and Measurement Technology Conference (I2MTC*), Dubrovnik, Croatia, 2020, pp. 1-6, doi: 10.1109/I2MTC43012.2020.9129157.
Impact: The work reports the measurement principles and analysis of the data simultaneously acquired from a multimodal metering device that combines Gamma-Ray tomography and Electric Capacitance tomography. First results of the multimodal approach performance show agreement in the periodic structures measured, with a significant impact in enhancing measurement accuracy.
4. **Y. Arellano**, A. Hunt, and L. Ma. "Electromagnetic technique for hydrocarbon and sand transport monitoring: proof of concept using computer simulation". in *IEEE Access*, vol. 8, pp. 120766-120777, 2020, doi: 10.1109/ACCESS.2020.3006444.
Impact: The study demonstrates, through the solution of the electromagnetic Forward Problem, that the temporal, spatial and frequency related permittivity and conductivity changes are all captured by the induced electrical voltage measurement. The findings disclose that an electromagnetic metering system offers advantages in continuously monitoring and measuring hydrocarbon contents and solid concentrations.

5. **Y. Arellano**, A. Hunt, O. Haas, and L. Ma. “On the life and habits of gas-core slugs: Two-phase gas-liquid intermittent structures in co-current horizontal flow”. Journal of Natural Gas Science and Engineering. https://doi.org/10.1016/j.jngse.2020.103475 (In press)
   Impact: A proposed unified flow pattern classification for gas-liquid flow enables a direct comparison of the prediction accuracy of various regime maps to the dataset. The characterisation of an intermittent hydrodynamic phenomenon is presented, and the transition to other flow regimes is provided based on dimensional and non-dimensional numbers. Reconstructed permittivity distribution of two-phase gas-liquid flow using high-speed electrical capacitance tomography enabled the identification of intermittent flow patterns in a pipeline without prior knowledge of the flow characteristics. The work provides a thorough evaluation of intermittent structures and a detailed characterisation of the gas-core slug flow.

Conference articles:

1. **Y. Arellano**, A. Hunt, O. Haas, H. Ahmed, and L. Ma. If cheap, easy oil is over, what now?. ICESF, Nottingham, UK, 2019
2. **Y. Arellano**, A. Hunt, O. Haas, H. Ahmed, and L. Ma. Water cut determination in co-current liquid-liquid flow using electrical capacitance metering. 18th FLOMEKO, Lisbon, Portugal, 2019
3. **Y. Arellano**, L. Ma. A. Hunt, O. Haas. Characterisation of the effects of sensor geometry on the performance of magnetic induction tomography systems. 9WICIPT, Bath, UK, 2018

Patent applications:

1. **Arellano, Y** and Ma, L. “Method and apparatus for monitoring of the multiphase flow in a pipe,” Patent application number: GB1810733.4.
   Applicant: iPhase ltd
   Contributions: The contribution of the present work to the patent document are withdrawn from the qualitative and quantitative analyses of the sensor performance presented in Section 4.5 and Sections 4.6
2. **Arellano, Y** and Ma, L. “Apparatus for monitoring of the multiphase flow in a pipe,” Patent application number: GB1810735.9
   Applicant: iPhase ltd
   Contributions: The contributions to the patent, that derives from this work, comprises the studies of shielding effectiveness of soft and hard shields presented in Section 5.3.3, the shielding effectiveness of hard shields in Section5.3.4, and the sensor structure discussed in Section 5.4.

Appendix B Filed patent documentation

Content removed on confidentiality grounds.

Content removed on confidentiality grounds.

Appendix C Summary of simulation models

Table C-1. Summary of simulation approaches used in the thesis chapters

Chapter	Model characteristics	Justification
Chapter IV Coil Geometry assessment	*Model A – CST studio Student version (mesh size ~9000 tetrahedral elements)* *Model B – COMSOL AC/DC module (mesh size ~500000 tetrahedral elements)*	
	Free space: Model A: Cube Model B: Cylinder with outer Infinite Elements layer Size (Model A/ Model B): 3 times larger than the largest dimension in the model.	From Section 3.6.1: "The proximity of results suggests that the size considered for the free space domain is sufficiently large to confine the extent of the physical effect." The Infinite Elements built-in feature avoids truncation of the field (Section 3.5.1.1)
	Coil model: Model A: Geometry Approximation (stranded conductors). Dual-coil model enclosed in dummy toroid. Model B: Geometry Approximation (multi-turn coils). Dual-coil model.	The built-in coil domain approximation reduces the computational cost of the models while ensuring a closed current path in agreement with Maxwell's equations (see Section 3.5.2). Furthermore, the use of a dual-coil model ensures decreased computational cost. In Section 3.6.4, it was proven that a dual coil model provides a good approximation to the full coil model. To overcome the limitation on the number of mesh elements of the software for Model A the coils were enclosed in dummy toroid (refer to Section 3.6.3). The geometry approximation was found to agree with laboratory data, as discussed in Section 3.6.5.2.
Chapter IV Self-resonance Frequency determination	*Model C – Eigenfrequency study in COMSOL/RF module*	
	Free space: Sphere: 3 times the larger than the largest dimension in the model terminated in PML.	PML provides a boundary condition where waves are absorbed into the domain without reflection (Section 3.5.1.1)
	Coil model: Detailed geometry. Single coil model.	From Section 3.5.1.2: Determination of the fundamental frequency of the coils required modelling the detailed features of the geometry and performing an eigenfrequency study. The alternative approach of modelling the coils using stranded blocks to simulate the coil geometry do not account for winding capacity and thus is not fit for purpose.
Chapter V Attenuation materials	*Model D – CST studio Student version (mesh size ~9000 tetrahedral elements)*	

	Free space: Same as Model A **Coil model:** Same as Model A **Attenuation materials:** (a) Rectangular / Aluminium sheet / Thickness: 2.1 mm (b) Rectangular / Aluminium sheet / Thickness: 6.3 mm (c) Cylindrical / Aluminium / Thickness: 2.1 mm	The modelling approach where the material properties are included in the simulation model, and no boundary condition are set to truncate the fields, allows for the electrical properties of the shielding material to be considered and the decay of the magnetic field through the thickness of the barrier evaluated (see Section 3.6.5)
Chapter VI Stratified flow	*Model E – COMSOL AC/DC module (mesh size ~2MM tetrahedral elements)*	
	Free space: Same as Model B	
	Coil model: Geometry Approximation (same as Model B). Full 8-coil model	Although the full coil model has a high computational cost, the full setup is required to identify the sensitivity of the measurements to the position of the coils around the pipe.
	Shield: Aluminium cylinder / Thickness: 1 mm / sf: 1.5 / TBC model approach	The shielding material was selected to provide a close representation to the hardware setup (discussed in detail in Chapter V) The TBC model approach is selected as it considers the material properties as well as the thickness of the material, leading to a drop in the transmitted electric field. This, in combination with a stand-off distance of 1.5 times the coil diameter allows modelling the field attenuation without truncation of the phenomena under evaluation (see discussion in Section 3.5.1.3 and results in Section 3.6.5.1).
	Materials inside pipe: Oil and Water (electrical properties as in Table VI-3)	
Chapter VII Three-phase measurement	*Model F – COMSOL AC/DC module (mesh size ~2.5MM tetrahedral elements)*	
	Free space: Same as Model B **Coil model:** Same as Model E **Materials inside pipe:** Oil and Water (electrical properties as in Table VII-1)	Refer to justification for Model B and Model E above.

Medium to High Risk Research Ethics Approval

Content removed on data protection grounds.

Content removed on data protection grounds.

Content removed on data protection grounds.

Content removed on data protection grounds.

Content removed on data protection grounds.

Content removed on data protection grounds.

Content removed on data protection grounds.

Content removed on data protection grounds.

Content removed on data protection grounds.

Content removed on data protection grounds.

Content removed on data protection grounds.

Content removed on data protection grounds.

Content removed on data protection grounds.